



HAL
open science

Luminescent surfaces to fight or detect bacteria

Gabriela Morán Cruz

► **To cite this version:**

Gabriela Morán Cruz. Luminescent surfaces to fight or detect bacteria. Material chemistry. Université Paris-Saclay, 2019. English. NNT : 2019SACLS214 . tel-02319018

HAL Id: tel-02319018

<https://theses.hal.science/tel-02319018>

Submitted on 17 Oct 2019

HAL is a multi-disciplinary open access archive for the deposit and dissemination of scientific research documents, whether they are published or not. The documents may come from teaching and research institutions in France or abroad, or from public or private research centers.

L'archive ouverte pluridisciplinaire **HAL**, est destinée au dépôt et à la diffusion de documents scientifiques de niveau recherche, publiés ou non, émanant des établissements d'enseignement et de recherche français ou étrangers, des laboratoires publics ou privés.

Luminescent Surfaces to Kill or Detect Bacteria

Thèse de doctorat de l'Université Paris-Saclay
préparée à l'Université Paris-Sud

École doctorale n°571 : Sciences Chimiques : Molécules, Matériaux,
Instrumentation Et Biosystèmes (2MIB)
Spécialité de doctorat: Chimie

Thèse présentée et soutenue à Orsay, le 25 juillet 2019, par

M^{lle} Gabriela Morán Cruz

Composition du Jury :

Antoine PALLANDRE Professeur, Université Paris-Sud (LCP)	Président
Alain JONAS Professeur, Université Catholique de Louvain	Rapporteur
Andreas REISCH Maître de Conférences, Université de Strasbourg (LBP)	Rapporteur
Michel SLIWA Charge de Recherche, Université de Lille (LASIR)	Examineur
Pamela PENNINGTON Professeur, Universidad del Valle de Guatemala (UVG)	Examinatrice
Rachel MÉALLET-RENAULT Professeure, Université Paris-Sud (ISMO)	Directrice de thèse
Bianca SCLAVI Directrice de Recherche, CNRS, Sorbonne Université (LCQB)	Co-Directrice de thèse
Gilles CLAVIER Directeur de Recherche, CNRS, École Normale Supérieure Paris-Saclay (PPSM)	Invité
Nienke BUDELMEIJER Directrice de Recherche, Institut Pasteur	Invitée

Titre : Surfaces luminescentes pour la detection ou la lutte contre les bacteries

Mots clés : Fluorescence, Surfaces, Bactéries, Nanoparticules, Microscopie

Résumé : Résumé : Le 20ème siècle a vu le recul des maladies infectieuses grâce aux antibiotiques. Cependant leur importante utilisation a rendu certaines bactéries, comme *Staphylococcus aureus* ou *Pseudomonas aeruginosa* (multi)résistantes. Un des moyens de lutte est de réduire la consommation d'antibiotiques ou de cibler ceux qui seront actif sur une souche identifiée. Nous souhaitons développer des surfaces et des dispositifs sensibles pour la détection précoce, rapide de bactéries pathogènes dans des fluides. Cela permettra de limiter la contamination et donc l'usage de médicaments. Ce projet regroupe 3 partenaires qui travaillent en synergie en mettant à profit leur expertise en physico-chimie, chimie de synthèse et microbiologie. Des nano-objets fluorescents, biocompatibles, et sensibles à la croissance bactérienne seront immobilisés sur des surfaces de verre. Ils seront rendus sélectifs de bactéries pathogènes par des traitements post-synthétiques. Il s'agit in fine de mettre au point un dispositif de détection miniaturisé et de tester la résistance aux antibiotiques des pathogènes détectés.

Title : Luminescent Surfaces to Kill or Detect Bacteria

Keywords : Fluorescence, Surfaces, Bacteria, Nanoparticles, Microscopy

Abstract : Infectious diseases have recessed during the 20th century thanks to antibiotics. However, some bacterial strains like *Staphylococcus aureus* or *Pseudomonas aeruginosa* have become (multi)resistant to antibiotic treatments because of overuse. One way to combat this is to reduce consumption of drugs or to better target those that will eliminate a given strain. We wish to develop sensitive surfaces and devices for the early and rapid detection of pathogenic bacteria in fluids. They will help limit contaminations and the use of drugs. The project gathers 3 partners working in synergy because they combine expertise in physical-chemistry, synthetic chemistry and microbiology. Fluorescent nanoobjects that are biocompatible and sensitive to bacterial growth will be immobilized on glass surfaces. They will be selective for pathogenic bacteria by post-synthetic modifications. The final goal is to build miniaturized sensitive devices that can detect pathogens and further test their resistance to antibiotics.

L'Organisation mondiale de la santé (L'OMS) a récemment signalé que «la résistance aux antibiotiques représente une menace croissante pour la santé et la sécurité publique dans le monde». Au moins 50000 décès annuels, uniquement en Europe et aux États-Unis, sont dus à des infections résistantes aux antibiotiques. Comme proposé par le Centre de contrôle et de prévention des maladies (CDC), quatre actions essentielles sont nécessaires pour prévenir la résistance aux antibiotiques: premièrement, la prévention des infections qui permet la prévention de la propagation de la résistance; deuxièmement, suivre et rassembler des données sur les infections résistantes aux antibiotiques; troisièmement, améliorer la prescription et l'utilisation des antibiotiques. Et enfin, développer de nouveaux médicaments et tests de diagnostic. Afin de participer à l'effort mondial de lutte contre la résistance, deux stratégies différentes seront explorées dans ce manuscrit en suivant deux des quatre actions principales proposées par le CDC: premièrement, par le développement et la caractérisation d'un capteur pour la détection de bactéries; deuxièmement, par l'étude et la caractérisation de nouveaux matériaux antibactériens utilisés pour éviter l'adhésion des pathogènes ou tuer les bactéries, afin de prévenir les infections associées aux biofilms.

Le manuscrit est organisé comme suit:

Première partie:

La croissance bactérienne est souvent associée à une diminution du pH du milieu de croissance en raison de la libération de métabolites acides tels que l'acide acétique, l'acide lactique et le CO₂. Par conséquent, différents types de capteurs de pH ont été utilisés pour mesurer la croissance des bactéries. Grâce à des travaux précédents, des nanoparticules fluorescentes (FNP) auto-stabilisées, solubles dans l'eau et ultra-brillantes, facilement synthétisables ont été mises au point. Récemment, ces FNP ont été utilisées pour préparer un nouveau nanocapteur ratiométrique du pH. Notre objectif est de développer des surfaces sensibles au pH, offrant une configuration plus robuste, technologique, transportable et facile à manipuler, capable de détecter les bactéries en quelques heures à l'aide d'un signal de fluorescence ratiométrique. La partie centrale de l'appareil utilisera les nanocapteurs immobilisés préparés à partir de nos nanoparticules fluorescentes (FNP). La synthèse, la caractérisation et la réponse au pH d'un nouveau type

de FNP seront présentées (**chapitre 2**). Par la suite, comme preuve de concept, nous avons commencé à mettre au point des surfaces qui pourront par la suite être embarquées dans un microdispositif : la préparation, la caractérisation et l'étude des surfaces sensibles au pH à l'aide de ces nouveaux FNP seront présentées (**chapitre 3**).

Deuxième partie:

Un problème majeur de santé publique est lié aux infections associées aux biofilms. Les bactéries prolifèrent rapidement après avoir adhéré sur une surface, sécrétant une matrice extracellulaire et formant ainsi des biofilms (colonies). Plusieurs stratégies visant à éviter la fixation de bactéries sur les surfaces ont été proposées au cours de la dernière décennie. Parmi celles-ci, deux catégories générales peuvent être distinguées: premièrement, tuer des bactéries par des composés antimicrobiens présentes à la surface (par libération ou contact direct) et deuxièmement, empêcher l'adhésion bactérienne grâce à des interactions physico-chimiques ou à des approches morphologiques.

Nous avons exploré la voie consistant à « repousser » les bactéries et nous avons étudié l'interaction des pathogènes avec de nouveaux films polymères superhydrophobes et luminescents (**chapitre 4**), ceux-ci se sont révélés efficaces contre l'adhésion bactérienne et donc la formation de biofilm. Par ailleurs, nous avons déterminé l'efficacité bactéricide d'un nouveau polymère imprimé par lithographie. Les surfaces bien organisées sont formées d'un polymère contenant un colorant, capable de libérer et de permettre la diffusion de l'oxygène singulet lors d'une irradiation (**chapitre 5**).

Table of contents

Abbreviations	9
Synthesized Structures Summary	13
General Introduction.....	17
Part I: Bacterial Growth Detection	19
Chapter 1: State-of-art	21
Antimicrobial resistance	23
Bacterial Detection	25
i. Traditional Methods	25
ii. Emerging Methods	26
iii. Group expertise and approach.....	29
iv. pH sensing surfaces	33
Chapter 2: Fluorescent Nanoparticles.....	41
Introduction.....	43
Materials & Methods	49
1.1.1. Materials	49
1.1.2. Synthetic Methods	49
1.1.3. FNP Characterization Methods	64
Results & Discussion	66
Conclusions & Perspectives.....	94
Chapter 3: pH sensing surfaces	99
Introduction.....	101
Materials & Methods	103
3.1.1. Materials	103
3.1.2. Surface Functionalization	103
3.1.3. Surface Characterization.....	105
Results & Discussion	109
Conclusions & Perspectives.....	128
Part II: Antibacterial Surfaces	135
Chapter 4: Repelling Bacteria Surfaces.....	137
Introduction.....	138

4.1 Article 1: “Superhydrophobic Surfaces Toward Prevention of Biofilm-Associated Infections”	142
4.2 Article 2: “Superhydrophobic polypyrene films to prevent <i>Staphylococcus aureus</i> and <i>Pseudomonas aeruginosa</i> biofilm adhesion on surfaces: high efficiency deciphered by fluorescence microscopy”	158
4.3 Article 3: “Anti-bacterial and fluorescent properties of hydrophobic electrodeposited non-fluorinated polypyrenes”	180
4.4 Article 4: “Superhydrophobic and fluorescent properties of fluorinated polypyrene surfaces using various polar linkers prepared via electropolymerization”	193
Conclusions & Perspectives.....	206
Chapter 5: Killing Bacteria Surfaces	209
Introduction.....	211
5.1 Article 5: “Highly Virulent Bactericidal Effects of Curcumin-based μ -Cages Fabricated by Two-Photon Polymerization.”	215
General Conclusion & Perspectives	223

Abbreviations

A	Absorbance
AA	Acrylic acid
ACPA	4,4'-azobis(4-cyanopentanoic acid)
AFM	Atomic force microscopy
AIBN	2,2'-Azobisisobutyronitrile
B	Brilliance
BODIPY / BDP	4-difluoro-4-bora-3a,4a-diaza-s-indacene
BDPMA	BODIPY- methacrylate
CFU	Colony-forming units
Chloranile	Tetrachloro-1,4-benzoquinone
D _h	Hydrodynamic diameter
DBU	1-8-diazabicyclo[5,4,0]undec-7-ene
DCC	N,N'-dicyclohexylcarbodiimide
DCM	Dichloromethane
DDQ	2,3-dichloro-5,6-dicyano-1,4-benzoquinone
D.I.	Deionized
DIBO	4-dibenzocyclooctynol
DIPEA	N,N-diisopropylethylamine
DLS	Dynamic light scattering
DMAP	4-dimethylaminopyridine
DMF	Dimethylformamide

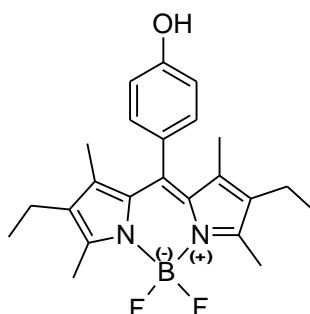
DMSO	Dimethylsulfoxyde
EDC	N-(3-Dimethylaminopropyl)-N'-ethylcarbodiimide hydrochloride
EDSA	3-(Ethoxydimethylsilyl) propylamine
ϵ	Molar extinction coefficient
Et ₃ N	Triethylamine
EtOAc	Ethyl acetate
EtOHNH ₂	Ethanolamine
FA	Fluorescein Amine
FITC	Fluorescein isothiocyanate
FNP	Fluorescent nanoparticle
FRET	Förster Resonance Energy Transfer
HD	Hexadecane
IR	Infrared
Kryptopyrrole	2,4-dimethyl-3-ethylpyrrole
LB	Lysogeny broth
λ_{abs}	Absorption wavelength
λ_{exc}	Excitation wavelength
λ_{em}	Emission wavelength
NMR	Nuclear magnetic resonance
NTA	Nanoparticle tracking analysis
OD	Optical density
PA	<i>Pseudomonas aeruginosa</i>
PBS	Phosphate buffer saline
PEG	Poly(ethylene glycol)

PEO	Poly(ethylene oxide)
PTA	Phosphotungstic acid
Φ_F	Fluorescence quantum yield
PDMS	Polydimethylsiloxane
PMMA	Poly(methyl methacrylate)
PS	Polystyrene
QD	Quantum dot
R_h	Hydrodynamic radius
RAFT	Reversible addition-fragmentation chain-transfer
RI	Refraction index
SA	<i>Staphylococcus aureus</i>
SDS	Sodium dodecyl sulfate
SEM	Scanning electron microscopy
σ	Polydispersity index
t	Time
T	Temperature
τ	Luminescence lifetime
TEM	Transmission electron microscopy
TFA	Trifluoroacetic acid
THF	Tetrahydrofuran
TSA	Tryptic soy agar
TSB	Tryptic soy broth
TTCA	2-methyl-2-[(dodecylsulfanyl-thiocarbonyl)sulfanyl] propanoic acid
UV-VIS	Ultraviolet-visible

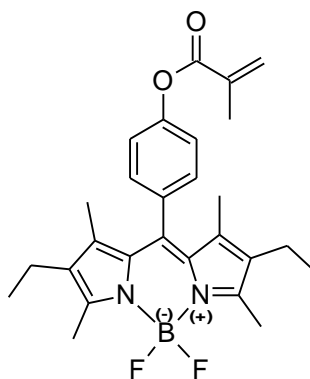
US	Ultrasounds
XPS	X-ray photoelectron spectroscopy
ζ	Zeta potential

Synthesized Structures Summary

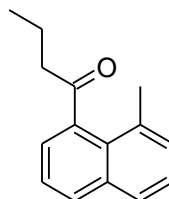
- 1 **Green BDP**
2,6-diethyl-4,4-difluoro-8-(4-hydroxyphenyl)-1,3,5,7-tetramethyl-4-bora-3a,4a-diaza-s-indacene



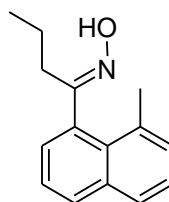
- 2 **Green BDPMA**
2,6-diethyl-4,4-difluoro-8-(4-(methacryloyloxy)phenyl)-1,3,5,7-tetramethyl-4-bora-3a,4a-diaza-s-indacene



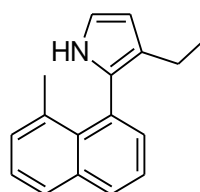
- 3 **1-(8-Methylnaphthalene-1-yl)butane-1-one**



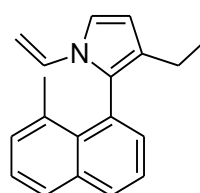
4 Oxime of 1-(8-Methylnaphthalene-1-yl)butane-1-one (Z,E)



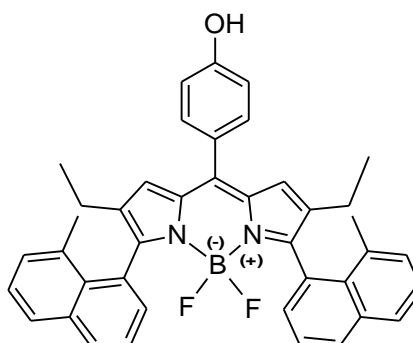
5 Methylnaphthalene Pyrrole
3-ethyl-2-(8-methylnaphthalene-1-yl)-1H-pyrrole



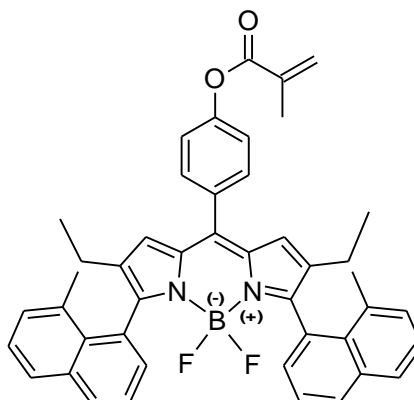
6 N-vinyl Pyrrole
3-ethyl-2-(8-methylnaphthalene-1-yl)-1-vinyl-1H-pyrrole



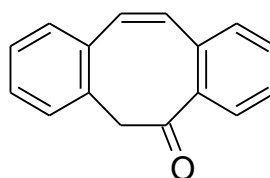
7 Red-BDP
2,6-diethyl-4,4-difluoro-8-(4-hydroxyphenyl)-5,3-(9-methyl-1-naphthyl)-4-bora-3a,4a-diaza-s-indacene



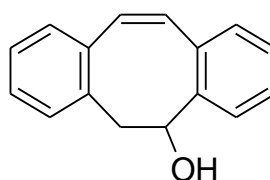
- 8 **Red-BDPMA**
2,6-diethyl-4,4-difluoro-8-(4-(methacryloyloxy)phenyl)-5,3-(9-methyl-1-naphthyl)-4-bora-3a,4a-diaza-s-indacene



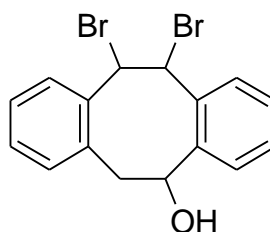
- 9 **6H-Dibenzo[a,e]cyclooctatrien-5-one**



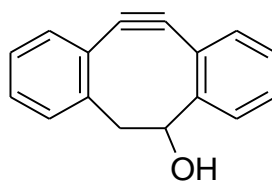
- 10 **5,6-Dihydro-dibenzo[a,e]cycloocten-5-ol**



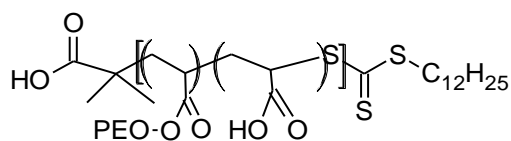
- 11 **11,12-Dibromo-5,6,11,12-tetrahydro-dibenzo[a,e]cycloocten-5-ol**



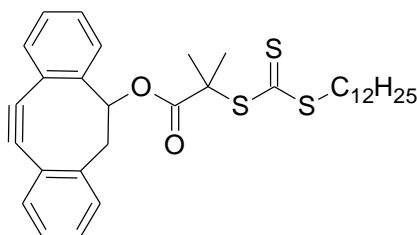
- 12 **DIBO**
5,6-Dihydro-11,12-didehydro-dibenzo[a,e]cycloocten-5-ol



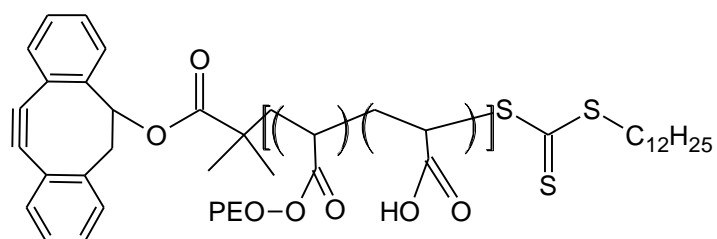
- 13 **(PEOA-co-AA)-TTCA**



- 14 **DIBO-TTCA**



- 15 **(PEOA-co-AA)-TTCA- DIBO**



General Introduction

The World Health Organization (WHO) recently reported that ‘Antimicrobial resistance (AMR) represents a growing threat to global public health and security’. At least 50000 annual deaths, across Europe and the US alone, are due to antimicrobial-resistant infections. As proposed by the Center for Disease Control and Prevention (CDC), four core actions are needed to prevent AMR: first, the prevention of infections and the spread of resistance; second, tracking and gathering data on antibiotic-resistant infections; third, improving antibiotic prescribing practices and use; and lastly, developing new drugs and diagnostic tests. In this manuscript two different strategies will be investigated that follow two of the four core actions proposed by the CDC: first, by the development and characterization of a sensor for bacterial detection; secondly, by the study and characterization of new antibacterial materials as repelling films or bacteria killing surfaces, to prevent biofilm-associated infections.

The manuscript is organized as follows:

First part:

Bacterial growth is often associated with a pH decrease of the growth medium due to a release of acidic metabolites such as acetic acid, lactic acid and CO₂. Therefore, different kinds of pH-based sensors have been developed to measure the growth of bacteria. Taking advantage of formerly developed self-stabilized, water-soluble, ultra-bright fluorescent nanoparticles (FNPs), we aimed to develop pH-sensitive surfaces, offering a more robust, transportable and easy to handle set up, able to detect bacteria within a few hours by a ratiometric fluorescence signal. The central part of the device will use immobilized nanosensors. The synthesis, characterization and pH-response of new

kinds of FNPs is presented (**Chapter 2**). Later, as proof-of-concept, in an early step to our final goal of developing a point-of-care device: the preparation, characterization and study of pH-sensitive surfaces (**Chapter 3**) by using these new FNPs will be investigated.

Second part:

A major public health problem in nosocomial environments is due to biofilm-associated infections. Bacteria rapidly proliferate after adhering on surfaces, secreting an extracellular matrix and thus forming biofilms. Several strategies to avoid bacteria attachment on surfaces have been proposed over the last decade. Among these strategies, two general categories can be differentiated: first, surfaces that kill bacteria through antimicrobial compounds (by release of direct contact) and second, repelling bacterial attachment through physical-chemical interactions or morphological approaches.

Relying on the bacteria-repelling surface strategy, we studied the interaction of new, luminescent, superhydrophobic polymer films with bacteria (**Chapter 5**), which have proven to be effective against bacterial adhesion and thus, biofilm formation.

In addition, considering bacteria-killing surfaces, we determined the efficiency of killing bacteria of a new lithography-printed polymer. The well-organized surfaces consisted on a polymer containing a dye, which was able to release and allow the diffusion of singlet oxygen upon irradiation (**Chapter 6**).

Part I: Bacterial Growth Detection

Chapter 1: State-of-art

Antimicrobial resistance

Bacterial infections have been dangerous for the human species since the beginning of human existence (1). After the discovery of the first antibiotic drug, penicillin, by Alexander Fleming, a huge decrease in the number of deaths caused by infectious diseases occurred (1). Nevertheless, for some antibiotics it took only a few years for bacteria to develop antimicrobial resistance (AMR). For example, methicillin-resistant *Staphylococcus aureus* (MRSA) was reported just one year after methicillin was introduced (1). After almost nine decades of extended use of antibiotics, AMR has reemerged as a major and alarming threat to worldwide health.

In addition to AMR, very few new antibiotics molecules are approved each year for use in the clinic, and according to the World Health Organization (WHO), current clinical developments show that the drugs in the clinical pipeline are mainly modifications of existing antibiotics. This represents only short-term solutions and has been shown to be insufficient against the pathogens on the priority pathogens list of AMR (2).

AMR is caused by different factors, including poor sanitary conditions, inappropriate food handling, poor infection prevention and control practices in hospitals, but mainly it is due to the misuse and overuse of antibiotics in health care and for the breeding of crops and animals (3). AMR is caused by mutations in the DNA, which means that it is triggered by genetic alterations and is heritable (4). Some of the mechanisms bacteria use to resist antimicrobial agents are presented in Figure 1.1. A more detailed description of each mechanism has been described elsewhere (5, 6).

As mentioned before, the Center for Disease Control and Prevention (CDC) has proposed four core actions needed to prevent AMR (3):

1. preventing the spread of resistance by the prevention of infections;
2. tracking and gathering data on antibiotic-resistant infections;
3. improving antibiotic prescription protocols and use;
4. developing new drugs and diagnostic tests

Summary of resistance mechanisms

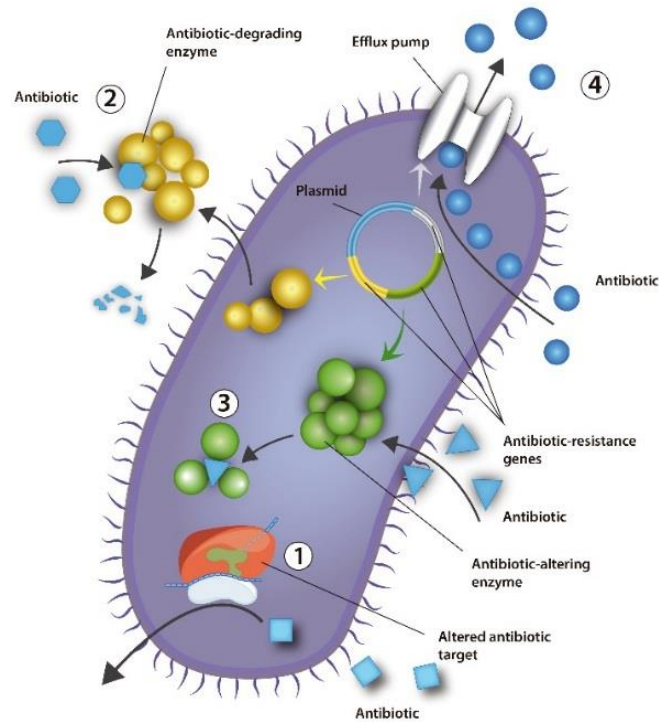


Figure 1.1 Mechanisms of bacterial resistance. Adapted from Kenneth Todar, www.textbookofbacteriology.net

1. Altered antibiotic target by molecular modification to reduce affinity
2. Enzymatic degradation of the antibiotic
3. Enzymatic or molecular modification of the antibiotic
4. Efflux pump expression or modification of the membrane permeability

Herein, we approached two different strategies of the four core actions proposed by the CDC: first, we aimed to build a diagnostic test by the development and characterization of a sensor for early and sensitive bacterial detection and AMR screening. Secondly, to prevent the spread of the resistance by the study and characterization of new antibacterial materials as repelling films or killing bacteria surfaces, such surfaces might prove to be useful to prevent biofilm-associated infections. Next, the state-of-art concerning bacterial detection will be presented.

Bacterial Detection

i. Traditional Methods

Fast, sensitive and accurate bacterial detection plays an important role for medical diagnostics and for the subsequent correct antibiotic prescription, reducing their misuse. Ideally, an assay should be able to detect a few specific CFUs within one hour or less, with a low cost and easy manipulation by the user. Conventional techniques to identify bacterial pathogens and the effect of antibiotics against them rely on laboratory assays such as plate counting, which allows one to identify the number of growing cells in a sample by the colony-forming unit (CFU). Moreover, plate counting can be used to determine the minimum inhibitory concentrations (MIC) for the detection of AMR (4). Nevertheless, this approach is time consuming for the user and slow to obtain a result (requiring between 37-48 hours), also it cannot be used for the bacterial strains that cannot be cultured in agar plates (7).

The development of molecular methods such as Real-Time Quantitative Polymerase Chain Reaction (qPCR), has helped to overcome some limitations of the classical techniques to detect bacteria. PCR results for the specific detection of genes responsible for resistance can be obtained within hours (in between 5 to 24 hours), however it does not provide information on the viability of the bacteria (8,9). Viability is critical to monitor the efficacy of antibiotics as well as assessing the presence or absence of viable pathogens in the samples (10). qPCR therefore precisely detects gene expressions but is not reliable for an absolute quantification in microbiology (11).

Mass spectroscopy-based techniques like MALDI-TOF (Matrix-Assisted Laser Desorption ionization-time of Flight), have emerged as a potential tool for bacterial detection (12). MALDI-TOF is currently used in clinical microbiology laboratories as routine technique for pathogens detection (13). The MALDI-TOF limit of detection (LOD) is as low as 10^5 CFU/ml, using few μ L of sample in couple of hours (specimen dependent) (14). A new antibiotic susceptibility commercial test coupled with MALDI-TOF (Sepsityper®) normally requires 10-20 min to be completed but requires a pre-culturing step, which is adding extra hours to the analysis. Efforts are being done to improve the direct detection of proteins associated with antibiotic resistance, as this

technique is being limited by a spectral database of mass fingerprints of bacterial strains (12,15).

Complementary to these techniques, immunological techniques rely on the specific binding of an antibody to an antigen, being widely used for medical diagnosis, such as Enzyme-Linked Immunosorbent Assay (ELISA) (16). Even though specificity is obtained, improvements in sensitivity remain necessary ($\sim 10^6$ CFU/ mL). While this approach sets the standard for all other assays for bacteria detection, the cost of antibodies remains quite high, in addition to the large reaction volumes required, and to being time consuming for the researcher or medical technician.

ii. Emerging Methods

With the advances in nanotechnology, new biosensors have been developed as an attempt to improve the commonly used techniques described above by implementing different types of nanoparticles. A biosensor must have a recognition element (such as enzymes, antibodies, nucleic acids, *etc.*) and a transduction element, which translates this interaction into an electrical, optical, thermometric signal (17) (Fig. 1.2).

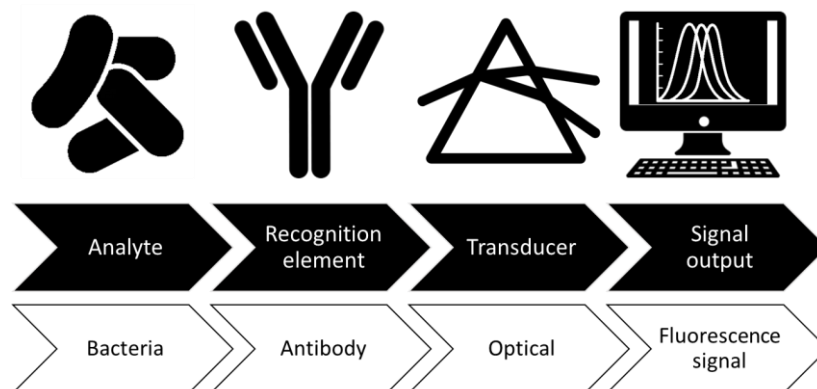


Figure 1.2 Schematic representation of a biosensor. Optical transducing and antibody recognition are shown as examples.

In the last decades, with the recent development in nanotechnology new solutions have been proposed to improve bacterial detection. For example, W. Chunglok, *et al.*

(18), by coating with antibodies single walled carbon nanotubes, they improved detection from a LOD of 10^6 CFU(Traditional ELISA) to a LOD of 10^3 CFU for *Salmonella enterica* serovar *Typhimurium* detection.

Another example for an improvement to immunoassays tests was done by Joo *et al* (19). This was done by implementing magnetic beads (MNPs) conjugated with antibodies specific for *Salmonella enterica*. After capturing selectively *Salmonella* over a mixture of proteins, lipids and other bacterial strains, the MNPs-*Salmonella* complexes were efficiently separated by applying an external magnetic field. In the next step, the MNPs-*Salmonella* complexes were labeled with TiO_2 nanocrystals (TNs), also conjugated with the same antibodies, in order to increase UV absorption. The sensitivity of the assay could thus be increased and has allowed the detection of low concentrations of *Salmonella* until reaching a detection limit of 100 CFU/ mL in milk. (Figure 1.3).

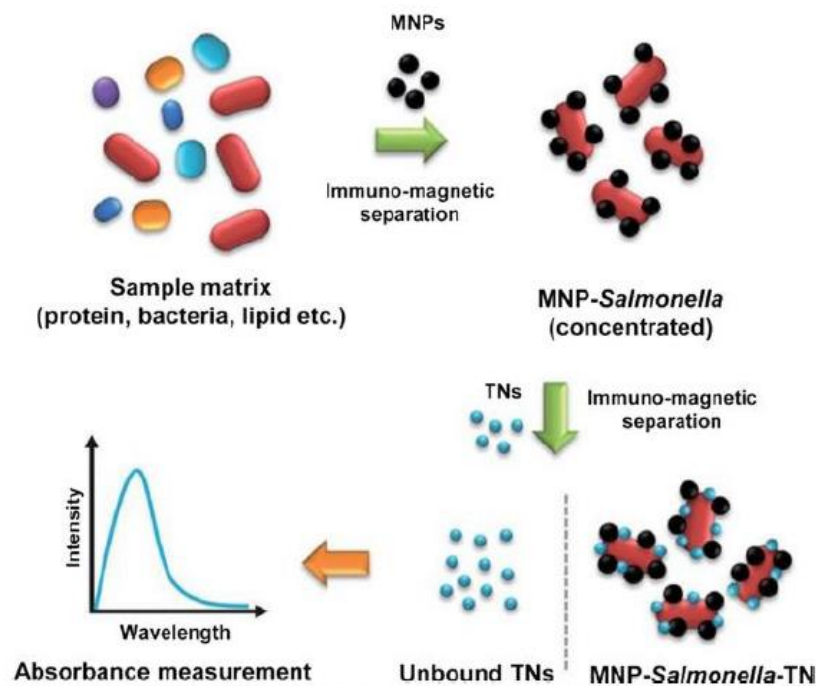


Figure 1.3 Schematic representation of the method using magnetic nanoparticles and optical nanoprobe (Ref. 19).

Gold nanoparticles have also been used as biosensors (20, 21). Shafiee *et al.*, developed a paper-based biosensor by depositing by capillary effect gold nanoparticles which aggregate, within 10 min, only when *E. coli* is present in the solution. Specific

detection was obtained by covalently grafting Lipopolysaccharide Binding Protein (LBP) on the gold nanoparticles. The presence of the bacteria resulted in a change of color (pink to dark blue) on the paper. LOD was as low as 8 CFU/mL (20).

Quantum Dots have been used as fluorescent markers for bacteria detection (22, 23). Wang *et al.* prepared CdSe/ZnS QDs incorporated into SiO₂ spheres to avoid toxicity. A linear relationship was obtained for the concentration of *Salmonella typhimurium* and fluorescence intensity, with a final LOD of 100 CFU/mL (22).

S. Agrawal *et al.* (23), developed a multiplexed system for waterborne pathogens (*Escherichia coli* and *Salmonella typhimurium*) in a microfluidic circular set-up (Fig. 1.4). First, using mobile magnets, antibodies conjugated with magnetic nanoparticles were entrapped by a magnetic field. In the next step, a mixture of bacteria and non-specific components (such as other bacteria and proteins) were flowed through the channel. Finally, the captured bacteria were labeled with antibody-conjugated QDs (using different color for each bacterial strain), which were used to obtain an amplified signal. The fluorescence signal from QDs was directly proportional to CFU/ mL of bacteria. The LOD was 10³, which is higher in comparison with Wang *et al.*, but the implementation of a microfluidic system opened many possibilities of use of microchannels to screen different bacterial strains in addition to being reusable. Nevertheless, it is not possible with this technique to detect the viability of bacteria.

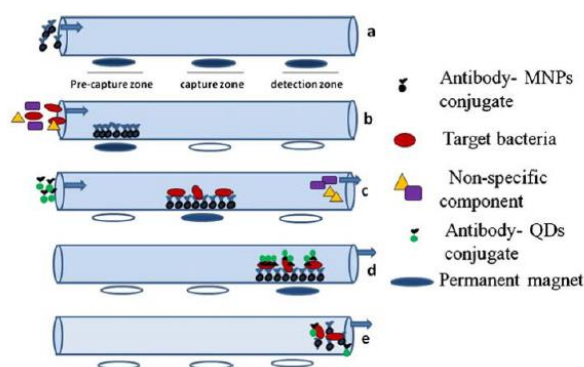


Figure 1.4 Schematic representation of the method using magnetic nanoparticles and QDs (Ref. 23).

A real-time measurement on a microfluidic device for single bacteria detection was presented by Yasaki *et al.* (24), combining ionic current sensing and fluorescence observation (with an epifluorescence microscope). This method could discriminate the bacteria by size (from polystyrene particles) and by using a fluorescent dye it could

discriminate between gram positive and gram negative bacterial strains (*B. subtilis* and *E. coli*) in 300 ms. This approach is interesting for real-time measurements, but it is still limited in having to stain the bacteria (however live/ dead test could be implemented).

Jalali et al. (25), proposed a microfluidic device obtained by modifying a gold microelectrodes surface and obtaining hierarchical 3D nano-/ micro protrusions, which were shown to attract bacteria. The introduction of these hierarchical 3D nano-/ micro protrusions improved greatly bacteria concentration and deposition, nevertheless, detection was done using dyes and antibodies to label the bacteria. LOD was 50 CFU/mL for *E. coli* and Methicillin-resistant *Staphylococcus aureus*.

While these biosensors were designed to detect bacteria in a more accurate and faster way (as *Shafiee et al.*, 8 CFU in 10 min), they left behind the measurement of the viability of the bacteria and most importantly, the screening of the resistance of bacteria to antibiotics, which remains one of the priorities to fight against AMR.

iii. Group expertise and approach

Different acidic species such as acetic acid, lactic acid and other metabolites are released upon bacterial growth resulting in a decrease of the pH of the growth medium (26). Considering this principle, different pH-sensors have been developed to detect bacteria (as examples: *Escherichia coli*, *Lactococcus lactis*, *Staphylococcus epidermidis*..., 27, 28, 29). Our research group has been working over the last years on self-stabilized, water-soluble and ultra-bright fluorescent nanoparticles, which are easily synthesized and highly tunable (30, 31, 32). This work started with the doctoral thesis Chloé Grazon (33), by optimizing the synthesis of polymer nanoparticles focusing on Green-BODIPY FNPs (Fig. 1.5). But also investigating the nanoparticles' versatility (fluorescent color core, polymer shell, monomers moiety, grafting of different chemical species on shell). As demonstrated by our group, organic nanoparticles can be smartly designed (besides having a tunable fluorescent core) their shell can provide functional groups to enable post-functionalization and facilitating the grafting over other nanoparticles. Nevertheless, organic nanoparticles remain scarcely investigated.

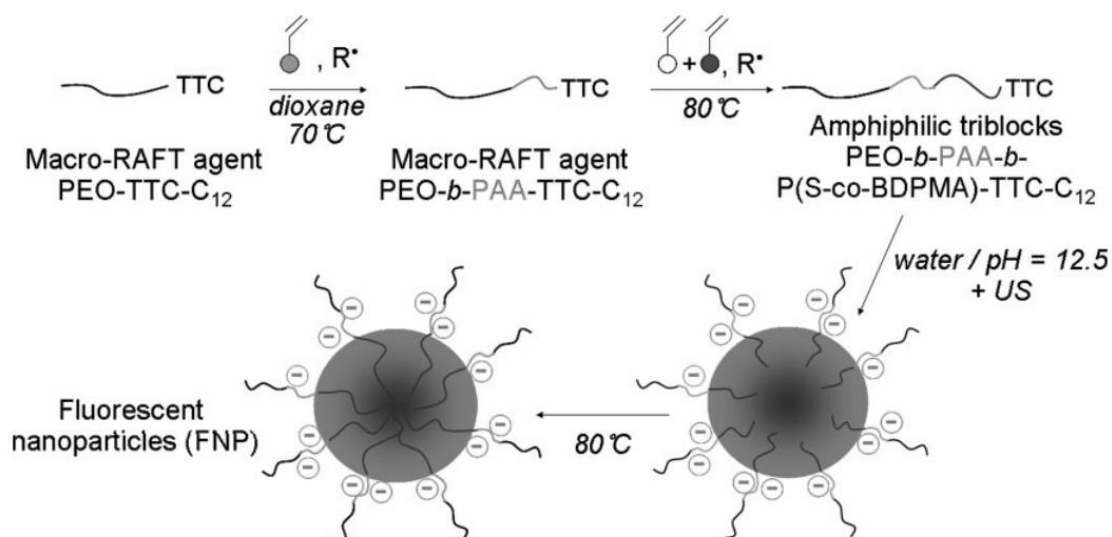


Figure 1.5 Synthetic pathway employed for the synthesis of FNPs proposed by G. Clavier Group (PPSM) (Ref. 30). The general protocol for synthesis starts by a reversible addition-fragmentation transfer (RAFT) polymerization. Obtained from a hydrophilic Poly(ethylene oxide) and Poly(acrylic acid) macromolecular RAFT agent which is block-extended with styrene and fluorescent BODIPY monomer. Then, a mini-emulsion is formed, following by the completion of the polymerization. (Please refer to abbreviations section for definitions).

By taking advantage of these FNPs, the following PhD. in our group, Yang Si (34), designed new FNPs without BODIPY in the core (only Styrene), but fluorescein in the shell as pH-sensitive FNPs. Y. Si *et al.* (35), were able to detect bacterial growth with a low starting concentration ($<10^3$ CFU/mL, OD: 0.00001) and using only 20 μ L. Figure 1.6 explains the central experiment. Assays were done in 96-well plates measuring *E. coli* bacteria growth incubated either with fluoresceinamine (FA) molecules or with nanoparticles grafted with Fluorescein on the shell (FANP1 and FNP2 correspond to higher and lower concentration of FA grafted on the shell respectively). Measurements were obtained using either optical density (600 nm, dotted lines) or the decrease of fluorescence intensity (% , full lines). The pH decreased from 7 to 5.8 in 300 min as the bacteria grew.

It is clearly seen in Fig. 1.6 that OD measurements are not sensitive enough in the early stages of bacterial growth, besides, the measurements are not reproducible during this phase (from 0 to 100 min). From Fig. 1.6 it can be seen that the slope obtained with FANP1 is higher than that of FANP2 and of the free FA. Quantitatively, the fluorescence intensity of the FANP1 decreased by almost 40 %, more than twice comparing to free FA. With this, FANPs proved to be more sensitive than the currently used molecular

sensors (Free FA) but also more sensitive and reliable than typical optical density (OD) meters (Fig. 1.6).

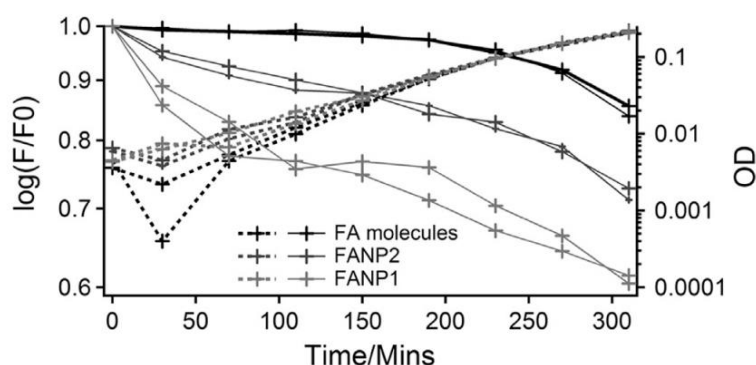


Figure 1.6 Growth of *E. coli* bacteria incubated with fluoresceinamine molecules (FA), Fluorescent nanoparticles with Fluorescein grafted on the shell (FANP1 and FNP2: higher and lower concentration of FA grafted on the shell respectively) using either the optical density (600 nm, dotted lines) or the decrease of fluorescence intensity (% , full lines) (Ref. 35).

Besides bacterial growth detection, screening of bacterial growth inhibition by antibiotics was studied. The inhibitory effect of three antibiotics was measured and compared to OD measurement. pH-sensitive FNPs allow to continuously monitor bacterial growth via real-time detection over long time scales (up to several hours) in small volumes (from one mL to a few μL) and can thus be used for high-throughput applications such as screening for the presence of antibiotic resistant strains (Y. Si *et al.* 35).

Recently, another publication from our group by C. Grazon *et al.* (36), introduced a work on a new ratiometric fluorescent pH nanosensor (Fig. 1.7). A ratiometric measurement uses two different fluorophores: one is not sensitive to the environment (reference dye) and the second one is (sensing dye). They used green-BODIPY FNPs with two spatially separated fluorophores: 4-difluoro-4-bora-3a,4a-diaza-s-indacene (Green-BODIPY) in the core of the nanoparticle and fluorescein covalently attached to the external surface. In this model, BODIPY was used as the reference dye and fluorescein as the sensing molecule. Meaning by this that the fluorescence of the reference dye (BODIPY) will remain stable upon the change in pH, while the fluorescence of the sensing molecule will change. Ratiometric measurements have the advantage over single-emission measurements of being independent of external fluctuations of the fluorescence

signal, such as photobleaching or leakage of the dye. Ratiometric measurements are also insensitive to ambient or scattered light and any instrumental fluctuations.

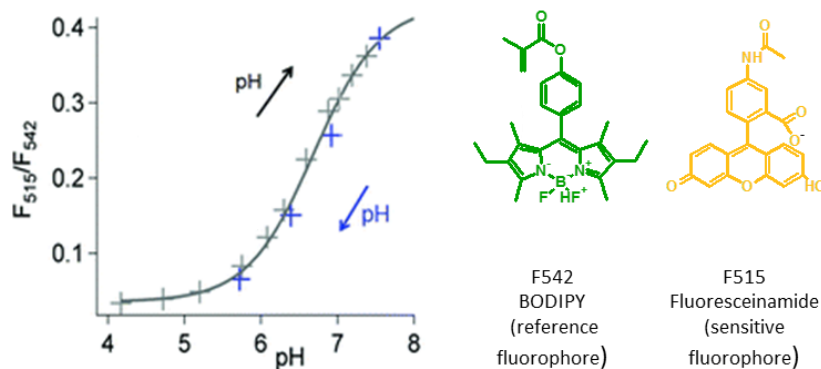


Figure 1.7 Variation of the ratio of fluorescence intensity at 515 nm (fluoresceinamide) and 542 nm (BODIPY – internal reference) of FNPs as a function of the pH. Adapted from ref. 36.

As previously presented, LOD and time are crucial parameters since bacterial infections from most common pathogens (such as *E. coli* and *S. aureus*) pose a major threat even at low concentrations such as 10 to 1000 CFU/ mL in food poisoning, sepsis, peritonitis and skin infections (which may also lead to sepsis) (26, 27). The faster and the more accurate (1 CFU/mL) the better. Point-of-care devices could offer a great potential concerning bacterial infections detection, where the common techniques such as ELISA, cell culturing and qPCR are limited. As told by *Rajapaksha et al.* (37), a new bacterial detection method should: *increase specificity; reliability; the availability of use; rapid turnaround; low cost; be standardized and high throughput.*

Motivated by these previous works, we aimed to develop a point-of-care device (long-term objective), which would offer a more robust, transportable and easy to handle set up, able to detect and identify specific bacteria strains within a few hours by ratiometric fluorescence signal to study antibiotic resistance. The central part of the device will use the immobilized nanosensors prepared from our FNPs. To achieve this, our first goal was to develop a surface sensitive to pH. Before explaining our methodology, we will expose some literature data to give an idea of the context in the following section.

iv. pH sensing surfaces

The development of surfaces to be used as pH-sensors has been subject of interest over the last few decades (38). Grant and Glass prepared a fiber-optic pH sensor by sol-gel encapsulation of a self-referencing dye, seminaphthorhodamine-1 carboxylate (SNARF-1C) (39). Calibration of the sensor was obtained with PBS buffer with a pH from 6.8 to 8 (average increment of 0.12 units), using 2 mL of sample and changing the pH by adding 0.1 M HCl or 0.1 M NH₄OH (1-5 μ L increments). The response of the sensor was linear in the pH range 6.8-8. Stability of the sensor was observed after 24h, the sensor showed some cracks, but this was improved by adding a coat of polyurethane. Response of the sensor in blood was similar to PBS, but the intensity ratio decreased. The presence of high concentrations of proton acceptors found in the blood may perturb the ratio and apparent pH values as stated by Whitaker (40). Reproducibility was compared by using 4 different sensors using the same formulation. The difficulty in preparing sensors reproducibly was evident, since the sensors should be calibrated individually before use.

Niu *et al*, prepared a new ratiometric pH-sensing surface by the attachment of a pH-sensitive porphyrin and a dye as reference (N-2(methacryloxyethyl) benzo[k,l]thioxanthene-3,4-dicaboximide, MBTD) (41). The immobilization of the dyes was obtained by silanization of the glass surface, followed by the incorporation of a sensing photopolymerized membrane (40 μ m thick). This surface allowed a linear ratiometric measurement of the pH between 1.0 and 5.0 (pH increments around 0.25), in a reversible manner. Nevertheless, the fluorophores are not commercial and need to be synthesized. The sensor detected the pH successfully even under the presence of certain ions simulating waste water (ions like Pb²⁺, Hg²⁺, Cd²⁺, Cd²⁺).

Kateklum *et al*, compared the pH-sensitivity efficiency of two different amino-silane molecules, grafted with fluorescein (42). The first method uses only 3-aminopropyl trimethoxysilane (APTMS), producing a flat available layer of amine. The second method uses first APTMS and then a second layer of 3-aminopropyl dimethoxymethylsilane (APDMS), producing a volume of brush-like structure resulting in more available amine groups (first time reported). Amine quantification was obtained using Fourier Transform Infrared Spectroscopy (FTIR). Buffers with various pH were tested in a range of 6.5 to 8.5 (6.5, 7.0, 7.2, 8.5). Few microliters of buffer were used, leaving about 10 min of

reaction time to reach chemical equilibrium. The brush-like configuration proved to be more efficient than a single monolayer of silane by a factor of 5.

A different approach, using thiolene chemistry was done by Craciun *et al.*, immobilizing polymer nanocompartments on glass surfaces (43). Glass cover slips were used as substrate and functionalized with a 3-(mercaptopropyl) trimethoxysilane linker according to previously published procedures (Fig. 1.8). Before attachment, the pH responsive dye (pyranine) was encapsulated within nanocompartments and the pH responsiveness of the particles in solution at pH 8 to pH 6 was established. A decrease in the fluorescent signal was observed upon addition of lactic acid (measured pH range 8-6, 0.5 increments) and an increase in fluorescence was observed upon addition of ethylenediamine, a biogenic amine (measured pH range 6 – 8). These last two studies were only a proof of concept, without any application, and the measurements were carried out with only one sensing dye as a single-emitter, which can lead to a bias in the results, unlike with ratiometric detection.

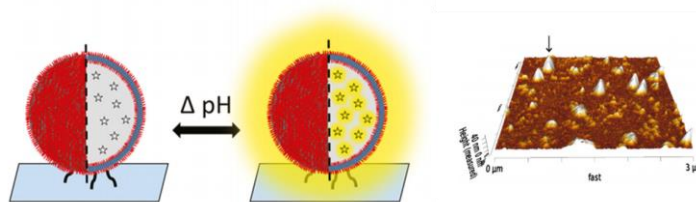


Figure 1.8 Single-emitter pH sensitive surfaces prepared by Craciun *et al.* Adapted from 43.

Rigo *et al.*, used a different approach to immobilize fluorescent nanoparticles on glass, based on click-chemistry (DBCO, figure 1.9) (44). They used co-immobilized polymersomes micelle assemblies (polymersomes are made using amphiphilic synthetic block copolymers to form the vesicle membrane). The surface was activated by plasma, followed by silanization. No direct application was shown but the encapsulation of an hydrophobic dye was done as a proof of concept of the loading capability of the polymersomes. The DBCO molecule was covalently attached by peptide coupling.

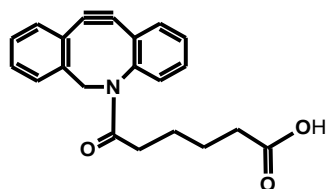


Figure 1.9 Scheme of DBCO molecule used by Rigo *et al.* (44), allowing both click-chemistry and peptide coupling.

As shown in this summary, different approaches to design pH-sensitive surfaces have been proposed. Nevertheless, the application of pH-sensing surfaces for bacterial growth detection and high-throughput applications such as screening for the presence of antibiotic resistant strains, remains uninvestigated. As mentioned above, the first part of this manuscript describes the initial steps for the development of a ratiometric fluorescence pH-sensor on a glass surfaces (Figure 1.10), with the aim to accurately detect and identify bacterial growth and antibiotic resistance in just a few hours and starting from a low OD (0.01). In this first part, **Chapter 2** will detail the synthesis and characterization of a new family of FNPs. **Chapter 3** will focus on preparation and characterization of pH-sensing surfaces, based on the new family of FNPs, finishing with the study of bacterial growth detection.

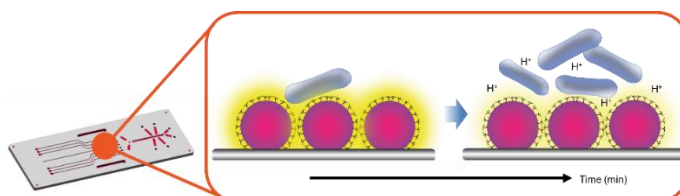


Figure 1.10 Working principle of the point-of-care device: upon bacterial growth, acidic species will be released to the medium resulting in a decrease of pH. The sensing dye (Fluorescein) will be quenched by this change, while the reference dye (BODIPY) in the core of the nanoparticles shall remain stable. The change of the ratio of fluorescence intensity at 525 and 600 nm of FNPs as a function of pH (an expected change of pH between 7 to 5.5) will be correlated with bacterial growth, allowing for further screening for AMR.

- (1) D. Debatov, 'Antibiotic Resistance: origins, mechanisms, approaches to counter', *Appl. Biochem. Microbiol*, 2013, 49, 9, 665.
- (2) WHO, Antibacterial agents in clinical development. <https://apps.who.int/iris/bitstream/handle/10665/258965/WHO-EMP-IAU-2017.11-eng.pdf?sequence=1>
- (3) Center for Disease Control and Prevention (CDC), drug resistance report. <https://www.cdc.gov/drugresistance/threat-report-2013/pdf/ar-threats-2013-508.pdf>
- (4) A. Brauner *et al.*, Distinguishing between resistance, tolerance and persistence to antibiotic treatment. *Nat. Rev. Microbiol*, 2016, 14, 5, 320.
- (5) F. Depardieu *et al.*, Modes and modulations of antibiotic resistance gene expression. *Clin. Microbiol. Rev.*, 2007, 20, 79.
- (6) J. M. Blair *et al.*, Molecular mechanisms of antibiotic resistance. *Nat. Rev. Microbiol*, 2015, 13, 42.
- (7) M. Farhat *et al.*, Metagenomic study on the composition of culturable and non-culturable bacteria in tap water and biofilms at intensive care units, *J Water & Health*, 2018, 17, 1, 72.
- (8) R. M. Anthony *et al.*, Rapid diagnosis of bacteremia by universal amplification of 23S ribosomal DNA followed by hybridization to an oligonucleotide array. *J. Clin. Microbiol*, 2000, 38, 781.
- (9) P. Francois *et al.*, Rapid detection of methicillin-resistant *Staphylococcus aureus* directly from sterile or nonsterile clinical samples by a new molecular assay. *J. Clin. Microbiol*, 2003, 41, 254.
- (10) S. Aellen, *et al.*, Detection of live and antibiotic-killed bacteria by quantitative real-time PCR of specific fragments of rRNA, *Antimicro. Agents Chemother.*, 2006, 50, 6, 1913.
- (11) P. Kralik and M. Ricchi. A Basic Guide to Real Time PCR in Microbial Diagnostics: Definitions, Parameters, and Everything. *Front Microbiol.*, 2017, 8, 108.

- (12) S. Shannon *et al.*, Routine use of MALDI-TOF MS for anaerobic bacterial identification in clinical microbiology., *Anaerobe*, 2018, 54, 191.
- (13) A. Clark *et al.*, Matrix-Assisted Laser Desorption Ionization–Time of Flight Mass Spectrometry: a Fundamental Shift in the Routine Practice of Clinical Microbiology. *Clin Microbiol Rev.* 2013, 3, 547.
- (14) B. Huang *et al.*, Direct Detection and Identification of Bacterial Pathogens from Urine with Optimized Specimen Processing and Enhanced Testing Algorithm. *J. Clin. Microbiol.*, 2017, 55, 5, 1488.
- (15) N. Singhal *et al.*, MALDI-TOF mass spectrometry: an emerging technology for microbial identification and diagnosis., *Front. Microbiol.*, 2015, 6, 791, 1.
- (16) E. Galikowska *et al.*, Specific detection of *Salmonella enterica* and *Escherichia coli* strains by using ELISA with bacteriophages as recognition agents. *European Journal of Clinical Microbiology & Infectious Diseases*, 2011, 30, 9, 1067.
- (17) I. Palchetti and M. Mascini, *Biosensor Technology: A Brief History*, *Sensors and Microsystems, Lecture Notes in Electrical Engineering*, Springer, 2010, 54, 15.
- (18) W. Chunglok, *et al.*, Immunoassay based on carbon nanotubes-enhanced ELISA for *Salmonella enterica* serovar Typhimurium, *Biosensors & Bioelectronics*, 2011, 26, 3584.
- (19) J. Joo *et al.*, A facile and sensitive detection of pathogenic bacteria using magnetic nanoparticles and optical nanocrystal probes, *The Analyst*, 2012, 137, 16, 3609.
- (20) H. Shafiee *et al.*, Paper and flexible substrates as materials for biosensing platforms to detect multiple biotargets, *Scientific Reports*, 2015, 5, 8719.
- (21) Y.-C Chang *et al.*, Rapid single cell detection of *Staphylococcus aureus* by aptamer-conjugated gold nanoparticles, *Sci. Rep.*, 2013, 3, 1863.
- (22) R. Wang *et al.*, Sensitive quantification and visual detection of bacteria using CdSe/ZnS@SiO₂ nanoparticles as fluorescent probes, *Analytical Methods*, 2014, 17.
- (23) S. Agrawal *et al.*, Multiplexed Detection of Waterborne Pathogens in Circular Microfluidics, *Appl Biochem Biotechnol.*, 2012, 67, 6, 1668.

- (24) H. Yasaki *et al.*, A real-time simultaneous measurement on a microfluidic device for individual bacteria discrimination. *Sensors and Actuators, B: Chemical* 2018, 260, 746.
- (25) Jalali *et al.*, A hierarchical 3D nanostructured microfluidic device for sensitive detection of pathogenic bacteria. *Small*, 2018, 14, 1801893.
- (26) M. L. Pourciel-Gouzy *et al.*, Development of pH-ISFET sensors for the detection of bacterial activity, *Sens. Actuators B*, 2004, 103, 247.
- (27) F. Wang *et al.*, Development of luminescent pH sensor films for monitoring bacterial growth through tissue, *Adv. Healthc. Mater.* 2014, 3, 197.
- (28) X. Wang *et al.*, Fluorescent pH-Sensitive Nanoparticles in an Agarose Matrix for Imaging of Bacterial Growth and Metabolism, *Angew. Chem. Int. Ed.* 2013, 52, 406.
- (29) Y. Tang *et al.*, Rapid Antibiotic Susceptibility Testing in a Microfluidic pH Sensor, *Anal. Chem.* 2013, 85, 2787.
- (30) C. Grazon *et al.*, One-Pot Synthesis of Pegylated Fluorescent Nanoparticles by RAFT Miniemulsion Polymerization Using a Phase Inversion Process, *Macromol. Rapid Commun.* 2011, 32, 699.
- (31) C. Grazon *et al.*, Ultrabright Fluorescent Polymeric Nanoparticles Made from a New Family of BODIPY Monomers, *Macromol.*, 2013, 46, 13, 5167.
- (32) C. Grazon *et al.*, Fluorescent core-shell nanoparticles and nanocapsules using comb-like macromolecular RAFT agents: synthesis and functionalization thereof, *Polym. Chem.* 2016, 7, 25, 4272.
- (33) C. Grazon. Élaboration de nanoparticules fluorescentes à base de BODIPY par polymérisation RAFT en miniémulsion : synthèse, caractérisation et fonctionnalisation de surface. Autre. École normale supérieure de Cachan - ENS Cachan, 2012. Français. (NNT : 2012DENS0049). (tel-00841491v2).
- (34) Yang Si. Fluorescent Nanomaterials for Bioimaging and Biosensing : Application on E.coli Bacteria. Other. École normale supérieure de Cachan - ENS Cachan, 2015. English. (NNT : 2015DENS0038). (tel-01221690).

- (35) Y. Si *et al.*, Rapid and accurate detection of Escherichia coli growth by fluorescent pH-sensitive organic nanoparticles for high-throughput screening applications. *Biosens. Bioelectron.*, 2016, 75, 320.
- (36) C. Grazon *et al.*, Core-shell polymeric nanoparticles comprising BODIPY and fluorescein as ultra-bright ratiometric fluorescent pH sensors, *Photochemical & Photobiological Sciences*, 2019, 18, 5, 1156.
- (37) P. Rajapaksha *et al.*, A review of methods for the detection of pathogenic microorganisms, *Analyst*, 2019, 2, 396.
- (38) J. Lin, Recent development and applications of optical and fiber-optic pH sensors, *Trends in analytical chemistry*, 2000, 19, 9, 541.
- (39) S. Grant and R. Glass, A sol-gel based fiber optic sensor for local blood pH measurements, *Sensors and actuators B*, 1997, 45, 35.
- (40) J. Whitaker *et al.*, Spectral and photophysical studies of benzo[c]xanthene dyes: dual emission pH sensors, *Anal. Biochem.* 194, 1991, 1247.
- (41) CG. Niu *et al.*, Fluorescence ratiometric pH sensor prepared from covalently immobilized porphyrin and benzothioxanthene, *Anal Bioanal Chem.* 2005, 383, 349.
- (42) R. Kateklum *et al.*, Improving the sensitivity of amino-silanized sensors using self-structured silane layers: Application to fluorescence pH measurement, *Sensors and actuators B*, 2017, 248, 605.
- (43) I. Craciun *et al.*, Surfaces Decorated with Polymeric Nanocompartments for pH Reporting, *Helv. Chim. Acta* 2018, 101, e1700290.
- (44) S. Rigo *et al.*, Surfaces with dual functionality through specific co-immobilization of self-assembled polymeric nanostructures, *Langmuir*, 2018.

Chapter 2: Fluorescent Nanoparticles

Introduction

In this work, we introduce a new family of fluorescent nanoparticles (FNP), based on the previously reported synthesis by our research group and collaborators (1, 2). These FNP are based on a core-shell structure (Figure 2.1): the core is made of styrene copolymerized with 4-difluoro-4-bora-3a, 4a-diaza-s-indacene (BODIPY) and the shell consists of a poly-(ethylene oxide) PEO and poly-(acrylic acid) PAA random copolymer.

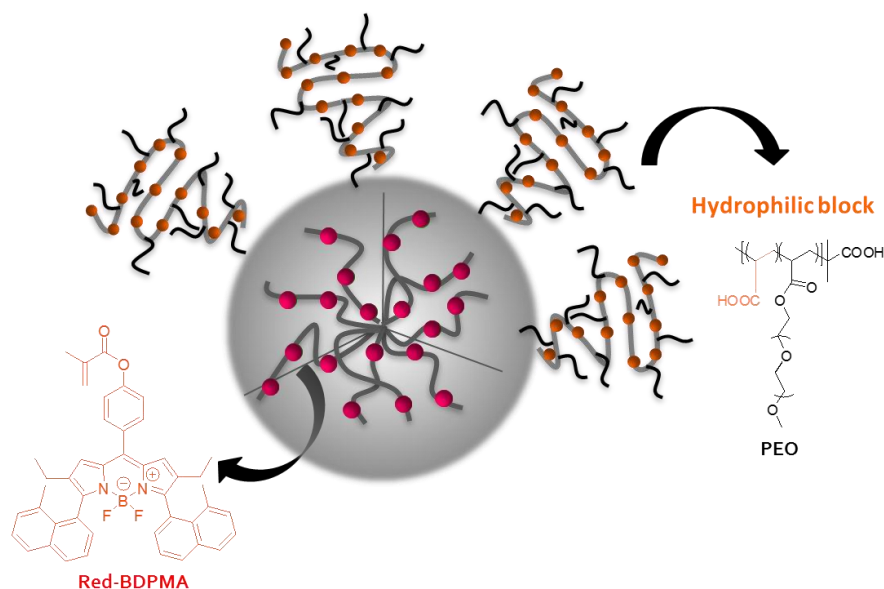


Figure 2.1 Design of the core-shell FNP were: the core is made of a polymer block of styrene and BODIPY; the shell is made of a random copolymer of PEO and PAA.

BODIPY (Figure 2.2) is a well-known fluorophore with very good photophysical properties, like usually high fluorescence quantum yields ($\Phi_F \sim 0.7$) and good photostability (3). Besides, if designed properly, the spectroscopic properties of BODIPY can be considered independent of the environment or can be designed to be sensitive. Thus they can be used as tracer or internal reference (for instance in ratiometric systems) (3, 4).

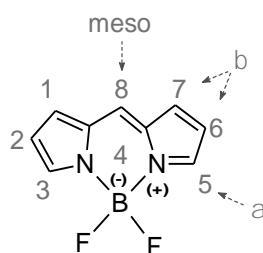


Figure 2.2 Structure and numbering scheme for BODIPY.

The extension of the π conjugated system allows the shift of the maximum emission wavelength towards red. This is mainly achieved by substitution in positions 3 and 5 of the pyrrole. Substitutions in positions 1 and 7 would have the same consequences on the spectroscopic properties but are more difficult to achieve due to the conditions of pyrrole synthesis. The insertion of an aromatic group can be carried out by a synthesis of the corresponding pyrrole via a Trofimov reaction (5), like in the case of the ‘red’ BODIPY (Red BDP) in comparison with ‘green’ BODIPY (Green BDP), where the fluorescence emission is shifted from 540 to 600 nm (Figure 2.3).

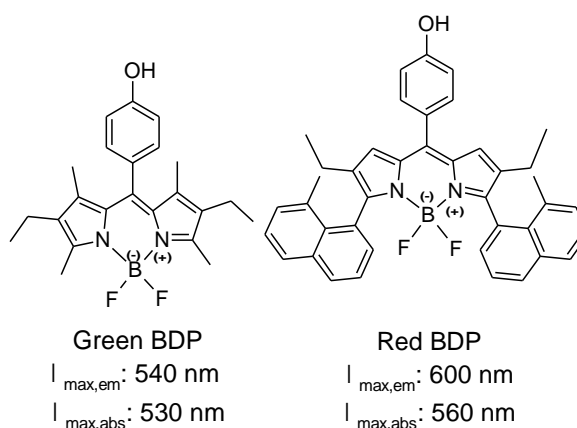


Figure 2.3 Scheme of ‘green’ BODIPY (Green BDP) and ‘red’ BODIPY (Red BDP), used in this manuscript as fluorophores in the core of FNP. Maximum absorbance and emission wavelengths recorded in dichloromethane (DCM).

As mentioned, C. Grazon *et al.* (1, 2) developed a straightforward synthesis strategy to prepare fluorescent polymeric nanoparticles FNP. The shell made of a copolymer of acrylic acid (AA) and poly (ethylene oxide) (PEO) prepared by RAFT polymerization. It is first block extended with a mixture of styrene and BODIPY monomers by partial bulk polymerization (approx. 20% conversion) to afford an amphiphilic copolymer. The mixture is then poured in basic water and submitted to

ultrasound treatment to yield a mini-emulsion of nanoparticles that are brought to 80 °C to terminate the polymerization. Here for the first time, we propose to implement such synthesis on a red BDP (Figure 2.4).

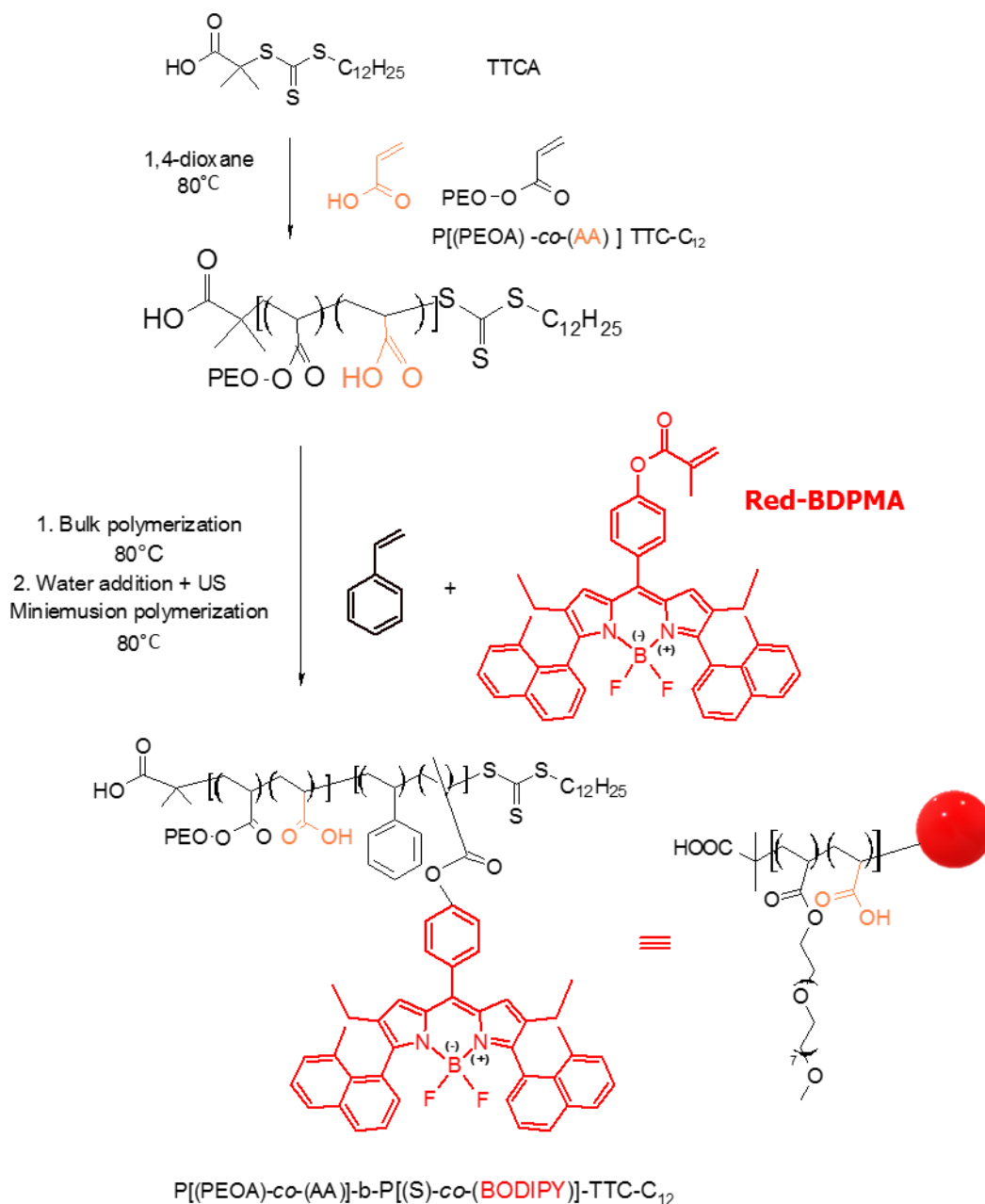


Figure 2.4 General synthetic scheme for the synthesis of FNP, i.e. FNP_{Red}: composed of ‘red’-BDPMA in the core, stabilized by a hydrophilic random diblock copolymer shell.

This methodology does not require the use of surfactants, nor ultra-hydrophobic additives, providing stable FNP over time (2). The inclusion of acrylic acid moieties on the shell polymer, provides carboxylic acid functions which allow post-functionalization and, in our case, the grafting of FNP on substrates by peptide coupling.

A new family of FNP was synthesized to allow ‘click chemistry’ by incorporating in the diblock copolymer (on the shell of FNP) a moiety of 4-dibenzocyclooctynol (DIBO, figure 2.5). ‘Click Chemistry’ is a term introduced by Sharpless *et al.* in 2001 (8), given to reactions with very high yields, the use of no solvent or water as solvent by simple reaction conditions with ‘small building blocks’ due to a very high thermodynamic driving force. DIBO reacts *very fast* with azide groups (N₃), to give stable triazoles in the absence of a copper iodide catalyst, known as ‘click chemistry’ (9, 10). DIBO can be synthesized in a simple approach (described in materials section) and has shown nontoxicity and straightforward attachment in a variety of probes (9). Commercially available kits allow the specific-site azide labeling of monoclonal antibodies ensure their orientation while ‘clicked’.

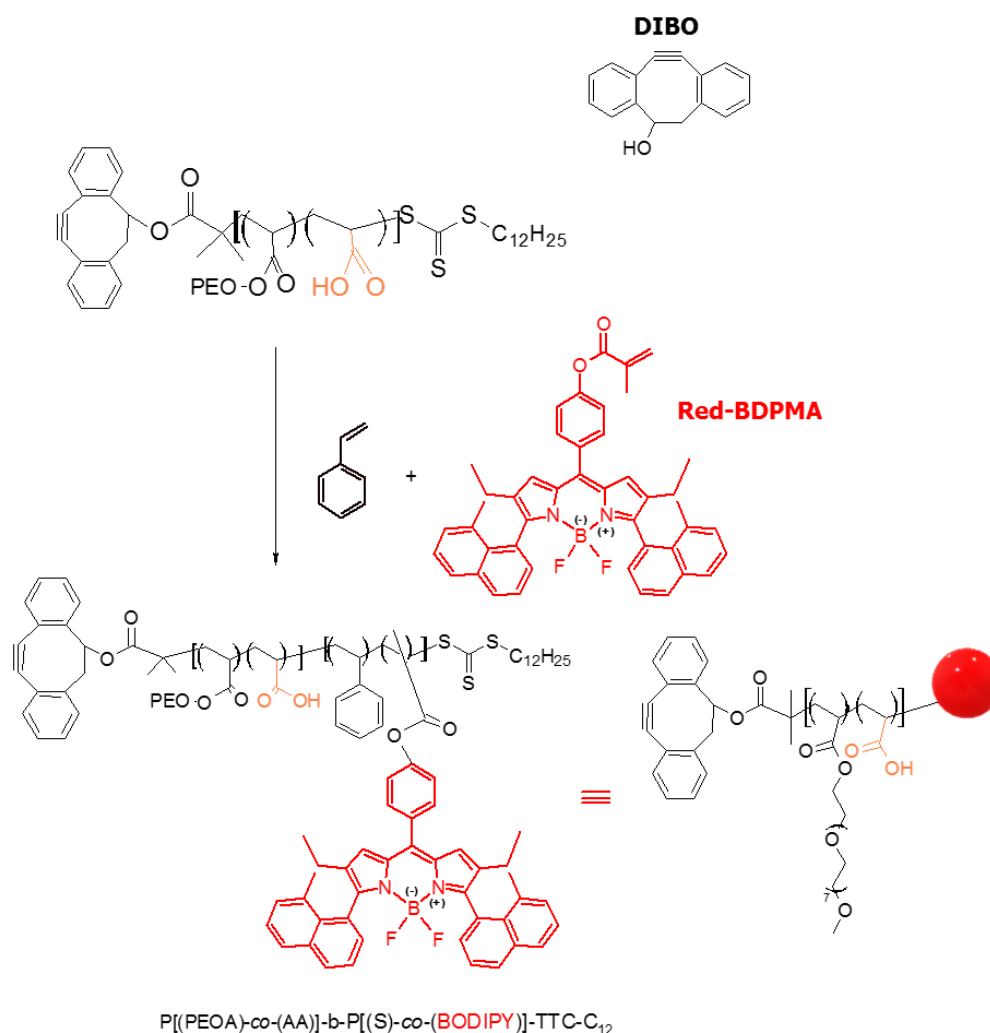


Figure 2.5 A new RAFT agent is prepared including DIBO moiety in its structure. Equal synthetic route as shown in Figure 2.4 is followed to obtain a new family of FNP including DIBO in the shell for click-chemistry reactions.

A descriptive summary along with the abbreviated name used for each synthesized and characterized FNPs in this project are presented in Table 2.1.

Table 2.1 Abbreviated name for each type of FNPs along with their core and shell composition

FNP Name	Core Composition	Shell Composition
FNP _{Green}	Green BDPMA	Carboxylic terminals
FNP _{Red}	Red BDPMA	Carboxylic terminals
FNP _{G-DIBO}	Green BDPMA	Carboxylic terminals + DIBO moiety
FNP _{R-DIBO}	Red BDPMA	Carboxylic terminals + DIBO moiety

Chronologically, due to their *easy* synthesis, FNP_{Green} were first synthesized and characterized. These FNPs were used to set all the protocols of characterization and surface modification (which will be introduced in the following chapter). ‘Green’ surfaces were obtained (data are not presented in this manuscript), but both bands of emission of BODIPY and FA are too close (515 and 547 nm, respectively). For this, we proceeded to synthesize FNP_{Red} although its synthesis is complex and time consuming. Anticipating future needs, FNP_{G-DIBO} and FNP_{R-DIBO} were synthesized in parallel.

The last part of this chapter is focused in the preparation of a *new* fluorescent ratiometric pH-nanosensor based on FNP_{red} grafted by peptide coupling with a very well-known pH-sensitive fluorophore: Fluoresceinamine (FA), obtaining FNP_{Red-FA}. C. Gazon *et al.* (2), have already developed a similar sensor based on ‘green’ FNP. Nevertheless, the proximity of the emission bands of FNP_{Green} and FA makes difficult the analysis of the data obtained from the sensor. This proof-of-concept, by using ‘red’ BODIPY (FNP_{Red}) and FA (grafted in the shell of the nanoparticles), will be translated to a solid substrate (glass slides) to aim at a more robust and transportable device for our final goal to obtain pH-sensing surfaces.

Fluorescein in solution (11), exhibits different species depending on pH (Figure 2.5):

- as cation
- neutral either lactonic or quinonoid molecule
- monoanion
- dianion

The pK_a from anion to dianion is 6.4, the dianion being the most fluorescent species. This property makes fluorescein appropriate as pH-sensing fluorophore in a ratiometric measurement for bacterial growth detection.

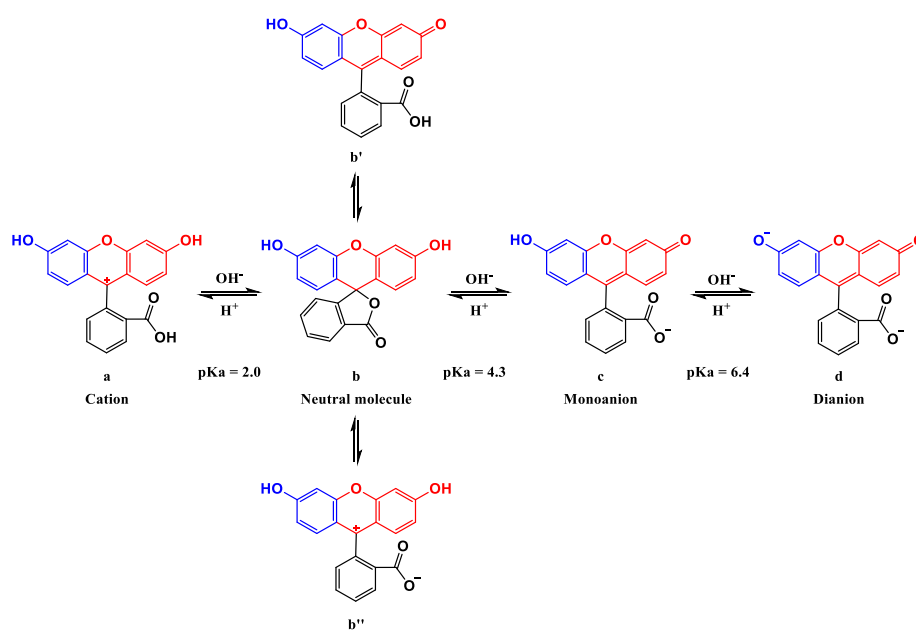


Figure 2.6 Scheme of different species of fluorescein depending on pH.

Next, the synthetic routes used will be described, as well as the techniques used to characterize the different FNP.

Materials & Methods

1.1.1. Materials

Phenylacetaldehyde (Sigma), Trimethylsilyl iodide (97%, Sigma), n-butyllithium solution (1.6 M in hexane, Sigma), Bromine (99.6%, Acros), N,N'-Dicyclohexylcarbodiimide (99%, Sigma, DCC), 4-(Dimethylamino)pyridine (99%, Sigma, DMAP), 3-chloropropylamine hydrochloride (98%, Aldrich), sodium azide (99%, Acros), 5-carboxyfluorescein (99%, Sigma-Aldrich), O-(Benzotriazol-1-yl)-1,1,3,3-tetramethyluronium tetrafluoroborate (TBTU, Sigma-Aldrich), N,N-diisopropylethylamine (99.5%, Sigma-Aldrich, DIPEA), 1-methylnaphthalene (95%, Aldrich), butyryl chloride (98%, Aldrich), hydroxylamine hydrochloride ($\geq 96\%$, Sigma), mercury acetate ($\geq 99\%$, Sigma-Aldrich), 4-hydroxybenzaldehyde (98%, Aldrich), 2-bromoethanol (95%, Aldrich), acryloyl chloride (97%, Aldrich), propargyl alcohol (99%, Aldrich), triethylamine ($\geq 99\%$, Sigma-Aldrich), Bromotris(triphenylphosphine)copper(I) (98%, Aldrich, $(\text{PPh}_3)_3\text{CuBr}$), tetrachloro-1,4-benzoquinone (99%, Aldrich, Chloranil), boron trifluoride diethyletherate (2 M in diethyl ether, 98%, Alfa Aesar), methacryloyl chloride ($\geq 97\%$, Sigma-Aldrich), 1,8-diazobicyclo[5,4,0]undec-7-ene ($\geq 98\%$, Fluka, DBU), Poly(ethylene glycol) methyl ether acrylate (Sigma-Aldrich, $M_n = 454 \text{ g mol}^{-1}$, PEOA), 2-methyl-2-[(dodecylsulfanylthiocarbonyl)sulfanyl] propanoic acid (97%, Strem, TTCA), acrylic acid (99%, Aldrich, AA), 4,4'-Azobis(4-cyanopentanoic acid) (98%, Sigma, ACPC) were used as received without further purification. Solvents were of synthetic grade and purified according to standard procedures. 18 M Ω Millipore water was used throughout and further pH-adjusted with either HCl or NaOH. All solvents were dried on an automatic M. Braun SPS-800 instrument.

1.1.2. Synthetic Methods

NMR: ^1H NMR spectra were recorded in CDCl_3 on a JEOL ECS (400 MHz) spectrometer. All chemical shifts were referenced to Me_4Si (TMS). In order to monitor

the individual molar conversion of acrylic acid (AA) and PEOA, DMF (7.95 ppm) was used as internal standard and conversions were determined by the relative decrease of the acrylate signals between 6.4 and 5.8 ppm to DMF.

1.1.2.1. Molecular Synthesis: Dyes

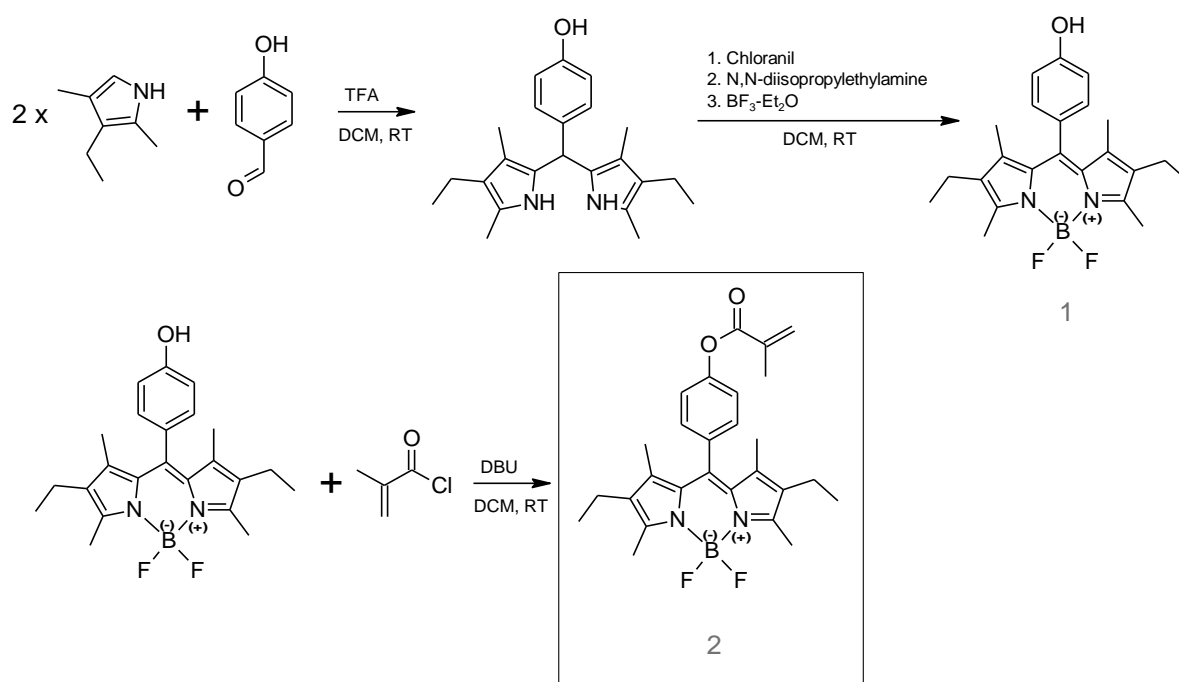
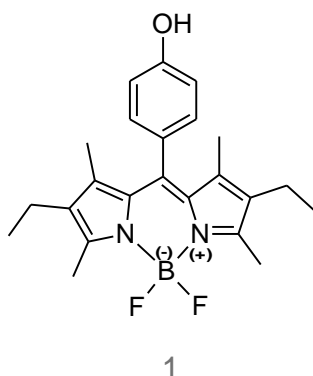


Figure 2.7 Scheme of synthesis of ‘green’ BODIPY (phenol) and polymerizable BODIPY (Methacrylate).

GREEN BODIPY (Green-BDP)

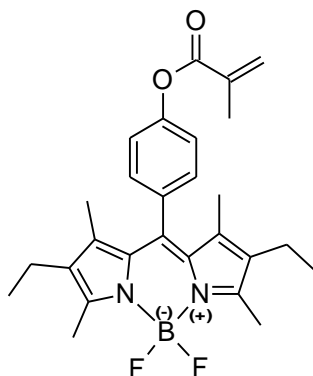


2,6-diethyl-4,4-difluoro-8-(4-hydroxyphenyl)-1,3,5,7-tetramethyl-4-bora-3a,4a-diaza-s-indacene (1)

In a round flask, 4-hydroxybenzaldehyde (1 eq., 20.30 mmol, 2.48 g) was dissolved into 500 mL of DCM at room temperature. It was added to the mixture Kryptopyrrole (2 eq., 40.60 mmol, 5 g) and 10 drops of TFA. Followed by TLC, after full consumption of pyrrole Chloranile (1 eq., 20.30 mmol, 5 g) was added, followed by the addition of N,N-diisopropylethylamine (7 eq., 142.10 mmol, 18.36 g). After 15 minutes of stirring the mixture, Boron trifluoride diethyletherate (11 eq., 223.20 mmol, 31.68 g) was slowly added. After one hour the solvent was evaporated and the compound was purified by chromatography column (SiO₂, Petroleum ether/DCM, 1:4). The final product was a green-orange powder obtained with 80 % yield.

¹H NMR (400 MHz, CDCl₃): δ/ppm: 7.12 (d, 2H, J: 8.7), 6.94 (d, 2H, J: 8.7 Hz), 5.23 (s, 1H), 2.53 (s, 6H), 2.30 (q, J: 7.6 Hz, 4H), 0.98 (t, J: 7.6 Hz, 6H). ¹³C NMR (100 MHz, CDCl₃): δ/ppm: 156.2, 153.7, 138.6, 132.9, 131.3, 129.9, 128.3, 116.2, 17.2, 14.8, 12.6, 12.0. ¹⁹F NMR (376 MHz, CDCl₃): δ/ ppm: -145.6 (q, J_{F-B}: 32.3 Hz). ¹¹B NMR (128 MHz, CDCl₃): δ/ ppm: -0.13 (t, J_{B-F}: 33.2 Hz). HRMS m/z: 419.2097 [M + Na]⁺; calc. for C₂₃H₂₇BF₂N₂ONa: 419.2082

GREEN BODIPY-METHACRYLATE (Green-BDPMA)



2

2,6-diethyl-4,4-difluoro-8-(4-(methacryloyloxy)phenyl)-1,3,5,7-tetramethyl-4-bora-3a,4a-diaza-s-indacene (2)

In a round flask, BODIPY-Phenol **1** (1 eq., 1.25 mmol, 0.5 g) was dissolved into 100 mL of DCM at room temperature. Followed by the addition of 1,8-diazabicyclo[5.4.0]undec-7-ene (DBU, 2 eq., 2.5 mmol, 0.38 g) and Methacryloyl chloride (1.5 eq., 2.0 mmol, 0.2 g). The mixture was stirred overnight, after the solvent was evaporated and the compound was purified by chromatography column (SiO₂, Petroleum ether/DCM, 3:7). The final product was obtained with 78 % yield.

¹H NMR (400 MHz, CDCl₃): δ/ppm: 7.32 (d, 2H, J: 8.7 Hz), 7.27 (d, 2H, J: 8.7 Hz), 6.39 (s, 1H), 5.80 (s, 1H), 2.52 (s, 6H), 2.28 (q, J: 7.6 Hz, 4H), 2.00 (s, 3H), 1.33 (s, 6H), 0.97 (t: 7.6 Hz, 6H). ¹³C NMR (100 MHz, CDCl₃): δ/ppm: 165.7, 154.0, 151.4, 139.2, 138.5, 135.8, 133.3, 133.0, 130.9, 129.5, 127.7, 122.6, 18.5, 17.2, 14.7, 12.6, 11.9. ¹⁹F NMR (376 MHz, CDCl₃): δ/ ppm: -145.7 (q, J_{F-B}: 32.9 Hz). ¹¹B NMR (128 MHz, CDCl₃): δ/ ppm: -0.15 (t, J_{B-F}: 32.9 Hz). HRMS m/z: 487.2349 [M + Na]⁺; calc. for C₂₇H₃₁BF₂N₂O₂Na: 487.2344.

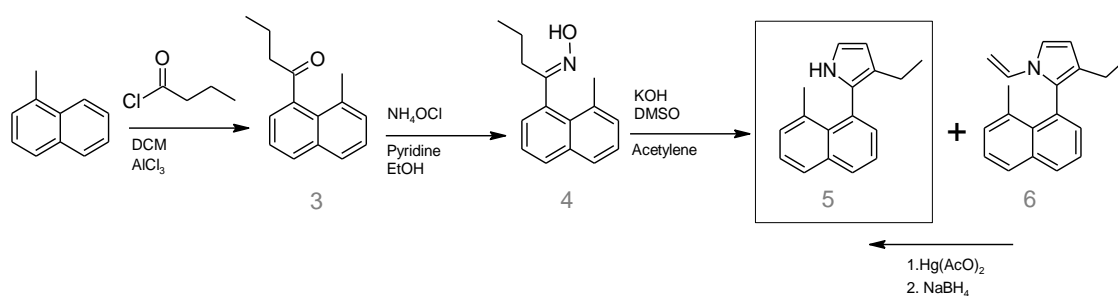
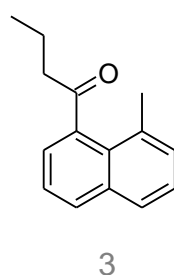


Figure 2.8 Scheme of Trofimov synthesis of MethylNaphthalene-Pyrrole starting from MethylNaphthalene.

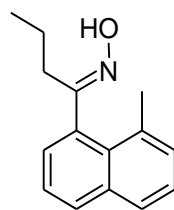
1-(8-Methylnaphthalene-1-yl)butane-1-one (3)



1-methylnaphthalene (1 eq., 35.2 mmol, 5 g), was dissolved in 100 mL of DCM in a round bottom flask and cooled down to 0 °C. Meanwhile, a suspension of butyryl chloride (1.1 eq., 38.7 mmol, 4.12 g) and aluminum trichloride (1.8 eq., 61.5 mmol, 8.2 g) dissolved in 50 mL of DCM was cooled down. This suspension was added to the initial mixture and stirred 2 h at room temperature. After, the mixture was poured over ice and mixed until it became colorless. The organic phase was recovered and washed with a basic solution of KHCO_3 , followed by washing with a saturated sodium chloride (NaCl) solution. The organic phase was dried over MgSO_4 , filtered and the solvent was evaporated. The compound was purified by chromatography column (SiO_2 , Petroleum ether/DCM, 2:1). The final product was obtained with 86 % yield.

^1H NMR (400 MHz, CDCl_3): δ /ppm: 8.64 (m, 1H), 7.76 (d, 1H, J: 7.3 Hz), 7.58 (m, 2H), 7.34 (dd, 1H, J: 0.9 Hz), 3.02 (t, 2H, J: 7.3), 2.74 (s, 3H), 1.82 (m, 2H), 1.03 (t, 3H, J: 7.3 Hz). ^{13}C NMR (100 MHz, CDCl_3): δ /ppm: 205.0, 139.4, 134.9, 133.1, 130.4, 127.5, 127.4, 126.5, 126.4, 125.4, 44, 1, 20.2, 18.5, 14.0. $\text{C}_{15}\text{H}_{16}\text{O}$: 212.12.

Oxime of 1-(8-Methylnaphthalene-1-yl)butane-1-one (Z,E) (4)

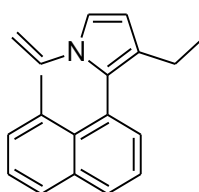


4

A mixture of 1-methylnaphthyl propyl ketone **3** (1 eq., 37.7 mmol, 8 g), hydroxylamine hydrochloride (2 eq., 75.4 mmol, 5.24 g), 100 mL of pyridine and 100 mL of ethanol, were stirred at 80 °C overnight. After cooling down the mixture, this one was poured in water. The precipitated solid was recovered by filtration, washed and dried. If no precipitate was formed, the mixture was washed with HCl (1M), and extracted with diethyl ether. No further purification was done. The final product was obtained with 93 % yield.

^1H NMR (400 MHz, CDCl_3): δ /ppm: 8.02-7.17 (m, 6H), 2.84 (m, 1H), 2.69 (s, 3H), 2.58 (m, 1H), 2.50 (m, 2H), 0.90 (m, 3H). ^{13}C NMR (100 MHz, CDCl_3): δ /ppm: 161.6, 159.4, 135.4, 135.4, 133.0, 132.9, 132.6, 131.6, 129.6, 126.3-126.0, 124.7, 124.6, 123.9, 38.8, 32.3, 20.0, 19.7, 19.7, 14.5, 14.0. $\text{C}_{15}\text{H}_{17}\text{NO}$: 227.13.

3-ethyl-2-(8-methylnaphthalene-1-yl)-1-vinyl-1H-pyrrole (6)



6

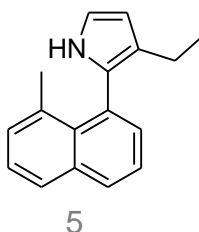
A mixture of the oxime **4** (1 eq., 38.1 mmol, 8.66 g), KOH (2 eq., 76.2 mmol, 4.28 g) and DMSO (175 mL) was heated until 110 °C. The mixture was fluxed with acetylene over 2 h, followed by TLC. After cooling down the mixture, the reaction was hydrolyzed by adding NH_4Cl (2 eq., 76.2 mmol, 4.08 g). The organic phase was extracted with diethyl ether (5 x 100 mL), followed by washing with saturated sodium chloride (NaCl) solution,

dried, filtered and the solvent was evaporated. The compound was purified by chromatography column (SiO₂, Petroleum ether/DCM, 3:7). A mixture of N-vinyl pyrrole and the desired pyrrole were obtained. The N-vinyl pyrrole was isolated and reconverted as the following step.

¹H NMR (400 MHz, CDCl₃): δ/ppm: 8.05 (d, 1H), 7.55-7.32 (m, 5H), 7.17 (d, 1H, J: 3.2 Hz), 6.32 (m, 2H), 4.98 (d, 1H, J: 16.0 Hz), 4.32 (d, 1H, J: 9.2 Hz), 2.75 (s, 3H), 2.23 (m, 2H), 1.03 (t, 3H, J: 7.6 Hz) . ¹³C NMR (100 MHz, CDCl₃): δ/ppm: 135.3, 134.0, 132.8, 131.8, 130.0, 127.2-124.4, 115.7, 110.0, 96.0, 19.7, 19.5, 15.7. C₁₉H₁₉N: 261.15.

N-vinyl Pyrrole reversion to Methylnaphthalene Pyrrole

3-ethyl-2-(8-methylnaphthalene-1-yl)-1H-pyrrole (5)



The vinylpyrrole **6** (1 eq., 17.1 mmol, 4.47 g) and mercury acetate (3 eq., 51.3 mmol., 16.35 g), were separately dissolved in 60 mL of acetonitrile, each. The mercury acetate solution was dropwise added to the vinylpyrrole one. The mixture was warmed to 55 °C for 30 min. After cooling down the mixture, a solution of sodium borohydride (6 eq., 102.6 mmol, 3.88 g) was added portion-wise very slowly. The suspension was filtered and the liquid phase was diluted with 80 mL of diethyl ether. The organic phase was washed with brine (3 x 80 mL) and dried over K₂CO₃. The solution was filtered and the solvent was evaporated. The final product was obtained with 55 % yield.

¹H NMR (400 MHz, CDCl₃): δ/ppm: 8.05 (m, 2H), 7.84 (m, 1H), 7.55-7.32 (m, 3H), 6.89 (t, 1H, J: 2.8 Hz), 6.31 (t, 1H, J: 2.8 Hz), 2.74 (s, 3H), 2.42 (m, 2H), 1.12 (t, 3H, J: 7.6 Hz). ¹³C NMR (100 MHz, CDCl₃): δ/ppm: 132.9, 128.0, 126.9, 126.2, 125.9, 125.8, 124.5, 117.2, 108.8, 19.6, 15.8. C₁₇H₁₇N: 235.14.

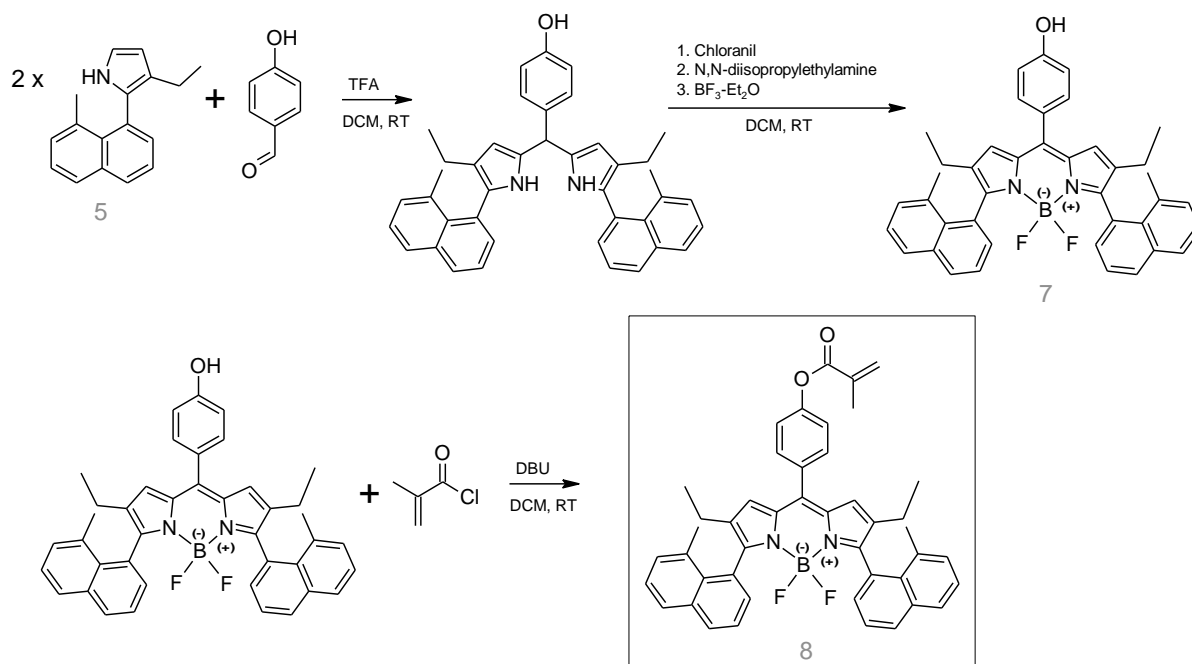
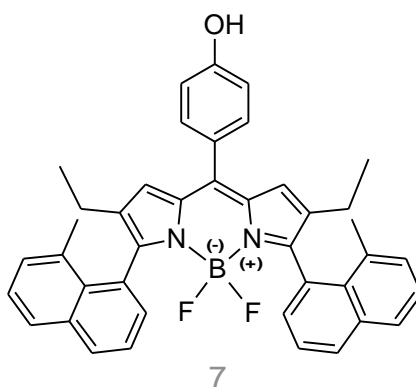


Figure 2.9 Scheme of synthesis of 'red' BODIPY **7** and polymerizable BODIPY **8** (Methacrylate).

RED BODIPY-METHYL-NAPHTHALENE-PHENOL **7** (also referred as Red-BODIPY)

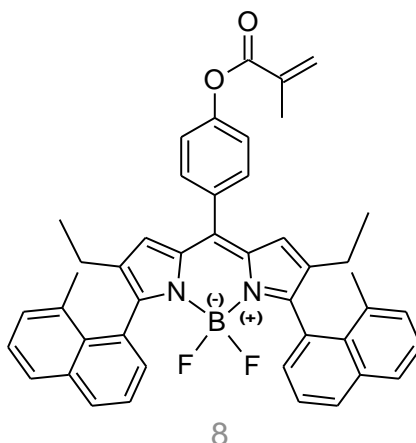
2,6-diethyl-4,4-difluoro-8-(4-hydroxyphenyl)-5,3-(9-methyl-1-naphthyl)-4-bora-3a,4a-diaza-s-indacene



Same protocol as green BDP **1** was used replacing kryptopyrrole by methyl-naphthalene pyrrole **5**. The final product was a pink-violet powder with (2.299 g) 28.0 % yield.

^1H NMR (400 MHz, CDCl_3): δ /ppm: 7.96 (d, 2H, J: 8.2 Hz), 7.90 (d, 2H, J: 8.2 Hz), 7.6-7.1 (m, 12H), 6.75 (m, 2H), 2.64 (s, 6H), 2.03 (m, 2H), 1.91 (m, 2H), 0.90 (m, 6H). ^{13}C NMR (100 MHz, CDCl_3): δ /ppm: 156.2, 137.6, 135.7, 134.4, 132.4, 130.0, 128.9, 128.3, 126.7, 126.0, 125.6, 124.5, 115.2, 19.9, 19.7, 14.4, 14.2. ^{19}F NMR (376 MHz, CDCl_3): δ /ppm: -125.9 (m, 0, 8F), -137.5 (q, 2F, $J_{\text{F-B}}$: 32.3 Hz), -147.7 (m, 0, 8F). ^{11}B NMR (128 MHz, CDCl_3): δ /ppm: -0.29 (t, $J_{\text{B-F}}$: 29.5 Hz). HRMS m/z : 619.2732 $[\text{M} + \text{Na}]^+$; calc. for $\text{C}_{41}\text{H}_{34}\text{BF}_2\text{N}_2\text{O}$: 619.2749.

RED BODIPY-NAPHTHALENE-METHACRYLATE 8 (Red-BDPMA, in Figure 2.3)



2,6-diethyl-4,4-difluoro-8-(4-(methacryloyloxy)phenyl)-5,3-(9-methyl-1-naphtyl)-4-bora-3a,4a-diaza-s-indacene (referred as 8 or Red-BDPMA)

Same protocol as green-BODIPY-methacrylate **2** was used replacing green BDP **1** by red BDP **7**. The final product **8** was a pink-violet powder with (332 mg) 88.6 % yield.

^1H NMR (400 MHz, CDCl_3): δ /ppm: 7.89 (d, 2H, J: 8.2 Hz), 7.83 (d, 2H, J: 7.8 Hz), 7.76 (m, 2H), 7.71 (m, 1H), 7.47-7.19 (m, 8H), 7.21 (m, 1H), 6.69 (s, 2H), 6.38 (s, 2H), 5.78 (s, 1H), 2.64 (s, 6H), 2.14 (s, 3H), 2.02 (m, 2H), 1.88 (m, 2H), 0.88 (m, 6H, J: 7.6 Hz). ^{13}C NMR (100 MHz, CDCl_3): δ /ppm: 165.8, 156.4, 152.4, 137.7, 135.8, 135.7, 134.5, 132.45, 132.46, 132.1, 132.0, 131.8, 131.0, 128.9, 128.1, 127.0, 126.8, 126.0, 125.74, 125.66, 124.5, 121.8, 19.7, 19.4, 14.3. ^{19}F NMR (376 MHz, CDCl_3): δ /ppm: -125.8 (m,

0.8F), -137.6 (q, 2F, J_{F-B} : 32.3 Hz), -147.7 (m, 0.8F). ^{11}B NMR (128 MHz, CDCl_3): δ /ppm: -0.25 (t, J_{B-F} : 30.8 Hz). HRMS m/z : 711.2970 $[\text{M} + \text{Na}]^+$; calc. for $\text{C}_{45}\text{H}_{39}\text{BF}_2\text{N}_2\text{O}_2\text{Na}$: 711.2992.

1.1.2.2. Molecular Synthesis: DIBO

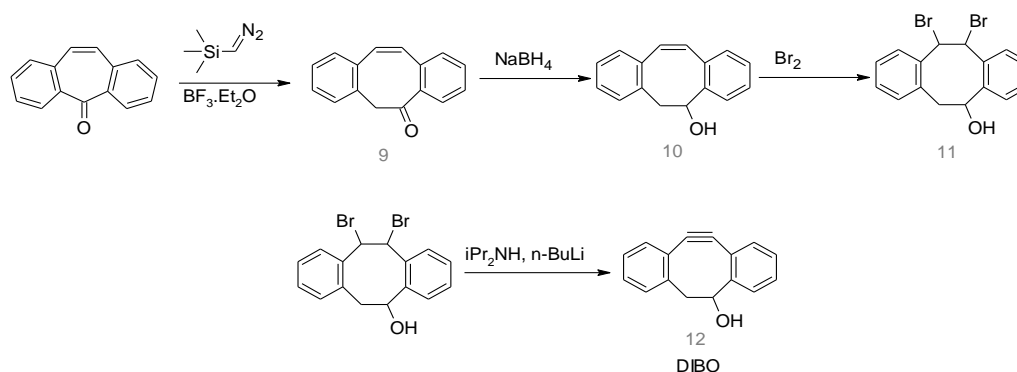
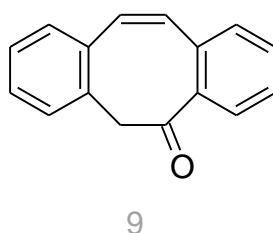


Figure 2.10 Scheme of synthesis of ‘DIBO’. (From Ref. 9)

6H-Dibenzo[a,e]cyclooctatrien-5-one (9)

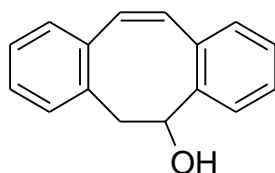


Trimethylsilyl diazomethane (1.6 eq., 21.9 mmol, 10.5 mL) was dissolved in 20 mL of DCM. Meanwhile a solution of dibenzosuberone (1 eq., 14.0 mmol, 2.88 g) and $\text{BF}_3 \cdot \text{OEt}_2$ (1.5 eq., 21.0 mmol, 2.59 mL) in 30 mL of DCM, was prepared. Both solutions were mixed dropwise at -10°C over 1 h period. After the reaction was stirred over 2 h at -10°C and then poured into ice water. The organic phase was extracted with DCM (3 x

100 mL), washed with brine, dried, filtered and the solvent was evaporated. The compound was purified by chromatography column (SiO₂, Petroleum ether/DCM, 1:2). The final product was obtained with 55 % yield.

¹H NMR (400 MHz, CDCl₃): δ/ ppm: 8.26 (q, 1 H, J=1.4, 6.6 Hz), 7.13–7.43 (m, 7 H), 7.05 (q, 2H, J=3.8, 12.9 Hz), 4.06 (s, 2H); ¹³C NMR (100 MHz, CDCl₃): δ/ ppm: 196.6, 136.9, 136.3, 135.4, 133.8, 133.1, 132.4, 131.4, 130.6, 129.3, 128.8, 128.0, 127.3, 126.9, 48.4. HRMS m/z: 243.0767 [M + Na]⁺; calc. for C₁₆H₁₂NaO⁺: 243.0780.

5,6-Dihydro-dibenzo[a,e]cycloocten-5-ol (10)

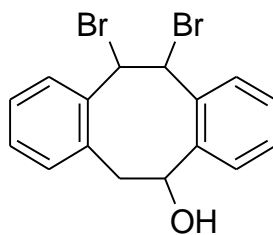


10

The previous compound **9** (1 eq., 4.5 mmol, 1 g) was dissolved in a mixture of EtOH/THF (1:1, v/v, 54 mL). Sodium borohydride (2 eq., 9.08 mmol, 0.34 g) was added slowly and portion-wise to the mixture. The reaction mixture was stirred up to 7 h, followed by TLC. The reaction was quenched by dropwise addition of 1 mL of acetic acid. The solvent was evaporated. The residue was dissolved in DCM, washed with brine and extracted with DCM (4 x 100 mL). The organic phase was dried, filtered and the solvent evaporated. The obtained compound was used in the following reaction without further purification. The final product was obtained with <98 % yield.

¹H NMR (400 MHz, CDCl₃): δ/ ppm: 7.50 (m, 1 H), 7.14–7.30 (m, 7H), 6.90 (q, 2H, J= 2.7, 12.0 Hz), 5.31 (q, 1H, J=6.3, 10.0 Hz), 3.41 (m, 2H); ¹³C NMR (100 MHz, CDCl₃): δ/ ppm: 141.7, 136.7, 136.2, 134.5, 131.7, 131.5, 130.1, 129.9, 129.3, 128.7, 127.4, 127.2, 126.9, 125.9, 74.4, 42.7. HRMS m/z: 245.0949 [M + Na]⁺; calc. for C₁₆H₁₄NaO⁺: 245.0937.

11,12-Dibromo-5,6,11,12-tetrahydro-dibenzo[a,e]cycloocten-5-ol (**11**)



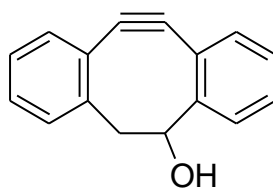
11

The previous compound **10** (1 eq., 1.7 mmol, 0.38 g) was dissolved in 10 mL of DCM. Bromine (1 eq., 1.7 mmol, 0.27 g) was added dropwise to the previous solution and stirred for 30 min, followed by TLC. The solvent was evaporated, and the compound was purified by chromatography column (SiO₂, Petroleum ether/DCM, 1:2). The final product was obtained with 50 % yield.

¹H NMR (400 MHz, CDCl₃): δ/ ppm: 7.54–7.47 (2 H), 7.31–6.72 (6 H), 5.77 (d, 1H, CHBr, J=5.4 Hz), 5.22 (dd, 1H, CHOH, J=3.6, 5.9 Hz), 5.19 (d, 1H, CHBr, J=5.4 Hz), 3.50 (dd, 1H, CH₂, J=3.6, 15.9 Hz), 2.75 (dd, 1H, CH₂, J=3.6, 15.9 Hz); ¹³C NMR (100 MHz, CDCl₃): δ/ ppm: 141.3, 140.0, 137.2, 134.0, 133.4, 131.5, 131.3, 130.9, 127.8, 126.2, 123.7, 121.3, 76.5, 70.0, 62.3, 32.2. HRMS m/z: 402.9313 [M + Na]⁺; calc. for C₁₆H₁₄Br₂NaO⁺: 402.9304.

DIBO

5,6-Dihydro-11,12-didehydro-dibenzo[a,e]cycloocten-5-ol (**12**)



12

Diisopropylamine (4.1 eq., 1.26 mmol, 0.18 mL) was dissolved in dry THF (10 mL) at 0 °C under Ar. Butyl Lithium (BuLi, 4 eq., 1.22 mmol, 0.77 mL) was added dropwise and the mixture was stirred at 0 °C for 30 min. The previous bromide compound **11** was dissolved in 10 mL of dry THF and added dropwise to the Lithium diisopropylamide (LDA) solution. The reaction was stirred for 1.5 h and then quenched by adding a

saturated solution of ammonium chloride. The aqueous phase was extracted twice with AcOEt and the organic phase was dried, filtered and solvent was evaporated. The compound was purified by chromatography column (SiO₂, heptane/AcOEt, 9:1). The final product was a white powder obtained with 50 % yield.

¹H NMR (400 MHz, CDCl₃): δ/ ppm: 7.67 (1 H, aromatics), 7.37–7.18 (7 H, aromatics), 4.57 (dd, 1H, CHOH, J=2.1, 14.7 Hz), 3.04 (dd, 1H, CH₂, J=2.1, 14.7 Hz), 2.86 (dd, 1H, CH₂, J=2.1, 14.7 Hz); ¹³C NMR (100 MHz, CDCl₃): δ/ ppm: 154.5, 150.6, 128.6, 127.1, 1127.0, 126.0, 125.8, 125.1, 124.7, 123.0, 122.7, 121.7, 111.9, 109.6, 74.2, 47.7.

1.1.2.3. Macromolecular Synthesis: Polymers

MacroRAFT Agent: (PEOA-co-AA)-TTCA (13)

In a round bottom flask 9.7 mL of dioxane were mixed with the following reactants: acrylic acid (1 eq., 10 mmol, 0.72 g), poly(ethylene oxide) acrylate (PEOA, 1 eq., 10 mmol, 4.54 g), 2-methyl-2-[(dodecylsulfanyl-thiocarbonyl)sulfanyl] propanoic acid (TTCA, 0.08 eq., 0.8 mmol, 0.29g), 4,4'-azobis-4-cyanopentanoic acid (ACPA, 0.005 eq., 0.05 mmol, 0.015 g) and dimethylformamide (DMF, 0.4 eq., 4 mmol, 0.29 g). The mixture was degassed (Ar) 30 min in ice bath. Immediately after, the mixture was placed in oil bath at 75 °C and stirred for 140 min. The reaction was stopped by putting the flask in an ice bath. The copolymer was isolated after two consecutive precipitations in cold diethyl ether and dried under vacuum for 2 days. The conversion rate and polymer mass were estimated based on the total monomer conversion followed by NMR (≥87% yield).

Macro-RAFT Agent: (PEOA-co-AA)-TTCA- DIBO

STEP 1: DIBO-TTCA (14)

A mixture was prepared in 5 mL of DCM by adding DIBO (1 eq., 0.7 mmol, 0.153 g), TTCA (2 eq., 1.39 mmol, 0.507 g) and 4-(dimethylamino) pyridine (DMAP, 0.24 eq., 0.17 mmol, 0.02 g). N-N'-dicyclohexylcarbodiimide (DCC, 2 eq., 1.39 mmol, 0.287 g)

was dissolved in 5 mL of DCM and added dropwise to the previous mixture. The reaction mixture was stirred 10 h at room temperature. The compound was purified by chromatography column (SiO₂, heptane/AcOEt, 4:1). The final product was a yellow oil with (139.4 mg) 75 % yield.

¹H NMR (400 MHz, CDCl₃): δ/ ppm: 0.88 (t, 3H, CH₃CH₂, J = 7.0 Hz), 1.24-1.28 (m, CH₃(CH₂)₉, 18H), 1.61-1.63 (m, 2H, CH₂CH₂S), 1.79 (s, 3H, CH₃C), 1.83 (s, 3H, CH₃C), 2.89 (dd, 1H, CHHCHO, J= 15.1, 4.0 Hz), 3.15 (dd, 1H, CHHCHO, J= 15.1, 2.0 Hz), 3.26 (app dt, 2H, CH₂S, J= 7.3, 4.2 Hz), 5.49 (br s, 1H, CH₂CHO), 7.25-7.33 (m, 7H, 7×CH_{ar}), 7.60 (d, 1H CH_{ar}, J= 8.0 Hz); ¹³C NMR (100 MHz, CDCl₃): δ (ppm) = 14.3 (CH₂CH₃), 22.8 (CH₂CH₃), 25.5 (CH₃), 25.9 (CH₃), 28.0 (CH₂CH₂S), 29.1 (CH₂), 29.2(CH₂), 29.5 (CH₂), 29.6 (CH₂), 29.7 (CH₂), 29.8 (2×CH₂), 32.0 (CH₂), 37.1 (CH₂S), 46.1 (CH₂CHO), 56.1 (C(CH₃)₂), 77.9 (OCHCH₂), 109.5 (C≡C), 113.1 (C≡C), 121.3 (C_{ar}), 123.6 (CH_{ar}), 124.3 (C_{ar}), 125.9 (CH_{ar}), 126.3 (C_{ar}), 127.2 (CH_{ar}), 127.3 (CH_{ar}), 128.0 (CH_{ar}), 128.3 (CH_{ar}), 130.4 (CH_{ar}), 151.1 (2×C_{ar}), 171.7 (C=O), 220.9 (SC=S).

STEP 2: (PEOA-co-AA)-TTCA- DIBO (15)

Same protocol as the MacroRAFT agent: (PEOA-co-AA)-TTCA was used replacing TTCA by DIBO-TTCA. The conversion rate and polymer mass were estimated based on the total monomer conversion followed by NMR (≥77%yield).

1.1.2.4. Nanoparticles Preparation

FNP_{Green}

In a 5 mL round bottom flask, the macroRAFT agent (PEOA-co-AA)-TTCA **13** (1 eq., 0.07 mmol, 0.42 g), the green-BDPMA **2** (3.2 eq., 0.21 mmol, 0.097 g), 2,2'-Azobisisobutyronitrile (AIBN, 0.5 eq., 0.03 mmol, 0.005 g) were dissolved in styrene (157 eq., 10.20 mmol, 1.06 g). The mixture was placed in ice bath and degassed with Ar flux for 30 min. Just after, the reaction was placed in an oil bath at 80 °C and stirred for 70 min. The reaction was quenched in an ice bath and 5 mL of NaOH (0.1 M) solution

was added. The reaction was placed in an ice bath, under ultrasounds at 120 W for 10 min. The miniemulsion was placed in an ice bath and degassed for 30 min with Ar flux. Subsequent, the reaction was placed in an oil bath at 80 °C and stirred overnight to restart the polymerization.

FNP_{Red} (Figure 2.3)

In a 5 mL round bottom flask, the macroRAFT agent (PEOA-co-AA)-TTCA **13** (1 eq., 0.041 mmol, 0.261 g), the red-BDPMA **8** (3.2 eq., 0.131 mmol, 0.090 g), 2,2'-Azobisisobutyronitrile (AIBN, 0.5 eq., 0.02 mmol, 0.003 g) were dissolved in styrene (157 eq., 6.40 mmol, 0.666 g). The mixture was placed in ice bath and degassed with Ar flux for 30 min. Just after, the reaction was placed in an oil bath at 80 °C and stirred for 70 min. The reaction was quenched in an ice bath and 5 mL of NaOH (0.1 M) solution was added. The reaction was placed in an ice bath, under ultrasounds at 120 W for 10 min. The miniemulsion was placed in an ice bath and degassed for 30 min with Ar flux. Subsequent, the reaction was placed in an oil bath at 80 °C and stirred overnight to restart the polymerization.

FNP_{G-DIBO}

In a 5 mL round bottom flask, the macroRAFT agent (PEOA-co-AA)-TTCA **13** (1 eq., 0.35 mmol, 0.225 g), the macroRAFT agent DIBO-TTCA **15** (0.5 eq., 0.019 mmol, 0.113 g), the green-BDPMA **2** (4.9 eq., 0.17 mmol, 0.080 g), 2,2'-Azobisisobutyronitrile (AIBN, 0.7 eq., 0.027 mmol, 0.005 g) were dissolved in styrene (241 eq., 8.48 mmol, 0.882 g). The mixture was placed in ice bath and degassed with Ar flux for 30 min. Just after, the reaction was placed in an oil bath at 80 °C and stirred for 70 min. The reaction was quenched in an ice bath and 6.7 mL of NaOH (0.1 M) solution was added. The reaction was placed in an ice bath, under ultrasounds at 120 W for 10 min. The miniemulsion was placed in an ice bath and degassed for 30 min with Ar flux. Subsequent, the reaction was placed in an oil bath at 80 °C and stirred overnight to restart the polymerization.

FNP_R-DIBO

In a 5 mL round bottom flask, the macroRAFT agent (PEOA-co-AA)-TTCA **13** (1 eq., 0.38 mmol, 0.242 g), the macroRAFT agent DIBO-TTCA **15** (0.5 eq., 0.020 mmol, 0.122 g), the Red-BDPMA **8** (4.9 eq., 0.187 mmol, 0.129 g), 2,2'-Azobisisobutyronitrile (AIBN, 0.7 eq., 0.029 mmol, 0.005 g) were dissolved in styrene (241 eq., 9.15 mmol, 0.952 g). The mixture was placed in ice bath and degassed with Ar flux for 30 min. Just after, the reaction was placed in an oil bath at 80 °C and stirred for 70 min. The reaction was quenched in an ice bath and 7.2 mL of NaOH (0.1 M) solution was added. The reaction was placed in an ice bath, under ultrasounds at 120 W for 10 min. The miniemulsion was placed in an ice bath and degassed for 30 min with Ar flux. Subsequent, the reaction was placed in an oil bath at 80 °C and stirred overnight to restart the polymerization.

1.1.2.1. Fluorescein Grafting on FNP_{Red}

FNP_{Red}-FA

300 µL FNP_{Red} (0.1 mg/mL) was diluted in 4 mL of water in the dark. In parallel, 1 equivalent of FA (6.7 mg) compared to the acrylic acid units (from synthesis) in FNP_{Red} was dissolved in 0.4 mL of ethanol. The solution was added to the nanoparticles solution and the mixture was stirred at 4°C. Then, a solution of EDC (4 equiv., 15 mg) in water (1 mL) was added to the previous mixture. Lastly, ethanolamine (2 equiv., 2.3 µL) was added after 2 hours. The reaction solution was still stirred at 4°C overnight in the dark. Finally, the mixture was purified with a tangential filtration cassette ready-to-use (Vivaflow 50 (230 V), Sartorius, France), for 8 hours.

1.1.3. FNP Characterization Methods

1.1.3.1. DLS

For each type of FNPs, 1.2 µL of stock solution were diluted to 2.0 mL using filtered deionized (D.I.) water to achieve a concentration of 0.01% in weight. Diluted

samples were placed into dispensable 50 μL cuvette cells. Samples were inserted into the Particle Size Analyzer Vasco Flex by Corduran Technologies (from LAC – Laboratoire Aimé Cotton – UMR CNRS 9188). The laser of the Vasco Flex was calibrated by visually comparing it to the calibration laser of the equipment. Three measures of three scans were performed for each sample.

1.1.3.2. TEM

Transmission Electron Microscopy (TEM) was performed on a JEOL1400 operating at 80kV. The samples were diluted in water prior to analysis and then deposited on a carbon-coated copper grid. Phosphotungstic acid (PTA) was used as contrast agent.

The present work has benefited from the core facilities of Imagerie-Gif, (<http://www.i2bc.paris-saclay.fr>).

1.1.3.3. ZETA-POTENTIAL

Zeta potentials (ζ) were performed on a Zetasizer Nanoseries (Malvern) apparatus at the from LAC – Laboratoire Aimé Cotton – UMR CNRS 9188). Samples were prepared at concentration of 0.01 wt % diluted in buffered with 200 mM of phosphate/citrate salts (pH values varied from 4 to 8) at 25°C. Six measures of ten scans were performed for each sample.

1.1.3.4. NANOSIGHT

Particle size, concentration and dispersion was determined by Nanoparticle Tracking Analysis (NTA) on a NanoSight NS300 by Malvern Analytical (PPSM - Laboratoire de Photophysique et Photochimie Supra-et Macromoléculaires – UMR CNRS 8531). For each sample, 1.2 μL of FNP stock solution were diluted to 2.0 mL using filtered D.I. water as solvent. A further dilution of 50 μL of already diluted FNP solution in 10 mL of water for green FNPs was performed. Three measurements of 60 seconds each were recorded to determine size and concentration for each type of FNPs. The FNP stock concentrations were found from the measured concentration of the diluted samples.

1.1.3.5. ABSORPTION & EMISSION

UV-visible spectra were recorded on a UV-2600 UV-VIS Spectrometer by Shimadzu Scientific Instruments. Excitation and emission spectra were measured on a FluoroMax-4 Spectrofluorometer (Horiba Jobin-Yvon). Optical density of the samples was checked to be less than 0.1 to avoid reabsorption artifacts. Fluorescence quantum yields Φ_F were determined using Rhodamine 6G ($\Phi_F = 0.95$ in ethanol) and Sulforhodamine 101 ($\Phi_F = 0.90$ in ethanol) as a references (12).

Fluorescence decay curves were obtained with a time-correlated single-photon-counting method using a titanium-sapphire laser (82 MHz, repetition rate lowered to 4 MHz thanks to a pulse-peaker, 1 ps pulse width, a doubling crystals is used to reach 485 nm excitation) pumped by an argon ion laser from Spectra Physics (Mountain View, CA USA). Decays were measured with a band-pass of 21 nm.

Average fluorescence lifetimes were calculated by global integration of the decays using the equation 1.1 (13):

$$\langle \tau \rangle = \frac{\int_0^{\infty} t I(t) dt}{\int_0^{\infty} I(t) dt} \quad (1.1)$$

where $I(t)$ is the fluorescence intensity at time t of the decay.

Results & Discussion

Synthesis of Dyes

The synthesis of 'green' BODIPY **1** was done following a classic protocol (Figure 2.7), starting from the condensation of benzaldehyde with two kryptopyrrole units, catalyzed by TFA and then oxidized and complexed by BF_3 . Afterwards, the esterification with methacryloyl chloride was proceeded to obtain Green BDPMA **2**, which can be easily polymerized.

For the synthesis of red BODIPY **7**, the synthesis of naphthalene-pyrrole was done first by following the Trofimov reaction (5), which requires the preparation of the oxime of the aromatic considered and then its reaction with acetylene (gas) (see experimental part: 3-ethyl-2-(8-methylnaphthalene-1-yl)-1-vinyl-1H-pyrrole).

The scheme of the synthesis is detailed in Figure 2.8. At first, methylnaphthalene is functionalized with a ketone via a Friedel and Craft reaction using propionyl chloride. Then, the ketone was converted into an oxime according to a classical method of synthesis. The synthesis of the pyrrole is then carried out by a Trofimov reaction. The oxime is placed in a very basic solution of KOH in DMSO and then the reaction is heated to 120 °C. Once the temperature is stabilized, an acetylene flow is installed for about 5 hours. At the end of the reaction, three products are generally collected after chromatography: pyrrole, N-vinyl pyrrole and the starting ketone. Vinyl-pyrrole can be deprotected in pyrrole by treatment with mercury acetate followed by reduction with sodium borohydride with almost quantitative yields. The synthesis of red BDPMA **8** (Figure 2.9) as well as the esterification to a phenyl methacrylate derivative are made under the same conditions as for green BDPMA **2**.

FNP Synthesis

As previously described, FNP were synthesized with the general methodology described by C. Grazon *et al.* (1, 2). After the preparation of the random copolymer, they were covalently linked to a BODIPY monomer and styrene. It is first block extended with a mixture of styrene and BODIPY monomers by partial bulk polymerization (approx. 20% conversion) to afford an amphiphilic copolymer. The mixture is then poured in basic water and submitted to ultrasound treatment to yield a mini-emulsion of nanoparticles that are brought to 80 °C to terminate the polymerization overnight.

FNP Size Characterization

Dynamic Light Scattering (DLS), alternatively called photon correlation spectroscopy, was the first technique used to determine the size of the nanoparticles in an aqueous solution. DLS measures the rate of diffusion of the particles using scattered light (14). During measurement, the Brownian motion of the particles, given by the

bombardment with each other, is monitored and related to time-dependent fluctuations in scattering intensity (15).

DLS measures the hydrodynamic diameter, which encompasses the diameter of the particle and a double layer thickness associated to the spread of the surrounding polymer chain. This is particularly important for these FNP, where the carboxylic terminals surrounding the core are hydrophilic. DLS correlates light scattering data to the size of moving particles in solution. However, if there are multiple populations of nanoparticles, also known as polydispersity, there is a possibility that large particles are overshadowing small ones affecting the accuracy of the recorded hydrodynamic diameter.

The DLS measurement device analyzes the data using 2 algorithms for polydisperse colloids. The cumulant algorithm provides a Gaussian distribution, which provides a good fit for samples with primarily one kind of nanoparticle. The Pade Laplace algorithm provides a discrete distribution that accounts for polydispersity among synthesized particles. The Pade Laplace algorithm is considered to be the most accurate since the cumulant algorithm is an average of all sizes. As it can be seen in Table 2.2, the average size (according to cumulant fit) of FNP_{Green} is **80 nm**. FNP_{Green} average radio obtained is in good agreement with previous data from particles synthesized with the same conditions (**77 nm** from ref. 2, FANP_{2BOD}). These are the only FNP which have been published. For DIBO-FNP there is not comparable data already published. FNP_{Red} average hydrodynamic diameter was **110 nm**, which is slightly larger in comparison with FNP_{Green}. However, only with this measurement is not possible to state FNP_{Red} are larger than FNP_{Green}, since the value represents an average of all the populations present on the sample. ~~The difference in size between green and red FNP could be explained by the red BODIPY dye being more sterically hindered than the green BODIPY and thus occupying a larger volume.~~ Comparing to literature (2),

From the Pade Laplace algorithm, it was shown that all these FNP are polydispersed. For FNP_{G-DIBO} the average size was found to be **100 nm** and for FNP_{R-DIBO} **240 nm**. As it can be seen from the Pade Laplace algorithm, the presence of a 'big' nanoparticle or aggregate increased the average value when using the Cumulant algorithm.

From Pade-Laplace two populations, with similar intensity, can be observed whatever the FNPs. As an example, FNP_{Green}: 54 ± 8 nm and 140 ± 40 nm, those values

are very distant from the Cumulant (80 nm) and both standard deviations are big (~15-30% of the FNP size). This is general for all the types of nanoparticles, it confirms the large polydispersity of the FNP. Besides, it seems that the introduction of DIBO polymer in the nanoparticle structure, results in an increase of their diameter (from 54 nm for FNP_{Green} to 70 nm for FNP_{G-DIBO} and from 100 nm for FNP_{Red} to 150 nm for FNP_{R-DIBO}).

From this data, it is easy to observe that DLS measurements are strongly dependent on the polydispersity of the nanoparticles and the algorithm used to determine their size. DLS analysis is an easy and fast technique to obtain the average hydrodynamic radio of a sample. However, for poly-disperse samples is not the best strategy to obtain reliable data. For this reason, other techniques used to evaluate the size of the nanoparticles will be discussed.

Table 2.2 Average hydrodynamic diameters (nm) for all FNP from DLS measurements using two different methods (Cumulant and Pade-Laplace).

Sample	Cumulant	Pade Laplace			
		Population 1	Intensity	Population 2	Intensity
FNP_{Green}	80 ± 2	54 ± 8	0.4 ± 0.2	140 ± 40	0.5 ± 0.2
FNP_{Red}	110 ± 2	100 ± 2	0.8 ± 0.0	430 ± 4	0.2 ± 0.0
FNP_{G-DIBO}	100 ± 4	70 ± 9	0.6 ± 0.1	290 ± 85	0.4 ± 0.1
FNP_{R-DIBO}	240 ± 3	150 ± 5	0.5 ± 0.0	460 ± 30	0.5 ± 0.0

Nanoparticle Tracking Analysis (NTA) is another technique used for particle characterization, which provides insights with respect to size distribution and concentration of particles with diameters ranging from 40 nm to 2000 nm. NTA obtains particle distribution and concentration measurements based on light scattering and Brownian motion (16). Nanoparticles exposed to a laser beam scatter light that can be visualized with the microscope embedded in the device. Since the sample flows underneath the laser, the camera of the microscope records a video that is immediately

analyzed to track individual particles (16). The hydrodynamic diameter of the FNP is then calculated using the Stokes-Einstein Equation.

The size and concentration from the experimental results using NTA for each of FNP are summarized in Table 2.3. On one side, NTA provided both the mean diameter of the flowing nanoparticles as well as the mode, which represents the most repeated nanoparticle size in the sample. The software of the device creates a plot showing the sizes in relation with their FNP concentration, which gives insights about the presence of multiple nanoparticle populations. Moreover, the polydispersity index (PDI) is calculated from the intensity level associated to each size, which represents the width of the overall size distribution and gives a quantitative measure of the appearance frequency of the average particle diameter. PDI is an indicator of polydisperse system (when higher than 0.5), and if it is closer to zero it denotes a monodisperse system. For all the samples the PDI was higher than 0.5, showing a polydisperse population. It seems consistent with the DLS analysis, Pade-Laplace fitting showing two populations.

On the other hand, the number of particles per mL of solution is automatically calculated by the software since the flowing rate throughout the recorded video is constant. Having the particle concentration of the diluted solution allows for the determination of the FNP concentration in the stock solution by using the dilution factors applied to each sample. Concerning “Green” particles, the concentration seems to be in the same order of magnitude (approx. 4 to $5 \cdot 10^{14}$ particles per mL). Surprisingly for “red” particles, stock concentration is $9 \cdot 10^{13}$ particles per mL for FNP_{R-DIBO} and approximately $4 \cdot 10^{15}$ particles par mL for FNP_{Red}.

Table 2.3 Summary of results after NTA data analysis of all FNP

FNP Type	Mean (nm)	Mode (nm)	PDI (-)	Concentration (Particles/mL)	Stock Concentration (Particles/mL)
FNP_{Green}	80 ± 1	70 ± 1	0.61	$7.3 \cdot 10^8$ $3.4 \cdot 10^7$	$\pm 4.9 \cdot 10^{14} \pm 2.3 \cdot 10^{13}$
FNP_{Red}	110 ± 1	80 ± 1	0.81	$1.0 \cdot 10^9$ $3.6 \cdot 10^7$	$\pm 3.6 \cdot 10^{15} \pm 1.3 \cdot 10^{14}$
FNP_{G-DIBO}	100 ± 1	80 ± 2	0.93	$1.1 \cdot 10^9$ $3.0 \cdot 10^7$	$\pm 3.7 \cdot 10^{14} \pm 9.9 \cdot 10^{12}$
FNP_{R-DIBO}	130 ± 2	110 ± 4	0.92	$1.4 \cdot 10^8$ $6.2 \cdot 10^6$	$\pm 9.0 \cdot 10^{13} \pm 4.1 \cdot 10^{12}$

By comparing FNP average sizes from DLS and NanoSight NTA, it can be seen that the hydrodynamic diameters obtained throughout the characterization process are similar for the FNP_{Green}, FNP_{Red}, and FNP_{G-DIBO} (Table 2.4). DLS measurements for the remaining FNP_{R-DIBO} are also close in magnitude. However, their hydrodynamic diameters seem to be much smaller according to NTA (average value), which could be explained by the underestimation of less frequent, yet present, larger FNP populations in the average diameter calculations (Table 2.2: Pade Laplace).

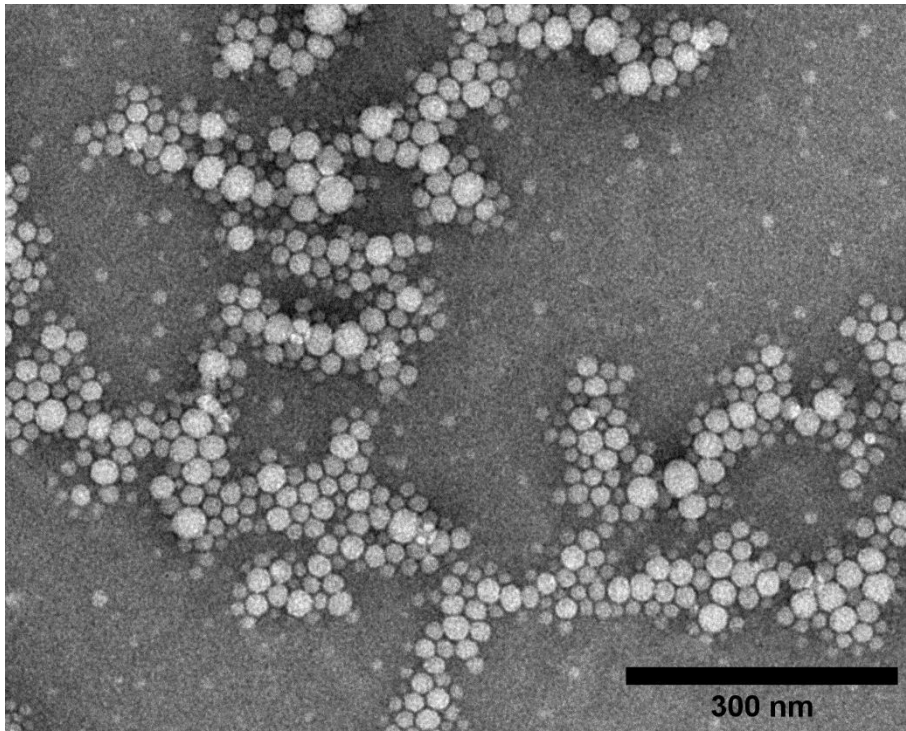
Table 2.4 FNP size comparison using different size characterization techniques.

FNP	DLS Cumulant (nm)	NTA (nm)
FNP_{Green}	80 ± 2	80 ± 1
FNP_{Red}	110 ± 2	110 ± 1
FNP_{G-DIBO}	100 ± 4	100 ± 1
FNP_{R-DIBO}	240 ± 3	130 ± 2

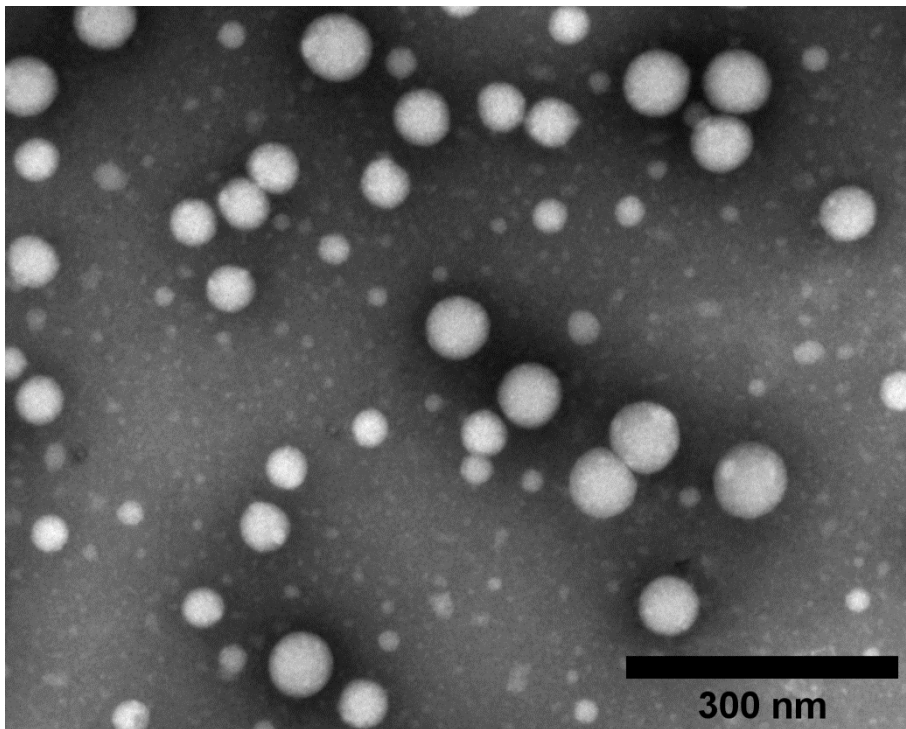
Transmission Electron Microscopy (TEM) was used to visualize the nanoparticles and determine their size in a “dry” state (which shall be different from the hydrodynamic radius), shape, and aggregation state. In this technique, electrons are emitted through a vacuum column until reaching the sample. Depending on the density of the surface, electrons either passed through it or get scattered. Since the nanoparticles are not good conductors, a contrast agent (phosphotungstic acid, PTA) to better visualize. PTA was used as negative stain, which means the background is stained and the sample is untouched. Due to short time, no further comparisons were done by changing or not using the contrast agent.

Table 2.5 FNP size distribution found by TEM (Mean, Mode, Standard deviation of TEM analysis), and DLS (cumulant), NTA and the difference in comparison with TEM.

	N	Mean	Mode	Standard	DLS Cumulant	NTA	$\Delta (D_{DLS} - D_{TEM})$	$\Delta (D_{NTA} - D_{TEM})$
	Total	(nm)	(nm)	Deviation	(nm)	(nm)	(nm)	(nm)
FNP_{Green}	1595.0	29.0	20.1	± 7.7	80 ± 2	80 ± 1	51	51
FNP_{Red}	3549.0	44.6	22.3	± 16.2	110 ± 2	110 ± 1	65	65
FNP_{G-DIBO}	428.0	38.2	50.5	± 15.3	100 ± 4	100 ± 1	62	62
FNP_{R-DIBO}	63.0	31.7	22.0	± 10.3	240 ± 3	130 ± 2	207	67

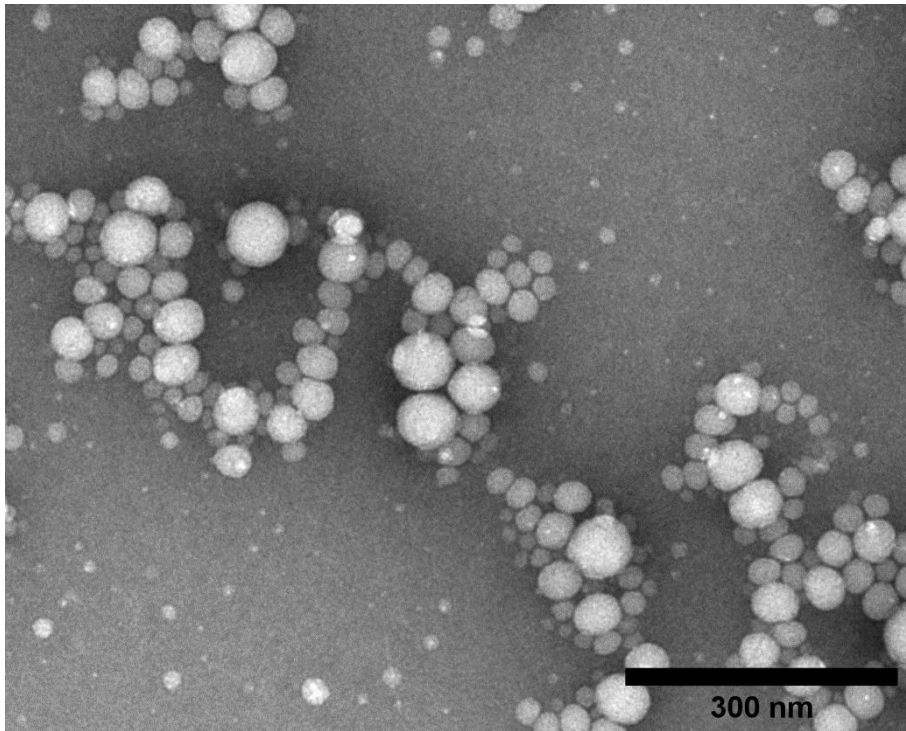


FNP_{Green}

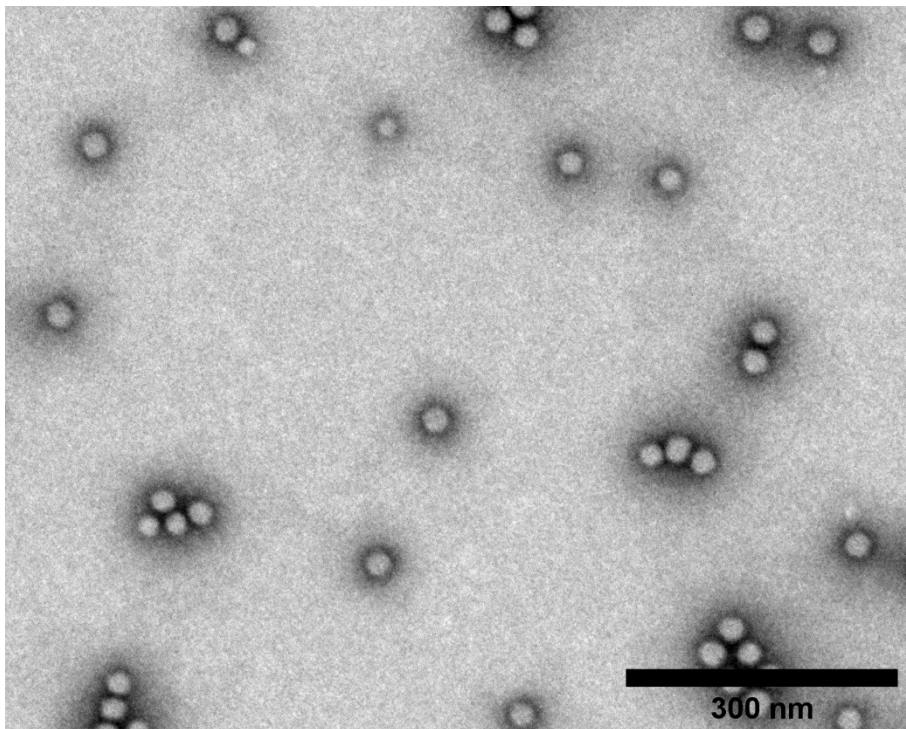


FNP_{Red}

Figure 2.10 FNP images from TEM using contrast agent.



FNP_G-DIBO



FNP_R-DIBO

Figure 2.11 FNP images from TEM using contrast agent.

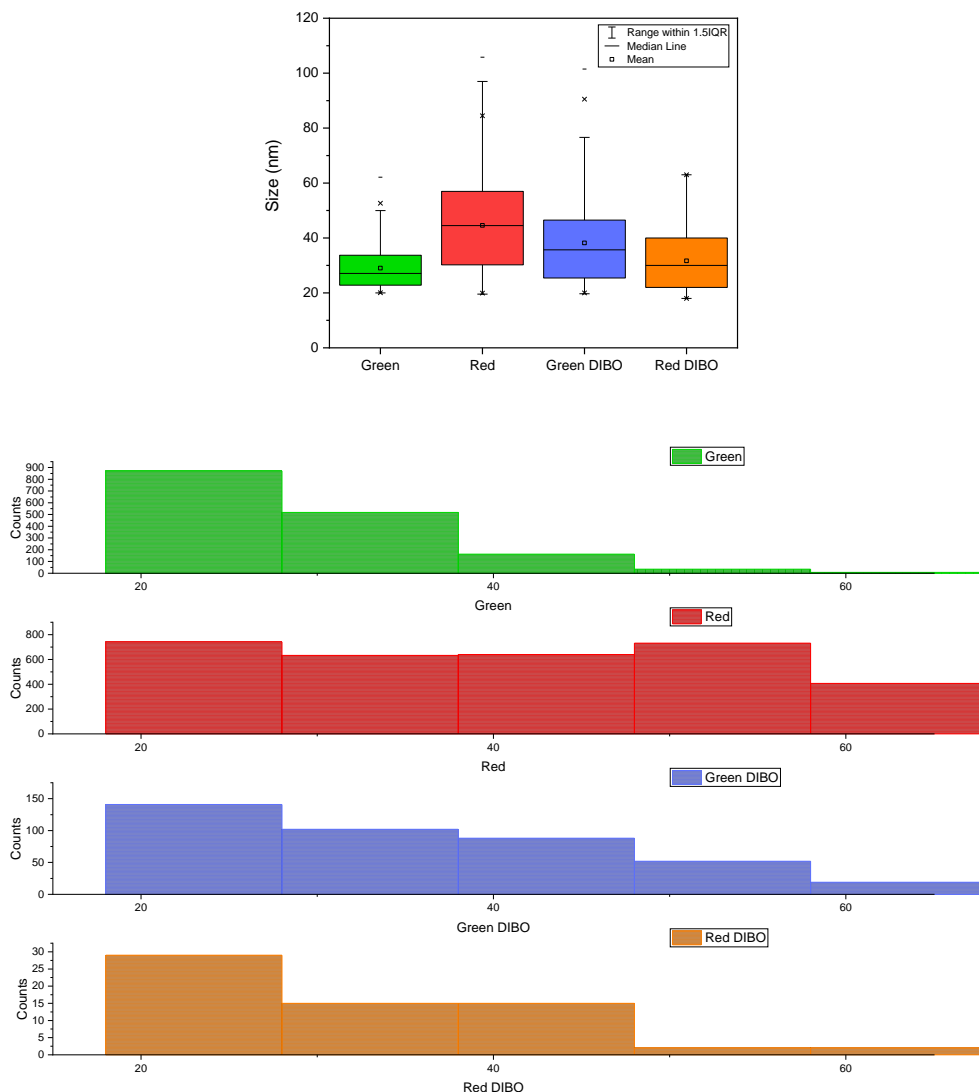


Figure 2.12 FNP images from TEM using contrast agent and subsequent size analysis.

In Figure 2.10 and 2.11 different nanoparticles by TEM can be observed. FNP_{Green} and FNP_{G-DIBO} aggregation state looks alike, only changing in size distribution, being FNP_{G-DIBO} bigger than FNP_{Green} . Whereas for red particles, FNP_{R-DIBO} are slightly smaller than FNP_{Red} . As it can be seen in Table 2.5 and Figure 2.12, the average size of FNP_{Green} is **29 nm**, FNP_{Red} with a diameter of **38 nm**, FNP_{G-DIBO} is **38 nm** and FNP_{R-DIBO} with a diameter of **31 nm**. The difference in size between DLS and NTA in comparison with TEM comes from the dry state, in solution the shell polymer of the FNP is hydrated and elongated. In Table 2.5 an estimated of the PEG-shell is shown comparing either DLS-TEM or NTA-TEM. PEG-Shell can be estimated between **51 to 67 nm**. In Figure 2.12

from the histogram chart it can be observed there are many size distributions of the particles. This is in agreement with the PDI measured from NTA.

FNP Surface Charge Characterization

Zeta potential (ζ) of the different FNP were determined at different pH values (Figure 2.13). Seems that the macromolecular architecture of the hydrophilic block did not affect in great matter the surface charge. All values are negative, which is in accordance with values reported for pegylated polystyrene particles without PAA (17). The protonation of the acrylic acid units was not detected (18). All particles were stable in the measured pH range.

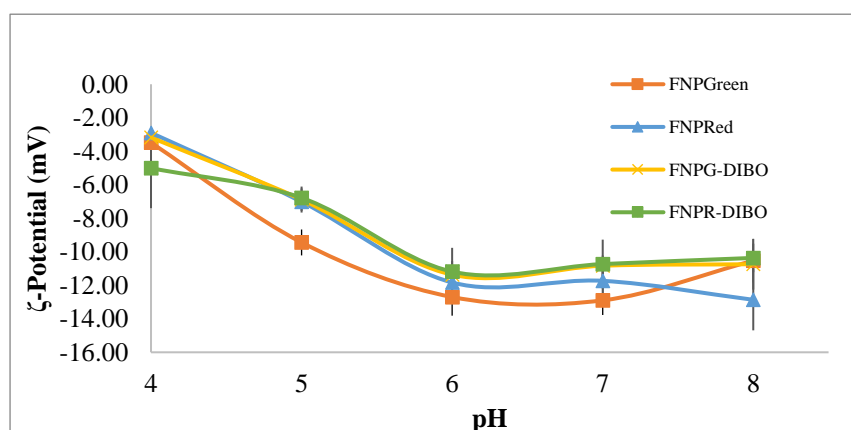


Figure 2.13 Zeta potentials in mV recorded at room temperature in saline water ($[\text{NaCl}] = 14\text{mM}$) for different pH values (phosphate-Citrate buffers 1 mM) for FNP (a) $\text{FNP}_{\text{Green}}$, (b) FNP_{Red} (c) $\text{FNP}_{\text{G-DIBO}}$, (d) $\text{FNP}_{\text{R-DIBO}}$.

To summarize, after all the different size characterizations, the polydispersity of the FNPs is evident. The charge of the particles behaves similarly independently of the type of nanoparticle (color, shell structure), all particles zeta-potentials decrease with the increment of pH and the elongation of the PEG-Shell is also a similar value for all FNP (50- 65 nm), Since our main objective is to build a sensor for bacterial detection, we decided to proceed with a polydisperse population of FNP without further size differentiation, expecting this will not affect the sensitivity of the sensor. Following, the spectroscopic properties of the FNP will be introduced.

FNP Spectroscopy Characterization

The absorption and fluorescent emission spectra for the FNP are presented in Figure 2.14. The absorption spectra showed the classical expected shape of the BODIPY dyes with one intense band in the visible range representing the transition energy between the ground state and the first excited state and it is in good agreement with reported literature (2). The smaller band closer to UV of the absorption spectra represents the energy transition from the ground state to the second excited state.

Figure 2.14 shows green FNP spectra ($\text{FNP}_{\text{Green}}$ and $\text{FNP}_{\text{G-DIBO}}$), in comparison with green-BODIPY monomer in DCM. Data (not shown) were also recorded in toluene as this solvent has close properties with polystyrene. Green FNPs' absorption maximum (529 nm) is very close to the one in toluene (528nm) and is the same as in DCM. A red-shift in the emission maximum is observed (compared to the monomer in toluene) : 7 nm for $\text{FNP}_{\text{Green}}$ and 8 nm for $\text{FNP}_{\text{G-DIBO}}$. Similar observation is seen in comparison with DCM : 9 nm for $\text{FNP}_{\text{Green}}$ and 10 nm for $\text{FNP}_{\text{G-DIBO}}$. Such bathochromic shift on emission maximum has already been observed by our group (19) and was previously reported by Alvarez *et al.* (20) for krypto-BODIPY copolymerized with MMA. Such behavior was attributed to the fluorophore confinement within the matrix.

For red FNPs, a bathochromic shift in absorption and emission is observed on going from the monomer in an organic solvent to FNPs. Indeed in comparison with Red-BODIPY in DCM or toluene (558 nm), the maximum in absorption is 1 nm red-shifted for FNP_{Red} , and 3 nm for $\text{FNP}_{\text{R-DIBO}}$ (1nm band-pass). Concerning emission, a red-shift is observed from DCM or toluene to FNPs: 6 or 5 nm for FNP_{Red} and 2 nm for $\text{FNP}_{\text{R-DIBO}}$. Thus polymerization and polydispersity seem to have a weak impact on band-position.

Stokes shift in toluene is around 420 cm^{-1} for Green-BODIPY and 1255 cm^{-1} for the Red-BODIPY. Such increase from “green” to “red” monomer in an organic solvent, is connected to the change in electronic density between the ground-state and the excited-state. Thus looking at Figure 2.2, the naphthalene groups are likely to rotate from ground- to excited state inducing a larger Stokes shift than “green” dye (no aromatic ring present).

From table 2.6, it can be observed that ‘green’ (including DIBO) FNPs have a smaller Stokes shift in comparison with ‘red’ FNP. It is in agreement with monomers behavior (as discussed above). In any FNPs, Stokes shift is higher than for the monomer

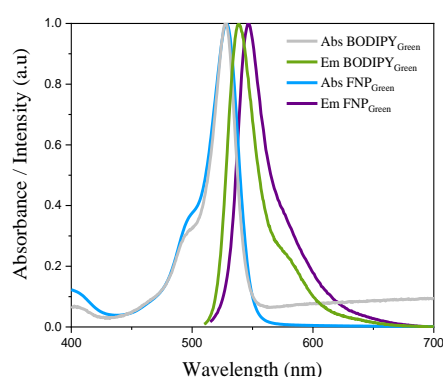
in a solvent (approx. +200 cm^{-1} for green-FNPs and +100 to 200 cm^{-1} for red FNPs). This is connected to the emission red-shift already discussed above.

Looking at Full Width at Half-Maximum (FWMH), for Green-BODIPY monomer in toluene, FWHM in absorption is around 830 cm^{-1} and 1000 cm^{-1} for the emission band. For red-BODIPY monomer in toluene, FWHM in absorption is around 1340 cm^{-1} and 1520 cm^{-1} for the emission band. The increase in FWHM between the two different monomers may arise from the enlargement of conjugated system, which is also consistent with the absorption wavelength red shift (529 nm for green monomer and 548 nm for the red-one).

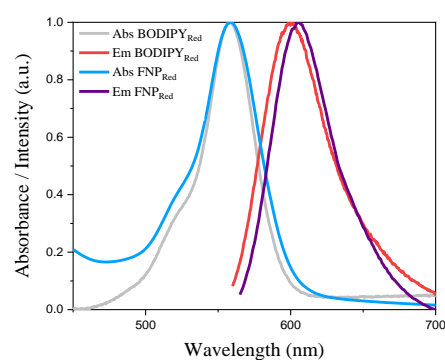
From monomer to polymer (Table 2.6), whatever the BODIPY involved is, absorption band FWHM is increased (830 to 1015 and 1030 cm^{-1} for Green FNPs, and 1340 to 1582 and 1916 cm^{-1} for Red-FNPs). As discussed above band-position is slightly affected by polymerization, whereas FWHM is. This might be consistent with aggregation of the fluorophore within the matrix. It might also be connected to polydispersity (different size may induce different environment for the dyes). Now looking at emission FWHM, polymerization induces a decrease, emission band is thinner, whatever the BODIPY and FNPs. Indeed for $\text{FNP}_{\text{Green}}$ a decrease of more than 40 cm^{-1} is observed, and about 180 cm^{-1} $\text{FNP}_{\text{G-DIBO}}$. For FNP_{Red} a FWHM decrease of 180 cm^{-1} is observed, and about 50 cm^{-1} $\text{FNP}_{\text{R-DIBO}}$. Such decrease in emission might be connected to both aggregation and confinement of the emitting species. If aggregates are present, we can suppose that they are not or very little emissive, they won't contribute to emission. If we make the assumption that emission is mainly coming from "monomer-like BODIPY" (isolated fluorophores *i.e* non-aggregated), such molecules shall have less degrees of freedom within the polymer, which leads to less accessible states which may explain the FWHM decrease from monomer in toluene to BODIPY in FNPs. Another hypothesis would be that only small particles will emit (low loading of fluorophore), whereas bigger won't (higher concentration and thus aggregation of fluorophore).

Table 2.6 Spectroscopy parameters for the different FNPs in D.I. and BODIPY dyes in DCM, at room temperature.

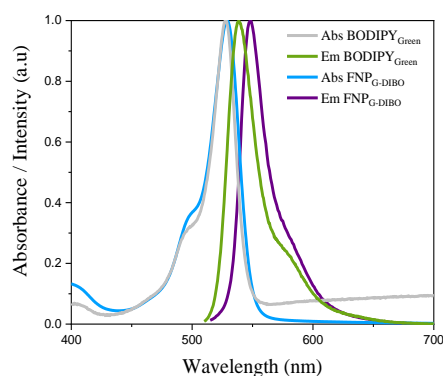
FNP	$\lambda_{\text{abs,max}}$ (nm)	$\lambda_{\text{em,max}}$ (nm)	FWHM_{abs} (cm^{-1})	FWHM_{em} (cm^{-1})
FNP_{Green}	529	547	982	921
FNP_{Red}	559	605	1582	1325
FNP_{G-DIBO}	548	558	1030	822
FNP_{R-DIBO}	562	602	1916	1469
Green BODIPY	529	540	830	1000
Red BODIPY	558	600	1340	1520



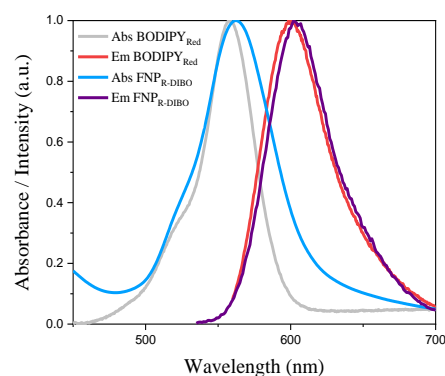
FNP_{Green}



FNP_{Red}



FNP_{G-DIBO}



FNP_{R-DIBO}

Figure 2.14 Normalized absorption and fluorescent emission spectra recorded in D.I. water at room temperature for FNPs (a) FNP_{Green}, (b) FNP_{Red} (c) FNP_{G-DIBO}, (d) FNP_{R-DIBO}; compared with their respective BDPMA in DCM.

Fluorescence Quantum Yield (Φ_F) provides a measure of fluorescence efficiency represented by the ratio between the numbers of emitted and absorbed photons. The nanoparticles used in this project have fluorescent properties attributed to the BODIPY

fluorophore in their core. As previously mentioned, rhodamine 6G dye was used as reference for green FNP, while sulforhodamine was used for red FNP. From the slopes of the linear fits (area under the curve from the emission spectrum *vs* absorbance) and using the literature values of the reference dyes, Φ_F was calculated using Equation 1.1.

For FNP_{Green} it was found Φ_F : 15 %, for FNP_{G-DIBO} 13 %, which are lower in comparison to the one found for Green-BDPMA in toluene (Φ_F : 69 %). Similarly, for FNP_{Red} it was found Φ_F : 35 %, for FNP_{R-DIBO} 28 %, which are lower in comparison to the one found for Red-BDPMA in toluene (Φ_F : 53 %). These differences might come from the local environment of the dye in the core of the FNPs, in comparison with the free dye (2). Such decrease is consistent with fluorophore aggregated state. For green BODIPY, going from toluene to FNPs leads to almost a five-time decrease in fluorescence quantum yield. Whereas for Red BODIPY, the decrease is always less than twice. Thus the decrease in fluorescence quantum yield is more limited with the bulky red dye. Moreover, comparing red-FNPs (FNP_{Red} and FNP_{R-DIBO}) with green-FNPs (FNP_{Green} and FNP_{G-DIBO}), Φ_F are around 2 times higher for red-FNPs than green ones. Again, this might come from the steric-hindrance coming from the more ‘bulky’ red-BDPMA, while in the green-FNPs BODIPY probably is more aggregated.

BODIPY concentration in the analyzed solutions was calculated from the Beer-Lambert Law, which relates concentration with maximum absorption Abs_{max} , extinction coefficient ϵ , and length L of quartz cuvettes where measurements were taken (21):

$$C_{Bodipy} = \frac{Abs_{max}}{L\epsilon} \times \frac{1 L}{1000 mL} [=] \frac{mol}{mL} \quad (1.2)$$

BODIPY concentration was converted to number of BODIPY molecules per mL using Avogadro’s number, which was multiplied by the dilution factor of the analyzed solutions to obtain the magnitudes at the stock conditions:

$$Nb_{BODIPY} = C_{Bodipy} \times 6.022 \times 10^{23} \times \frac{1}{1000} [=] \frac{Number\ of\ BDY\ per\ molecule}{mL} \quad (1.3)$$

From the ratio between the previously found FNP stock concentrations (NTA data, Table 2.3) and the number of BODIPY per mL of stock solution, the number of BODIPY molecules per FNP was found and presented in Table 2.7. The number of dyes per particle seems very high and may not reflect reality. This might come from unreliable

concentration measurements from NTA. No correlation between quantum yield and BODIPY number is clear even though the number of BODIPY calculated per particle is consistent with the number of moles of BODIPY introduced during synthesis.

Table 2.7 Fluorescent quantum yield and BODIPY per particles in **D.I. water**. As previously mentioned, reference dyes were used as follows: rhodamine 6G dye was used for green FNP, while sulforhodamine 101 was used for red FNP.

FNP Type	Φ_{FNP}	$\lambda_{em, max}$ (nm)	ϵ (18) ($10^3 \text{ Lmol}^{-1}\text{cm}^{-1}$)	BODIPY Ratio From NTA (BODIPY/FNP)	Moles introduced from synthesis (mmol)	Final Volume of Stock solution (mL)	BODIPY Ratio from synthesis (BODIPY/FNP)
FNP _{Green}	15 ± 2	547	73	1.8x10 ⁴ ± 8.5x10 ²	0.208	8	3.2x10 ⁴
	35 ± 5			2.8x10 ³ ± 9.8x10 ¹			
FNP _{Red}	13 ± 3	605	66	3.6x10 ⁴ ± 9.7x10 ²	0.173	6.7	4.2x10 ⁴
	28 ± 5			1.6x10 ⁵ ± 7.3x10 ³			
FNP _{G-DIBO}							
FNP _{R-DIBO}							

Until now, different types of FNPs have been studied, each one with a different purpose in this project. Chronologically, FNP_{Green} were first prepared and studied due to their simple and fast synthesis (one week, starting with a commercial reactant). They were used to implement all the protocols of characterization and to set the protocols of surface preparation (described in the following chapter). ‘Green’ surfaces were obtained (data are not presented in this manuscript), but similarly as C. Grazon *et al* (2), the emission band of BODIPY and FA are too close (515 and 547 nm, respectively). Subsequently, FNP_{Red} were synthesized to improve the facility of ratiometric measurement when grafting FA. FNP_{G-DIBO} and FNP_{R-DIBO} were prepared with the aim to improve selectivity of the sensor by targeting actively specific bacterial strains with the introduction of antibodies.

In the following part, FNP_{Red-FA} photophysical properties in comparison with FNP_{Red} upon pH will be described. The next chapter will focus in the preparation and characterization of surfaces grafted with these nanoparticles.

FNP_{Red-FA} Synthesis and Spectroscopy Characterization

As previously described, in order to obtain ratiometric pH-sensitive nanoparticles, FluoresceinAmine (FA) was grafted on FNP_{Red-FA}. Fluorescein has five acid-base forms (Figure 2.5). Its properties of absorption and fluorescence emission are completely dependent on the pH. In this work we focused mainly on forms **c** and **d** whose pKa is 6.4 (11). The spectroscopic characteristics of forms **c**, and **d** are summarized in Table 2.8 (11). The **d**-form has a strong absorption and fluorescent with a quantum yield of 0.93 and emits at 520, whereas the **c**-form is much less fluorescent and emits in the form of a wide band between 520 and 540 nm. These characteristics make it a molecule of interest for the elaboration of pH probes coupled with FNP_{Red}, which absorbs at 560 nm.

Table 2.8 Spectroscopy parameters for fluorescein forms **c** and **d** water at room temperature (from 11).

Specie	$\lambda_{\text{abs,max}}$ (nm)	$\lambda_{\text{em,max}}$ (nm)	E ($10^3 \text{ L}\cdot\text{mol}^{-1}\cdot\text{cm}^{-1}$)	Φ_{F}	τ (ns)
c-form	472	520-540	29	0.37	3.0
d-form	490	520	77	0.93	4.1

In our work, we chose to work with the commercial Fluoresceinamine (FA). FA has a quantum yield of 1.5% which is much lower than fluorescein or FITC (93%). This drop in quantum yield is due to the presence of the amine (photo-induced electron transfer). When the FA is converted to amide, the fluorescence quantum yield increases to 80%, depending on the nature of the group carried by the acid (22).

FA can be grafted onto FNP_{Red} (AA monomers) by peptide coupling in water, activated with EDC (23, 24). At first, FA was grafted on FNP_{Red} choosing to initially have one FA for ten acrylic acid moieties (calculated from synthesis stoichiometry). (5 red-BODIPY per AA). FA was solubilized in ethanol and added to EDC activated FNP_{Red} solution. Two hours after, an excess of ethanolamine was added to the solution in order to passivate the residual carboxylic acid functions. Thus, the FNP_{Red-FA} should be stable whatever the pH. The FNP_{Red-FA} were purified by a viva-flow membrane cassette system to remove the free FA in solution. Absorption spectra of supernatant were recorded till only a very weak signal from free FA can be seen (data not shown).

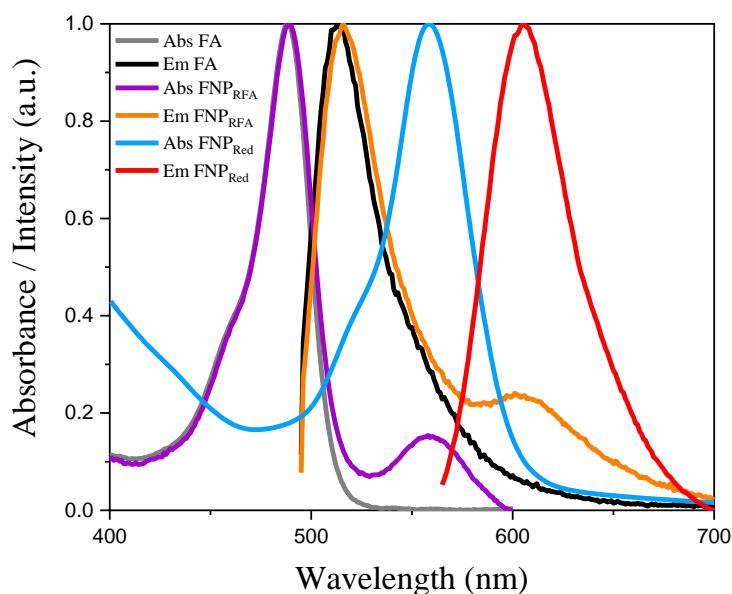


Figure 2.15 Normalized absorption (Abs) and emission spectra (Em) (λ_{exc} : 485 nm) at pH 8 (Citrate/Phosphate buffer 0.2M) at room temperature for FA, FNP_{Red} and FNP_{Red-FA}.

Fluorescence absorption and emission spectra of FA and FNP_{Red} are shown on Figure 2.15, there is a good spectral overlap between the fluorescence emission spectrum of FA (donor) at pH 8 and the absorption spectrum of FNP_{Red} (red dye as acceptor). Now let's have a look at FNP_{Red-FA}, the absorption spectrum shows two main bands: one maximum is around 488 nm: it corresponds to the FA band. Another maximum is found at 558 nm: it corresponds to the red-BODIPY in the FNPs core. The fluorescence emission spectrum (λ_{exc} : 485 nm, excitation of FA, and close to the "isobestic" point) of the grafted FNPs (FNP_{Red-FA}) have also two bands, one corresponding to the FA at 515 nm, the other corresponding to the red-BODIPY at 605 nm. Thus the two contributions, both in absorption and in emission, are clearly seen on the spectra and correspond to the two fluorophores spectral signature.

Concerning pH influence, both absorption and emission spectra of FNP_{Red-FA} are modified upon pH changes. On absorption spectra, clear changes on FA band shape are consistent with literature data and fluorescein behavior as a function of pH. The red-BODIPY contribution seems to be slightly affected by pH changes, except when pH is below 6. At this stage we cannot find any reasonable explanation why.

The maximum in fluorescence emission of the FA band decreases with pH (Figure 2.16), which gets closer to the maximum intensity of ‘red’ BODIPY band. Such behavior is also consistent with fluorescein behavior in aqueous solutions as pH changes. On the other hand the intensity of BODIPY emission seems to be much less affected by pH than FA-contribution. Thus we plotted the ratio of FA contribution and of BODIPY contribution as a function of pH (2.17).

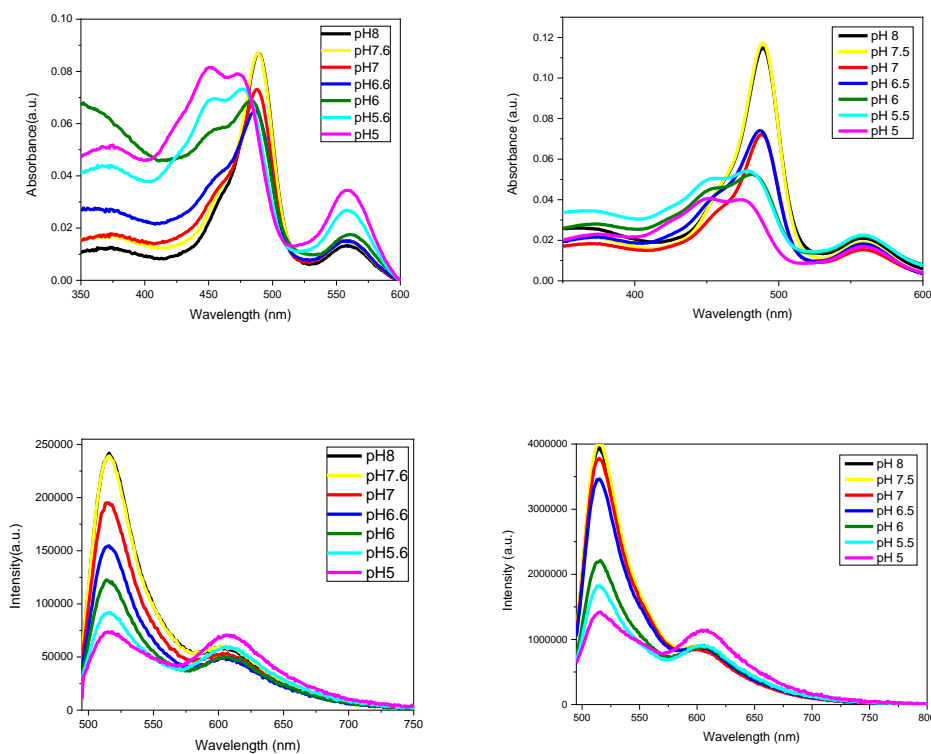


Figure 2.16 Absorption (upper) and emission (bottom) spectra (λ_{exc} : 485 nm) at different pH (Citrate/ Phosphate buffer) at room temperature for $\text{FNP}_{\text{Red-FA}}$. The left spectra were taken by adjusting the maximum of absorbance below 0.1. The right spectra were taken by fixing the dilution factor of the nanoparticles from stock solution.

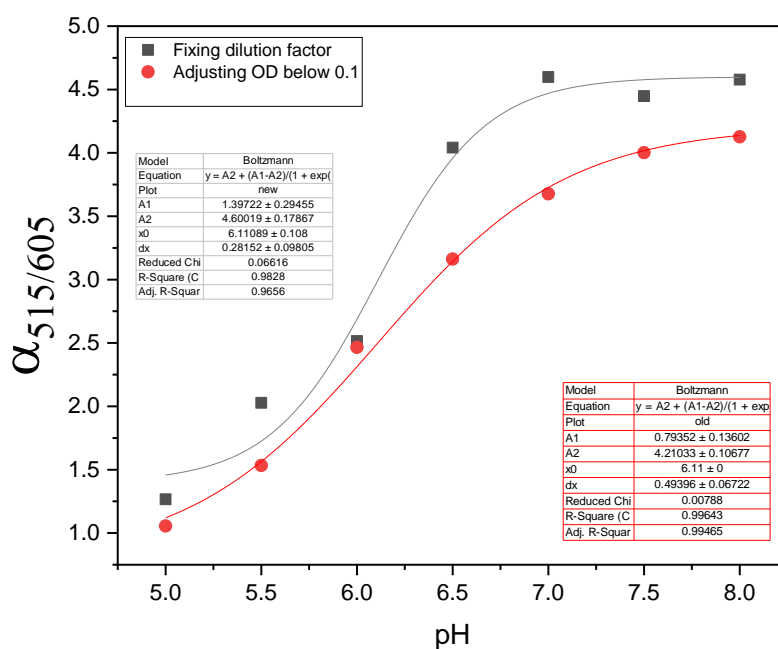


Figure 2.17 Ratio $\alpha_{515/605}$ (λ_{exc} : 485 nm) at different pH (Citrate/ Phosphate buffer 0.2M) at room temperature for FNP_{Red-FA}. Red spots spectra were taken by adjusting the maximum of absorbance below 0.1. Grey spots were taken by fixing the dilution factor of the nanoparticles from stock solution.

From Figure 2.17, which represents the variation of the ratio $\alpha_{515/605}$ according to pH, it was possible to estimate by a Boltzmann fit a pKa of 6.11 ± 0.05 , which is similar to the pKa from anion to dianion of FA (6.4). From this we can observe it is possible to estimate the pH by the ratiometric change in fluorescence between FA in the shell and red-BODIPY in the core of the FNPs for the pH in between 5 and 8. This pH corresponds well to the pH of bacterial growth. As shown in Figure 2.17, the pH dependence is obtained no matter the conditions of the experiments (by fixing or not the dilution factor from stock solutions).

Föster radius of the donor-acceptor in basic conditions was estimated to 5 nm, while in acidic medium was estimated 7 nm. From this, it is possible that FRET occurs from FA to Red-BODIPY and might be modulated with pH changes (2).

To better observe the presence of energy transfer from the FA (donor) to the BODIPY (acceptor), excitation spectra were obtained at $\lambda_{em} = 620$ nm and collected from 400 to 600 nm (Figure 2.18 and 2.19). At 620 nm, red-BODIPY is the only emitting specie (not FA), nevertheless, a second band around 500 nm corresponding to the FA is observed.

This means, there is energy transfer between red BODIPY in the core and FA from the shell, and it seems to be pH dependent (which is consistent with measured R_0). The ratio $\alpha_{500/560}$ (excitation maximums) vs pH are represented in Figure 2.18 and 2.19 and corresponds well to Figure 2.17.

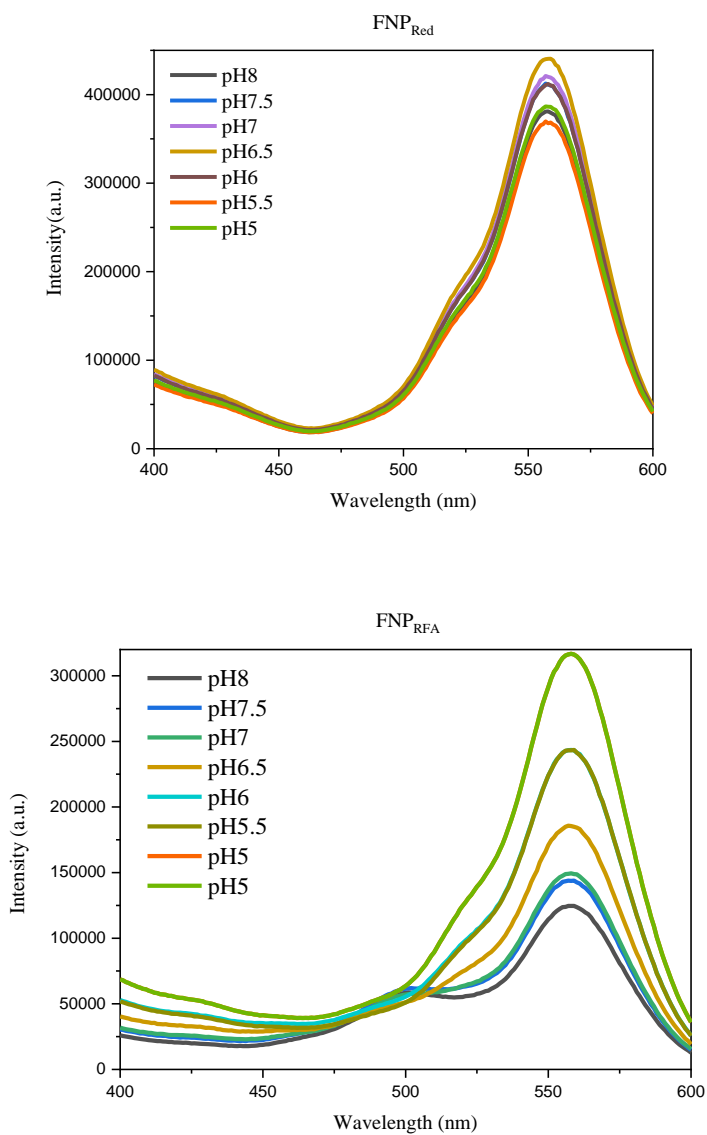


Figure 2.18 Excitation spectra (λ_{em} : 620 nm) at different pH (Citrate/ Phosphate buffer) at room temperature for FNP_{Red} (upper) and FNP_{Red-FA} (bottom). Spectra were taken by adjusting the maximum of absorbance below 0.1.

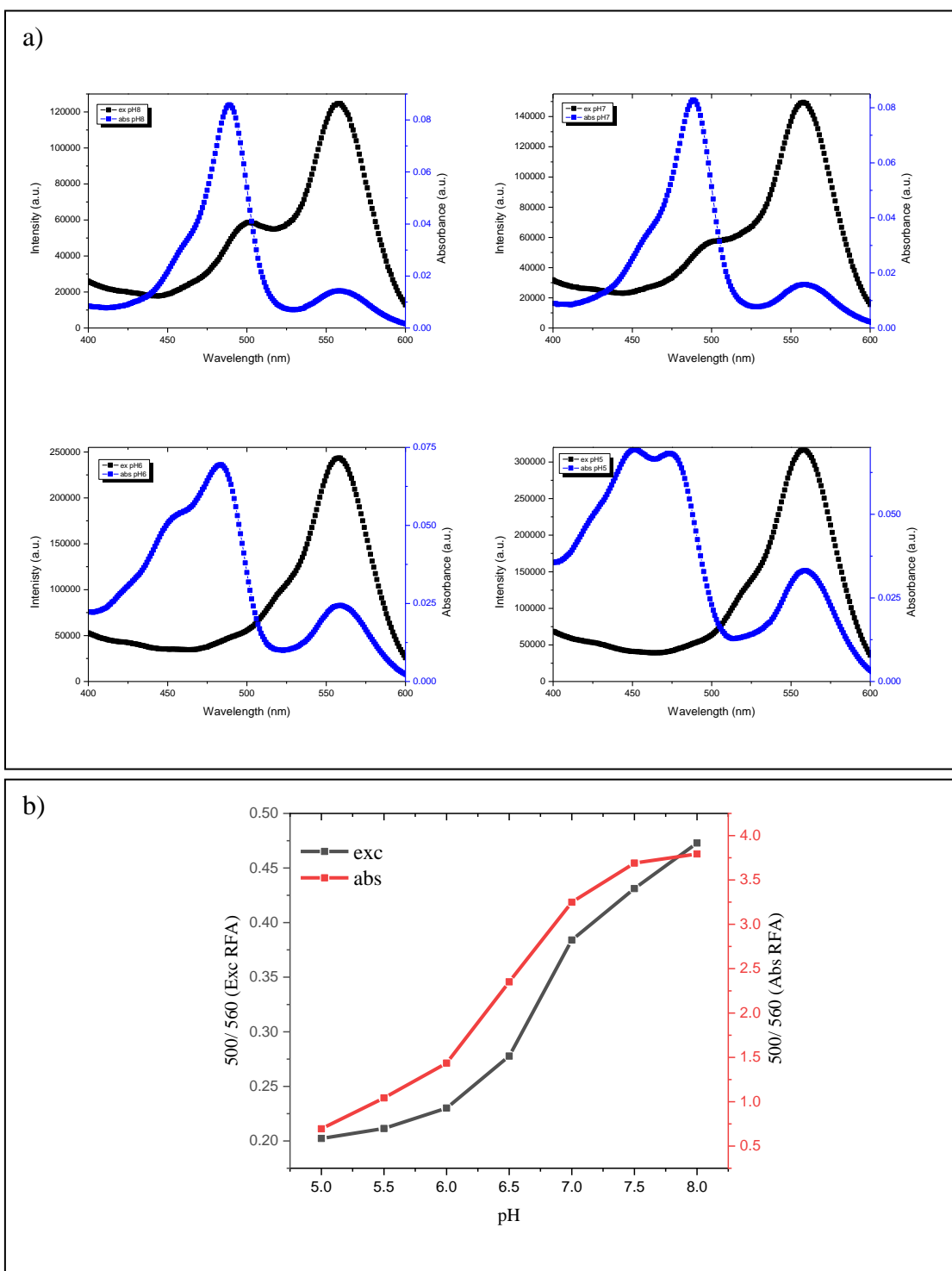


Figure 2.19 a) **Absorption** and **excitation spectra** (λ_{em} : 620 nm) at different pH (8, 7, 6, 5, Citrate/ Phosphate buffer 0.2M) at room temperature for FNP_{Red-FA}, b) ratio 500/560 for **absorption** and **excitation** spectra at different pH (Citrate/ Phosphate buffer 0.2M) at room temperature for FNP_{Red-FA}. Spectra were taken by adjusting the maximum of absorbance below 0.1.

Next, the variation of quantum yield (Φ_F) vs pH was analyzed. As previously mentioned, rhodamine 6G dye was used as reference for green FNP, it can be also used for FA contribution in grafted FNPs. Sulforhodamine was used as a reference for red BODIPY dye and red FNPs. From the slopes of the linear fits (Area under the curve from Emission spectrum vs Absorbance at the excitation wavelength) and using the literature values of the reference dyes, Φ_F was calculated using Equation 1.1. In $\text{FNP}_{\text{Red-FA}}$ there are two bands which correspond to a ‘green part’: $\text{FNP}_{\text{Red-FA-green}}$ which corresponds to FA emission (from 495 to 569) and ‘red part’: $\text{FNP}_{\text{Red-FA-red}}$ which belongs to ‘red’ BODIPY emission (from 570 to 750)]. These results are shown in table 2.9.

Table 2.9 Fluorescence Quantum Yields for $\text{FNP}_{\text{Red-FA}}$ (Green part: $\text{FNP}_{\text{Red-FA-green}}$ and red part: $\text{FNP}_{\text{Red-FA-red}}$) and FNP_{Red} at different pH (Citrate/ Phosphate buffer 0.2M) at room temperature.

pH	$\Phi_F \text{ FNP}_{\text{red}}$ (%)	$\Phi_F \text{ FNP}_{\text{Red-FA-green}}$ (%)	$\Phi_F \text{ FNP}_{\text{Red-FA-red}}$ (%)
8	10.5	3.1	7.1
7.5	10.9	3.2	10.3
7	12.2	2.7	7.9
6.5	11.3	2.3	10.1
6	10.9	1.3	9.8
5.5	12.0	1.1	11.1
5	10.8	1.2	9.6

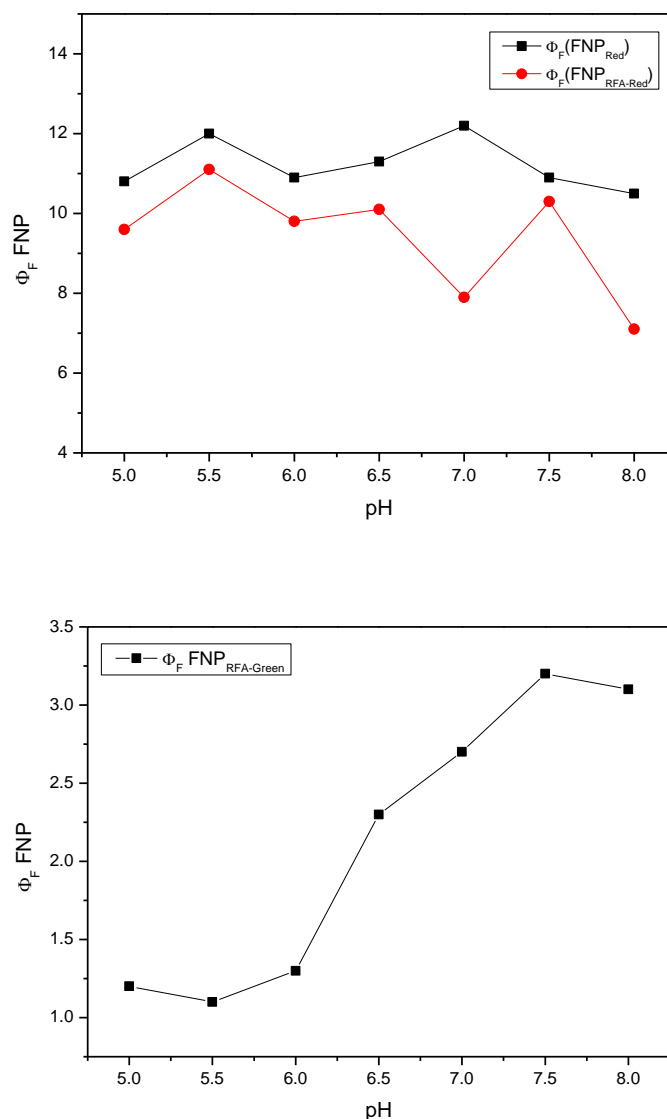


Figure 2.20 Fluorescence Quantum Yields vs pH (Citrate/ Phosphate buffer 0.2M) at room temperature found for FNP_{Red-FA} (red part) and FNP_{Red}, left image, and FNP_{Red-FA} (green part) right image.

From Figure 2.20 FNP_{Red-FA} (green part) bottom image, pKa was estimated with Boltzmann fit, finding to be pKa: 6.5, which is very close to the one found by the ratio $\alpha_{515/605}$ (pKa: 6.11).

Nevertheless, the values of Φ_F for FNP_{Red-FA} are still very low compared to Fluorescein-amide (expected up to 80%). Even though we performed purification, still a weak signal from free FA was measured, thus we cannot rule out some free FA contribution, but it shall be weak and it shall not “shade” the Fluorescein-amide signal. Since we have doubt about the NPs concentration, it is hard to estimate the number of

grafted FA. Nevertheless one possible explanation for such a weak fluorescence quantum yield might be consistent with a high number of grafted FA, which then tend to aggregate through π - π stacking. This phenomenon, also called self-quenching, was described earlier by Charreyre *et al.* (20).

Another issue shall be arisen, if energy transfer occurs then Fluorescein-amide (donor) shall be quenched (as observed from excitation spectra, Figure 2.19) at pH 8. The higher the pH is, the more quenched it shall be. When pH decreases, energy transfer shall be less efficient (see R_0 value given p. 78 and see Figure 2.19), thus Φ_F should increase for FA but also decrease due to pH change. At this stage, we have difficulty to rationalize such opposite effects. From table 2.9 and Figure 2.20, it is possible to observe that Φ_F for FNP_{Red-FA} 'red part' remains very similar to Φ_F FNP_{Red} .

Moreover we decided to perform time-resolved fluorescence experiments to check if such unexpected behavior occurred with decays as well.

The variation of fluorescence lifetime (τ) vs pH was investigated at a wavelength where mainly the donor is excited (FA, λ_{exc} : 485 nm) fixing the collection time to 10 min. Such experiment was also carried out for FNPs without FA (FNP_{RED}). From Figure 2.21, and from a qualitative point of view, the decays, in the 'green part' of FNP_{Red-FA} , decrease notably while pH decreases, meanwhile for the 'red part' this is much less evident. FNP_{Red} decays seem to be weakly sensitive to pH (it shall be noted here that even though absorption is weak at the excitation wavelength, an emission signal is collected, thus when donor and acceptor are present, both shall be excited).

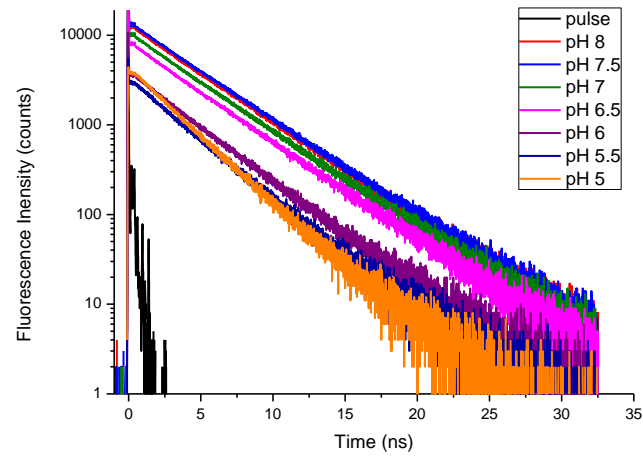
Looking at decays' shape, in the 'red' range, it seems that the presence of FA extends the decay time, for a same pH "red range" emission seem to decay less when FA is grafted. Unfortunately, due to a lack of time, we did not perform fits.

We evaluated the mean lifetime, $\langle\tau\rangle$, thanks to the equation 1.1 (from section Material and Methods) see table 2.10. Decays are represented in Figure 2.21 and the evolution of $\langle\tau\rangle$ versus pH is found in Figure 2.22.

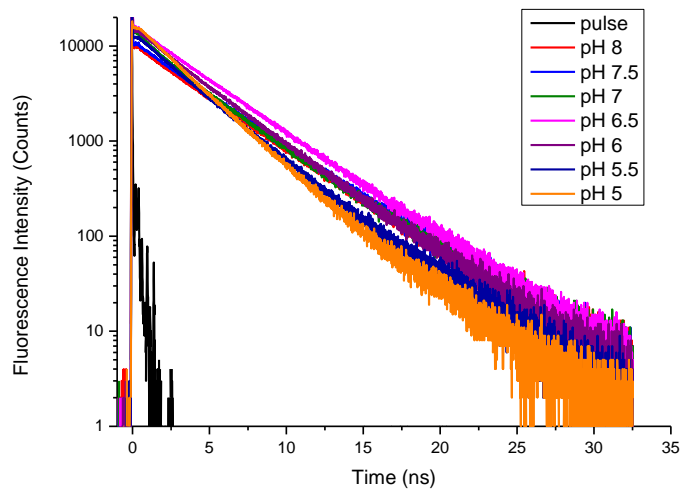
Table 2.10 Average Fluorescence Lifetimes for FNP_{Red-FA} and FNP_{Red} (λ_{exc} : 485 nm) at different emission ranges vs pH (Citrate/ Phosphate buffer 0.2M) at room temperature.

pH	$\langle\tau\rangle$ FNP_{Red-FA} λ_{em}: 525 nm (ns)	$\langle\tau\rangle$ FNP_{Red-FA} λ_{em}: 600 nm (ns)	$\langle\tau\rangle$ FNP_{Red} λ_{em}: 600 nm (ns)
8	4.01	3.98	3.54
7.5	4.01	3.99	3.75
7	3.97	3.63	3.67
6.5	3.90	3.89	3.67
6	3.60	3.60	3.13
5.5	3.31	3.31	2.73
5	2.95	2.94	3.32

Decays of FNP_{Red-FA}
 λ_{em} : 525 nm (Green band)



Decays of FNP_{Red-FA}
 λ_{em} : 600nm (Red band)



Decays FNP_{Red}
 λ_{em} : 600nm (Red band)

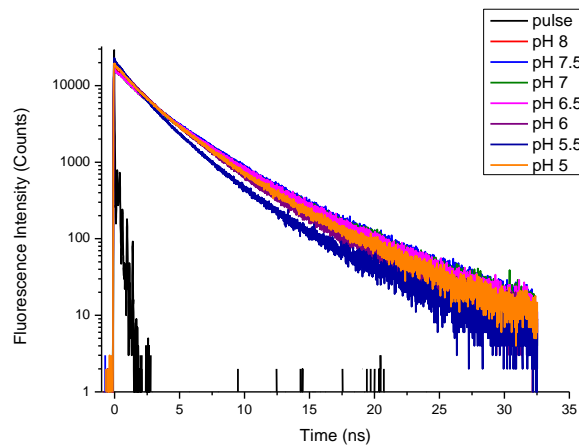


Figure 2.21 FNP decays vs pH (Citrate/ Phosphate buffer 0.2M) at room temperature found for FNP_{Red-FA} and FNP_{Red}, (OD < 0.1, λ_{exc} : 485 nm)

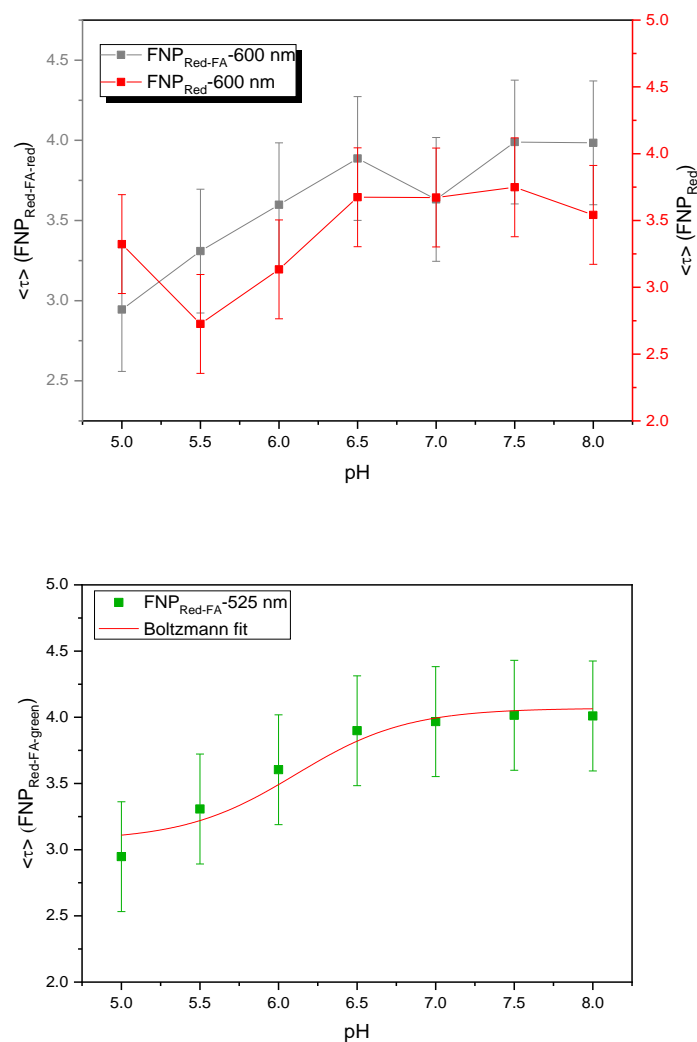


Figure 2.22 Average Fluorescence lifetimes ($\langle \tau \rangle$) vs pH (Citrate/ Phosphate buffer 0.2M) at room temperature found for FNP_{Red-FA} and FNP_{Red} (λ_{em} : 600 nm) left image, and FNP_{Red-FA} (λ_{em} : 525 nm) right image.

From Figure 2.22, it can be observed that the average lifetime for FNP_{Red-FA} (green-part) is decreasing with pH, which is totally consistent with Φ_F evolution as seen in Figure 2.20. From Figure 2.22 FNP_{Red-FA} (λ_{em} : 525 nm) bottom image, pK_a was estimated with Boltzmann fit, finding to be pK_a: 6.11, which remains consistent and still is alike to the one found by the ratio $\alpha_{515/605}$ (pK_a: 6.11) and quantum yield (pK_a: 6.18).

From table 2.10, it is possible to observe that mean lifetime (values and evolution vs pH) for FNP_{Red-FA} in the ‘red part’ is somehow similar to the one in FNP_{Red}. Nevertheless the “red” decay time value is higher when FA is grafted on red FNPs

($\text{FNP}_{\text{Red-FA}}$) than for FNP_{Red} (except for pH 5). It could be eventually a clue of energy transfer from donor (FA) to acceptor (BODIPY). At this stage, we do not have NP_{FA} which could allow us to investigate the “donor” alone behavior and measure fluorescence quantum yield and lifetime in absence of acceptor.

Looking closer at decays of red-BODIPY in any FNPs, lifetime decreases with pH. In FNP_{red} (no grafted FA), the decrease is quite small, about 6% from pH=8 to pH=5. In $\text{FNP}_{\text{Red-FA}}$ the decrease reaches 26% from pH=8 to pH=5. Going back to the ‘red’ fluorescence quantum yield issue raised above, ‘red’ decay time evolution with pH does not show the same trend as quantum yield. Since time-resolved experiments do not depend upon any reference, we believe quantum yields are indeed affected by experimental errors.

To summarize, in the ‘red’ band, pH effect on lifetime decrease is 4 times more visible in FA grafted FNPs compared to ungrafted. It seems that we have in $\text{FNP}_{\text{Red-FA}}$ decays a contribution of FA emission, this might be due to large slits used for the measurements.

The positive point is that decay time in FNP_{red} is very slightly affected by pH, thus red-BODIPY may act as an internal reference for further ratiometric measurements. The ‘green’ contribution of FA, in $\text{FNP}_{\text{Red-FA}}$, shows a sensitivity to pH, very similar to the fluorescence quantum yield evolution.

The plot of decay-time ratio as a function of pH is not informative and was not presented here.

Conclusions & Perspectives

In conclusion, the synthesis and characterization of different types of FNP were carried out successfully. Firstly, to our knowledge, new kinds of particles were obtained for the first time (FNP_{Red} -with high 'red' BODIPY initial molarity-, FNP_{G-DIBO} and FNP_{R-DIBO}). The new family of DIBO particles containing 'DIBO' moiety may allow the post-functionalization by the highly efficient 'click-chemistry'. Such coupling is bio-friendly since it doesn't require copper. Looking further for applications, these FNP_{DIBO} could be used to target not only bacteria strains, but also different eukaryotic cell lines by changing the antibody grafted on them. Due to lack of time, the application of these FNP will not be studied, but they are being incorporated in a new project (heavy metals detection, with Labex Charmmmat fundings) and the continuation of this one (bacterial growth detection, with CSC Grant).

The surface charge of the different particles was estimated by ζ -potential. The size of all particles was characterized in different ways (DLS for hydrodynamic radius, NTA for size and concentration, TEM for dried diameter). Particles are highly dispersed. Nevertheless, for our main objective (to produce a surface sensitive to pH for bacterial growth detection), we chose to proceed without further purification or size-classification (*i.e.* by NanosepTM nanopore filters) of the particles.

Besides and most importantly, a new ratiometric fluorescent pH nanosensor was designed and characterized based on 'red' BODIPY and FA. The nanoparticles were stable down to pH=5 and contained a very large number of both fluorescent species. Their spectroscopic characteristics were studied in water at various pH and the pKa of the grafted fluorescein was determined to be close to the tabulated one. Even though excitation spectra showed that energy transfer occurs at $\text{pH} \geq 7$, it was extremely difficult to quantify and probe it from quantum yield and fluorescence lifetime.

Nevertheless, the FNP_{Red-FA} particles could be used as ratiometric pH-sensors. τ_F of the red-band of FNP_{Red-FA} particles is weakly affected by pH, whereas Φ_F and τ_F of green-band of FNP_{Red-FA} is strongly affected. The plot of intensity ratio shows a very nice pH sensitivity in between 5.5 and 7, this is a perfect window for biological applications such as bacterial growth. The grafting efficiency of FA was not calculated since we were not able to measure properly the particles' concentration.

- (1) C. Grazon *et al.*, Fluorescent core–shell nanoparticles and nanocapsules using comb-like macromolecular RAFT agents: synthesis and functionalization thereof, *Polym. Chem.* 2016, 7, 25, 4272.
- (2) C. Grazon *et al.*, Core-shell polymeric nanoparticles comprising BODIPY and fluorescein as ultra-bright ratiometric fluorescent pH sensors, *Photochemical & Photobiological Sciences*, 2019, Advance Article.
- (3) G. Ulrich, *et al.*, The Chemistry of Fluorescent Bodipy Dyes: Versatility Unsurpassed. *Angew. Chem. Int. Ed.*, 2008, 47, 1184-1201.
- (4) F. L. Arbeloa *et al.*, Structural, Photophysical and lasing properties of pyrromethene dyes, *International Reviews in Physical Chemistry*, 2005, 24, 339-374.
- (5) E. Y. Schmidt *et al.*, A general synthetic strategy for the design of new BODIPY fluorophores based on pyrroles with polycondensed aromatic and metallocene substituents. *Chem. Eur. J.*, 2011, 17, 3069-3073.
- (6) G. Conzatti *et al.*, PNIPAM grafted surfaces through ATRP and RAFT polymerization: Chemistry and bioadhesion, *Colloids Surf. B*, 2017, 151, 143-155.
- (7) J. T. Lai *et al.*, Functional polymers from novel carboxyl-terminated trithiocarbonates as highly efficient RAFT agents. *Macromolecules.*, 2002, 35, 6754-6756
- (8) V. V. Rostovtsev *et al.*, A stepwise Huisgen cycloaddition process: copper (I)-catalyzed regioselective “Ligation” of azides and terminal alkynes. *Angew. Chem. Int. Ed.*, 2002, 41, 2708-2711.
- (9) N.Mbua *et al.*, Strain-Promoted Alkyne-Azide Cycloadditions (SPAAC) Reveal New Features of Glycoconjugate Biosynthesis, *ChemBioChem*, 2011, 12, 1912-1921
- (10) I. Potapova *et al.*, “Two-step labeling of *Staphylococcus aureus* with Lysostaphin-Azide and DIBO-Alexa using click chemistry,” 2013.
- (11) R. Sjöback, *et al.*, Absorption and fluorescence properties of fluorescein. *Spectrochimica Acta Part A*, 1995, 51, L7-L21.
- (12) K. H. Drexhage *et al.*, Fluorescence Efficiency of Laser Dyes, *Journal of Research of the National Bureau of Standards-A. Physics and Chemistry*. Val. BOA, No. 3, May- June 1976.
- (13) B. Valeur, in *Molecular Fluorescence*, Wiley-VCH Verlag GmbH, 2001.

- (14) S. K. Brar and M. Verma, Measurement of nanoparticles by light-scattering techniques, *Trends Anal. Chem.*, 2011, 30, 4–17.
- (15) F. Laborda *et al.*, Detection, characterization and quantification of inorganic engineered nanomaterials: A review of techniques and methodological approaches for the analysis of complex samples, *Anal. Chim. Acta*, 2016, 904, 10.
- (16) Malvern Panalytical Ltd, “NanoSight NS300.” [Online]. Available: <https://www.malvernpanalytical.com/en/products/product-range/nanosight-range/nanosight-ns300>. [Accessed: 06-May-2019].
- (17) S. Yang *et al.*, Hydrogen-Bonding-Driven Complexation of Polystyrene-block-poly (ethylene oxide) Micelles with Poly (acrylic acid), *Macromolecules*, 2010, 43, 3018.
- (18) A. Ranjan *et al.*, Drug delivery using novel nanoplexes against a Salmonella mouse infection model, *J. Nanopart. Res.*, 2010, 12, 905.
- (19) Chloé Grazon. Élaboration de nanoparticules fluorescentes à base de BODIPY par polymérisation RAFT en miniémulsion : synthèse, caractérisation et fonctionnalisation de surface. Autre. École normale supérieure de Cachan - ENS Cachan, 2012.
- (20) M. Alvarez *et al.*, Photophysical and laser emission studies of 8-polyphenylene-substituted BODIPY dyes in liquid solution and in solid polymeric matrices, *Photochemical and photobiological Sciences*, 2008, 7, 802.
- (21) PerkinElmer Ltd “An Introduction to Fluorescence Spectroscopy.” PerkinElmer: Buckinghamshire, 2000.
- (22) C. Munkholm *et al.*, Intramolecular fluorescence self-quenching of fluoresceinamine, *JACS*, 1990, 112, 2608.
- (23) U. Reibetanz *et al.*, Flow cytometry of HEF 293T Cells Interacting with Polyelectrolyte Multilayer Capsules Containing Fluorescein-Labeled Poly (acrylic acid) as pH Sensor, *Biomacromolecules*, 2007, 8, 1927.
- (24) C. Dejugnat *et al.*, Defined Picogram Dose Inclusion and Release of Macromolecules using Polyelectrolyte Microcapsules, *Macromolecular Rapid Communications*, 2005, 26, 961.

(25) M.T. Charreyre *et al.*, Fluorescence Energy Transfer from Fluorescein to Tetramethylrhodamine Covalently Bound to the Surface of Polystyrene Latex Particles, *Langmuir*, 1995, 11, 2423.

Chapter 3: pH sensing surfaces

Introduction

In the previous chapter, the synthesis and characterizations of different FNPs were described. In addition, we prepared a new ratiometric fluorescent pH nanosensor, following the same principle as the one described by C. Gazon *et al.* (1), but this time using FNP_{Red} with 'red' emitting BODIPY (reference dye) in the core of the nanoparticle and fluorescein (pH sensing dye) covalently attached to the external surface. As described above, ratiometric measurements have the advantage over single-emission measurements of being independent of several experimental parameters.

This chapter is devoted to the development and characterization of pH-sensing surfaces by taking advantage of the ratiometric fluorescent pH nanosensor formed by FA and FNP_{Red}. In this chapter, the study of pH-sensing with buffer solutions as proof-of-concept will be shown. The study of the interactions of the surfaces with bacteria, in an aim to detect bacterial growth will be introduced.

Our initial trials to graft FNP on glass substrates, were done in suspension. Nevertheless, the preliminary data shown a limited grafting of FNP and lack of stability over time. Thanks to our new collaborator at the time, Pr. Antoine Pallandre, a new protocol for gas-phase silanization proved to obtain good results.

After grafting and characterizing the surfaces grafted with the FNP, the introduction of FA is done in two different strategies as follows:

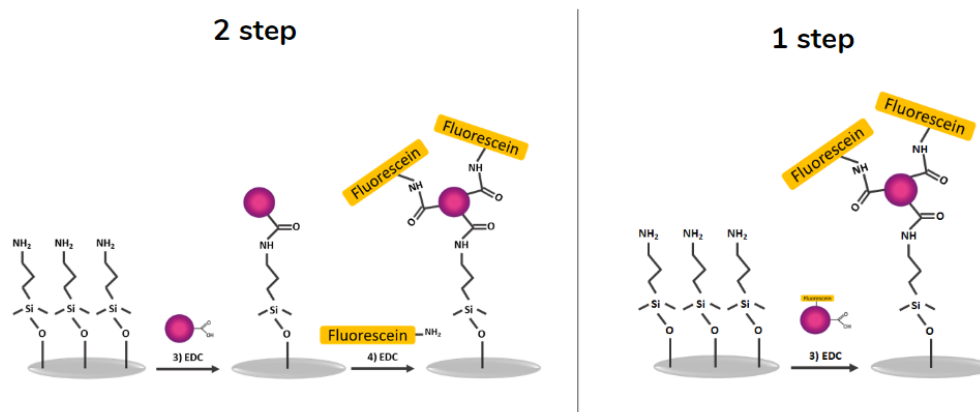


Figure 3.1 Two different strategies to introduce FA on glass substrates for pH-sensing surfaces. **2 step:** this implies the previous grafting of FNP_{Red} , followed by the grafting of FA in similar conditions (EDC coupling). **1 step:** grafting by EDC coupling of $\text{FNP}_{\text{Red-FA}}$ nanoparticles characterized in the previous chapter.

First, 2 step approach was used since all the protocols and characterization techniques were set for FNP_{Red} . Following, to introduce the pH-sensing molecule FA, same EDC coupling was done. However, as shown in the previous chapter, $\text{FNP}_{\text{Red-FA}}$ were synthesized and characterized (later in time). For this reason, 1 step protocol was introduced and used in the last steps of the pH study on surfaces. Nevertheless, both approaches provide the same characteristic fluorescence emission and sensitivity of pH, reason which they were used indiscriminately.

Next, the protocol used to prepare the surfaces sensitive to pH will be described, as well as the techniques used to characterize them. Lastly, pH analysis and bacterial interactions of the surfaces will be presented.

Materials & Methods

3.1.1. Materials

Reagents were used without further purification unless explicitly stated. Glass slides of 19 mm diameter and thickness #1.5 were purchased from Agar Scientific. EDSA (3-(Ethoxydimethylsilyl) propylamine) was purchased from Fluorochem Ltd. Absolute ethanol, Sulfuric acid 95 %, hydrogen peroxide 30 %, EDC (N-(3-Dimethylaminopropyl)-N'-ethylcarbodiimide hydrochloride) and FA (Fluoresceinamine) were purchased from Sigma Aldrich. For buffer preparation, sodium phosphate monobasic dehydrate, sodium phosphate dibasic dehydrate, and anhydrous citric acid were purchased from Sigma Aldrich.

3.1.2. Surface Functionalization

3.1.2.1. Gas-Phase Silanization

This protocol was adapted from a protocol belonging to Professor Alain Jonas (Louvain University-Belgium), given by Professor Antoine Pallandre. Glass slides were placed in a home-made Teflon slide-holder and immersed for 20 minutes in fresh piranha solution (1:1, H₂O₂ 30% : H₂SO₄ 95%). Slides were removed from the piranha solution and washed thoroughly with deionized water (D.I.). Subsequently, slides were immersed in absolute ethanol for 15 minutes, and dried one by one with nitrogen flux (N₂). Slides were placed in a Schlenk tube previously warmed at 80°C. The slides were left under vacuum for two hours to ensure anhydrous conditions, followed by three to five cycles of N₂-Vacuum and finalizing by Nitrogen. Then, 0.2 mL of silane were injected carefully in the Schlenk tube. The silanization process was left overnight at 80°C. Afterwards, the Schlenk tube was carefully opened under the fume hood letting the vapors to exit. The slide-holder was immersed in acetone and then placed in a Soxhlet (Figure 3.4). The Soxhlet system was run with acetone as solvent for a minimum of 3 cycles. When finished, the silanized-slides were dried with nitrogen flux and stored individually in small Petri dishes covered with aluminum foil to avoid contact with the plastic surface.



Figure 3.4 From left to right: Schlenk tube, home-made Teflon sample holder and lastly, Soxhlet system used to clean the slides after silanization.

3.1.2.2. Nanoparticle Grafting (either FNP_{Red} for 2 step protocol, or $\text{FNP}_{\text{Red-FA}}$ for 1 step protocol)

A FNP_{Red} solution was prepared by mixing 1 equivalent (188 μL) of FNP_{Red} stock solution (3.6×10^{15} particles/mL), 2.5 mL of pH:7 phosphate buffer saline (PBS) and 4 equivalents (40.3 mg) of EDC coupling agent, estimated to the acrylic acid units of the FNP introduced during synthesis. The pH of the FNP solution was estimated by using pH-indicator strips, to check stability of the pH during the peptide coupling reaction. 300 μL of this solution was deposited on each slide (Figure 3.5), and then transferred to a refrigerating chamber set at 4.0°C, letting the reaction run for two hours. Then, slides were washed with D.I water and dried with N_2 flux. Slides were again stored in Petri dishes with aluminum foil.



Figure 3.5 Fluorescent nanoparticle grafting procedure on glass surfaces.

3.1.2.3. Fluorescein Grafting: 2 step grafting (following FNP_{Red} grafting)

Fluoresceinamine (FA) grafting solution (1 mg/ mL) was initially prepared and mix with 5 mg of EDC using pH: 7 PBS buffer. Previously functionalized slides with FNPs were placed on small Petri dishes covered with aluminum foil and 300 μ L of the FA (3 μ mol / mL) and EDC solution. In similar manner as the previous to the protocol for grafting the FNPs (Figure 3.5). Samples were transferred to a refrigerating chamber set at a temperature of 4.0°C for two hours. Slides were washed with D.I water, dried with N₂ flux, and stored in Petri dishes with aluminum foil.

3.1.3. Surface Characterization

3.1.3.1. X-Ray Photoelectron Spectroscopy

XPS measurements were performed on a K Alpha spectrometer from ThermoFisher, equipped with a monochromated X-ray Source (Al K α , 1486.6 eV) with a spot size of 400 μ m. The hemispherical analyzer was operated in CAE (Constant Analyser Energy) mode, with an energy of 200 eV and a step of 1 eV for the acquisition of surveys spectra, and a pass energy of 50 eV and a step of 0.1 eV for the acquisition of narrow spectra. A “dual beam” flood gun was used to neutralize the charge build-up.

The data treatment was performed with Casa XPS software (Casa Software Ltd., UK) (with the help of Irma Liascukiene). The binding energy scale was set by fixing C 1s component due to carbon bound to only carbon and hydrogen [C-(C, H)] at 284.8 eV. The peaks were decomposed using a linear baseline, and a component shape defined by the product of a Gauss and a Lorentz function, in the 70:30 ratio. Molar concentration ratios were calculated using peak areas normalized according to Scofield factors. A minimum of 6 different zones from a minimum of 2 samples were analyzed for each type of surface.

3.1.3.1. Scanning Electron Microscopy

The observations were carried out using a scanning electron microscope ZEISS Sigma HD (FEG-SEM) operating at 1 kV (Field Electron Gun to be observe at low voltage to limit the destruction of organic molecules with low energy e-beam). The EBSD step size was 0.1 μm and the EBSD data acquisition and analysis were undertaken using the TSL Orientation Imaging Microscopy, OIMTM software. A minimum of 10 different zones from a minimum of 2 samples were analyzed for each kind of surface. Percentage of coverage was calculated by Image J software.

3.1.3.2. Atomic Force Microscopy

AFM studies were performed using a Nanowizard 3 AFM head (JPK Instruments AG, Germany) coupled to a commercial inverted microscope (Axio Observer Z1, Carl Zeiss, Germany). We used AFM cantilevers with nominal stiffness value in the range of 0.03 N/m, full tip cone angle around 40° and tip height larger than $3\mu\text{m}$. Cantilever and tip are made from bulk n-type silicon recovered by a native silicon dioxide layer (HQ:CSC38 AFM probe, MikroMasch, Nanoworld AG), For each cantilever the sensitivity of the system deflection was measured by performing force spectroscopy (approach/retract curves) in air on a clean glass surface. For the spring constant calibration, the cantilever was retracted $\sim 500\mu\text{m}$ away from the substrate and thermal oscillations were measured in air for few seconds. The resulting frequency curve (typical resonance frequency in air in the range of 10kHz) was then fitted using the JPK software to generate the correct spring constant value.

AFM data were acquired using a high-speed force spectroscopic mode (Quantitative Imaging mode, JPK). Under this mode which minimizes lateral interactions between tip and the surface, a complete force curve (approach and retract) was acquired at each pixel of the (128×128 pixels²) images whatever their lateral scan size.

For all the results that will be presented here, the approach and retraction speeds for every pixel were constant ($100\mu\text{m/s}$). The height extension of the AFM cantilever was

fixed at 1 μm . The digitization rate for every approach and retract curve was equal to 110kHz. The set-point force (maximum applied force during the tip approach) was chosen to fulfil the two next conditions: (i) reducing lateral interactions by minimizing the vertical force (to avoid sweeping away of the NP by AFM tip); (ii) getting stable and reproducible approach/retract curves. Thus typical optimal set-up forces were 1.5nN for silicon dioxide. Each AFM image was scanned line by line, starting from the bottom of the image to its top. For each of these lines, pixels are successively scanned from the left side to the right one. All the experiments were performed at a constant temperature of 22 $^{\circ}\text{C}$. A minimum of 10 different zones from a minimum of 2 samples were analyzed for each kind of surface. Percentage of coverage was calculated by Image J software.

3.1.3.3. Contact Angle

Water contact angles were measured under ambient atmosphere with an EasyDrop Contact Angle Measuring Instrument by KRUSS GmbH. A drop of 1 μL MiliQ water was used each time. A minimum of 6 different zones from a minimum of 2 samples were analyzed for each type of surface.

3.1.3.4. Absorption & Emission

Absorption spectra were measured on a UV-2600 UV-Vis Spectrometer by Shimadzu Scientific Instruments. Emission spectra were measured on a FluoroMax-4 Spectrofluorometer (Horiba Jobin-Yvon).

Fluorescence images and spectra in solution were acquired using Leica TCS SP5-AOBS confocal laser scanning microscope. The surfaces were imaged using a $\times 63 - 1.4$ numerical aperture plan apochromat oil immersion objective. The size of the xy image was either $246.03 \times 246.03 \mu\text{m}^2$ or $82.01 \times 82.01 \mu\text{m}^2$, (1024×1024 pixels) recorded on 12 bits. Laser (488 nm) was used as the excitation source and the corresponding fluorescence was collected in the 500–750 nm spectral range. Emission spectra were recorded using 5 nm bandwidth and an average of 2 frames.

Other than stated, images were taken using the confocal microscope. For those taken by epifluorescence, images were taken also in a Nikon ECLIPSE TI-E inverted epifluorescence microscope. Using an objective $\times 60 - 0.7$ numerical aperture (CFI S Plan Fluor ELWD). The microscope was set to take 6 x 6 images and merge in one big image of a final size of: $628.03 \times 473.34 \mu\text{m}^2$ (3784 x 2852 pixels). Images were excited at 482 nm and recorded using FITC-354C (λ_{em} : 530- 560 nm) and TRITC-B (λ_{em} : 555- 595) filters.

3.1.3.5. pH-Sensing

For acquisition, the samples were placed in a metallic holder (see Figure 3.6), and 60 μL of buffer solution was placed in the sample. To change buffer solution, the previous buffer was reabsorbed and then the surface was washed 3 times with the new buffer solution. After each acquisition, the pH of the buffer was checked with a pH paper. Three slides were analyzed (1-2 zones).



Figure 3.6 Glass slides metallic holder with an internal diameter of 19 mm and external of 3.5 cm.

3.1.3.6. Bacteria Growth Detection

The same glass holder and methodology were used as the pH-sensing experiments. For acquisition the samples were placed in a metallic holder (Figure 3.6), and 150 μL of bacterial solution (*E. coli* BW25113 and M9 minimal medium, OD_0 : 0.01) was placed onto the sample.

Modified M9 minimal medium was used with a lower concentration of phosphate salts in order to decrease the buffering capacity of the growth medium and thus obtain a more sensitive measure of bacterial growth from the response of the pH sensitive surface. The modified M9 minimal medium contains 5.9 mM $\text{Na}_2\text{HPO}_4 \cdot 2\text{H}_2\text{O}$, 4.4 mM KH_2PO_4 ,

3.7 mM NH₄Cl, 1.7 mM NaCl, 2 mM MgSO₄, 0.1 mM CaCl₂, 19.6 μM tryptophan, 20.6 μM thymidine, 0.5% casamino acids, 22.2 mM glucose.

To decrease evaporation of the sample, a wet tissue was placed surrounding the sample avoiding contact, then the sample holder was covered with a transparent cover. The temperature was set at 30 °C. A spectrum was acquired every 60 minutes. The pH of the bacterial culture was measured every 2 hours with a pH paper, and compared to a bulk bacteria solution incubated in the same conditions. A unique experiment was carried out. Bacteria were quantified using Image J.



Figure 3.7 Setting used for measurements of bacterial growth.

Results & Discussion

Surface Functionalization

The overall strategy for surface functionalization is schematically presented in Figure 3.8. Amino-silanized surfaces were prepared by gas-phase deposition. To start, glass slides were immersed in freshly prepared piranha solution: this step serves to clean the surfaces from any organic pollution, besides activating the surface by leaving hydroxylic groups available. Silanization was run overnight, allowing EDSA (3-(Ethoxydimethylsilyl) propylamine) to react from its ethoxy silane group with a silanol group of the surface by vapor deposition, as previously described by Pallandre *et al.* (23, 24). This group studied different commonly used aminosilane molecules, showing that EDSA is a good candidate to form good quality monolayers (judging from the electron density and from the roughness of the monolayer/ air interface). In this study, it is shown how difficult it is to obtain monolayers from triethoxy-silanes, as commonly used (3-Aminopropyl) triethoxysilane (APTES), due to probable gel formation leading to thick layers of silane. Following silanization, a Soxhlet system was used to wash the slides with a minimum of 3 cycles of acetone. This resulted in removal of other subspecies, such as

oligomers, that could have been attached to the surface through the silanization process. After silanization, glass slides were functionalized with FNP_{Red}, following by fluorescein (FA) addition. Both grafting reactions were done by peptide coupling.

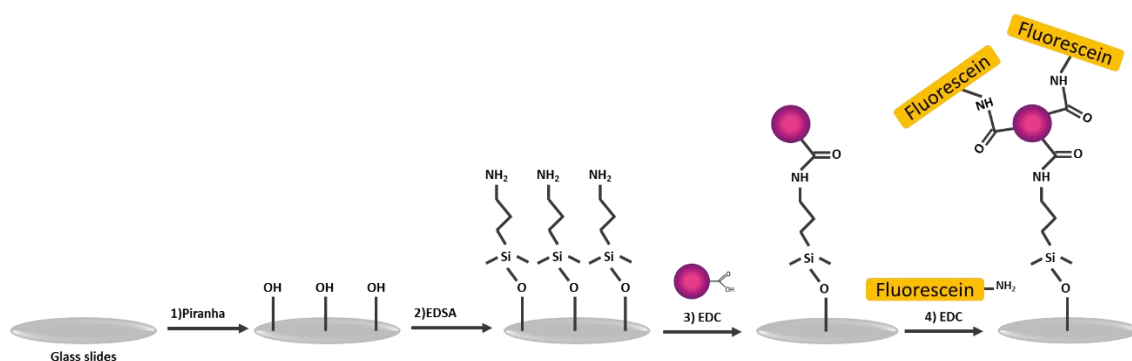


Figure 3.8 Scheme of gas-phase silanization and post-functionalization of glass slides. 1) Glass slides are cleaned with piranha solution to leave free OH⁻ groups available on the surface. 2) EDSA is allowed to react by gas-phase silanization, leaving the amine groups available on the surface for post-functionalization. 3) FNP_{Red} grafting on silanized-glass slides by peptide coupling. 4) FA (yellow rectangle, fluorescein) grafting on FNP_{Red} grafted on silanized-glass slides.

X-ray Photoelectron Spectroscopy

Surface elemental characterization was done by XPS analysis, considering only C, N, Si and O (Table 3.1). The relative atomic percentage of these four elements were obtained for analysis. Traces of Na, B, F and K were found in pristine glass; therefore, they were not considered for analysis. Nitrogen is only present in the aminosilane molecules, nevertheless, traces were found in activated glass, which are due to adventitious contamination (which can be expected. After activation, the negative surface charge of the glass attracts all the positive charged species). Nitrogen increased 4.5 times after silanization the decrease of 1.5 times in the percentage of Nitrogen after FNP grafting and an increment of 2.5 times in the percentage of Carbon corresponds well to the nanoparticle grafting.

Table 3.1 Binding energy (BE) peaks, Full Width at Half-Maximum (FWHM) and relative atomic percentages for glass after piranha, silanized and grafted surfaces are presented.

Sample	Name	Peak BE	FWHM (eV)	Relative Atomic (%)
Glass after piranha	Si2p	103.5	1.8	30.2
	C1s	285.2	1.7	4.2
	O1s	533.0	1.9	65.1
	N1s	401.0	3.2	0.4
Silanized surface	Si2p	103.6	2.0	29.7
	C1s	285.5	2.3	9.6
	O1s	533.1	1.9	58.8
	N1s	401.0	3.7	1.8
Grafted surface (FNP_{Red})	Si2p	103.1	2.0	24.6
	C1s	284.6	1.9	23.7
	O1s	532.4	2.0	50.6
	N1s	399.9	2.6	1.2

From the narrow windows on Nitrogen (Figure 3.9), it is easily observed that after silanization the concentration increased from the initial trace levels (glass after piranha). After silanization, both amine and protonated amine components were clearly observed. The N 1s peaks include two contributions: a component at 399.2 eV attributed to amine groups [C-NH₂], a component at 401.3 eV due to protonated amines C-NH₃⁺, in good agreement with literature (25, 26).

After grafting of particles, the component at 399.2 eV attributed to amine groups [C-NH₂] was highly increased. For Carbon, after silanization it is also possible to see an increment of 2 times after silanization, and a higher increment of 2.5 times after nanoparticle grafting. From the narrow windows on Carbon (Figure 3.9), two main species are seen after silanization [C-(C,H); C-(O, N)], which can be found in the EDSA (probably not coupled ethoxy groups). After nanoparticle grafting the appearance of [C=O], which can be found in the polymer on the shell, it is observed, besides the increment of the other two species.

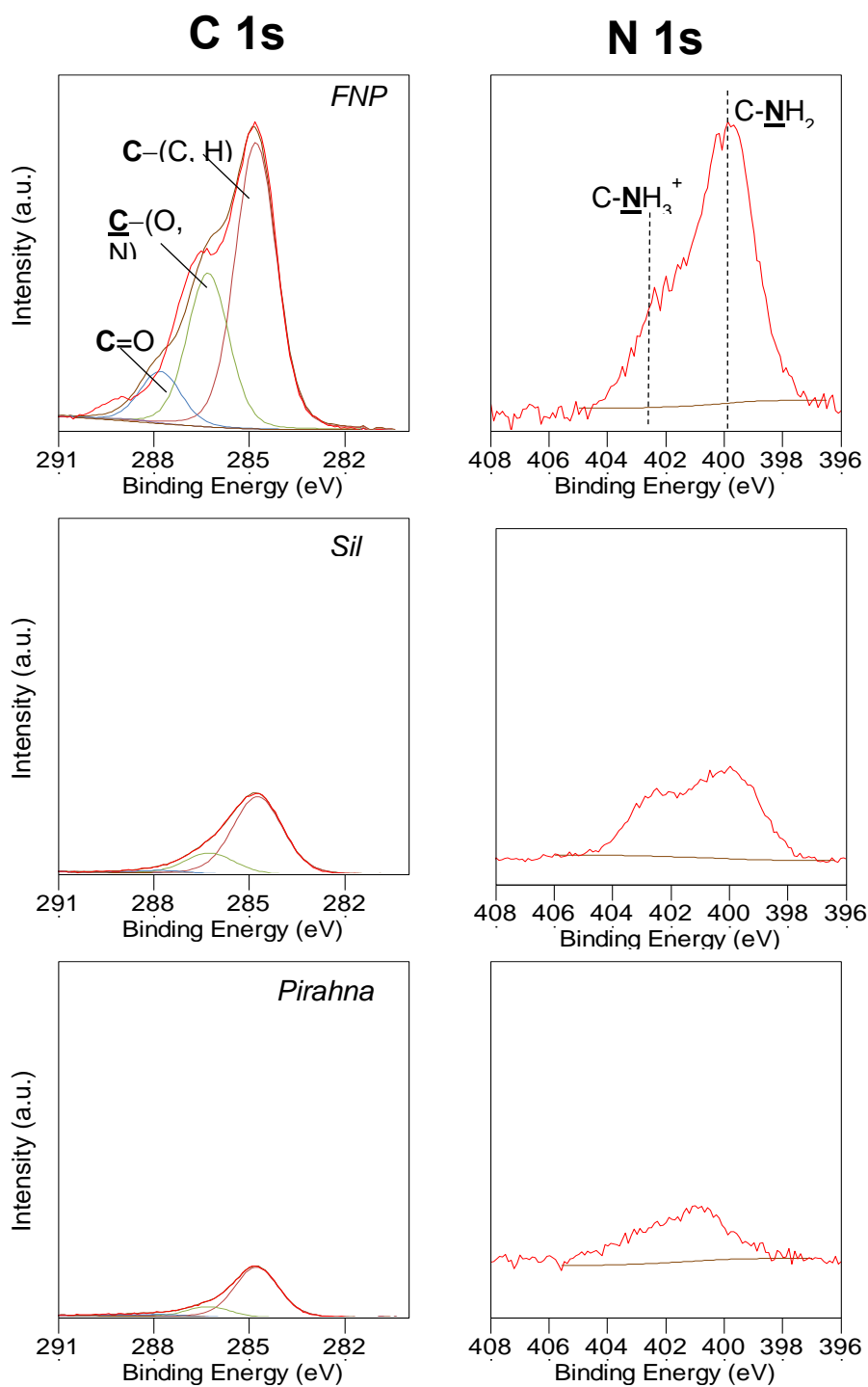


Figure 3.9 XPS Windows of Carbon (left) and Nitrogen (right) after different surface treatments: top graph : after FNP_{Red} grafting, middle graph : after glass silanization, bottom graph : after glass Piranha cleaning

Contact angle

Surface wettability was determined by measuring the contact angle of water drops on the different functionalized surfaces (Figure 3.10). The average water contact angle of glass after piranha was $4^\circ \pm 1^\circ$; for the silanized glass slide was $41^\circ \pm 2^\circ$; for FNP_{Red} surfaces it was $68^\circ \pm 2^\circ$ and for FNP_{Red-FA} surfaces it was $68^\circ \pm 1^\circ$. For glass, after piranha-treatment, it is reasonable to obtain a very hydrophilic surface, later with the addition of organic silane and FNP_{Red} the surface tends to become less and less hydrophilic as seen on the values of contact angles. These values are in good agreement with other silanized and organic-functionalized surfaces (23, 24). It can be observed that after fluorescein (FA) coupling to nanoparticles, the contact angle value did not change, probably because of a small amount of grafted organic molecule. Adding FA shall not tremendously change the composition and the nature of the shell thus hydrophobicity shall not be changed. Nevertheless changes in contact angle are directly connected to the different steps in surface functionalization and particles grafting. Such experiments allow to follow easily the surface chemistry.

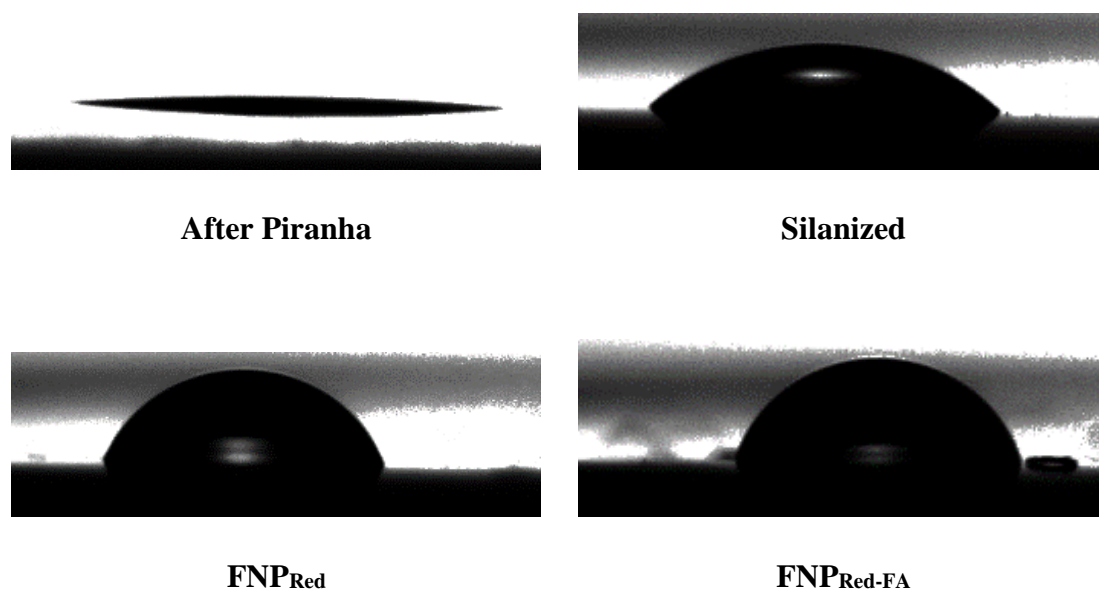


Figure 3.10 Contact angle images of each step of surface functionalization. Upper left: glass after piranha treatment, upper right: glass after silanization, bottom left: after FNP_{Red} grafting, bottom right: after FA grafting.

Surface coverage: SEM & AFM

To quantify nanoparticle grafting, SEM and AFM images were taken (Figure 3.11 and 3.12). For SEM, controls were taken without EDC, to probe electrostatic interactions between FNPs and silanized glass. The coverage area for FNP_{Red} was found to be 8.1 ± 0.7 % with EDC coupling, while without EDC was 0.8 ± 0.1 %. The surface coverage by EDC coupling was found to be 10 times higher than control (electrostatic interactions). From this result we can observe that peptide coupling is necessary to ensure the anchoring of the FNP on the surface. Meanwhile, for AFM the coverage area was found to be 13.1 ± 0.5 %. The nanoparticles are not good conductors, which leads to an underestimation of 1.6 of the coverage area. Nevertheless, SEM images are a good indicator to see the homogeneity of the surfaces as a larger area is screened, meanwhile AFM images are taken on a very small area due to long time-acquisition for larger images ($46 \mu\text{m}^2$ for SEM, 11.5 times larger compared to $4 \mu\text{m}^2$ for AFM).

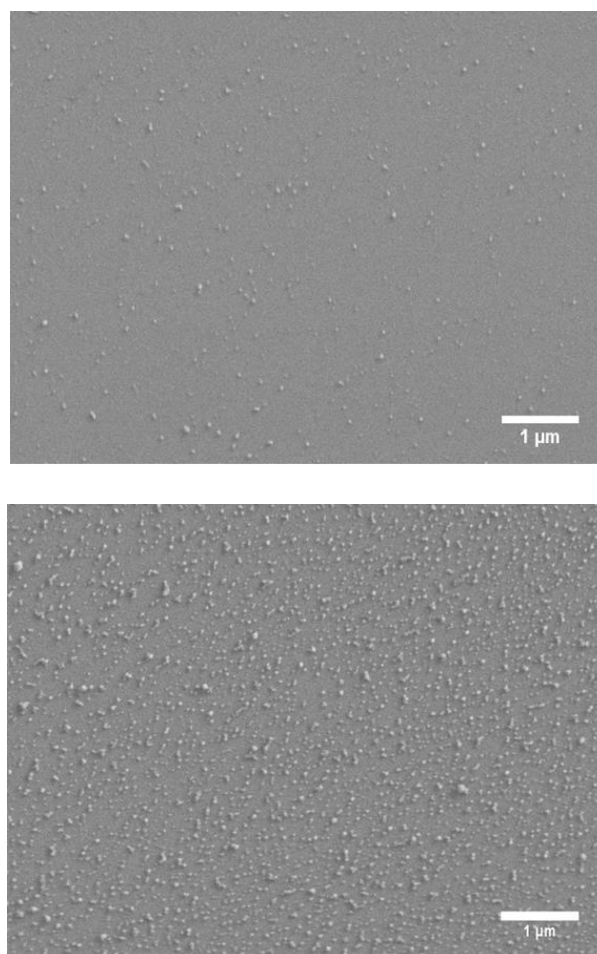


Figure 3.11 SEM images for a) FNP_{Red} left by electrostatic interactions on silanized surface, b) FNP_{Red} grafted on silanized surface by peptide coupling.

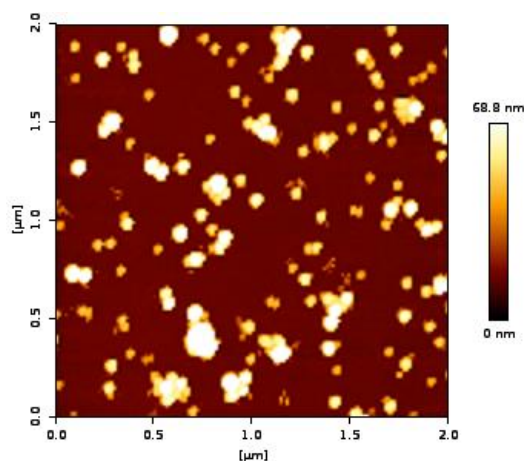


Figure 3.12 Typical AFM image from the same sample as the one observed on SEM of FNP_{Red} grafted on glass silanized surface (tapping mode).

Besides, from AFM image (Figure 3.12) we can observe in the color scale bar the maximum height of the grafted FNP (dry conditions) is around 69 ± 3 nm, but this value is not conclusive since many of the particles are stacked to each other, thus the average diameter was not estimated.

Surface Spectroscopy Characterization

Absorption and emission spectra of dry FNP_{Red-FA} surfaces were compared with FA and FNP_{Red} (D.I., pH~5). As shown in figure 3.13, both absorption and emission spectra correspond quite well to the convolution of FA and FNP_{Red} (with a shift to the red of FA, which might be due to a different environment than solution, or FA aggregates (27). These spectra allowed us to confirm the grafting of the FNP_{Red-FA} on silanized surfaces. Spectroscopy properties are found in table 3.2.

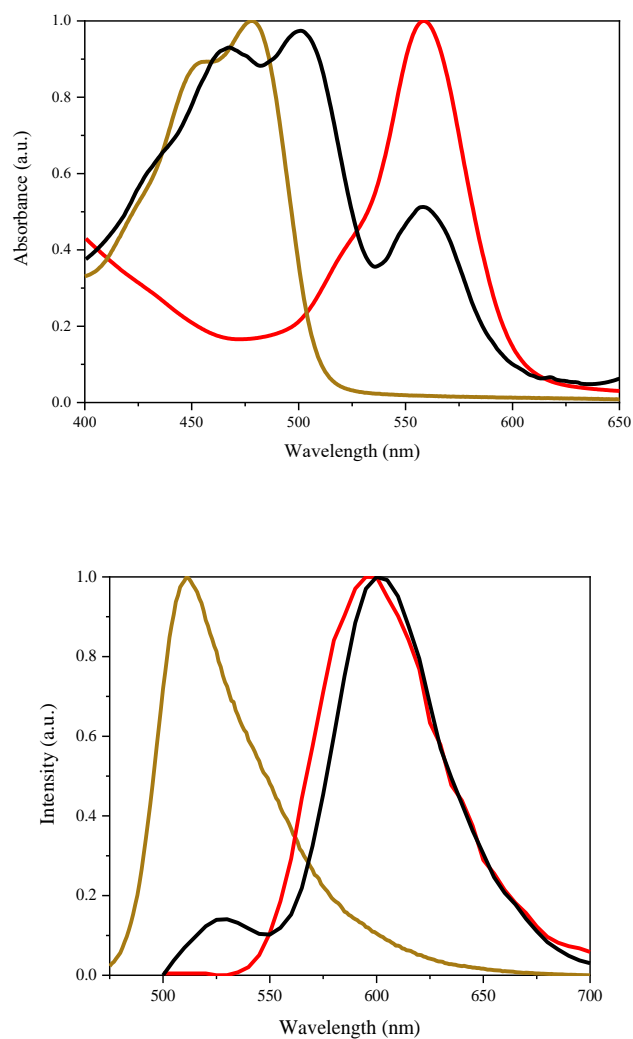


Figure 3.13 Normalized absorption (top) and Fluorescence emission (bottom) (λ_{exc} : 465 nm for FA and λ_{exc} : 485 nm for others). (—) Dry FNP_{Red-FA} surface, (---) FNP_{Red} nanoparticles in suspension, (—) FA in suspension (pH~5).

Table 3.2 Spectroscopic data of FNP_{Red-FA} surfaces compared to data of FA and FNP_{Red} in D.I. water (pH~5)

	$\lambda_{abs, max-1}$	$\lambda_{abs, max-2}$	$\lambda_{abs, max-3}$	$\lambda_{em, max-1}$	$\lambda_{em, max-2}$	FWHM _{em-1}	FWHM _{em-2}
	(nm)	(nm)	(nm)	(nm)	(nm)	(nm ⁻¹)	(nm ⁻¹)
FA in water	454	478	--	511	--	1954	--
FNP _{Red} in water	--	--	559	--	600	--	1951
FNP _{Red-FA} surface	467	501	559	525	600	1426	1583

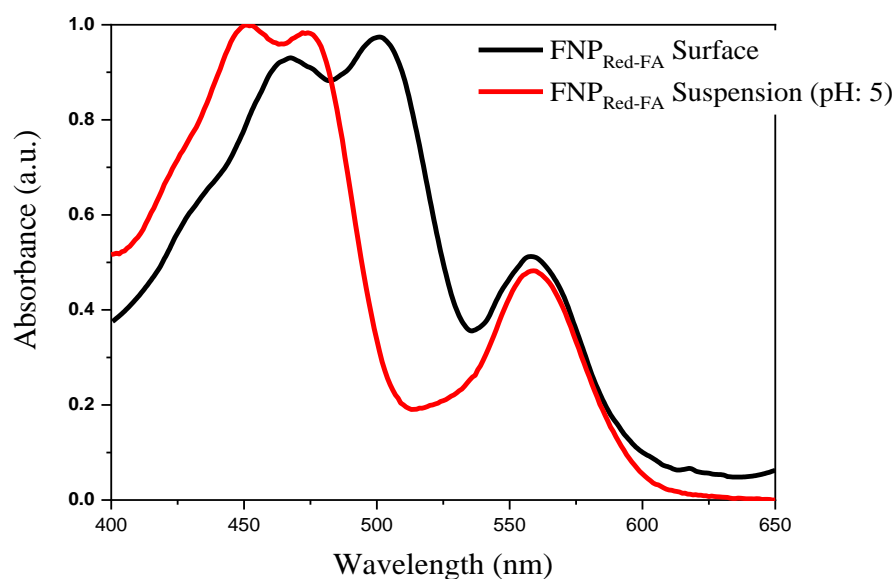


Figure 3.14 Normalized absorption spectra: (—) Dry $\text{FNP}_{\text{Red-FA}}$ surface, (—) $\text{FNP}_{\text{Red-FA}}$ nanoparticles in suspension at pH: 5.

After observing Figure 3.13, absorption spectrum from dry $\text{FNP}_{\text{Red-FA}}$ surfaces looks very similar to $\text{FNP}_{\text{Red-FA}}$ in suspension at pH:5. Indeed, after grafting of the nanoparticles and FA, surfaces are rinsed with D.I. water (pH:5 corroborated with pH paper). The overlap of both spectra is shown in Figure 3.14. As mentioned before, there is a red shift of the maximum of absorption of 27 nm for the $\text{FNP}_{\text{Red-FA}}$ after grafting, which can be the sign of fluorescein aggregates. Ratio between maximums remains the same (~0.5).

To observe the level of heterogeneity of the surfaces, fluorescence images were obtained with an epifluorescence microscope. Indeed, with such a technique it is possible to take 6 x 6 frames and create a large image. Indeed, final image is x 5 times larger than our habitual confocal microscope without zoom ($6,724 \mu\text{m}^2$ for confocal vs $297,044 \mu\text{m}^2$ for epifluorescence), and x 40 times larger than the average image for bacterial analysis from confocal microscope (Zoom 3, $82 \times 82 \mu\text{m}^2$) (image 3.15). $\text{FNP}_{\text{Red-FA}}$ surfaces seem to have quite homogeneous regions (3.15 a) but also very heterogeneous ones (3.15 b).

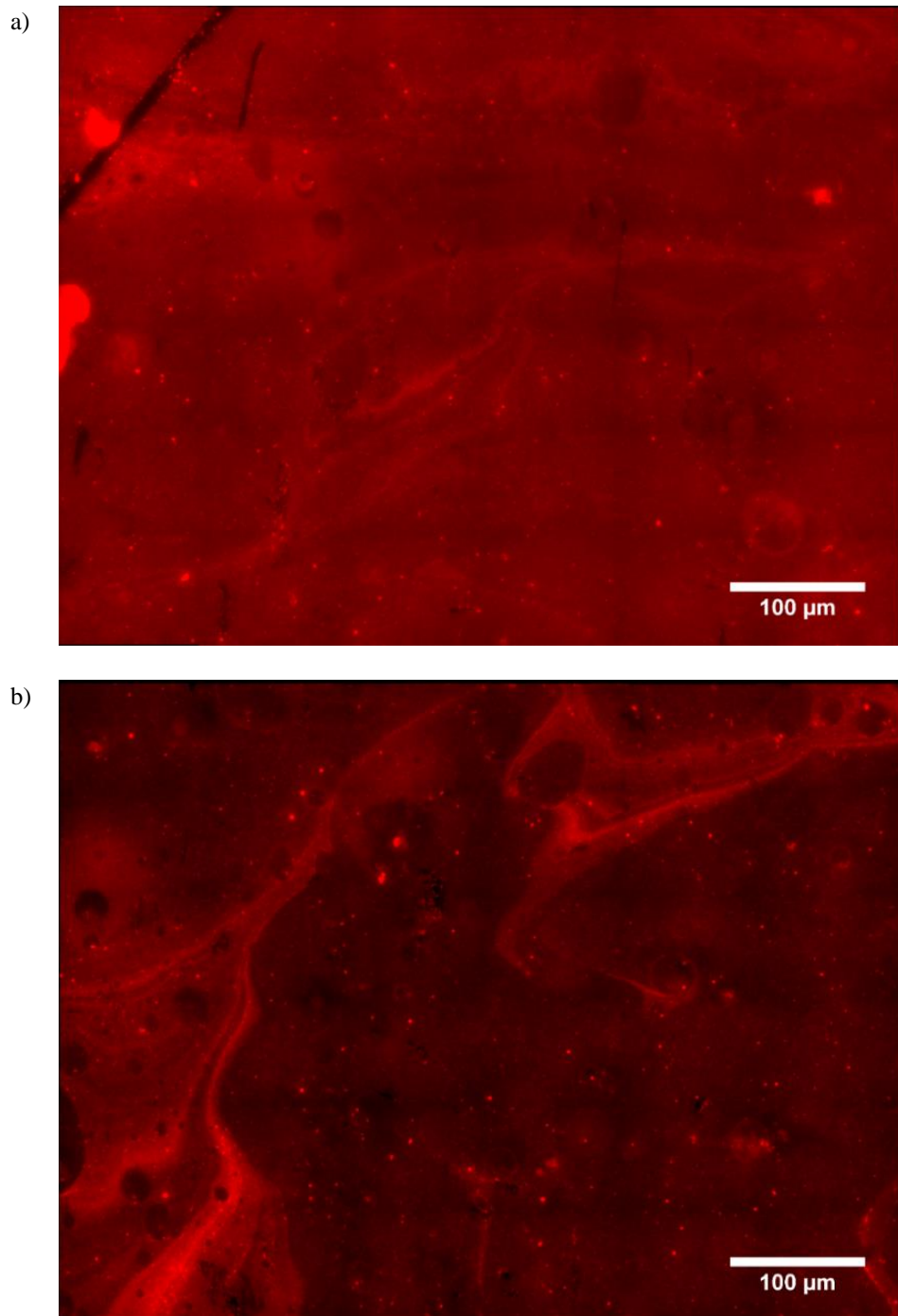


Figure 3.15 Fluorescence images from Epifluorescence microscope (λ_{exc} : 485 nm), from two different zones of the same surface at dry state.

Spectroscopy Characterization

Fluorescence emission spectra of FNP_{Red-FA} surfaces were analyzed at different pH buffer solutions (citrate / phosphate 0.2 M), from pH 5 to pH 8 every pH 0.5 with a confocal microscope using zoom 3 (image size: 82 x 82 μm^2 , recording directly spectra). The spectra are change from the one shown in Figure 3.13. In these spectra the red band is more emissive than the green band.

The response of the surfaces to the pH was later correlated with a linear model (better fit for the data), where the ratio ($\alpha_{520/600}$) of the intensity at 520 nm and 600 nm was related with a change in pH (Table 3.3 and 3.4). Three independent experiments from three different surfaces (from the same batch as in Figure 3.14) were analyzed, finding difficult to reproduce the results (obtain the same fit). On trial 2 a surface prepared with pre-grafted FNP_{Red-FA} was used (same conditions of grafting as described before). This might be due to the heterogeneity of the surfaces that it is visible at microscopic level and might be related to the polydispersity of the FNPs (Figure 3.15). With this result, it is clear that it becomes necessary to calibrate the pH-sensing surface before biological measurements.

Table 3.3 Average ratio $\alpha_{520/600}$ at different pH, for three individual trials. Trial 1 and 3 are from FNP_{Red-FA} surfaces and Trial 2 comes from pre-grafted FA on red FNP surface. All surfaces are from the same batch of silanization.

Trial	pH 5		pH 5.5			pH 6		pH 6.5		pH 7		pH 7.5		pH 8			
1 n=5	0.09	± 0.04	-	-	-	-	-	-	0.14	± 0.06	-	-	-	-	-	0.28	± 0.04
2 n=2	0.04	± 0.00	0.05	± 0.00	0.05	± 0.2	0.07	± 0.02	0.08	± 0.01	0.13	± 0.01	0.17	± 0.01			
3 n=5	0.05	± 0.00	0.06	± 0.00	0.07	± 0.00	0.09	± 0.00	0.12	± 0.00	0.15	± 0.02	0.17	± 0.00			

As seen in figures 3.16 to 3.21, the $\alpha_{520/600}$ decreases when the pH decreases. This is in congruence with the previous chapter, where it was demonstrated that the pH has little influence on the FNPs with BODIPY in the core, while spectroscopic properties of FNPs grafted with FA are dependent on pH (2). Thus, the properties of the grafted FNPs and post-functionalization with FA have proven to preserve the sensibility of the nanosensor. Data were fitted and correlated (linear fit, 28, 29, 30) the increase of $\alpha_{520/600}$

with the pH (Table 3.4). However, as previously described, it remains necessary to calibrate the measurement on each sensing zone (28), independently if the FA is grafted before or after on FNPs (as shown before, 1 or 2 steps).

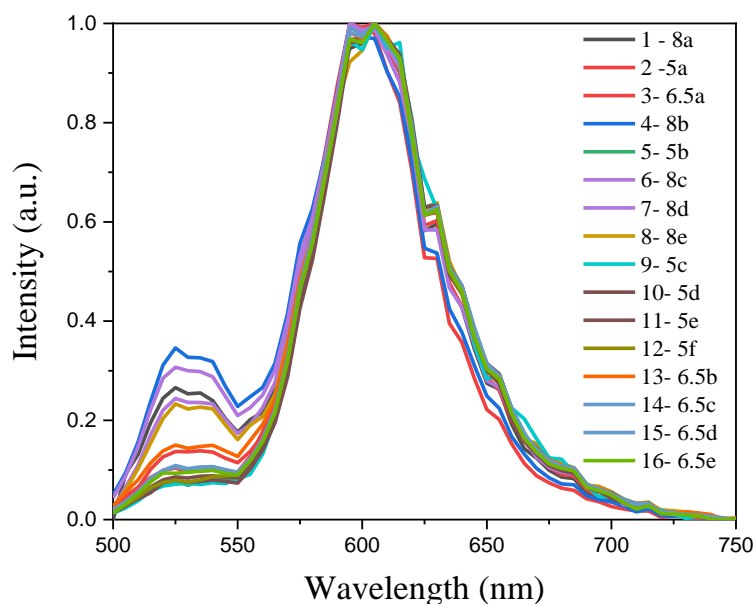


Figure 3.16 Normalized spectra at different pH for trial 1.

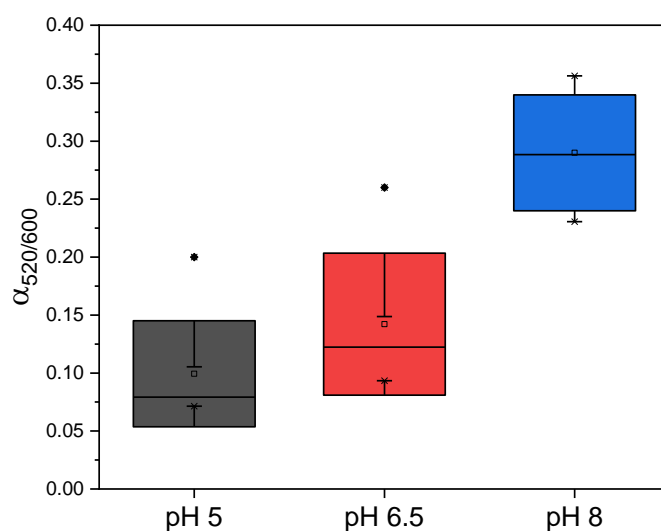


Figure 3.17 Statistical box chart of the average ratio at different pH for trial 1 ($\alpha_{520/600}$). The box represents the interquartile range (25-75 %), the \square is the mean value and the bars the data range.

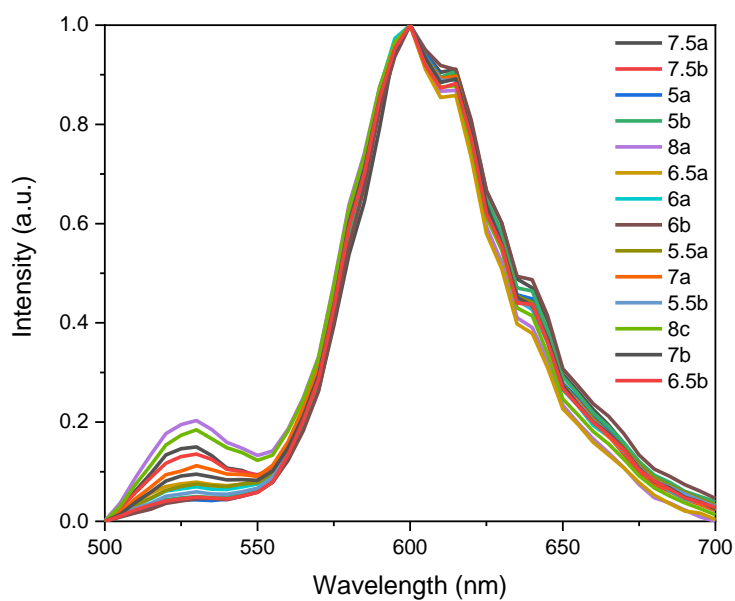


Figure 3.18 Normalized spectra at different pH for trial 2 (only trial on pregrafted FA on FNP, before FNP grafting on surface).

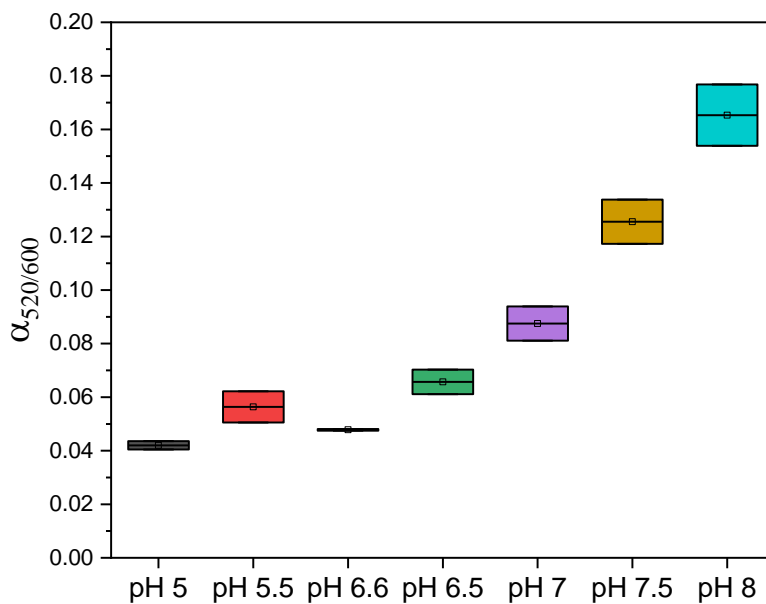


Figure 3.19 Statistical box chart of the average ratio at different pH for trial 2 ($\alpha_{520/600}$). The box represents the interquartile range (25-75 %), the \square is the mean value and the bars the data range.

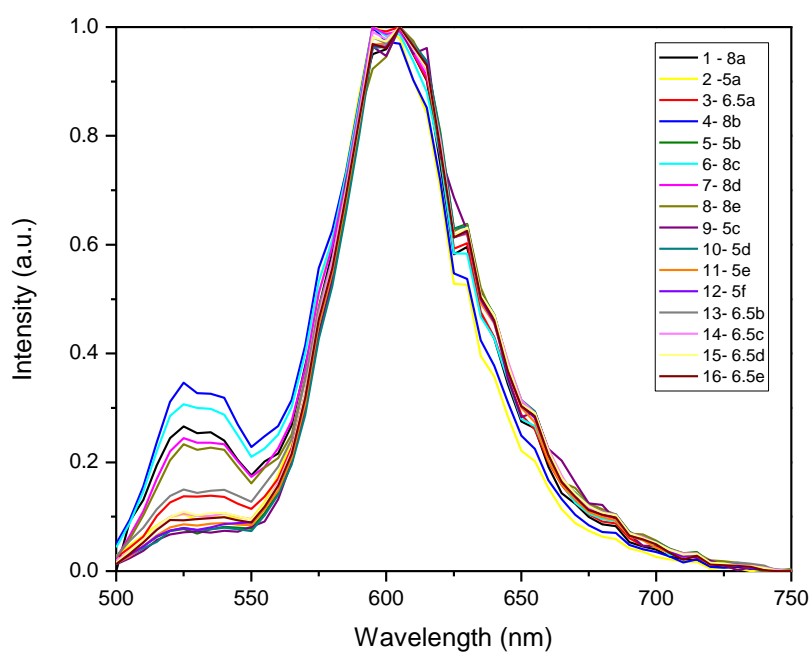


Figure 3.20 Normalized spectra at different pH for trial 3.

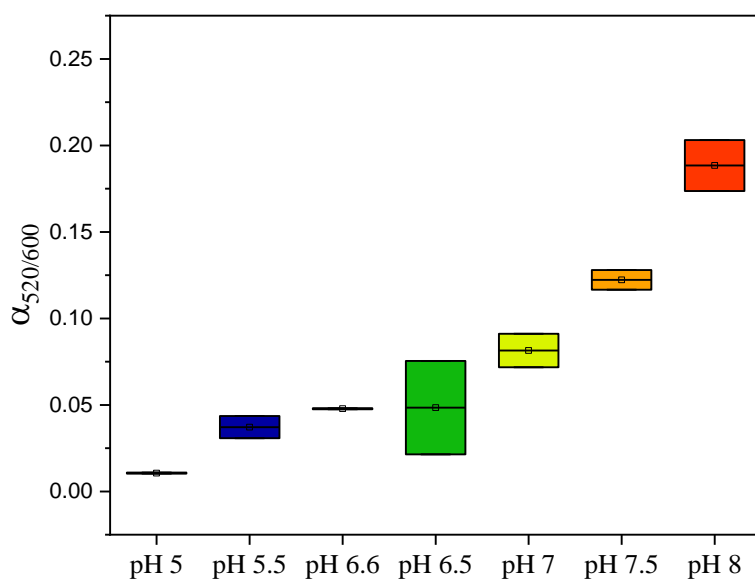


Figure 3.21 Statistical box chart of the average ratio at different pH for trial 3 ($\alpha_{520/600}$). The box represents the interquartile range (25-75 %), the \square is the mean value and the bars the data range.

Table 3.4 Linear fits for three individual trials, correlating pH and ratio of emission bands at 520 nm (FA) and 600 nm (Red BODIPY).

	Slope	Intercept	R-square	Model
Trial 1	0.06 ± 0.02	-0.24 ± 0.13	0.81	$pH = \frac{\alpha_{520/600} + 0.24}{0.06}$
Trial 2	0.04 ± 0.00	-0.17 ± 0.04	0.82	$pH = \frac{\alpha_{520/600} + 0.17}{0.04}$
Trial 3	0.05 ± 0.00	-0.25 ± 0.06	0.82	$pH = \frac{\alpha_{520/600} + 0.25}{0.05}$

Nevertheless, within the same zone, a good reproducibility and reversibility of the sensor is obtained, as it can be seen in figure 3.22 (from Trial 3). Different cycles of pH 5, 6.5 and 8 were carried out in the same zone, obtaining each time a similar ratio. The pH-sensing surface can thus be used from acid to base and from base to acid in the range between pH 5 and 8, which are in the range of biological samples such as bacteria. In comparison with Niu *et al.* (29) with a slope of 0.11 and range in between: 6.6- 7.6, the sensitivity of our sensor remains lower (average slope: 0.05, range: 5.0 – 8.0) but a larger pH range is considered.

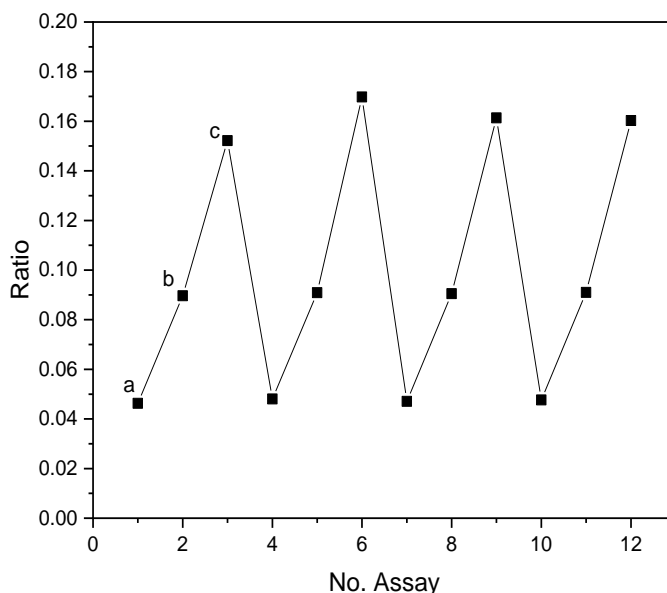


Figure 3.22 Reproducibility and reversibility for the pH-sensor. The measurement was carried out by exposing the pH-sensitive surface to different buffer solutions in turn: (a) 5.0, (b) 6.5 and (c) 8.0.

Consequently, we aimed to detect bacterial growth using these surfaces. For this experiment FNP_{Red-FA} were grafted on a surface. For this, we first quickly (~ 30 min) calibrated the surface with the same three buffers at pH 5, 6.5 and 8, obtaining the linear model in table 3.5 by taking the data presented in figure 3.23. The R-square obtained shows a good fit.

In the next step, a bacteria solution of *E. coli* in M9 minimal medium was diluted to an OD: 0.01 and deposited on the functionalized surface. Then, images and spectra were obtained every hour to determine the $\alpha_{520/600}$ and by brightfield channel to quantify the number of cells per image (to be considered for the bacterial growth) (Figure 3.24 and 3.25). Black lines seen in the fluorescence image are mechanical scratches and were used to confirm the position of the same zone.

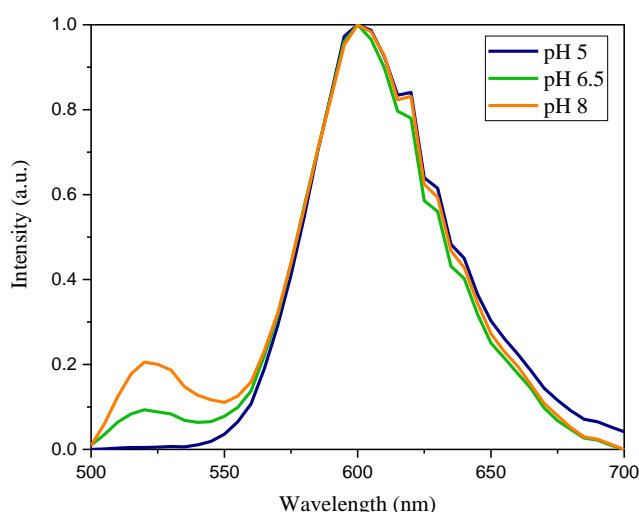


Figure 3.23 Normalized emission spectra at different pH to calibrate the FNP_{Red-FA} grafted surface used for bacterial growth study.

Table 3.5 Linear fit of the sample used for bacterial growth study.

	pH 5	pH 6.5	pH 8
Calibration $\alpha_{520/600}$	0.005	0.093	0.205
Slope	Intercept		R-square
0.06 ± 0	-0.33 ± 0.02		0.99
			Model
			$pH = \frac{\alpha_{520/600} + 0.33}{0.06}$

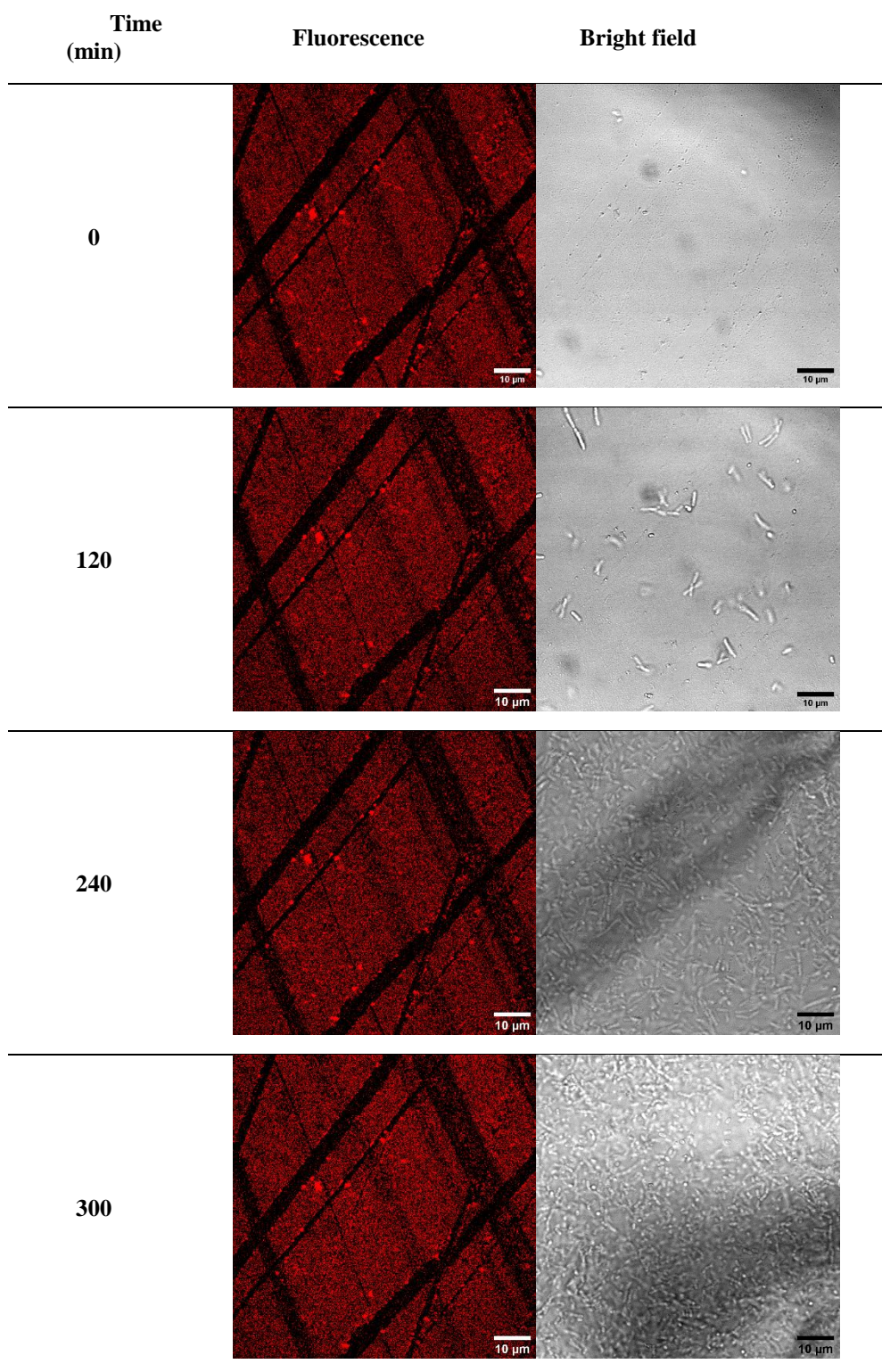


Figure 3.24 Fluorescence imaging of *E coli* growth on a FNP_{Red-FA} surface, in M9 minimal medium at different times. Fluorescence images corresponds to surface emission (red channel, λ_{ex} : 488 nm). Bacterial growth can be observed in the brightfield images.

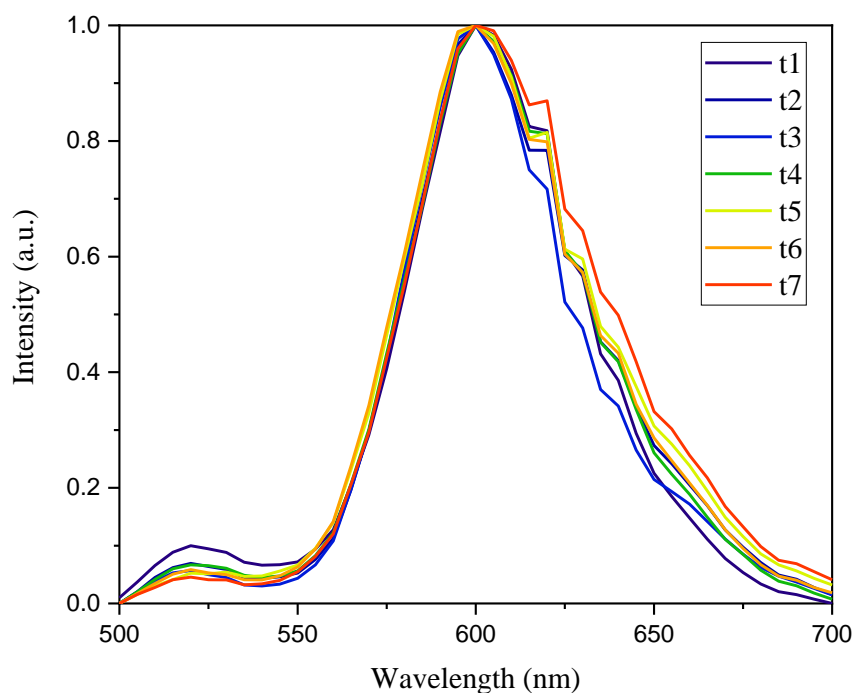


Figure 3.25 Normalized emission spectra obtained at different times for the bacterial growth study. (0 to 420 min).

As a control, bacteria were grown in bulk (cuvette, without shaking, under the microscope at the same temperature) in the same conditions as the surface. The pH and OD were measured for the control and compared to samples taken from the bacterial solution on the surface. The rate-limiting step was the small quantity of bacterial solution, which could only be measured by pH paper and just few times (3 times), to avoid the decrease of solution of the sample and finally drying it.

Afterwards, we estimated the pH with the linear model obtained from the calibration curve and it was found to be close to the measured one. Nevertheless, the calculated pH from spectral image analysis seemed to decrease faster than the measured pH. This could be related to the local pH of the bacteria, which are more concentrated on the surface (by their adhesion) than in the bulk solution.

Table 3.6 Data obtained from bacterial growth study, showing the ratio $\alpha_{520/600}$, calculated pH with the linear model obtained from the calibration, measured pH on surface and bulk, bulk OD and number of cells per image.

T	Time (min)	$\alpha_{520/600}$	Calculated pH	Measured pH	Measured Bulk pH	Bulk OD	#cells/image
1	0	0.0998	6.5	6.5	6.5	0.01	4
2	60	0.0692	6.0				9
3	120	0.0568	5.8				44
4	240	0.0668	6.0	6.5	6.5	0.10	652
5	300	0.0525	5.8				1120
6	360	0.0585	5.9	6	6	0.22	2208
7	420	0.0456	5.7				2384

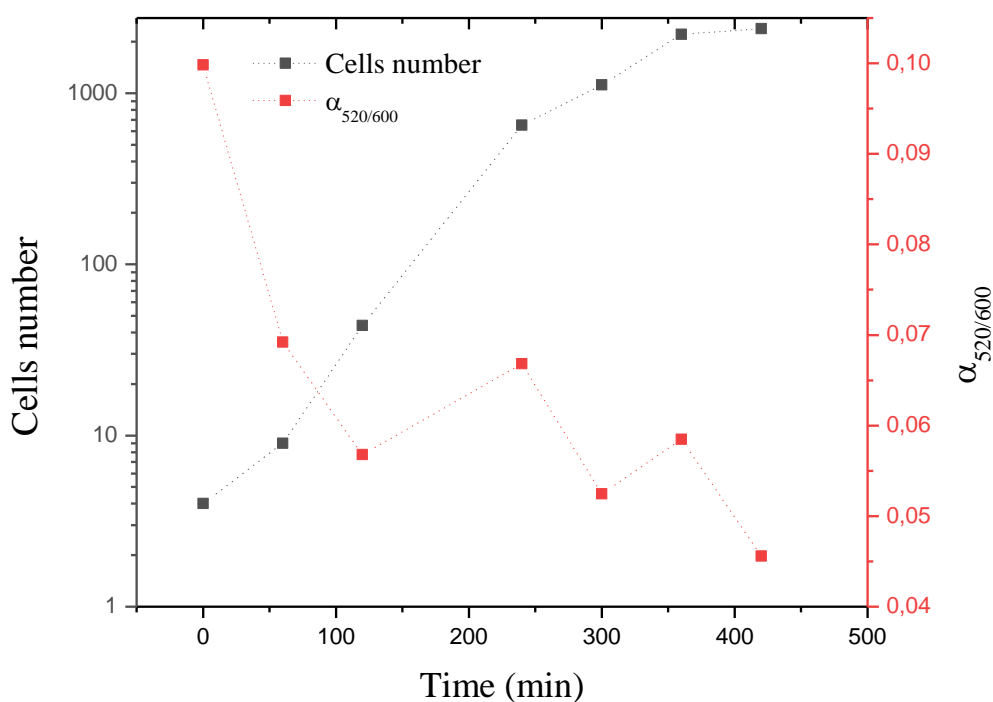


Figure 3.26 Ratio $\alpha_{520/600}$, (red axis, on the right) and number of cells (black axis on the left) per image as a function of time.

The change in $\alpha_{520/600}$ and number of cells (Figure 3.26) as a function of time are inversely proportional. The number of cells in exponential scale could be related to the decrease of $\alpha_{520/600}$. Nevertheless, it was not possible to find a good correlation between

them that can precisely predict the growth of the bacteria by knowing the ratio. For this, further experiments should be carried out to obtain more data in shorter time intervals.

Conclusions & Perspectives

In conclusion, the preparation of pH sensitive surfaces was carried out successfully. Firstly, the different steps to functionalize the glass substrates were presented. Then new pH sensitive surfaces were characterized by different techniques:

➤ By XPS analysis, the elementary composition of the surfaces after activation, silanization and grafting of the nanoparticles was by focusing mainly in the Nitrogen, since different states of Nitrogen and its different states we have obtained an evolution of the chemical composition at each step. Starting from the activated glass, only traces were found; after silanization it was observed an increment in the C-NH₂, and also in the protonated amines C-NH₃⁺were in good agreement with the literature. After Nanoparticle grafting, the decrease of 1.5 times in the percentage of Nitrogen and an increment of 2.5 times in the percentage of Carbon corresponds well to the addition of the nanoparticles.

➤ A good coverage from the nanoparticles was determined by SEM and AFM on the surface, 8.1 ± 0.7 % by SEM and 13.1 ± 0.5 % by AFM. As described above, AFM images allowed to obtain a more reliable quantification of the coverage, but SEM images permit to observe larger areas which allowed to measure the homogeneity of the coverage.

➤ The photophysical properties were found to be in good agreement with the spectroscopic properties from the grafted elements in suspension (FNP_{Red} and FA). Besides, the response of the surface as a function of pH was investigated, obtaining a linear correlation with the ratio $\alpha_{520/600}$. The sensitivity of the sensitive surfaces remains lower than Grant *et al.* (28), (average slope: 0.05, range: 5.0 – 8.0) but a larger pH range is considered.

➤ From bacterial growth study on the pH-sensitive surfaces, it can be observed the pH can be predicted efficiently. Nevertheless, to corroborate and evaluate the real accuracy it is needed to improve the method to measure the real pH, since only

with pH paper is not very accurate. For this a micro-electrode could be used. Besides, with more data in between points, a better fit can be done and thus a correlation between ratio $\alpha_{520/600}$ and bacterial growth will be obtained. This will be carried out in the coming weeks.

To the best of our knowledge, it is the first time pH-sensitive surfaces are used to effectively detect bacterial growth and also the first time thanks to a ratiometric measurement. Nevertheless, some critical aspects should be improved to obtain a more reliable and robust device. Herein some perspectives that are currently being evaluated to achieve this:

➤ **Improve the homogeneity of grafting**

It was clearly seen that grafting of the FNP is not homogeneous and some aggregates were observed. This could be improved by reducing the polydispersity of the FNP in solution, by using a filter with a size cut-off, allowing to separate the bigger particles from the smaller ones.

In addition, the improvement of the grafting of FA on the shell of FNP could be evaluated. It was tested to graft on the surface nanoparticles with FA already grafted on the surface, but the same sensitivity and heterogeneity was obtained as presented in this chapter (Trial 2 and bacteria test). Somehow this is expected, since the grafting of FA either in FNP or in grafted-FNP surfaces is done in both cases by peptide coupling, reaction which is not 100% efficient. This could be improved by using ‘click-chemistry’ instead of peptide-coupling, (by replacing FNP_{Red} by FNP_{R-DIBO} nanoparticles). FA could be ‘clicked’ on the nanoparticles before grafting them on the surface.

➤ **Slow decrease in pH during bacterial growth**

Different acidic species such as acetic acid, lactic acid, CO₂ and other metabolites are released upon bacterial growth, resulting in a pH decrease of the growth medium. Nevertheless, in an open system, the CO₂ that is produced can escape from the growth medium. For this reason, a PDMS microfluidics circuit was designed and is currently being tested to slow down the diffusion of gases (PDMS could be replaced by a glass microfluidics circuit) (Figure 3.27). The design of the circuit allows to inject a sample and diffuse it in 5 individual channels, in addition, the flow can be stopped, and all the metabolites and gases generated from bacterial growth will remain without escaping. We

hypothesized that in this case the pH will decrease faster allowing a faster detection. Furthermore, the microfluidic circuit would also allow the addition of different antibiotics and screening the resistance of bacteria to them.

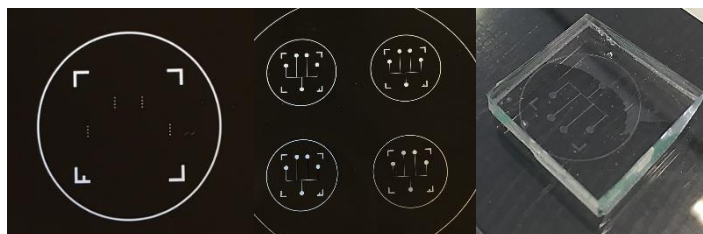


Figure 3.27 PDMS microfluidic circuit

- (1) C. Grazon *et al.*, Core-shell polymeric nanoparticles comprising BODIPY and fluorescein as ultra-bright ratiometric fluorescent pH sensors, *Photochemical & Photobiological Sciences*, 2019, Advance Article.
- (2) C. Haensch *et al.*, Chemical modification of self-assembled silane based monolayers by surface reactions, *Chem. Soc. Rev.*, 2010,39, 2323-2334
- (3) A. Singh *et al.*, Crystal growth on self-assembled monolayers, *CrystEngComm*, 2011,13, 24-32
- (4) S. Onclin *et al.*, Engineering Silicon Oxide Surfaces Using Self-Assembled Monolayers, *Angewandte Chemie International Edition*, 2005, 44: 6282-6304.
- (5) S. Casalin *et al.*, Self-assembled monolayers in organic electronics, *Chem. Soc. Rev.*, 2017, 46, 40-71.
- (6) B. Franklin *et al.*, Of the stilling of waves by means of oil. Extracted from sundry letters between, *Philos. Trans. R. Soc. London* 1774, 64, 445.
- (7) Schreiber, Structure and growth of self-assembling monolayers, *F. Progress in Surface Science* 2000, 65, 151.
- (8) A. Requincha *et al.*, Manipulation of nanoscale components with the AFM: principles and applications
- (9) J.F.Watts and J.Wolstenholme, *An Introduction to Surface Analysis by XPS and AES*, Wiley & Sons, 2003, UK, ISBN 978-0-470-84713-8.
- (10) D. K. Aswal *et al.*, Self assembled monolayers on silicon for molecular electronics, *Anal. Chim. Acta*, 2006, 568 (1–2), 84–108.
- (11) R. Maoz *et al.*, Self-replicating amphiphilic monolayers, *Supramolecular Science* 1995, 2, 9.
- (12) A. Taglietti, *et al.*, Antibiofilm activity of a monolayer of silver nanoparticles anchored to an amino-silanized glass surface, *Biomaterials*, 2014, 35, 6, 1779-1788.
- (13), S. Szunerits and R. Boukherroub, Different strategies for functionalization of diamond surfaces, *Journal of Solid State Electrochemistry*, 2008, 12, 10, 1205-1218.

- (14) A. Rodríguez-Contreras, Modification of titanium surfaces by adding antibiotic-loaded PHB spheres and PEG for biomedical applications, *Journal of Materials Science: Materials in Medicine*, 2016, 27, 124.
- (15) L. Yang, AFM and impedance spectroscopy characterization of the immobilization of antibodies on indium–tin oxide electrode through self-assembled monolayer of epoxysilane and their capture of *Escherichia coli* O157:H7, *Biosensors and Bioelectronics*, 2005, 20, 7, 1407-1416.
- (16) X. Jinlan et al., Biosensors for amino acids – A preliminary study, *Journal of Central South University of Technology*, 1994, 1, 1, 51-58.
- (17) H.J. Kim *et al.*, Enhancement of mechanical properties of aluminium/epoxy composites with silane functionalization of aluminium powder, *Composites Part B: Engineering*, 2012, 43, 4, 1743-1748.
- (18) M.L. Hair *et al.*, Reactions of chlorosilanes with silica surfaces, *J. Phys. Chem.* 1969, 73, 2372.
- (19) C.G. Armistead, Surface hydroxylation of silica, *J. Phys. Chem.* 1969, 73, 3947.
- (20) C.P. Tripp, Effect of fluoroalkyl substituents on the reaction of alkylchlorosilanes with silica surfaces, *Langmuir*, 1993, 9, 12, 3518-3522.
- (21) A.Y. Fadeev and T. J. McCarthy, Trialkylsilane Monolayers Covalently Attached to Silicon Surfaces: Wettability Studies Indicating that Molecular Topography Contributes to Contact Angle Hysteresis, *Langmuir*, 1999, 15 (11), pp 3759–3766.
- (22) A.Y. Fadeev and T. J. McCarthy, Self-Assembly Is Not the Only Reaction Possible between Alkyltrichlorosilanes and Surfaces: Monomolecular and Oligomeric Covalently Attached Layers of Dichloro- and Trichloroalkylsilanes on Silicon, *Langmuir* 2000, 16, 7268.
- (23) A. Pallandre *et al.*, Binary nanopatterned surfaces prepared from silane monolayers, *Nano Letters*, 2004, 4, 2, 365-371.
- (24) A. Pallandre, Macromolecular assemblies onto chemically nanopatterned surfaces, 2004, Doctoral thesis.

- (25) N. Graf *et al.*, XPS and NEXAFS studies of aliphatic and aromatic amine species on functionalized surfaces, *Surface Science*, 2009, 603, 2849-2860.
- (26) P.M. Dietrich *et al.*, Quantification of silane molecules on oxidized silicon: are there options for a traceable and absolute determination, *Analytical Chemistry*, 2015, 87, 10117-10124.
- (27) M.T. Charreyre *et al.*, Fluorescence Energy Transfer from Fluorescein to Tetramethylrhodamine Covalently Bound to the Surface of Polystyrene Latex Particles, *Langmuir*, 1995, 11, 2423.
- (28) S. Grant and R. Glass, A sol-gel based fiber optic sensor for local blood pH measurements, *Sensors and actuators B*, 1997, 45, 35.
- (29) CG. Niu *et al.*, Fluorescence ratiometric pH sensor prepared from covalently immobilized porphyrin and benzothioxanthene, *Anal Bioanal Chem.* 2005, 383, 349.
- (30) Y. Ando *et al.*, A ratiometric fluorescent pH glass optode based on a boron-dipyrrromethene derivative, *Sensors and Actuators B*, 2007, 121, 74.

Part II: Antibacterial Surfaces

Chapter 4: Repelling Bacteria Surfaces

Introduction

In the previous chapter, the synthesis and characterizations of pH-sensing surfaces were described. We have demonstrated that such surfaces could effectively detect bacterial growth by a ratiometric fluorescence measurement. In this part of the manuscript, the study and characterizations of new antibacterial materials as repelling films will be introduced.

Indeed, we focused on (super)hydrophobic surfaces due to their main advantages over other strategies to avoid bacteria. Among them are:

- easy manufacturing process in comparison with other surfaces which imply long synthetic steps or careful design of antimicrobial agent release;
- lack of antimicrobial agent, which in long term use can be a threat for the environment, we also avoid the issue of emptying reservoir with time;
- self-cleaning properties, which simplifies the elimination of the dead cells or prevents the attachment of biofilms and facilitates its removal.

Besides, the innovation of this project relies on the use of a luminescent surface. For the first time, our group and collaborators demonstrated the advantages of combining such properties : fluorescence and superhydrophobicity. This allowed to colocalize the bacteria and the substrate at the same time. More details about the properties of superhydrophobic surfaces and the results obtained with these new materials will be found in the publications below.

This project was done with significant the contribution of our collaborators. The preparation of the electropolymerized films was done by Thierry Darmanin and Gabriela Ramos-Chagas from NICE lab belonging to Université Côte d'Azur (Nice, France) with monomers from Institut Lavoisier de Versailles (Versailles, France). From our group, we

contributed with the photophysical characterizations of different films, as well as the interaction of some of the coatings with different bacterial strains. This work was supported by LabEx CHARMMMAT.

The results are presented in the form of four publications as follows:

- 4.1 Superhydrophobic Surfaces Toward Prevention of Biofilm-Associated Infections**, published in INTECH OPEN, 2017 (doi.:10.5772/intechopen.72038), which is a review introducing the concepts of superhydrophobic surfaces and their application to prevent bacterial adhesion as *State of art for this chapter*. Pages 120 to 135.
- 4.2 Superhydrophobic polypyrene films to prevent *Staphylococcus aureus* and *Pseudomonas aeruginosa* biofilm adhesion on surfaces: high efficiency deciphered by fluorescence microscopy**, published in Photochemical & Photobiological Sciences, 2018 (doi: 10.1039/c8pp00043c), presenting the results about polypyrene electropolymerized films proving to be efficient to prevent bacterial adhesion. This work was also done in collaboration with Siewert Hugelier and Michel Sliwa from LASIR, Université de Lille, whom optimized the image analysis. Pages 137 to 157.
- 4.3 Anti-bacterial and fluorescent properties of hydrophobic electrodeposited non-fluorinated polypyrenes**, published in Applied Surface Science, 2018 (doi: 10.1016/j.apsusc.2018.04.268), where other pyrene derivate polymers were characterized and their antibacterial properties were studied (our contribution was the photophysical properties characterization and bacterial interaction). Pages 158 to 170.
- 4.4 Superhydrophobic and fluorescent properties of fluorinated polypyrene surfaces using various polar linkers prepared via electropolymerization**, published in Reactive and Functional Polymers, 2019 (doi: 10.1016/j.reactfunctpolym.2018.12.001), similarly, other pyrene derivatives were implemented by changing polar linkers and studied. Our contribution was the photophysical properties characterizations. Pages 171 to 183.

Publication in section **4.1**, was our first approach to superhydrophobic surfaces for biomedical research. In this context, the main concepts of superhydrophobicity are explained followed by a short review about the use of these materials for biological and long term medical applications. Following, in section **4.2**, our first and most important results on luminescent superhydrophobic polypyrene films are presented. With this work we established the working methodology which could be extended to the following publications on section **4.3**. Both publications show for the first time the combination of luminescence and superhydrophobicity for antimicrobial substrates. Lastly, in section **4.4**, new and complementary polypyrene films were characterized. Nevertheless, only its photophysical properties were studied, leaving behind the antibacterial properties.

- (1) J.W. Costerton *et al.*, Bacterial Biofilms: A Common Cause of Persistent Infections, *Science*, 1999, 284, 1318.
- (2) R.D. Wolcott and G.D. Ehrlich, Biofilms and Chronic Infections, *J. Am. Med. Assoc.*, 2008, 299, 2682.
- (3) M. Vincent *et al.*, Contact killing and antimicrobial properties of copper, *Journal of Applied Microbiology*, 2017, 125, 5, 1032.
- (4) C.K. Yeo *et al.*, Hydrogel Effects Rapid Biofilm Debridement with ex situ Contact-Kill to Eliminate Multidrug Resistant Bacteria in vivo, *ACS Appl. Mater. Interfaces*, 2018, 10, 24, 20356.
- (5) H. Chen *et al.*, Synthesis of chitosan-based micelles for pH responsive drug release and antibacterial application, *Carbohydrate Polymers*, 2018, 189, 65.
- (6) J.S. Price *et al.*, Controlled release of antibiotics from coated orthopedic implants, *J. Biomed. Mater. Res.*, 1996, 30, 281.
- (7) L. Tan *et al.*, Silver-Infused Porphyrinic Metal–Organic Framework: Surface-Adaptive, On-Demand Nanoplatfrom for Synergistic Bacteria Killing and Wound Disinfection, *Small*, 2018, 14, 9, 1703197.

- (8) M. Tischer et al., Quaternary ammonium salts and their antimicrobial potential: targets or nonspecific interactions?, *ChemMedChem*, 2012, 7, 22.
- (9) K. Ali et al., Comparative in situ ROS mediated killing of bacteria with bulk analogue, Eucalyptus leaf extract (ELE)-capped and bare surface copper oxide nanoparticles, *Materials Science and Engineering: C*, 2019, 100, 747.
- (10) P. Sautrot-Ba et al., Eosin-mediated synthesis of polymer coatings combining photodynamic inactivation and antimicrobial properties, *J. Mater. Chem. B*, 2017, 5, 7572.
- (11) I. Kurtz and J.D. Schiffman, Current and Emerging Approaches to Engineer Antibacterial and Antifouling Electrospun Nanofibers, *Materials*, 2018, 11, 7, 1059.
- (12) F. Wang et al., Constructing membrane surface with synergistic passive antifouling and active antibacterial strategies through organic-inorganic composite modifier, *Journal of Membrane Science*, 2019, 576, 150.
- (13) K. Manoharan and S. Bhattacharya, Superhydrophobic surfaces review: Functional application, fabrication techniques and limitations, *Journal of Micromanufacturing*, 2019, 2, 1, 59.
- (14) H. Qian et al., Mussel-inspired superhydrophilic surface with enhanced antimicrobial properties under immersed and atmospheric conditions, 2019, 465, 267.

4.1 Article 1: “Superhydrophobic Surfaces Toward Prevention of Biofilm-Associated Infections”

G. Morán and R. Méallet-Renault

Chapter 5 from the book: Bacterial Pathogenesis and Antibacterial Control

INTECH OPEN

Superhydrophobic Surfaces Toward Prevention of Biofilm-Associated Infections

Gabriela Morán and Rachel Méallet-Renault

Additional information is available at the end of the chapter

<http://dx.doi.org/10.5772/intechopen.72038>

Abstract

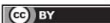
In this chapter, we briefly review the different strategies for surface modification as a method to fight against bacteria adhesion and biofilm formation. We focus on superhydrophobic materials and biofilm medical infections. We give some insights into common materials and preparation techniques for superhydrophobic surfaces before discussing recent bacteria interacting with superhydrophobic surfaces. These surfaces have indeed demonstrated great potential in preventing bacterial adhesion and biofilm formation due to the presence of micro- and nanostructures. Although much work has been done, further investigations are still required to improve the surface mechanical properties over time and to understand the underlying mechanism behind their antimicrobial and antifouling capability. Moreover, there is a lack of standard methodology for evaluating antibacterial properties, and biofilm prevention should be studied with longer incubation times. We strongly believe in the potential of superhydrophobic surfaces, and we encourage more research on its magnificent properties, especially for their advantages over other antimicrobial surfaces.

Keywords: superhydrophobic surfaces, biofilm-associated infections, antibacterial surface, bacterial adhesion, biofilm formation, anti-biofilm surface

1. Strategies on surface modification for antibacterial properties

The rapid proliferation of pathogenic bacteria, which is responsible for nosocomial infections, is becoming a major public health problem because of bacterial resistance to antimicrobial treatments (antibiotics and biocides) [1]. It is now well established that bacterial populations attach to solid substrates for survival, forming biofilms. Biofilms are dense microbial communities, adhering to surfaces, which secrete an extracellular matrix mainly composed of water, polysaccharides, DNA and proteins [2]. Many different strategies on surface modification have been studied over the last few years to reduce bacterial adhesion and to avoid biofilm formation.

IntechOpen

© 2018 The Author(s). Licensee IntechOpen. This chapter is distributed under the terms of the Creative Commons Attribution License (<http://creativecommons.org/licenses/by/3.0>), which permits unrestricted use, distribution, and reproduction in any medium, provided the original work is properly cited. 

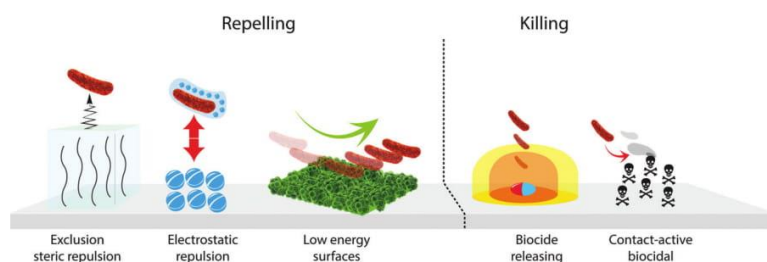


Figure 1. Antibacterial surfaces.

In general, two different global strategies can be distinguished (**Figure 1**). The first strategy relies on killing bacteria through antimicrobial compounds (either release or direct contact), such as silver ions [3] and antibiotics [4]. However, this strategy can involve tedious preparations and might represent a threat to the environment and biological systems. The second strategy relies on repelling bacterial attachment through morphological or physical-chemical interactions such as steric impediment, electrostatic interactions and low surface energy [5]. Many of the steric and electrostatic repulsion techniques proposed until now show no persistence, and surface hydrolysis may occur. Wet surfaces can provide the ideal conditions for biofilm formation; therefore, wettability properties of surfaces play a crucial role on biofilm formation. Low-surface-energy surfaces have a great potential since their antibacterial properties depend mostly on surface roughness [6]. In the present chapter, our discussion focuses on superhydrophobic surfaces. For further information regarding other techniques, useful information can be found in the review by Griesser et al. [7] and in the work by Siedenbediel and Tiller [8].

2. Superhydrophobicity

Surface wettability is an interface phenomenon reflecting the behavior of a liquid in contact with a solid surface. The control of surface wettability is present in nature and in our daily life in many applications such as waterproof coatings, cooking utensils and bathroom accessories. A material's property can be evaluated by the measurement of the contact angle (CA) between a droplet of liquid and the material surface [9].

It is well known that the interface liquid-gas (LG) area tends to be minimized due to the surface tension. When a drop is in contact with a solid surface, a balance between three-phase surface tension occurs (**Figure 2**), and it can be described by the Young's equation as follows:

$$\gamma_{SG} = \gamma_{SL} + \gamma_{LG} \cos\theta \quad (1)$$

where γ_{SG} , γ_{SL} and γ_{LG} are the solid – gas (SG), solid – liquid (SL) and liquid – gas (LG) surface tensions and θ the contact angle, also referred to as the intrinsic contact angle or smooth surface contact angle [10].

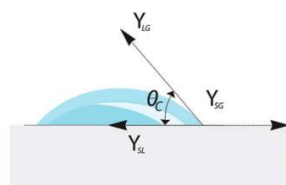


Figure 2. Liquid droplet on solid surface.

Depending on the CA value, different materials are said to be either hydrophilic or hydrophobic. For instance, if the liquid is water (or oleophilic/oleophobic when the liquid is an oil), a surface in contact with water is said to be hydrophilic if the CA is below 90° . For a $CA > 90^\circ$, it is hydrophobic, and for a $CA > 150^\circ$, it is referred to as a superhydrophobic surface. This last term refers to the repellent capability of such surfaces toward water [10].

Lotus leaves are an excellent example of superhydrophobic surfaces, as they are known to be self-cleaning. On a self-cleaning surface, particles can 'roll-off' it by their adhesion to water droplets [11]. With the technological development over the last decade, lotus leaves have been the subject of many studies. It has been found that its repellent properties are due to a hierarchical micro- and nanostructured topography. As nature demonstrates, the design of nonwetable surfaces must take parameters such as the roughness and the chemical nature of the material into consideration. The aim of this chapter is to highlight the use of superhydrophobic surfaces to prevent bacterial adhesion and biofilm formation. The main models to determine CA measurement for non-flat surfaces are described in the following section.

2.1. Wenzel and Cassie-Baxter model

As for the lotus leaf, the presence of micro- and nanostructures will contribute to the wettability of the surface, playing a crucial role on superhydrophobicity. Higher apparent CA values cannot be achieved by chemical modification, but by changing the roughness. According to Wenzel [12], the real contact area of the solid-liquid interface could be increased by changing the roughness more than changing the microscale apparent area. Wenzel's model considers that there is no gas layer between the solid-liquid interface, so the liquid fills the grooves on the surface (**Figure 3**). This angle can be referred to as the wetted contact with the surface.

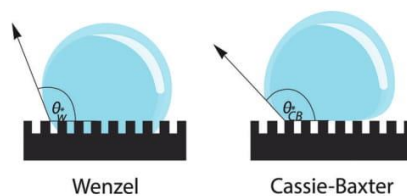


Figure 3. Wenzel and Cassie-Baxter models.

The relationship between the apparent CA θ_w and the intrinsic CA at equilibrium is:

$$\cos \theta_w = r \cos \theta \quad (2)$$

where r is the ratio of the surface area over the apparent area, defined as the Roughness r of the material. By increasing the roughness (a bigger height difference between the posts and grooves, and the density of posts), superhydrophobicity can be achieved.

Cassie and Baxter [13] studied composite materials present in nature, finding that if the surface is hydrophobic enough, the gas phase between the solid-liquid interface will remain and the droplet will not fill the grooves on the rough surface (**Figure 3**, right). For this case, the relationship is as follows:

$$\cos \theta_{CB} = f(1 + \cos \theta_w) - 1 \quad (3)$$

The Cassie-Baxter equation adapts to any composite surface contact, which is represented as follows:

$$\cos \theta_{CB} = f_1 \cos \theta_1 + f_2 \cos \theta_2 \quad (4)$$

where θ_{CB} is the apparent CA of the composite surfaces, θ_1 and θ_2 are the intrinsic CA of two materials, and f_1 and f_2 are the fractions of two materials of the composite surfaces. f is the solid fraction of the substrate. For very rough surfaces, f will tend to zero, while θ_{CB} will tend to 180° .

Bittoun et al. [14] theoretically studied different types of surface topographies by changing roughness scales, on drop 2D systems. They studied sinusoidal, flat-top pillars and triadic Koch curves finding that Cassie-Baxter state is thermodynamically more stable, in comparison with the Wenzel state. In addition, they concluded that multi-scale roughness increases the mechanical stability of the surface and is beneficial for superhydrophobicity. Among the three topographies, round-top protrusions (sinusoidal) were shown to be the best for non-wettability, as nature has already proved.

It has been suggested that by changing the surface topography from flat to structured and by including a hierarchical organization, the water CA will be modified and superhydrophobicity may be achieved [9]. Lotus leaves have proved this theory, regardless of hydrophilic coating on their surface, the presence of hierarchical micro- and nanoscale features are responsible for their superhydrophobicity [15]. **Figure 4** shows different structures varying from flat to hierarchical.

2.2. Hysteresis

For many medical and industrial applications, the interest of a self-cleaning surface is very attractive; nevertheless, on many occasions, the CA hysteresis has been ignored in investigations. For real-life applications of repellent surfaces, the dynamic movement of the liquid drops has to be taken into consideration because it depends on the CA hysteresis. A high hydrophobicity in static CA does not imply a high hydrophobicity in dynamic CA, as proved by Oner et al. A low hysteresis CA is ideal [16].

Wetting of four different surfaces

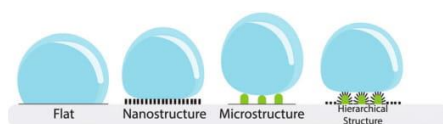


Figure 4. Different types of surface roughness and wettability.

Furthermore, CA hysteresis is important for the removal of surface contaminants when water droplets are moved along a tilted surface [9]. As we showed previously, the uniform flow of the droplet will allow or not allow the transport of the contaminant along the surface. When the flow is uniform, the material can be considered to behave as a self-cleaning surface. On the contrary, if the CA hysteresis is too high, the transport will not be very efficient and is possible that not all the contaminants will be carried by the drop (Figure 5) [9].

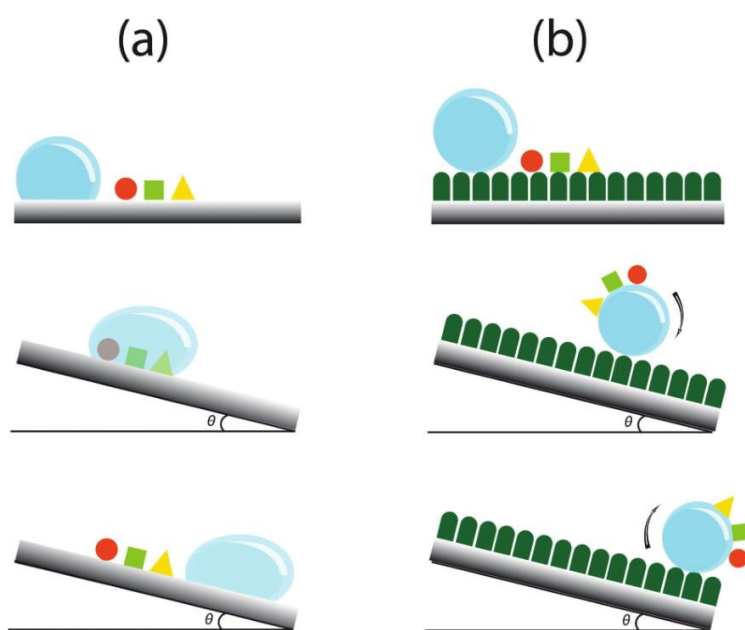


Figure 5. Dirty flow on surfaces with high (a) and low (b) CA hysteresis. While the drop is moving on a high CA hysteresis surface, it will not be efficient enough to transport the contaminants on the surface.

2.3. Superhydrophobic surfaces toward biofilm prevention

Biofilms represent a high risk for nosocomial infections in which different pathogenic bacteria are involved in biofilm-associated infections (BAI) [1]. Remarkable efforts have been made toward superhydrophobic surfaces, as they are considered self-cleaning. As we have previously mentioned, superhydrophobicity is usually achieved by a combination of surface structure, often at a micro/nanoscale, with low-surface-energy compounds. Numerous studies have been published over the last decade, regarding the use of superhydrophobic surfaces or coatings to reduce bacterial adhesion and thus to prevent biofilm formation.

Figure 6 shows how the interest in the development and study of antibacterial superhydrophobic surfaces has increased dramatically over the last decade. Despite all the efforts made until now, there is still a lack of standard methodology to assess the effectiveness of materials against biofilm formation. Incubation times and bacterial strains differ dramatically from publication to publication. In the following sections, we try to review the most relevant publications, first discussing the main preparation techniques and then describing some of the results obtained according to the bacterial strains studied and the incubation times. The aim of this review is to give the reader general tools to be able to compare and understand the key conclusions from different studies, since the conditions change from one to another.

2.4. Common materials and preparation techniques for superhydrophobic surfaces

As previously mentioned, superhydrophobic surfaces can be obtained by a wise combination of factors, among which, surface roughness and low surface energy are of particular importance. These features can be achieved using a wide variety of materials, involving organic and inorganic substrates. Among the most common techniques to modify the surface of the substrate, we find laser ablation, vapor deposition, electrochemical polymerization, lithography, sol-gel processing and layer-by-layer deposition (**Figure 7**). As a result, a vast range of surfaces are available. Unfortunately, only a few of these surfaces could be used for practical applications due to the high cost of production and feasibility.

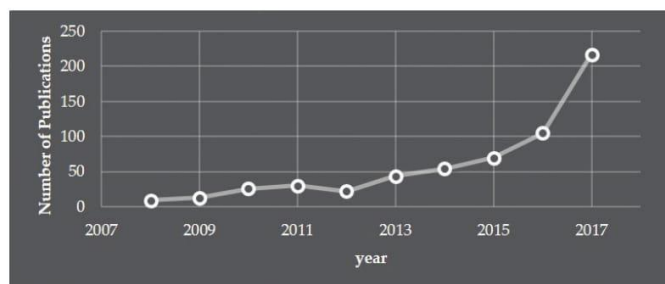


Figure 6. Number of publications per year based on the keywords: Superhydrophobic and antibacterial, from science direct database.

Surfaces with controlled wettability

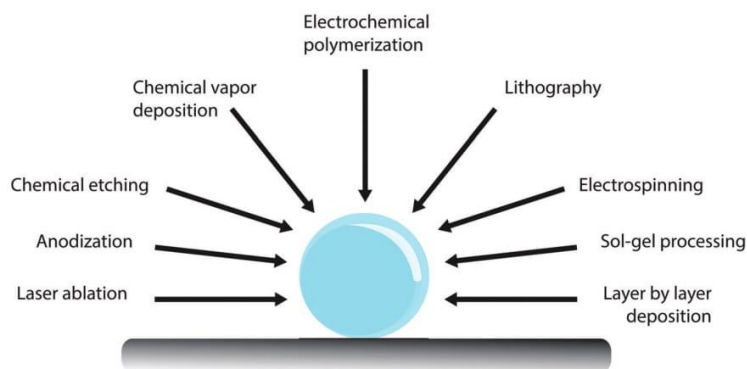


Figure 7. Most used techniques to obtain superhydrophobic surfaces and coatings.

A brief summary of different substrate materials and processing techniques is given below (Table 1) on superhydrophobic surfaces where bacterial interaction was tested (nonexhaustive list).

Among these techniques, we can distinguish two categories: the first category concerns the intrinsic superhydrophobic surfaces, in particular, where the surface structuration is applied directly on the substrate. In the second category, we can find the films and surface coatings, such as polymeric or oleic coatings deposited on a substrate. We focus here on biomedical infections and biomedical applications. Medical implants require a very homogenous and stable surface. The main materials used for medical implants are titanium, stainless steel, cobalt-chromium and some polymers. For this reason, many of the superhydrophobic studies made until today concern titanium surfaces [28]. In most of the cases, titanium surfaces belong to the first category, since their main application is in medical implants. Infections due to medical implants represent about 60–70% of nosocomial infections. BAI have been found in almost 100% of medical implants, such as prosthesis (heart valves, orthopedic, vascular, ocular), urinary catheters, contact lenses and intrauterine contraceptive devices [29]. Biofilms are found to be 100–1000 times more resistant to antibiotics [30]. BAI can cause a number of health complications such as chronic inflammation, antibiotic resistance, chronic and recurrent infections and, in the worst cases, sepsis [29]. Nowadays, BAI are related not only to medical implants and intensive care units but also to non-intensive care hospital areas and many other healthcare settings [29]. Thus, the implementation of self-cleaning surfaces, which facilitate the removal of microorganism on any common surfaces such as desks, tables, walls and clothes, has become a key step in preventing BAI in nosocomial settings.

Transfer from the laboratory to real-life applications, from an applied material point of view, requires testing the mechanical stability over time, in both dry and wet conditions. Even if a

Substrate material	Material processing and coating	Ref.
Titanium	Electrochemical anodization. TiO ₂ nanoscale tubes and after silanization deposition.	Tang et al. [17]
	Laser ablation self-organized micro- and nanostructures.	Fadeeva et al. [18]
	Laser ablation self-organized micro- and nanostructures.	Truong et al. [19]
Polyurethane	Soft lithography micro and nano pillar-structured surface.	Xu and Siedlecki [20]
Silicon	Plasma etching and Teflon/oil coating micro- and nanostructured porous surface.	Epstein et al. [21]
Silica	Based-catalyzed hydrolysis and condensation. Nanostructured silica fluorinated colloids with xerogel coating.	Privett et al. [22]
Aluminum	Anodization, post-etching process and Teflon coating. Al ₂ O ₃ nanoporous and nanopillared surface obtained.	Hizal et al. [23]
Steel, glass, polystyrene	Thermal deposition of n-paraffin and fluorinated waxes.	Pechook et al. [24]
Stainless steel	Multilayer depositions of polydopamine (PDA) and silver (Ag) nanoparticles followed by post-modification with 1H, 1H, 2H, 2H-perfluorodecanethiol.	Qian et al. [25]
Aluminum wafer	Electrochemical deposition of silver coating.	Che et al. [26]
Poly-dimethylsiloxane (PDMS)	Aerosol assisted chemical vapor deposition of copper nanoparticles.	Oskan et al. [27]

Table 1. Example of most common substrates and techniques used to obtain superhydrophobic surfaces.

surface is considered self-cleaning, mechanical stress will be applied under normal conditions through disinfection and wear. Besides mechanical stability, thermal and chemical resistance would be required due to the oxidation in the environmental conditions of almost any application. There are many other fields that would benefit from self-cleaning surfaces, such as naval, the food industry, the energy industry and also for fuel storage. **Figure 8** shows some examples of medical devices that could implement superhydrophobic surfaces.



Figure 8. Example of medical devices which could implement superhydrophobic surfaces.

2.5. Bacterial adhesion and biofilm formation

We can find in the literature tests on several bacterial strains, among which we can highlight *Staphylococcus aureus* and *Staphylococcus epidermidis* (Gram positive, coccus), and *Pseudomonas aeruginosa* and *Escherichia coli* (Gram negative, rod shape), as well as all facultative anaerobic bacteria. *S. aureus* and *P. aeruginosa* recently have been cataloged by the World Health Organization (WHO) as priority pathogens to be considered as threat because of their resistance to antibiotics [31]. *S. epidermidis* is among the leading causes of nosocomial sepsis [29], and *E. coli* can be found on almost any surface, besides being the most prevalent microbe identified from positive blood cultures [32].

As it is known, biofilm formation can be described in five different stages as follows (Figure 9) [33]:

Stage I: Reversible planktonic cell landing on a surface and initial attachment.

Stages II and III: Bacterial growth and microcolony formation, irreversible attachment.

Stage IV: biofilm maturation.

Stage V: dispersion of planktonic cells capable of forming new colonies.

It is important to highlight the fact that the formation of a mature biofilm will be dependent on the bacterial strain and incubation conditions. For discussion, as an example, we can consider *P. aeruginosa* biofilm as a representative. Rasamiravaka et al. [33] studied the development of *P. aeruginosa* biofilm over time by using fluorescence microscopy. After 2 h of incubation, the bacteria culture could be cataloged at Stage I; after 8 h, bacteria attachment was considered irreversible. Microcolony formation was observed after 14 h and biofilm formation and maturation from 1 to 4 days. Stage V was observed after 5 days. Although much research has been made so far, many studies ignored the biofilm formation, focusing only on a few

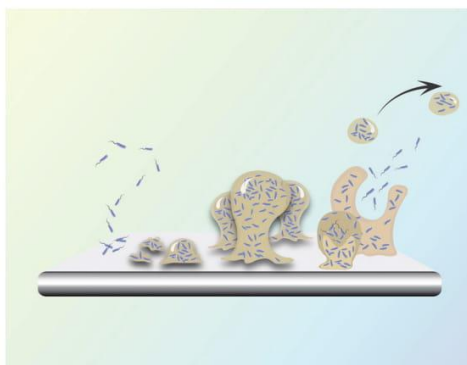


Figure 9. Dirty flow on surfaces with high (left) and low (right) CA hysteresis. While the drop is moving on a high CA hysteresis surface, it will not be efficient enough to transport the contaminants on the surface.

hours of incubation (<24 h). In such cases, we must say that only bacterial adhesion has been studied, without any knowledge as to whether the attachment is either reversible or irreversible. Nevertheless, to study biofilm prevention properties of surfaces, longer incubation times should be considered and for real-life application even longer times where all the phases should be observed. In **Table 2**, we present recent examples of relevant studies of bacterial interactions on superhydrophobic surfaces.

Although **Table 2** does not summarize all the studies to date on antibacterial superhydrophobic surfaces, we can observe that most of the studies have focused only on bacterial adhesion rather than the prevention of biofilm formation. Qian et al. [25] recently published a remarkable work on superhydrophobic multilayer film deposition on stainless steel with antibacterial properties,

Ref.	Bacterial strain	Incubation time	Mode	Biofilm prevention
Tang et al. [17]	<i>S. aureus</i>	2, 4 h	Stationary	Not tested
Fadееva et al. [18]	<i>S. aureus</i>	18 h	Stationary	No for <i>S. aureus</i>
	<i>P. aeruginosa</i>			Yes for <i>P. aeruginosa</i>
Truong et al. [19]	<i>S. aureus</i>	1 h	Stationary	Not tested
	<i>S. epidermidis</i>			
	<i>P. maritimus</i>			
Xu and Siedlecki [20]	<i>S. epidermidis</i>	1, 2 h	Flow	Not tested
Epstein et al. [21]	<i>P. aeruginosa</i>	24, 48 h and 7 days	Flow	Yes
	<i>S. aureus</i>			
	<i>E. coli</i>			
Privett et al. [22]	<i>S. aureus</i>	1.5 h	Flow	Not tested
	<i>P. aeruginosa</i>			
Hizal et al. [23]	<i>S. aureus</i>	1 h	Both	Not tested
	<i>E. coli</i>			
Pechook et al. [24]	<i>B. cereus</i>	24 h and 7 days	Stationary	Yes
	<i>P. aeruginosa</i>			
Qian et al. [25]	<i>S. aureus</i>	1, 3 days	Stationary	Yes
	<i>E. coli</i>			
Che et al. [26]	<i>E. coli</i>	12 h	Stationary	Reduced
Oskan et al. [27]	<i>S. aureus</i>	1 h	Stationary	Not tested
	<i>E. coli</i>			

Table 2. Recently published studies on antibacterial properties of superhydrophobic surfaces, summarizing the bacterial strains, incubation mode and times and more importantly, if biofilm formation prevention was evaluated or not (nonexhaustive list).

evaluating the incubation with *E. coli* and *S. aureus* at 1 or 3 days. The surfaces were prepared with hierarchical micro/nanostructures using polydopamine (PDA) and silver (Ag) nanoparticles. These were compared against non-structured surfaces. For both strains, no cells were observed after day 1, and until day 3, cell quantity was by far less than the other surfaces studied. They proved that the biofilm formation could be prevented using these hierarchical micro/nanostructured superhydrophobic surfaces. They studied two different bacterial strains, gram positive and negative, and also long incubation times to thoroughly assess if biofilm formation is prevented or not.

Fadeeva et al. [18] prepared microstructured superhydrophobic titanium surfaces by femto-second laser ablation. They incubated samples with *S. aureus* or *P. aeruginosa* for 18 h, finding significant reduction for *P. aeruginosa*, but not for *S. aureus*. The aim of the study was to investigate further the behavior of two different shaped pathogens on their surfaces in order to evaluate antifouling properties; nevertheless, they were not able to determine the mechanism by which this was achieved. They suggested that the ability of *S. aureus* to colonize the superhydrophobic surfaces could be dependent on their shape. However, this assumption cannot be generalized as other studies [21, 22] have shown that some surfaces are effective independent of the shape of bacteria. It is important to insist on the need of testing superhydrophobic surfaces with different bacteria (shape, gram positive and negative). Moreover, it would be even more interesting to test a mixture of bacteria to see if the antibacterial capability of the surface is independent of these multiple factors.

2.6. Insights into the mechanisms below prevention of biofilm formation by superhydrophobic surfaces

It has been proved that the Lotus leaf superhydrophobicity originates from the hierarchical micro/nanostructures on their surface even though a hydrophilic layer covers these structures [15]. Micro-/nanostructuring allows the surface to encapsulate air between, creating an air cushion which reduces the water adhesion onto the surface, thus preventing the adhesion of microorganisms and other fouling molecules.

Studying bacterial distribution on the surfaces by imaging techniques has provided important insights on the mechanisms used by the bacteria to attach to the surfaces. With SEM images, Truong et al. [19] observed the distribution of different bacterial strains on superhydrophobic titanium surfaces, finding that the upper regions of the surfaces were not covered by bacteria as much as the crevices between the upper regions. This suggested that the capability to reduce bacterial adhesion of superhydrophobic surfaces can be reduced over time after the trapped air is completely excluded under complete submersion conditions. However, Ma et al. [34] compared the adhesion of bacteria (*P. aeruginosa*) and non-biological adhesion under partially and completely submersion conditions on superhydrophobic *Colocasia esculenta* leaves. They found that the adhesion was dependent on the nanostructure density on the surface rather than the air-cushions trapped on micro/nanostructures. These results demonstrate the efficacy of superhydrophobic surfaces in reducing bacterial adhesion and preventing biofilm formation even under submerged conditions, when they are properly designed at the nanoscale.

3. Perspectives

Much work has been carried out to date on superhydrophobic surfaces, allowing us to understand a little more clearly about the mechanism behind their antimicrobial properties. These surfaces have demonstrated great potential in preventing bacterial adhesion and biofilm formation. Many techniques have been proposed for their preparation and application in different fields. Even so, there is still much work to be done, such as improving the surface mechanical properties over time, and mainly toward our understanding of the underlying mechanism behind their antimicrobial and antifouling capability. With the work so far, we can conclude that micro- and nanostructures have great influence on their antibacterial properties, so this requires further in-depth studies. As discussed in this chapter, there is a lack of standard methodology for evaluating antibacterial properties; however, we can highlight the need to evaluate not only bacterial adhesion but also the prevention of biofilm formation with longer incubation times. Much work has been done so far, but there is still a long way to go from the laboratory to reach real-life applications. We strongly believe in the potential of superhydrophobic surfaces and we encourage continued research on its magnificent properties, especially for their advantages over other antimicrobial surfaces.

Acknowledgements

This work has been supported by the Region Ile-de-France in the framework of DIM Nano-K; by LabEx CHARMMMAT; by fédération Lumière Matière (LUMAT FR2764) and was supported by a grant from the Ministère de l'Éducation Nationale, de l'Enseignement Supérieur et de la Recherche, Université Paris-Sud Paris-Saclay, for Gabriela Moran's Ph.D. thesis (ED 2MIB N°571). Gustavo Martinez Cruz for his contribution on this work.

Author details

Gabriela Morán and Rachel Méallet-Renault*

*Address all correspondence to: rachel.meallet-renault@u-psud.fr

Institut des Sciences Moléculaires d'Orsay (ISMO, UMR8214), CNRS, Université Paris-Sud, Université Paris-Saclay, Orsay, France

References

- [1] Costerton JW, Stewart PS, Greenberg EP. Bacterial biofilms: A common cause of persistent. *Science*. 1999;**284**:1318-1322. DOI: 10.1126/science.284.5418.1318

- [2] Sun F, Qu F, Ling Y, Mao P, Xia P, Chen H, Zhou D. Biofilm-associated infections: Antibiotic resistance and novel therapeutic strategies. *Future Microbiology*. 2013;**8**(7):877-886. DOI: 10.1017/CBO9781107415324.004
- [3] Kumar R, Münstedt H. Silver ion release from antimicrobial polyamide/silver composites. *Biomaterials*. 2005;**26**(14):2081-2088. DOI: 10.1016/j.biomaterials.2004.05.030
- [4] Price JS, Tencer AF, Arm DM, Bohach GAJ. Controlled release of antibiotics from coated orthopedic implants. *Journal of Biomedical Materials Research*. 1996;**30**(3):281-286. DOI: 10.1002/(SICI)1097-4636(199603)30:3<281::AID-JBM2>3.0.CO;2-M
- [5] Poole K. Mechanisms of bacterial biocide and antibiotic resistance. *Journal of Applied Microbiology*. 2002;**92**(Levy 2000):55S-54S. DOI: 10.1046/j.1365-2672.92.5s1.8.x
- [6] Crawford RJ, Webb HK, Truong VK, Hasan J, Ivanova EP. Surface topographical factors influencing bacterial attachment. *Advances in Colloid and Interface Science*. 2012;**179-182**:142-149. DOI: 10.1016/j.cis.2012.06.015
- [7] Griesser HJ, Hall H, Jenkins TA, Griesser SS. Antimicrobial and anti-inflammatory intelligent surfaces. In: *Intelligent Surfaces in Biotechnology: Scientific and Engineering Concepts, Enabling Technologies, and Translation to Bio-Oriented Applications*. Wiley; 3 Feb 2012. pp. 183-241. DOI: 10.1002/9781118181249.ch6
- [8] Siedenbiedel F, Tiller JC. Antimicrobial polymers in solution and on surfaces: Overview and functional principles. *Polymer*. 2012;**4**(1):46-71. DOI: 10.3390/polym4010046
- [9] Zheng L, Wu X, Lou Z, Wu D. Superhydrophobicity from microstructured surface. *Chinese Science Bulletin*. 2004;**49**(17):1779-1787. DOI: 10.1007/BF03183400
- [10] Darmanin T, Guittard F. Wettability of conducting polymers: From superhydrophilicity to superoleophobicity. *Progress in Polymer Science*. 2014;**39**(4):656-682. DOI: 10.1016/j.progpolymsci.2013.10.003
- [11] Zhang X, Wang L, Levänen E. Superhydrophobic surfaces for the reduction of bacterial adhesion. *RSC Advances*. 2013;**3**(30):12003. DOI: 10.1039/c3ra40497h
- [12] Wenzel R. Resistance of solid surfaces to wetting by water. *Industrial and Engineering Chemistry*. 1936;**28**(8):988-994. DOI: 10.1021/ie50320a024
- [13] Cassie ABD, Baxter S. Wettability of porous surfaces. *Transactions of the Faraday Society*. 1944;**40**:546-550. DOI: 10.1039/TF94444000546
- [14] Bittoun E, Marmur A. The role of multiscale roughness in the lotus effect: Is it essential for super-hydrophobicity. *Langmuir*. 2012;**28**(39):13933-13942. DOI: 10.1021/la3029512
- [15] Tuteja A, Choi W, McKinley G, Cohen R, Rubner M. Design parameters for superhydrophobicity and superoleophobicity. *MRS Bulletin*. 2008;**33**(8):752-758. DOI: 10.1557/mrs2008.161
- [16] Öner D, McCarthy TJ. Ultrahydrophobic surfaces. Effects of topography length scales on wettability. *Langmuir*. 2000;**16**(20):7777-7782. DOI: 10.1021/la000598o

- [17] Tang P, Zhang W, Wang Y, Zhang B, Wang H, Lin C, Zhang L. Effect of superhydrophobic surface of titanium on *Staphylococcus aureus* adhesion. *Journal of Nanomaterials*. 2011;2011:1-8. DOI: 10.1155/2011/178921
- [18] Fadeeva E, Truong VK, Stiesch M, Chichkov BN, Crawford RJ, Wang J, Ivanova EP. Bacterial retention on superhydrophobic titanium surfaces fabricated by femtosecond laser ablation. *Langmuir*. 2011;27:3012-3019. DOI: 10.1021/la104607g
- [19] Truong VK, Webb HK, Fadeeva E, Chichkov BN, Wu AHF, Lamb R, Wang JY, Crawford RJ, Ivanova EP. Air-directed attachment of coccoid bacteria to the surface of superhydrophobic lotus-like titanium. *Biofouling*. 2012;28:539-550. DOI: 10.1080/08927014.2012.694426
- [20] Xu L, Siedlecki CA. *Staphylococcus epidermidis* adhesion on hydrophobic and hydrophilic textured biomaterial surfaces. *Biomedical Materials*. 2014;9(3):35003. DOI: 10.1088/1748-6041/9/3/035003
- [21] Epstein AK, Wong T, Belisle RA, Marie E, Aizenberg J. Liquid-infused structured surfaces with exceptional anti-biofouling performance. *PNAS*. 2012;109(33):13182-13187. DOI: 10.1073/pnas.1201973109
- [22] Privett BJ, Youn J, Hong SA, Lee J, Han J, Shin JH, Schoenfish MH. Antibacterial fluorinated silica colloid superhydrophobic surfaces. *Langmuir*. 2011;27(15):9597-9601. DOI: 10.1021/la201801e
- [23] Hizal F, Rungraeng N, Lee J, Jun S, Busscher HJ, van der Mei HC, Choi CH. Nanoengineered superhydrophobic surfaces of aluminum with extremely low bacterial adhesivity nanoengineered superhydrophobic surfaces of aluminum with extremely low bacterial adhesivity. *ACS Applied Materials & Interfaces*. 2017;9(13):12118-12129. DOI: 10.1021/acsami.7b01322
- [24] Pechook S, Sudakov K, Polishchuk I, Ostrov I, Zakin V, Pokroy B, Shemesh M. Bioinspired passive anti-biofouling surfaces preventing biofilm formation. *Journal of Materials Chemistry B*. 2015;3(7):1371-1378. DOI: 10.1039/C4TB01522C
- [25] Qian H, Li M, Li Z, Lou Y, Huang L, Zhang D, Xu D, Du C, Lu L, Gao J. Mussel-inspired superhydrophobic surfaces with enhanced corrosion resistance and dual-action antibacterial properties. *Materials Science and Engineering: C*. 2017;80:566-577. DOI: 10.1016/j.msec.2017.07.002
- [26] Che P, Liu W, Chang X, Wang A, Han Y. Multifunctional silver film with superhydrophobic and antibacterial properties. *Nano Research*. 2016;9(2):442-450. DOI: 10.1007/s12274-015-0925-5
- [27] Ozkan E, Crick CC, Taylor A, Allan E, Parkin IP. Copper-based water repellent and antibacterial coatings by aerosol assisted chemical vapour deposition. *Chemical Science*. 2016;7(8):5126-5131. DOI: 10.1039/C6SC01150K
- [28] Eltorai AEM, Haglin J, Perera S, Brea BA, Ruttiman R, Garcia DR, Born CT, Daniels AH. Antimicrobial technology in orthopedic and spinal implants. *World Journal of Orthopedics*. 2016;7(6):361-369. DOI: 10.5312/wjo.v7.i6.361

- [29] Bryers JD. Medical biofilms. *Biotechnology and Bioengineering*. 2009;**100**(1):1-18. DOI: 10.1002/bit.21838
- [30] Wolcott RD, Ehrlich GD. Biofilms and chronic infections. *Journal of the American Medical Association*. 2008;**299**(22):2682-2684. DOI: 10.1001/jama.299.22.2682
- [31] World Health Organization. Global priority list of antibiotic-resistant bacteria to guide research, discovery, and development of new antibiotics [Internet]. 27 February 2017. Available from: <http://who.int/medicines/publications/global-priority-list-antibiotic-resistant-bacteria/en/> [Accessed: 2017-09-23]
- [32] Opota O, Croxatto A, Prod'hom G, Greub G. Blood culture-based diagnosis of bacteraemia: State of the art. *Clinical Microbiology and Infection*. 2015;**21**(4):313-322. DOI: 10.1016/j.cmi.2015.01.003
- [33] Rasamiravaka T, Labtani Q, Duez P, El Jaziri M. The formation of biofilms by *Pseudomonas aeruginosa*: A review of the natural and synthetic compounds interfering with control mechanisms. *BioMed Research International*. 2015;**2015**:759348. DOI: 10.1155/2015/759348
- [34] Ma J, Sun Y, Gleichauf K, Lou J, Li Q. Nanostructure on Taro leaves resists fouling by colloids and bacteria under submerged conditions. *Langmuir*. 2011;**27**:10035-10040. DOI: 10.1021/la2010024

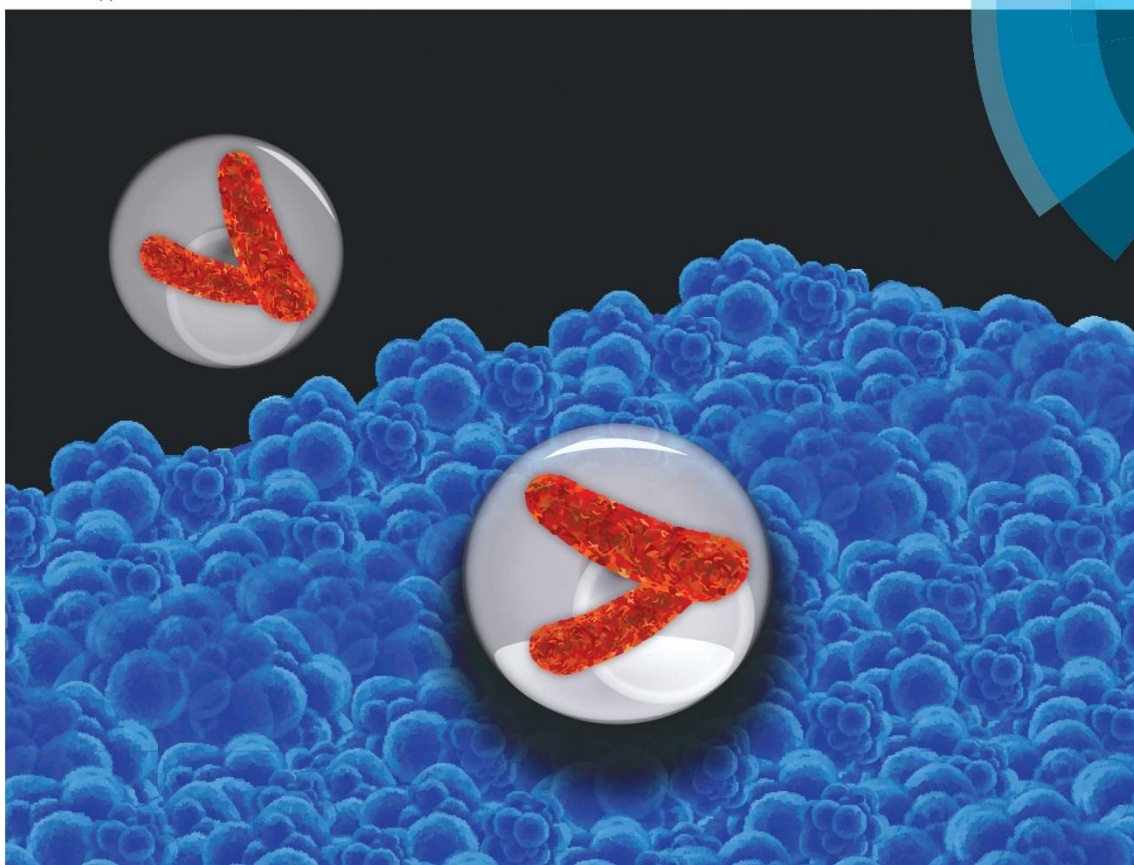
4.2 Article 2: “Superhydrophobic polypyrene films to prevent *Staphylococcus aureus* and *Pseudomonas aeruginosa* biofilm adhesion on surfaces: high efficiency deciphered by fluorescence microscopy”

G. Morán, G. Ramos-Chagas, S. Hugelier, X. Xie, R. Boudjema, C. Ruckebusch, M. Sliwa, T. Darmanin, A. Gaucher, D. Prim, G. Godeau, S. Amigoni, F. Guittard and R. Méallet-Renault

Photochemical & Photobiological Sciences

Photochemical & Photobiological Sciences

An international journal
rsc.li/pps



ISSN 1474-905X





Cite this: *Photochem. Photobiol. Sci.*,
2018, 17, 1023

Superhydrophobic polypyrene films to prevent *Staphylococcus aureus* and *Pseudomonas aeruginosa* biofilm adhesion on surfaces: high efficiency deciphered by fluorescence microscopy†

G. Morán,^a G. Ramos-Chagas,^b S. Hugelier,^c X. Xie,^a R. Boudjema,^a
C. Ruckebusch,^c M. Sliwa,^c T. Darmanin,^b A. Gaucher,^c D. Prim,^d
G. Godeau,^b S. Amigoni,^b F. Guittard^b and R. Méallet-Renault^{*,a}

A blue luminescent and superhydrophobic coating based on an electropolymerized fluorinated-pyrene monomer and its planktonic bacteria and biofilm repellent properties are reported. Two different pathogenic bacterial strains (Gram-positive and Gram-negative) at two different incubation times (2 h planktonic bacterial and 24 h biofilm adhesion) were studied and monitored (analyzed) using multicolor scanning confocal fluorescence microscopy. The coating was proved to reduce bacterial adhesion by 65%. It is highly effective against biofilm attachment, with 90% reduction of bacteria surface coverage. This blue fluorescent surface provides a facile method to characterize the coating, observe the bacterial distribution and quantify the bacterial coverage rate by fluorescence imaging of different colors. Furthermore, the film does not show significant bacterial toxicity during the working incubation times.

Received 29th January 2018,
Accepted 9th May 2018

DOI: 10.1039/c8pp00043c

rsc.li/paps

Introduction

Many decades since the discovery of penicillin and after many years of extended use of antibiotics, antimicrobial resistance (AMR) has emerged as a major threat to worldwide health. AMR has been attributed to different causes, such as the overuse and inappropriate prescribing of antibiotics (in agriculture or in medicine),¹ but also to the persistence of biofilm structures. Compared with their planktonic counterparts, bacterial biofilms have shown 100 to 1000 times greater resistance to antibiotics; thus, they are a serious threat and represent a high risk for infection.² Biofilm formation on a surface can be described in different stages: reversible binding of planktonic cells; multiplication to form a monolayer; growth of an extracellular matrix of polysaccharides, proteins, extracellular DNA and water; development of cells into a microcolony; develop-

ment and maturation of biofilm; and, finally, the detachment and dispersion of planktonic cells which may renew the cycle.³ Bacteria and surface interactions are essential to the whole process.

Biofilms, once developed and structured, are particularly difficult to treat and remove. One strategy to prevent biofilm formation thus consists in preventing initial bacterial adhesion. In hospitals as well as in industrial settings,⁴ different pathogenic bacteria are involved in biofilm-associated infections (BAI), including *streptococci* and *staphylococci* (Gram-positive bacteria) in addition to *Pseudomonas aeruginosa*, *Escherichia coli* and *Klebsiella pneumoniae* (Gram-negative bacteria).² *Staphylococcus aureus* (*S. aureus*) and *Pseudomonas aeruginosa* (*P. aeruginosa*) have been recognized to be the most frequent causes of BAI and were recently included by the World Health Organization (WHO) in a list of the most critical multidrug-resistant bacteria considered to be particular threats.^{5,6}

In general, two different approaches to avoid bacteria colonization on surfaces have been proposed. The first approach relies on the design of bacteria-killing surfaces, either by direct-contact,^{7,8} or by release of biocidal compounds, such as antibiotics⁹ and silver ions.¹⁰ However, these strategies can involve multi-step preparations and require expensive equipment. Moreover, they can represent a threat to the environ-

^aInstitut des Sciences Moléculaires d'Orsay (ISMO), CNRS, Univ. Paris-Sud, Univ. Paris-Saclay, F-91405 Orsay, France. E-mail: rachel.meallet-renault@u-psud.fr

^bUniv. Côte d'Azur, NICE Lab, IMREDD, 61-63 Av. Simon Veil, 06200 Nice, France

^cUniv. Lille, CNRS, UMR 8516 - Unité LASIR, F-59000 Lille, France

^dUniv. de Versailles St-Quentin, UMR CNRS 8180, Institut Lavoisier de Versailles, 45, avenue des Etats-Unis, 78035 Versailles Cedex, France

† Electronic supplementary information (ESI) available. See DOI: 10.1039/c8pp00043c

ment and biological systems due to the release of biocides, in addition to the risk of inactivation of the surface after complete release of the biocidal compound. The second approach consists of the development of repellent surfaces, which can be accomplished by steric or electrostatic repulsion.¹¹ However, most of these surfaces are not stable over long periods due to hydrolysis of their main structures.¹¹ Other well-known repellent surfaces are superhydrophobic surfaces. Superhydrophobicity is usually achieved by a combination of surface structure, often at a micrometer/submicrometer scale, with low surface energy compounds.^{6,12–14} As previously reported by Marmur *et al.*,¹⁵ multiscale roughness is not an indispensable requirement to achieve superhydrophobicity; however, micrometer/submicrometer structures will enhance the effects and in some cases will be the major factor contributing to superhydrophobicity on solid surfaces. Regarding the micrometer and submicrometer structuring, the shape is important; rounded-top protrusions have proved to be more effective than sharp edges, which is also observed in nature.^{15–17}

Remarkable efforts have been made with regard to superhydrophobic surfaces (with low water adhesion) to reduce planktonic bacterial and biofilm formation adhesion. For further information, a recent review was written by Zhang *et al.*⁶ Indeed, air trapped inside the surface structures can limit bacterial adhesion.

Different synthetic techniques have been proposed to obtain fluorescent superhydrophobic surfaces.^{18–22} Although a decade has passed since they were proposed,¹⁸ these techniques have been scarcely investigated; to date, no bacterial interaction on such surfaces has been studied. Previously, we reported the fabrication of superhydrophobic films by an electropolymerization process using various pyrene-based monomers.²³ The monomer Pyrene-F₆, shown in Scheme 1, also proved to be polymerized into a film, PPyrene-F₆, with good stability toward various applied electrochemical parameters (such as the solvent, electrolyte and electrodeposition method).²³ Herein, we compare different 'structured' and 'smooth' polymer films prepared with several pyrene monomers at different electrodeposition conditions. Both Poly-Pyrene (PPyrene) and Poly-Pyrene-F₆ (PPyrene-F₆) have smooth surfaces which do not show superhydrophobicity, unlike micrometer and submicrometer-structured films. Moreover, in comparison with the 'structured' PPyrene films, the 'structured' PPyrene-F₆ films were highly oleophobic. This indicates that the fluorinated moiety present on Pyrene-F₆ is responsible for the oleophobicity of the film, whereas the

micrometer and submicrometer structures are responsible for the superhydrophobic behavior for both fluorinated and non-fluorinated PPyrene films. These superhydrophobic-oleophobic films show interesting fluorescence properties; thus, they are likely to have good resistance against bacterial adhesion.

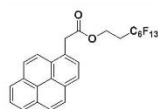
For this reason, in this paper, we demonstrate for the first time the efficacy of PPyrene-F₆, shown in Scheme 1, as a functional surface not only to reduce planktonic bacterial adhesion but also to prevent biofilm attachment on surfaces while providing optical functionality. *S. aureus* and *P. aeruginosa* were chosen as representative bacteria for the present study. Despite all the efforts made to date, there is still no standard methodology to assess the effectiveness of materials against biofilm adhesion on surfaces. Incubation times and bacterial strains differ dramatically from publication to publication. Most previous studies focused on planktonic bacterial adhesion without addressing the study of biofilm attachment. Thus, it is necessary to study not only bacterial adhesion, but also biofilm attachment on these surfaces. In contrast with previous publications,⁶ herein, two different incubation times (2 h and 24 h) and two different bacterial strains (Gram-positive and Gram-negative) are studied.

In addition, the luminescence properties of this surface demonstrate its added value, as they provide a tool to visualize bacteria co-localized at the substructures of the coatings with a multicolor scanning fluorescence microscope. Thorough analysis of images allowed us to obtain a nanometric (microscopic) view of the interaction between these films and bacteria for the first time.

Experimental

Film preparation

The monomer Pyrene-F₆ was synthesized from 1-pyreneacetic acid using a procedure previously reported in the literature.²³ The electropolymerization was carried out using a potentiostat from Metrohm (Autolab). The experiments were performed inside a glass cell, where 10 mL of anhydrous acetonitrile containing 0.1 M tetrabutylammonium perchlorate (Bu₄NClO₄) and 0.01 M Pyrene-F₆ were introduced and degassed with argon. The connection to the potentiostat was performed using a three-electrode system: indium tin oxide (ITO) plate was used as the working electrode (8 cm²), a carbon rod as the counter-electrode, and a saturated calomel electrode (SCE) as the reference electrode. Cyclic voltammetry was chosen as the deposition method because it leads to a highly homogenous film and superhydrophobicity.^{23,24} Two deposition scans were performed between -0.7 V and 1.64 V at a scan rate of 20 mV s⁻¹. After each deposition, the surfaces were washed with acetonitrile and slowly dried. The obtained surfaces are referred to as Poly-Pyrene-F₆ (PPyrene-F₆) films. As previously reported,²³ the polymerization degree of the PPyrene-F₆ films is 1.34. An example of a dimer is given in the inset in Fig. 2.



Scheme 1 Structure of Pyrene-F₆ monomer.

Characterization of PPyrene-F₆ film

Infrared spectra were obtained using a Spectrum Spotlight 300 FT-IR microscope (PerkinElmer) with 4 cm⁻¹ resolution in reflectance mode. The mean surface roughness (R_a) was determined by optical profilometry (Wyko NT 1100 of Bruker) with High Mag Phase Shift Interference (PSI), a 50× objective and a 0.5× field of view. The scanning electron microscopy (SEM) images were obtained with a JEOL 6700F microscope. The surfaces were characterized by apparent contact angle (θ) measurements with a DSA30 goniometer (Krüss). Droplets of 2 μ L were used for the static contact angle measurements, and 6 μ L droplets were used to determine the hysteresis (H) and the sliding angle (α).

Emission and excitation spectra

Spectra were measured on a Fluoromax-4 +Horiba spectrofluorometer. Emission spectra were measured with a 370 nm excitation wavelength using 15° geometry and a band pass of 2.45 nm. Excitation spectra were measured with a 550 nm emission wavelength using slit widths of 3.0 nm.

Bacteria strains

Two collection strains, methicillin-susceptible *S. aureus* (SA) ATCC 27217 and *P. aeruginosa* (PA) ATCC 15442, were maintained at -80 °C in Tryptic Soy Broth (TSB) (bioMérieux, France) containing 20% (vol/vol) glycerol as stock solutions. Before usage, cells were sub-cultured twice in TSB (one 8 h culture, followed by an overnight culture). Bacterial growth and incubation were carried out at 37 °C.

Confocal laser scanning microscopy

Fluorescence images were acquired using a Leica TCS SP5-AOBS confocal laser scanning microscope with a Leica 63× oil immersion objective (HCX Plan APO CS, NA 1.4, pinhole 1 AU). PPyrene-F₆ films and glass and ITO surfaces (as controls) were incubated with the bacterial strains in static mode over 2 h for bacterial adhesion and 24 h for biofilm formation. Prior to observation of 2 h bacterial adhesion on the PPyrene-F₆ film and controls (glass + ITO surfaces), the samples were washed 3 times by full immersion in 150 mM NaCl sterile saline solution to eliminate non-adherent cells. For biofilm formation, the culture medium was gently removed from all surfaces, the surfaces were washed with saline solution to gently eliminate floating cells, and the saline solution was carefully replaced. Prior to each observation, bacteria were stained with 0.4 μ M SYTOX® Red Dead Cell Stain (Life Technologies, France), a nucleic acid stain that easily penetrates cells with compromised plasma membranes (dead cells) only, and 50 μ g mL⁻¹ FM@5-95 dye (Life Technologies, France), which is believed to insert into the outer leaflets of the surface membranes of cells. The FM@5-95 and SYTOX® Red stains were sequentially excited at 488 nm and 633 nm, respectively; meanwhile, the PPyrene-F₆ films were excited at 364 nm (Fig. S1†).

Fluorescence emissions were collected between 700 nm and 800 nm for FM@5-95, between 650 nm and 700 nm for SYTOX® Red, and between 450 nm and 550 nm for the PPyrene-F₆ films. The size of the xy image was 512 × 512 pixels (image size as follows, zoom 1: 246.03 × 246.03 μ m², zoom 3: 82.01 × 82.01 μ m², zoom 5: 49.21 × 49.21 μ m²). Three different areas of each of the three zooms were collected on triplicate samples; thus, a minimum of 9 samples of each zoom was analyzed. Each fluorescence intensity image corresponds to an average of 3 frames. Z-Stacks were recorded using a step of 1 μ m. For the 3D representations of the biofilms, "Icy" and "Image J" software were used.

Image treatment and quantification

A total of 9 samples per zoom were analyzed, and statistical analysis was performed (*i.e.* *F*-test and *t*-test, as shown in Table S1 in the ESI,† in addition to the standard deviation shown in each graph). All calculations were performed with Matlab 2016a (The MathWorks, Natick, USA) using a home-made script. More information about this treatment can be found in the following section.

Bactericidal plating assay

To evaluate the toxicity induced on bacteria by contact with the polymer, the films were incubated with the bacterial strains for 24 h in static mode. Glass surfaces were used as a control. Bacteria deposited on PPyrene-F₆ films were scratched and rinsed with 150 mM NaCl sterile saline solution after incubation.

The solution was centrifuged for 10 min at 7000g at room temperature. The bacterial pellet was suspended in the same sterile saline solution, centrifuged again and suspended under the same conditions. Successive decimal dilutions were performed. Then, 6 drops (10 μ L) of each dilution were deposited on Tryptic Soy Agar (TSA) plates (bioMérieux, France), in triplicate, and incubated for 24 h. CFUs (colony-forming units) were counted for each dilution at each time point. The viable culturable limit of detection was 100 CFU mL⁻¹.

Results and discussion

Surface properties

The surface chemistry was analyzed by FTIR spectroscopy. The spectrum is shown in Fig. 1a. The spectrum shows the characteristic peaks at 1638 cm⁻¹, attributed to the stretching of C=C in the benzene units, and at 1744 cm⁻¹, attributed to the ester groups. Several peaks around 1100 and 1300 cm⁻¹ are also clearly present; these are attributed to the stretching of C-F bonding. The IR spectrum confirms the successful deposition of the monomer Pyrene-F₆ onto the ITO plate.

The SEM image of PPyrene-F₆ is presented in Fig. 1b. The surface morphology consists of spheres of micron size (1 to 2 μ m) with nanostructures in their surface particles. The surface roughness was also evaluated; R_a = 11 μ m, confirming the SEM image results. The combination of micro and nano-

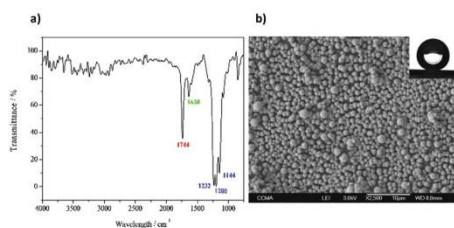


Fig. 1 (a) FTIR spectrum of the PPyrene-F₆ film; (b) SEM image of the PPyrene-F₆ film (right).

structuration with the use of low surface energy compounds, such as the fluorinated chains grafted on the pyrene monomer, provides superhydrophobic behaviour, with an apparent water contact angle $\theta_w = 154^\circ$ and very low water adhesion ($H = 1.3$ and $\alpha = 2.0$). Here, we show that both the surface energy and the surface chemistry have enormous impacts on the superhydrophobicity of the electrodeposited pyrenes. As reported in the literature, by the same electrochemical method, polypyrene without any substituent reached a very high $\theta_w = 152^\circ$; however, it showed sticky properties and non-oleophobic behaviour.²³ In another case, fluorinated indoles were electropolymerized, forming very smooth surfaces ($R_a = 10$ nm) with superhydrophobic behaviour (high θ_w and very low hysteresis); this is due only to the surface chemistry of the fluorinated compounds.²⁵

Many conductive and poorly oxidizable substrates can be used for polymerization, such as gold, platinum, stainless steel, titanium and nickel. In this work, ITO substrates were chosen due to their lower cost in comparison with other substrates as well as their transparency for fluorescence imaging. Additionally, ITO substrates have shown good adherence of polymeric films in wet conditions (ideal for bacterial tests).

The apparent contact angle was also measured for other liquids with lower surface tensions than water (72.8 mN m^{-1}): diiodomethane (50.0 mN m^{-1}) and hexadecane (27.6 mN m^{-1}). Very high oleophobicities were obtained for both liquids: 137.8° for diiodomethane and 107.5° for hexadecane. Due to its superhydrophobic and highly oleophobic properties, it was concluded that the PPyrene-F₆ film is a good candidate for potential application as an inhibitor of bacterial adhesion and biofilm formation.

Photophysical properties

The emission and excitation spectra of the PPyrene-F₆ film are shown in Fig. 2. Compared to the pyrene monomer in solution (343 nm–3.62 eV),²³ the excitation spectrum of the PPyrene-F₆ film shows a broad band with a maximum around 390 nm (3.2 eV) without any monomer contribution. Compared to the literature,²² this excitation spectrum is intense and well-defined. The red-shift of the excitation band from the monomer to the oligomer may be due to an increase in the

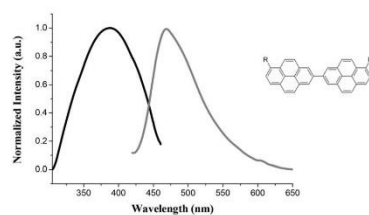


Fig. 2 Emission (black line, $\lambda_{em} = 465$ nm) and excitation (grey line, $\lambda_{ex} = 370$ nm) spectra of the PPyrene-F₆ film (normalization to 1 at the maximum intensity of each spectrum). Inset: Scheme of the pyrene dimer.

conjugated chain length;²² however, for PPyrene-F₆, the oligomerization appears to be limited (average repeating number: 1.34 units).²³ Thus, this red-shift is likely due to aggregates. The band position is at a lower energy than those of modified polypyrenes, such as polyacrylate pyrene²⁶ or water-soluble cationic olipopyrene.²⁷ It lies at a higher energy than polypyrene (band maximum at 2.76 to 2.95 eV).²² According to the onsets of the absorption curves, the band gap E_g ($E_g = 1241/\lambda_{onset}$) of PPyrene-F₆ was calculated to be 2.61 eV. This value falls between those of other reported pyrene oligomers (namely polyacrylate pyrene, $E_g = 2.82$ eV, and cationic olipopyrene, $E_g = 2.38$ eV).

The PPyrene-F₆ film shows broad fluorescence (full width at half maximum – FWHM): 7264 cm^{-1} in excitation and 3241 cm^{-1} in emission, respectively, which is in good agreement with previous studies.²³ The relatively large value of FWHM in the excitation spectrum is consistent with the presence of oligomers in the films and aggregates. The position and shape of the emission band suggest not only the presence of a conjugated backbone structure but also the presence of excimers (470 nm–2.64 eV). This is consistent with oligomer aggregation due to intermolecular π - π stacking interactions, leading to excimer-like emission within the solid film.²²

Fluorescence imaging

A major advantage of the PPyrene-F₆ film is control of the surface conditions by fluorescence imaging, as we previously reported.²³ As shown in Fig. 3a, the micro and sub-microstructures, thickness and homogeneity of the films can be easily and rapidly evaluated by optical imaging (~ 20 s per image, < 5 min per stack). The luminescence favors the morphological evaluation and provides an easier, faster and less expensive method to characterize structured surfaces, providing a reliable technique to evaluate the stability and homogeneity of the film with time. The use of fluorescence imaging to control the morphology of the film can avoid the use of common characterization techniques such as electron microscopies, which are comparatively more expensive, tedious and time-consuming with regard to the preparation of biological samples. As can be observed from the orthogonal images

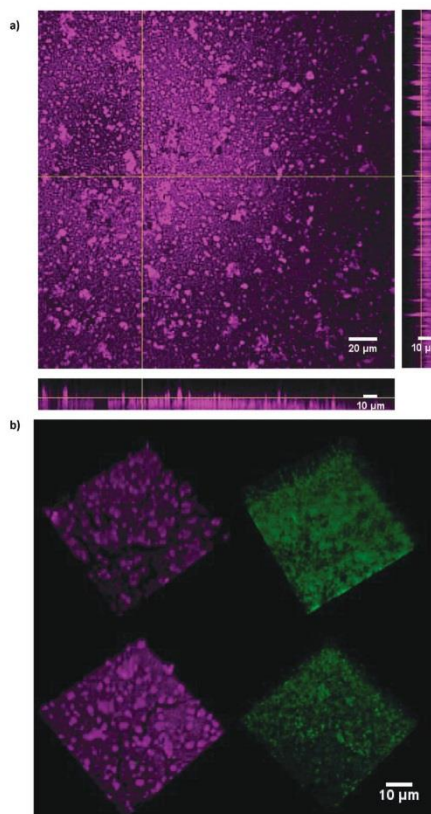


Fig. 3 (a) Fluorescence imaging of the PPyrène-F₆ film (magenta channel, λ_{exc} : 364 nm, λ_{em} : 450 to 550 nm). (b) 3D reconstruction of the fluorescence images of PPyrène-F₆ and control (glass) after 24 h incubation (*P. aeruginosa* PA 15442 upper panels, *S. aureus* SA 27217 bottom panels, zoom 5). Control (no fluorescence), PPyrène-F₆ (magenta channel), bacteria tagged with FM5-95 (green channel). The surrounding medium is an aqueous saline (150 mM) solution.

(Fig. 3a), the density, homogeneity or heterogeneity of the surface can be easily visualized by fluorescence imaging. Additionally, the microstructures can be easily observed. It is also possible to observe that the surface coverage is not homogeneous from one sample to another. Some holes or cracks can be observed prior to any biological studies. However, the stability of the surface over time and in biological culture medium or water is good (no deposition of culture medium was observed during the incubation times). In addition, with the use of fluorescence microscopy techniques, the mechanisms of anti-adhesion on luminescent

superhydrophobic surfaces can be more readily studied, providing real-time control and colocalization of bacteria on the surfaces (Fig. 3b).

Strength by image analysis

The mixture of multiple emitting species increased the difficulty of the image analysis. As shown in Fig. 1S,† there were three different emitting species in the system: the surface emission and two different dyes. Although filters are used to acquire each channel, some non-desired emission can “contaminate” the information. Additionally, the superhydrophobicity of the films resulted in a lack of water and affected the reflection index within the focal plane. To reduce this effect (produced by the nature of the film), the images were acquired in bidirectional scanning mode (which results in a more blurry image).

In order to improve quantification, a home-made script was developed. Additionally, it was helpful to exclude the bacteria growing inside the cracks to more accurately quantify the bacteria growing on the surface.

To determine the amount of bacteria that grow on the film after treatment, the analysis consisted of three steps. The first step is an intensity thresholding step on the channel of the bacteria to remove the signal from the dyes that did not stain within the bacteria. This thresholding step was performed by applying an iterative Isodata threshold.²⁹ In short, the image is initially divided into background and bacteria by applying a threshold based on the gray-level histogram. The mean of these two subsets is calculated to determine the threshold (see eqn (1)) for the next iteration. This procedure is continued until the thresholded image remains constant.

$$\text{Threshold} = \frac{av_{obj} + av_{bg}}{2} \quad (1)$$

in which av_{obj} is the mean of the object subset and av_{bg} is the mean of the background subset.

Once the threshold is applied to the bacteria channel, a mask is created based on the channel of the film (Fig. 4a). The goal of this mask is to divide the pixels into a zone where the film is present and another zone where the cracks in the film can be noted to take into account only the film area for precise determination of the efficiency of the film. A first consideration for this step is that this channel can suffer from uneven illumination; however, to counter this effect, the image can optionally be subdivided into ‘light’ and ‘darker’ zones. If this step is ignored, the mask will overestimate the amount of cracks in the film. The threshold for the mask is then set manually, but is easily determined (Fig. 4b). To avoid the consideration of single pixels as cracks in the film, an automatic selection step is added to remove them from the mask (Fig. 4c). Additionally, another consideration is that the point spread function (PSF) of the instrument should be taken into account (when using zoom 3 and zoom 5, the pixels are smaller than the PSF) by dilating the mask accordingly (Fig. 4d).

The third step of the procedure then consists of multiplying the colorant-free bacteria channel by the final mask obtained

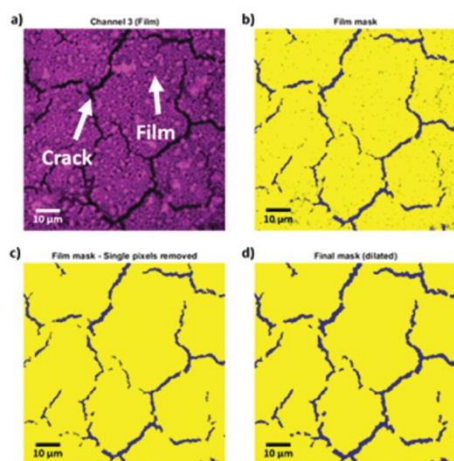


Fig. 4 Example of creating a mask. (a) The raw image obtained for the channel of the film (zoom 3); (b) the initial mask obtained after threshold selection; (c) mask in which single pixels considered as cracks are removed (automatic selection procedure); and (d) dilation of the mask to take into account the pixel size and the PSF.

in the previous step and determining the percentage of bacteria growing on the film (Fig. 5). For the control samples, additional care must be taken concerning the thresholding step on the bacteria channel. As bacteria are growing everywhere, the iterative Isodata threshold algorithm also removes contributions from the bacteria themselves (*i.e.* the threshold is too high). To accurately determine the coverage of the bacterial growth in the sample (most importantly on blurry images), the thresholding step is performed manually by taking care to not introduce structures in the residuals (*i.e.* the signal that is being removed). As shown in Fig. 6, if the threshold is low, too few pixels are removed from consideration and the result will be too high. If the threshold is high,

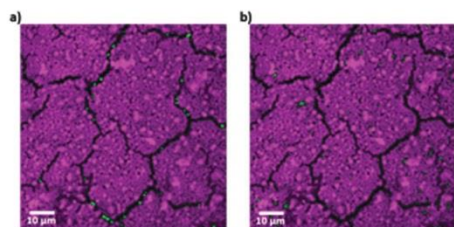


Fig. 5 Mask application on the bacteria, dividing the image into (a) bacteria located in the cracks of the film (0.61%) and (b) bacteria located on the film (0.84%).

bacterial structures will be present in the residuals and the result will be too low. Using an adequate threshold is thus important not only to have no structures in the residuals but also to remove contributions not coming from bacteria.

Reduction of bacterial and biofilm adhesion

By taking advantage of the fluorescence and superhydrophobic properties of the PPyrene-F₆ film, bacterial interaction tests were performed under two different conditions. First, bacterial adhesion on the PPyrene-F₆ film was tested by static incubation of two bacterial strains (*S. aureus* and *P. aeruginosa*) for 2 h. After the incubation time, the culture medium was replaced by 150 mM NaCl saline solution. Immediately after, each sample was washed three times with the same saline solution and stained with SYTOX® Red and FM@5-95 dyes prior to observation. Images were taken and processed as described in the Experimental section. The quantitative results presented in this section correspond to zooms 1, 3 and 5; however, the discussion is focused on zoom 1, which represents a larger area of analysis and avoids the bias that can be introduced by selecting specific areas, such as zooms 3 and 5. Glass and ITO surfaces were used as controls; the ITO percentage of coverage in comparison with the PPyrene-F₆ film can be found in the ESI (Fig. S2, S3 and S4†).

As shown in (Fig. 7), for *S. aureus*, the percentages of coverage after 2 hours are 6.50% for the glass surface (control) and 2.21% for the PPyrene-F₆ film, on which the bacterial adhesion is reduced by 3 times. For *P. aeruginosa*, the percentages of coverage are 24.75% for the glass surface (control) and 7.69% for the PPyrene-F₆ film, on which the bacterial adhesion is also reduced by 3 times. These results show a significant reduction in bacterial adhesion on the PPyrene-F₆ film.

The second part of the test focused on biofilm formation on the PPyrene-F₆ film by static incubation of the bacterial strains (*S. aureus* and *P. aeruginosa*) for 24 h. Similar conditions to those of the 2 h bacterial adhesion study were used prior to observation. However, the samples were gently washed with the same saline solution to avoid damage of any biofilm attached on the surface and stained with SYTOX® Red and FM@5-95 dyes prior to observation.

As shown in (Fig. 7), for *S. aureus*, the percentages of coverage are ~90% for the glass surface (control) and 4.2% for the PPyrene-F₆ film, which prevented biofilm formation. For *P. aeruginosa*, the percentage of coverage was ~90% for the glass surface, showing almost ten times less bacterial coverage and, thus, biofilm formation.

To summarize, the bacterial adhesion on the PPyrene-F₆ surface decreased by about 65% (for both strains, *P. aeruginosa* and *S. aureus*); these repellent efficiency effects are comparable to those of previously reported non-luminescent superhydrophobic surfaces, where the decreases in bacterial adhesion were between 50% and 90%.^{30,31} As mentioned before, there is no standard methodology to assess bacterial interactions on surfaces, and very few data on biofilm attachment can be found³¹ (studies longer than 14 hours of incubation). Herein, although bacterial adhesion was not completely avoided over

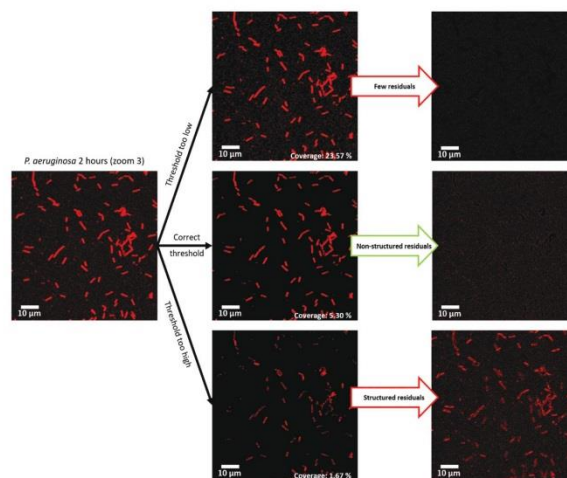


Fig. 6 Thresholding step for control samples (as shown on a control sample for *P. aeruginosa* after 2 hours, zoom 3).

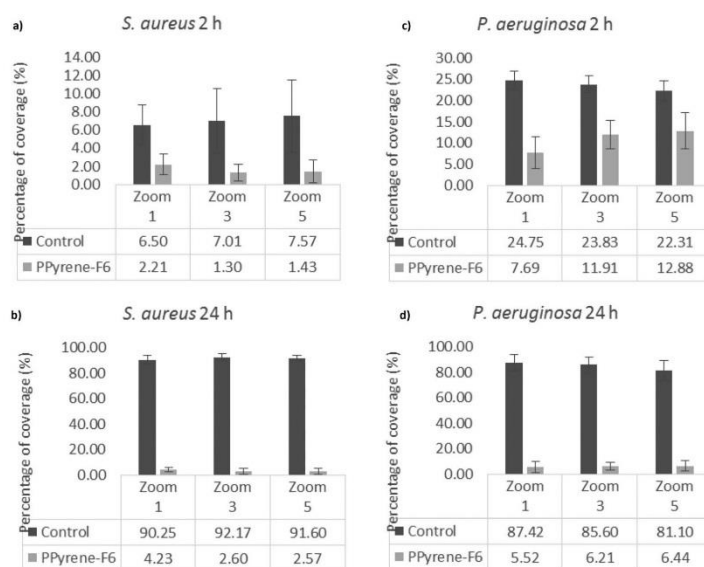


Fig. 7 Average percentage of coverage (%) of control (grey columns) and PPyrene-F₆ (dark grey columns) after (a) 2 h adhesion and (b) 24 h incubation with *S. aureus* (SA ATCC 27217); after (c) 2 h adhesion and (d) 24 h incubation with *P. aeruginosa* (PA ATCC 15442). Error bars represent the standard deviation.

2 h, biofilm attachment on the surfaces was totally prevented by decreasing the percentage of coverage of bacteria on PPyrene-F₆ films by 90% (both strains, *P. aeruginosa* and *S. aureus*), demonstrating the capability of highly efficient prevention of biofilm attachment on the film. We demonstrated that even if bacterial adhesion is not completely avoided, it does not necessarily lead to biofilm formation on the surface of the film, which is in good agreement with Cerca *et al.*³²

Biofilm formation, as mentioned previously, is considered to be a major hazard because it (i) is irreversible; (ii) promotes

further infections by the detachment of new bacteria that are capable of spreading and continuing the colonization cycle.³ These results show the promising potential of electrodeposited fluorescent and superhydrophobic polymers to prevent biofilm formation and attachment on surfaces. The ratio between the covering area of each dye (SYTOX® Red/FM@5-95) was used to evaluate the toxicity that might be induced by the PPyrene-F₆ film. For all samples (including controls), most of the bacteria were viable, and less than 0.5% of dead bacteria was found; this suggests the non-toxicity of the PPyrene-F₆ film during the

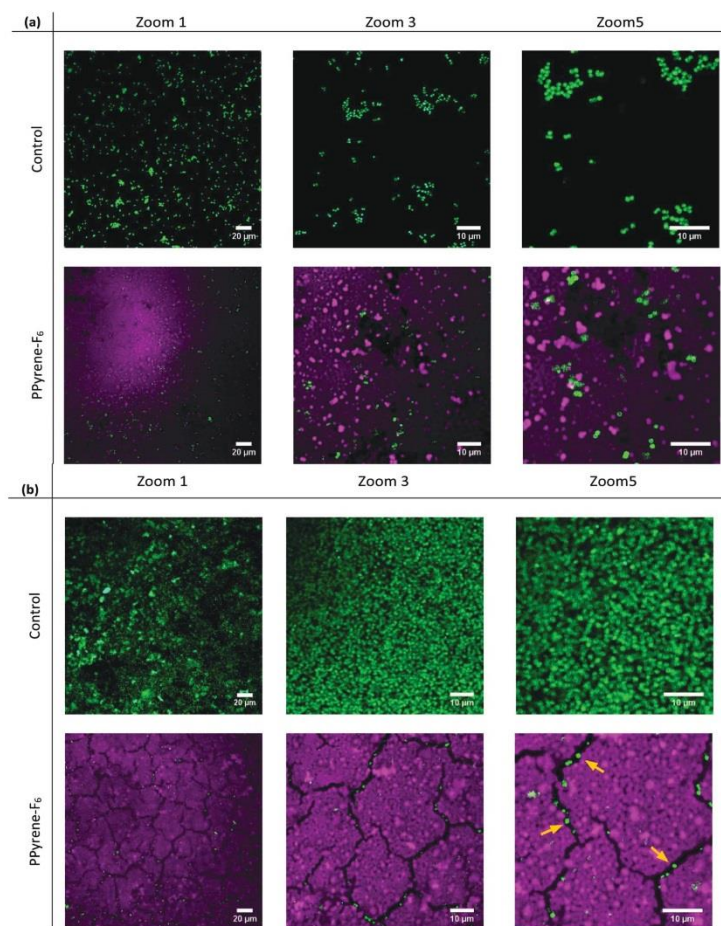


Fig. 8 Fluorescence imaging of control (upper panels) and PPyrene-F₆ (bottom panels, magenta channel), FM5-95 (green channel) and Sytox red (Cyan channel) after (a) 2 h adhesion and (b) 24 h incubation of *S. aureus* (SA ATCC 27217). The surrounding medium is an aqueous saline (150 mM) solution. From left to right: Zooms 1, 3 and 5.

incubation time as well as those of the control substrates (glass and ITO).

Bacterial distribution on films

Remarkable efforts have been made to reduce planktonic bacteria and biofilm adhesion on superhydrophobic surfaces. Many different techniques of surface preparation and multiple bacterial strains have been studied in recent years. In 2011, Fadeeva *et al.*³¹ observed that *P. aeruginosa* was not able to colonize superhydrophobic titanium surfaces; meanwhile,

S. aureus could colonize the same surfaces. This study suggested that the ability to colonize superhydrophobic surfaces is dependent on the shape of the bacteria; however, this assumption cannot be generalized, as has been proven by other studies^{28,33} as well as the present work. Indeed, it was shown that some surfaces are effective independently of the shape of the bacteria (*bacillus* or *coccus*).

Herein, in addition to quantifying the bacterial percentage of coverage, we analyzed the bacterial distribution on the surfaces. Indeed, many studies are based on CFU counts of

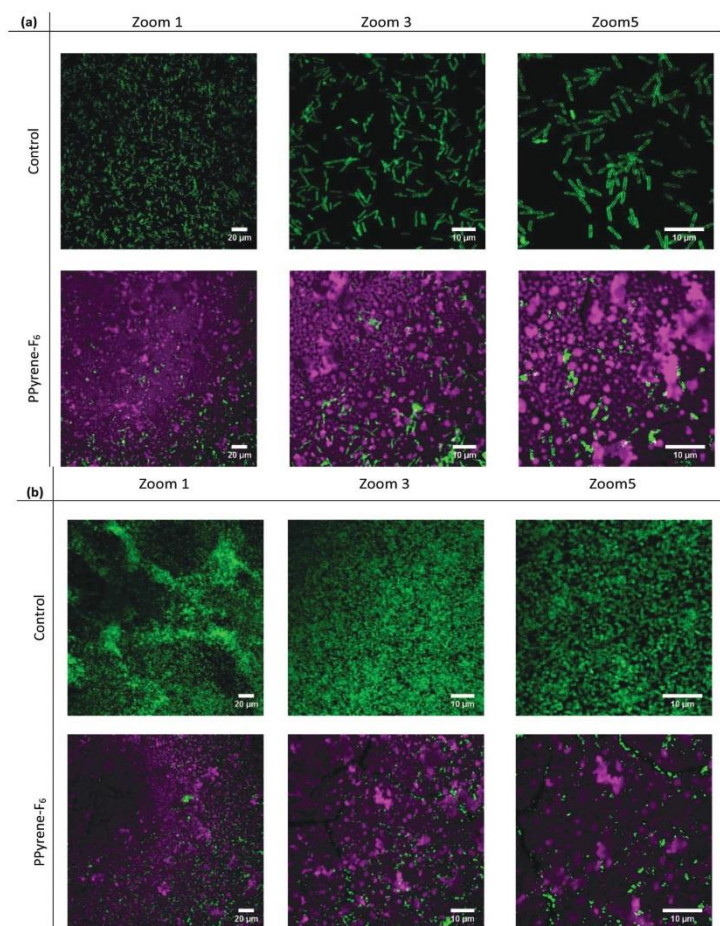


Fig. 9 Fluorescence imaging of control (upper panels) and PPyrene-F₆ (bottom panels, magenta channel), FM@5-95 (green channel) and Sytox red@ (Cyan channel) after (a) 2 h adherence and (b) 24 h incubation of *P. aeruginosa* (PA ATCC 15442). The surrounding medium is an aqueous NaCl (150 mM) solution. From left to right: Zooms 1, 3 and 5.

adhered bacteria without considering bacterial adhesion distribution on the surfaces, which can give insights on the attachment of planktonic bacteria on their surfaces. As we can observe in Fig. 8 and 9, after 2 h bacterial adhesion and 24 h biofilm formation with both bacterial strains (*S. aureus* and *P. aeruginosa*), bacterial distribution on the PPyrene-F₆ film can be observed. Bacteria adhere on specific zones of the surface and only where the superhydrophobic film coverage is not complete (preferentially in the surface defects). It was impossible to find any colonies where micro/nanostructures were present. Where PPyrene-F₆ structures stand, no bacteria can be co-localized, indicating the repellent efficiency of the material. For example, Fig. 8b (bottom right panel) shows that bacteria only can follow the pattern of the cracks when they are present in the micro/nanostructures of the PPyrene-F₆ film, which remained stable even after the 24 h incubation test (no conditioning film was observed). Another example can be observed in the Z-stacking images in Fig. 10; after 24 h incubation with *S. aureus*, only a single colony successfully attached to a hole on the surface. Unless a hole on the surface is large enough, bacterial colony attachment is inhibited on the PPyrene-F₆ surface. This is in good agreement with the bacterial distribution, which is governed by the homogeneity and density of micro/nanostructures on the films.³⁰

It has been suggested that the loss of trapped air contributes to bacterial adhesion over time;³⁴ furthermore, it was shown that bacterial adhesion on superhydrophobic surfaces is dependent on the density of the nanostructures on the topography,³⁵ even in completely wet conditions where there is no trapped air. These results prove the efficacy of superhydrophobic coatings in reducing planktonic bacteria and biofilm adhesion with proper design of the topography at nanoscale dimensions. These surfaces can prevent biofilm attachment even under submerged conditions. Biofilms are known to be 3D bacterial structures,³⁶ as can be observed in Fig. 3b (control

– right panels). In comparison, the complete prevention of biofilm attachment on the PPyrene-F₆ film was further demonstrated by the 3D reconstruction of Z-stacking after 24 hours of incubation with both bacterial strains in Fig. 3 (left panels). It was almost impossible to detect even a single colony that could remain in direct contact with the film.

Truong *et al.*³⁴ observed the distribution of different bacterial strains on superhydrophobic titanium surfaces by SEM; they found that the upper regions of the surfaces were not covered as much by bacteria as the crevices between the upper regions, which were more populated. In addition to the screening of bacterial distribution, imaging techniques can provide quantification of the planktonic bacterial percentage of coverage and, more importantly, powerful imaging of surfaces can reveal whether biofilms can adhere. Truong *et al.*³⁴ proposed a mechanism of adhesion where bacterial cells accumulate at the tri-phase interface on immersed superhydrophobic titanium surfaces. Hence, the capability of superhydrophobic surfaces to reduce bacterial adhesion can decrease over time (already 24 h) after trapped air is completely excluded. However, Ma *et al.*³⁵ compared the adhesion of bacteria (*P. aeruginosa*) and non-biological adhesion under partially and completely wetted conditions on superhydrophobic taro leaves (*Colocasia esculenta*). It was found that the adhesion was dependent on the density of the nanosized surface features.

These findings demonstrate for the first time the great potential of the dual-functionality of fluorescent and superhydrophobic polymeric films on the prevention of *S. aureus* and *P. aeruginosa* biofilm adhesion. The use of materials with low surface energy combined with high oleophobicity and micro/nanostructures inhibit bacterial contact and thus adhesion, consequently impeding aggregation of bacteria and biofilm formation on the surface even in the initial state. These findings are in good agreement with the literature.³⁷

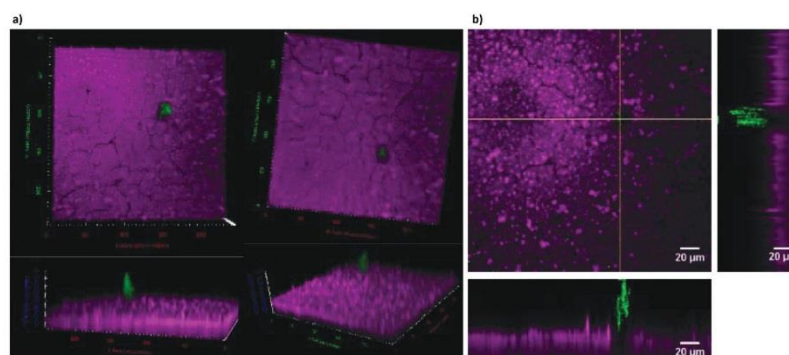


Fig. 10 Fluorescence imaging of (a) a 3D reconstruction of PPyrene-F₆ and (b) an orthogonal view of Z-stacking after 24 h incubation with *S. aureus* (SA ATCC 27217, zoom 1). PPyrene-F₆ (magenta channel); bacteria tagged with FM@5-95 (green channel). The surrounding medium is an aqueous saline solution (150 mM).

For further applications, mechanical stability can be achieved by different techniques without modifying the superhydrophobicity, for example by adding a sub-layer to enhance the anchorage of the polymer to the substrate. A remarkable study was presented by Xu and colleagues,²² demonstrating a large-scalable fabrication of fluorescent superhydrophobic coatings by electropolymerization of polypyrene; however, no biological studies have been performed.

Bactericidal plating assay

One limitation of bacterial staining with fluorescent dyes to determine the toxicity of antimicrobial compounds or surfaces is that the labelled damaged cells are not necessarily dead. Indeed, stains such as SYTOX® Red can penetrate the cells as soon as their membranes are compromised. Moreover, some bacterial populations can exhibit membrane damage but are still able to grow.³⁸ To complete these experiments, the possible cytotoxicity induced by the PPyrene-F₆ film was assessed using CFU counting after 24 h incubation of both bacterial strains (*S. aureus* and *P. aeruginosa*) on the films. As shown in Fig. S5 and Table S2,† an insignificant decrease of CFU mL⁻¹ is induced compared to glass surfaces (as a control). In conjunction with the live/dead tests performed with fluorescence images, by focusing on 24 h tests in which the samples are gently washed without removing the biofilm as in the 2 h adhesion tests, it can be concluded that the PPyrene-F₆ film is non-toxic to bacteria during these incubation times, and the reduced adhesion is due to the superhydrophobicity of the surface.

Our main objective in performing the bactericidal plating assay was to determine whether the bacteria were failing to attach to the surface due to its toxicity or whether they were being repelled. In order to implement these films in real-life applications, such as medical devices or implants, further investigations must be carried out involving eukaryotic cells to determine the cytotoxicity and mutagenesis of the films.

Conclusions

We demonstrated that fluorescent electrodeposited polymers are promising materials as micro/nanostructured coatings that can be readily prepared at low cost and with large scalable fabrication. For the first time, we demonstrated the potential of superhydrophobic fluorinated pyrene oligomer films to serve as coatings to prevent biofilm attachment, studying two different pathogenic bacterial strains (Gram-positive and Gram-negative) at two different incubation times (2 h adhesion and 24 h biofilm formation). The PPyrene-F₆ film was proved to reduce planktonic bacterial adhesion by 65% (in both strains, *P. aeruginosa* and *S. aureus*) and to be highly effective in preventing biofilm attachment on the surface by reducing the percentage of coverage of bacteria on the PPyrene-F₆ film by 90% (on both strains, *P. aeruginosa* and *S. aureus*). Moreover, the PPyrene-F₆ film provides a facile method to characterize the surface, observe the bacterial distribution and

quantify the bacterial percentage of coverage by fluorescence imaging. Furthermore, these films did not show significant bacterial toxicity towards *P. aeruginosa* or *S. aureus* during the studied incubation times. We strongly believe that the high density of micro/nanostructures and the high oleophobicity of the PPyrene-F₆ film are the main features enabling the inhibition of biofilm adhesion on the surface for both pathogenic bacterial strains. With this study, we wish to encourage further investigation, and we strongly believe that these multifunctional coatings (luminescent and superhydrophobic) have promising potential in further applications.

In addition to the biological studies, we successfully developed a home-made script that enabled us to treat and quantify the images in a completely adapted way by considering biological insights and removing external contributions of other fluorophores in difficult systems.

Conflicts of interest

There are no conflicts to declare.

Acknowledgements

This work has been supported by the Region Ile-de-France in the framework of DIM Nano-K; by LabEx CHARMMAT; by fédération Lumière Matière (LUMAT FR2764) and by CNPq, Conselho Nacional de Desenvolvimento Científico e Tecnológico – Brazil (Processo No. 202280/2014-4). This work was supported by a grant from the Ministère de l'Éducation Nationale, de l'Enseignement Supérieur et de la Recherche, Université Paris-Sud Paris-Saclay, for Gabriela Moran's Ph.D. thesis (ED 2MIB No. 571).

We thank the Centre de Photonique Biomédicale (CPBM) of the Centre Laser de l'Université Paris-Sud (CLUPS/LUMAT FR2764, Orsay, France) for allowing us to use the confocal microscope and L2 microbiology facilities; Gilles Clavier and Arnaud Brosseau for allowing us to measure the fluorescence lifetime at Ecole Normale Supérieure Paris Saclay; and Karine Steenkeste for fruitful discussions.

References

- 1 C. L. Ventola, The antibiotic resistance crisis: part 1: causes and threats, *Pharm. Ther.*, 2015, **40**, 277–283.
- 2 R. D. Wolcott and G. D. Ehrlich, Biofilms and Chronic Infections, *J. Am. Med. Assoc.*, 2008, **299**, 2682–2684.
- 3 F. Sun, F. Qu, Y. Ling, P. Mao, P. Xia, H. Chen and D. Zhou, Biofilm-associated infections: antibiotic resistance and novel therapeutic strategies, *Future Microbiol.*, 2013, **8**, 877–886.
- 4 J. W. Costerton, P. S. Stewart and E. P. Greenberg, Science, Bacterial Biofilms: A Common Cause of Persistent Infections, *Science*, 1999, **284**, 1318–1322.

- 5 World Health Organization, *Global priority list of antibiotic-resistant bacteria to guide research, discovery, and development of new antibiotics*, 2017 <http://www.who.int/medicines/publications/global-priority-list-antibiotic-resistant-bacteria/en/> accessed March 02, 2017.
- 6 X. Zhang, L. Wang and E. Levanen, Superhydrophobic surfaces for the reduction of bacterial adhesion, *RSC Adv.*, 2013, **3**, 12003–12020.
- 7 S. Roy and P. Prasanta, Antibacterial hydrogels of amino acid-based cationic amphiphiles, *Biotechnol. Bioeng.*, 2008, **100**, 756–764.
- 8 D. Salick, J. Kretsinger, D. Pochan and J. Schneider, Inherent Antibacterial Activity of a Peptide-Based β -Hairpin Hydrogel, *J. Am. Chem. Soc.*, 2007, **129**(47), 14793–14799.
- 9 J. S. Price, A. F. Tencer, D. M. Arm and G. A. Bohach, Controlled release of antibiotics from coated orthopedic implants, *J. Biomed. Mater. Res.*, 1996, **30**, 281–286.
- 10 M. Tischer, G. Pradel, K. Ohlsen and U. Holzgrabe, Quaternary ammonium salts and their antimicrobial potential: targets or nonspecific interactions?, *ChemMedChem*, 2012, **7**, 22–31.
- 11 K. Poole, Mechanisms of bacterial biocide and antibiotic resistance, *J. Appl. Microbiol.*, 2002, **92**, 55S–64S.
- 12 T. Darmanin and F. Guittard, Superhydrophobic and superoleophobic properties in nature, *Mater. Today*, 2015, **18**, 273–285.
- 13 A. B. D. Cassie and S. Baxter, Wettability of porous surfaces, *Trans. Faraday Soc.*, 1944, **40**, 546–551.
- 14 M. Cao, D. Guo, C. Yu, K. Li, M. Liu and L. Jiang, Water-Repellent Properties of Superhydrophobic and Lubricant-Infused “Slippery” Surfaces: A Brief Study on the Functions and Applications, *ACS Appl. Mater. Interfaces*, 2016, **8**, 3615–3623.
- 15 A. Marmur, Superhydrophobic and superoleophobic surfaces: from understanding non-wettability to design considerations, *Soft Matter*, 2013, **9**, 7900–7904.
- 16 E. Bittoun and A. Marmur, The Role of Multiscale Roughness in the Lotus Effect: Is It Essential for Superhydrophobicity?, *Langmuir*, 2012, **28**, 13933–13942.
- 17 E. Bittoun and A. Marmur, Optimizing Super-Hydrophobic Surfaces: Criteria for Comparison of Surface Topographies, *J. Adhes. Sci. Technol.*, 2009, **23**, 401–411.
- 18 J. Hong, W. Bae, H. Lee, S. Oh, K. Char, F. Caruso and J. Cho, Tunable Superhydrophobic and Optical Properties of Colloidal Films Coated with Block-Copolymer-Micelles/Micelle-Multilayers, *Adv. Mater.*, 2007, **19**, 4364–4369.
- 19 J. Chang, L. Zang, C. Wang, L. Sun and Q. Chang, Raspberry-like PS/CdTe/Silica Microspheres for Fluorescent Superhydrophobic Materials, *Nanoscale Res. Lett.*, 2016, **11**(114), 3–117.
- 20 X. Shi, R. Dou, T. Ma, W. Liu, X. Lu, K. J. Shea, Y. Song and L. Jiang, Bioinspired Lotus-like Self-Illuminous Coating, *ACS Appl. Mater. Interfaces*, 2015, **7**, 18424–18428.
- 21 R. de Francisco, M. Hoyos, N. García and P. Tiemblo, Superhydrophobic and Highly Luminescent Polyfluorene/Silica Hybrid Coatings Deposited onto Glass and Cellulose-Based Substrates, *Langmuir*, 2015, **31**, 3718–3726.
- 22 L. Xu, F. Tong, X. Lu, K. Lu and Q. Lu, Multifunctional polypyrrene/silica hybrid coatings with stable excimer fluorescence and robust superhydrophobicity derived from electrodeposited polypyrrene films, *J. Mater. Chem. C*, 2015, **3**, 2086–2092.
- 23 G. Ramos Chagas, X. Xie, T. Darmanin, K. Steenkeste, A. Gaucher, D. Prim, R. Méallet-Renault, G. Godeau, S. Amigoni and F. Guittard, Electrodeposition of Polypyrrenes with Tunable Hydrophobicity, Water Adhesion, and Fluorescence Properties, *J. Phys. Chem. C*, 2016, **120**, 7077–7087.
- 24 G. Ramos Chagas, T. Darmanin, G. Godeau, S. Amigoni and F. Guittard, Superhydrophobic properties of electrodeposited fluorinated polypyrrenes, *J. Fluorine Chem.*, 2017, **193**, 73–81.
- 25 G. Ramos Chagas, T. Darmanin and F. Guittard, Nanostructured superhydrophobic films synthesized by electrodeposition of fluorinated polyindoles, *Beilstein J. Nanotechnol.*, 2015, **6**, 2078–2087.
- 26 L. Qin, B. Lu, J. Xu, G. Zhang and S. Zhang, Novel functionalized conjugated polypyrrene with polyacrylate: synthesis, electrochemistry, luminescence, and chemical sensing properties, *RSC Adv.*, 2014, **4**, 28368–28376.
- 27 Y. Gao, H. Bai and G. Shi, Electrosynthesis of oligo(methoxyl pyrene) for turn-on fluorescence detection of volatile aromatic compounds, *J. Mater. Chem.*, 2010, **20**, 2993–2998.
- 28 B. J. Privett, J. Youn, S. A. Hong, J. Lee, J. Han, J. H. Shin and M. H. Schoenfish, Antibacterial Fluorinated Silica Colloid Superhydrophobic Surfaces, *Langmuir*, 2011, **27**, 9597–9601.
- 29 T. W. Ridler and S. Calvard, Picture Thresholding Using an Iterative Selection Method, *IEEE Trans. Syst. Man Cybern. B Cybern.*, 1978, **8**, 630–632.
- 30 P. Tang, W. Zhang, Y. Wang, B. Zhang, H. Wang, C. Lin and L. Zhang, Effect of superhydrophobic surface of titanium on *Staphylococcus aureus* adhesion, *J. Nanomater.*, 2011, **2011**, 8.
- 31 E. Fadeeva, V. K. Truong, M. Stiesch, B. N. Chichkov, R. J. Crawford, J. Wang and E. P. Ivanova, Bacterial Retention on Superhydrophobic Titanium Surfaces Fabricated by Femtosecond Laser Ablation, *Langmuir*, 2011, **27**, 3012–3019.
- 32 N. Cerca, G. B. Pier, M. Vilanova, R. Oliveira and J. Azeredo, Quantitative analysis of adhesion and biofilm formation on hydrophilic and hydrophobic surfaces of clinical isolates of *Staphylococcus epidermidis*, *Res. Microbiol.*, 2005, **156**, 506–514.
- 33 A. K. Epstein, T.-S. Wong, R. A. Belisle, E. M. Boggs and J. Aizenberg, Liquid-infused structured surfaces with exceptional anti-biofouling performance, *Proc. Natl. Acad. Sci. U. S. A.*, 2012, **109**, 13182–13187.
- 34 V. K. Truong, H. K. Webb, E. Fadeeva, B. N. Chichkov, A. H. Wu, R. Lamb, J. Y. Wang, R. J. Crawford and E. P. Ivanova, Air-directed attachment of coccoid bacteria to

- the surface of superhydrophobic lotus-like titanium, *Biofouling*, 2012, **28**, 539–550.
- 35 J. Ma, Y. Sun, K. Gleichauf, J. Lou and Q. Li, Nanostructure on Taro Leaves Resists Fouling by Colloids and Bacteria under Submerged Conditions, *Langmuir*, 2011, **27**, 10035–10040.
- 36 J. J. Harrison, H. Ceri, J. Yerly, C. A. Stremick, Y. Hu, R. Martinuzzi and R. J. Turner, The use of microscopy and three-dimensional visualization to evaluate the structure of microbial biofilms cultivated in the Calgary Biofilm Device, *Biol. Proced. Online*, 2006, **8**, 194–215.
- 37 S. Pechook, K. Sudakov, I. Polishchuk, I. Ostrov, V. Zakin, B. Pokroy and M. Shemesh, Bioinspired passive anti-biofouling surfaces preventing biofilm formation, *J. Mater. Chem. B*, 2015, **3**, 1371–1378.
- 38 L. Li, N. Mendis, H. Trigui, J. D. Oliver and S. P. Faucher, The importance of the viable but non-culturable state in human bacterial pathogens, *Front. Microbiol.*, 2014, **5**, 258.

Supplementary Information

Superhydrophobic polypyrene films to prevent *Staphylococcus aureus* and *Pseudomonas aeruginosa* biofilm adhesion on surfaces: high efficiency deciphered by fluorescence microscopy.

G. Morán,^a G. Ramos Chagas,^b S. Hugelier,^c X. Xie,^a R. Boudjemaa,^a C. Ruckebusch,^c M. Sliwa,^c T. Darmanin,^b A. Gaucher,^c D. Prim,^d G. Godeau,^b S. Amigoni,^b F. Guittard,^b R. Méallet-Renault,^{a*}

^a Institut des Sciences Moléculaires d'Orsay (ISMO), CNRS, Univ. Paris-Sud, Univ. Paris-Saclay, F-91405 Orsay, France

^b Univ. Côte d'Azur, NICE Lab, IMREDD, 61-63 Av. Simon Veil, 06200 Nice, France

^c Univ. Lille, CNRS, UMR 8516 - Unité LASIR, F-59000 Lille, France

^d Univ. de Versailles St-Quentin, UMR CNRS 8180, Institut Lavoisier de Versailles, 45, avenue des Etats-Unis, 78035 Versailles Cedex, France

*rachel.meallet-renault@u-psud.fr

F-test: difference between the variance of the two populations (important for the t-test)

T-test: difference between the mean of the two populations

<i>S. aureus</i> 2 h				
		Zoom 1	Zoom 3	Zoom 5
F-test ($\alpha = 0,025$)	F_{crit}	5.599623005	4.899340648	4.433259889
	F_{stat}	3.776097	14.10050694	9.214867557
	Conclusion	same	different	different
t-test ($\alpha = 0,025$)	t_{crit} (one-tail)	2.144786688	2.262157163	2.228138852
	t_{crit} (two-tail)	2.509569411	2.685010847	2.633766916
	T_{stat}	4.625246815	4.63701818	4.407182468
	Conclusion	different	different	different
<i>S. aureus</i> 24 h				
		Zoom 1	Zoom 3	Zoom 5
F-test ($\alpha = 0,025$)	F_{crit}	5.599623005	4.433259889	4.528562147
	F_{stat}	3.141930356	1.281203399	1.41296955
	Conclusion	same	same	same
t-test ($\alpha = 0,025$)	t_{crit} (one-tail)	2.144786688	2.119905299	2.131449546
	t_{crit} (two-tail)	2.509569411	2.472878322	2.489879703
	T_{stat}	60.73439936	78.60281736	-86.74658305
	Conclusion	different	different	different
<i>P. aeruginosa</i> 2 h				
		Zoom 1	Zoom 3	Zoom 5
F-test ($\alpha = 0,025$)	F_{crit}	4.528562147	4.433259889	4.528562147
	F_{stat}	3.108860472	2.782954339	3.471701199
	Conclusion	same	same	same
t-test ($\alpha = 0,025$)	t_{crit} (one-tail)	2.131449546	2.119905299	2.131449546
	t_{crit} (two-tail)	2.489879703	2.472878322	2.489879703
	T_{stat}	-11.80788054	-9.221212876	-5.685674249
	Conclusion	different	different	different
<i>P. aeruginosa</i> 24 h				
		Zoom 1	Zoom 3	Zoom 5
F-test ($\alpha = 0,025$)	F_{crit}	4.433259889	4.433259889	4.433259889
	F_{stat}	2.292959822	3.648605926	3.789425358
	Conclusion	same	same	same
t-test ($\alpha = 0,025$)	t_{crit} (one-tail)	2.119905299	2.119905299	2.119905299
	t_{crit} (two-tail)	2.472878322	2.472878322	2.472878322
	T_{stat}	-32.24124538	-35.06414306	-24.81441994
	Conclusion	different	different	different

General conclusion: the mean of the samples is always different when Ppyrene-F6 is used than when it is not used (meaning that the PPyrene-F6 has an influence)

Table S1. Statistical analysis of surface coverage for each zoom analyzed

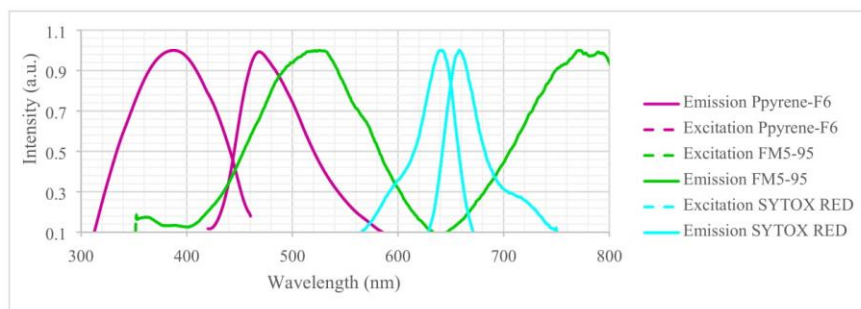


Figure S1. Emission and Excitation spectra of PPyrene-F₆ films (λ_{ex} : 364 nm, λ_{em} : 450 - 550 nm), and the dyes used to tag bacteria: FM5-95[®] (green lines, Solvent: water, λ_{ex} : 525 nm, λ_{em} : 770 nm), and Sytox red[®] (Cyan lines, Solvent: DMSO, λ_{ex} : 640 nm, λ_{em} : 658 nm).

ITO CONTROL RESULTS

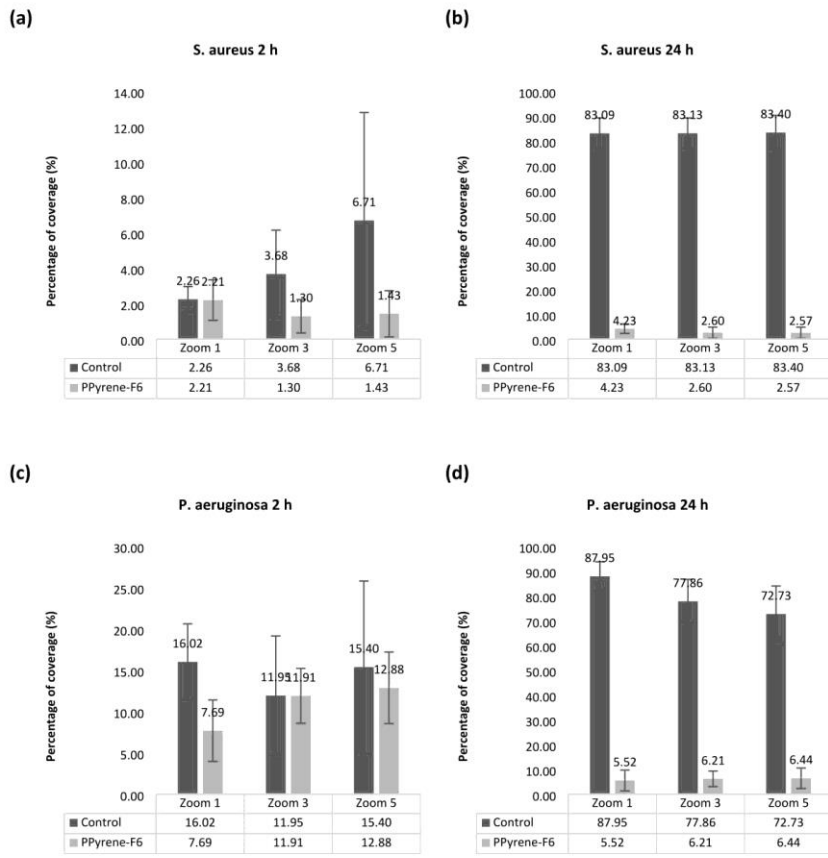


Figure S2. Average percentage of coverage (%) of ITO Control (grey columns) and PPyrene-F₆ (dark grey columns), (a) after 2h adhesion and (b) 24h incubation of *S. aureus* SA ATCC 27217. (c) after 2h adhesion and (d) 24h incubation of *P. aeruginosa* PA ATCC 15442. Error bars represent the standard deviation.

Bacterial adhesion and Biofilm formation

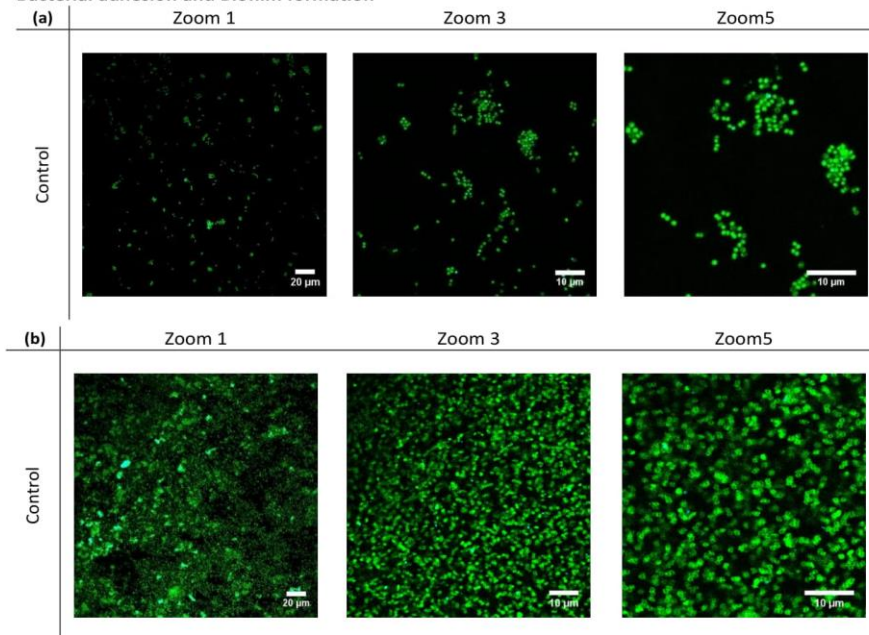


Figure S3. Fluorescence imaging of ITO, Bacteria tagged with FM⁺5-95 (green channel) and Sytox red⁺ (Cyan channel), (a) after 2h adhesion and (b) 24h incubation of *S. aureus* SA ATCC 27217. The surrounding medium is an aqueous saline (150mM) solution. From left to right zoom 1, 3 and 5.

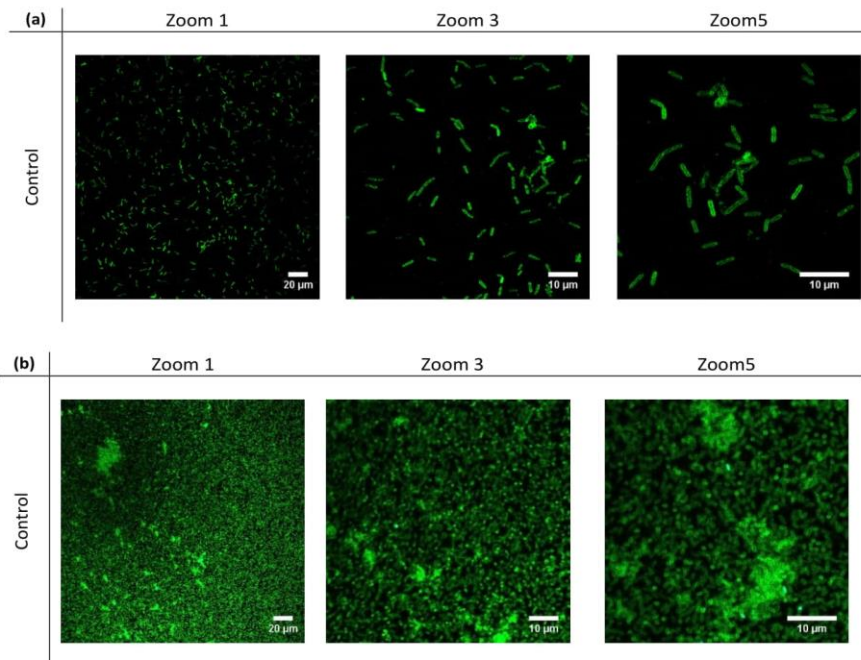


Figure S4. Fluorescence imaging of ITO, Bacteria tagged with FM⁵-95 (green channel) and Sytox[®] red (Cyan channel), (a) after 2h adhesion and (b) 24h incubation of *P. aeruginosa* PA ATCC 15442. The surrounding medium is an aqueous NaCl (150mM) solution. From left to right zoom 1, 3 and 5.

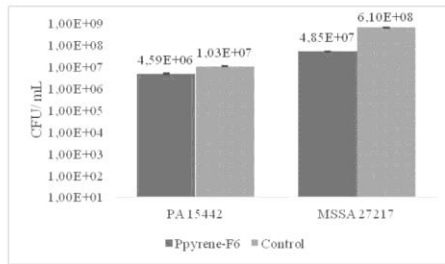


Figure S5. Number (CFU/mL) of *S. aureus* (SA ATCC 27214) and *P. aeruginosa* (PA ATCC 15442) after 24 h of static mode incubation; Control (grey columns) and PPyrene-F₆ (dark grey columns). Error bars represent the standard deviation.

CFU/mL		
	<i>P. aeruginosa</i>	<i>S. aureus</i>
Control	1.0 x10 ⁷	6.1 x10 ⁸
Ppyrene-F ₆ films	4.6 x10 ⁶	4.9 x10 ⁷

Table S2. CFUs per mL of Control and PPyrene-F₆ (a) after 2h adhesion and (b) 24h incubation of *S. aureus* (SA ATCC 27217) and *P. aeruginosa* (PA ATCC 15442).

4.3 Article 3: “Anti-bacterial and fluorescent properties of hydrophobic electrodeposited non-fluorinated polypyrenes”

G. Ramos-Chagas, **G. Morán**, G. Giraudon-Colas, F. Savina, R. Méallet-Renault, S. Amigoni, F. Guittard and T. Darmanin

Applied Surface Science



Contents lists available at ScienceDirect

Applied Surface Science

journal homepage: www.elsevier.com/locate/apsusc

Full Length Article

Anti-bacterial and fluorescent properties of hydrophobic electrodeposited non-fluorinated polypyrenes

Gabriela Ramos Chagas^a, Gabriela Morán Cruz^b, Gaël Giraudon-Colas^b, Farah Savina^b, Rachel Méallet-Renault^b, Sonia Amigoni^a, Frédéric Guittard^a, Thierry Darmanin^{a,*}

^a Université Côte d'Azur, NICE Lab, IMREDD, 61-G3 Av. Simon Veil, 06200 Nice, France

^b University Paris-Sud & Université Paris-Saclay, Institut des Sciences Moléculaires d'Orsay (ISMO), CNRS, F-91405 Orsay, France



ARTICLE INFO

Article history:

Received 10 February 2018

Revised 21 April 2018

Accepted 30 April 2018

Available online 1 May 2018

Keywords:

Polypyrene
Hydrophobic
Fluorescence
Anti-bacterial film
Electropolymerization

ABSTRACT

This work uses an innovative strategy to show a combination of highly hydrophobic films with fluorescence and anti-bacterial properties. Pyrene grafted with linear and branched alkyl chains of various length (from C₄H₉ to C₁₂H₂₅) were electropolymerized and their wetting behavior and surface morphology were first analyzed. The presence of microstructured spherical particles (1 μm) induces a high increase in the surface hydrophobicity ($\theta_{w,max} = 132^\circ$) even if the polymers are intrinsically hydrophilic ($\theta^V = 79\text{--}88^\circ$), while the surface oleophobicity decreases. The emission of the pyrene monomers and polymers is in the green region ($\lambda_{em} = 479\text{--}515\text{ nm}$) and showed to be related with the size and the architecture of the chain. The differences in the aggregations and interactions of the oligomers induce a blue-shift and a thinner spectral band for the branched pyrenes compared to the linear ones. A crescent bathochromic and hypsochromic shift are observed for linear and branched chains, respectively, as the number of carbons increase. The polypyrenes also have a potential application to serve as coatings towards to prevention of biofilm formation. A reduction between 30–70% was observed for the bacterial adhesion and between 91–94% for the biofilm formation for *S. aureus* and *P. aeruginosa* strains. Here we showed for the first time that hydrophobic surfaces bearing hydrocarbon chains without fluorine atoms can be used towards to repel bacteria. Furthermore, the pyrene molecules lead to fluorescent and microstructured hydrophobic surfaces by a one-step electropolymerization process and the combination of these properties enhances the range of applications for these surfaces.

© 2018 Elsevier B.V. All rights reserved.

1. Introduction

The demand in the control of the surface wettability is exponential for various potential applications including self-cleaning coatings [1], microfluidic systems [2], separation membrane [3], biosensors [4] or bioadhesion [5]. According to the Wenzel and Cassie-Baxter equations [6,7], the presence of roughness induced by surface structures can be a key parameter to control the surface hydrophobicity. Indeed, the surface hydrophobicity is highly dependent on geometrical parameters of the surface structures and the material surface energy [8].

The surface chemistry and structuration are also an important key for biological application in the surface science. To reduce or completely eliminate the extent of bacteria attachment and biofilm formation on the man-made materials have required many efforts from the academic and industrial researchers. Some works are

shown the use of nano and/or micro structures to avoid the attachment of microorganisms [9,10]. The nature already showed examples of anti-bacterial surfaces, such as the taro leaves and the cicada wings. Not only superhydrophobic, self-cleaning and anti-fouling, the nanostructures presented on the taro leaf are also highly resistant to the bacterial adhesion under completely wetting conditions [11]. On the other hand, the cicada wings are the first reported example existing naturally with a physical structure that exhibits effective bactericidal properties [12]. The nanopillars on the surface of the cicada wings are extremely efficient to kill individual *Pseudomonas aeruginosa* bacteria cells in only 3 min. This bactericidal property of the cicada wing is a physical and mechanical effect with no variation when the surface chemistry was changed.

On the other hand, it is known that surface chemistry plays an important influence on the bacterial adherence against the surface, such as using quaternary ammonium compounds or silver particles [13–18]. Therefore, polymers with special wettability have also been used to avoid the bacteria interaction. Bruzaud and co-

* Corresponding author.

E-mail address: thierry.darmanin@unice.fr (T. Darmanin).

<https://doi.org/10.1016/j.apsusc.2018.04.268>

0169-4332/© 2018 Elsevier B.V. All rights reserved.

authors reported the fabrication of a superhydrophobic coating of fluorinated poly(3,4-ethylenedioxythiophene) on stainless steel yielding anti-bioadhesive surfaces [10]. They observed that the anti-bacterial properties require the control of the topography associated with the low water adhesion behavior. Dou and co-authors observed that super-surfaces (highly hydrophilic and highly hydrophobic) presented a greater repellence to Gram-positive bacteria than surfaces with intermediate wettability [19]. Indeed, the bacteria adhesion is found to be crucially mediated by the adsorption of peptidoglycan which is one of the main components of the Gram-positive bacteria cell envelope. Taking into account the wetting behavior, Yoon and co-authors reported that the bacterial adhesion of superhydrophobic and superhydrophilic surfaces is quite different and dependent of the fluid flow conditions [20].

Conducting polymers are extremely promising materials for their unique optoelectronic properties, but especially for their high capacity to form various self-assembled structures in solution [21–23]. Structured conducting polymers can also be directly deposited on substrates and one of the most used technique is the electropolymerization process [24–26]. In order to modify the polymer assembly during electropolymerization and as a consequence the surface morphology, the electrochemical parameters (electrolyte, solvent, deposition method, for example) can be changed [27–29]. However, it was found that the polymerizable core (pyrrole, thiophene, aniline, for example) of the monomer has a considerable influence [25]. To increase the polymer surface energy, hydrophobic doping agents can be introduced in the polymer structure, but to obtain stable properties it is preferable to substitute the monomer with a hydrophobic group [30,31].

Aromatic molecules such as naphthalene [32], indole [33], phenanthrene [34] and pyrene [35–37] can also be used as polymerizable core. The choice in the aromatic molecule as monomer is crucial, because each molecule leads to different polymerization capacity, fluorescence properties and can highly influence the surface morphology. Another important parameter for the process is the monomer solubility, which decreases as the H/C ratio [38]. Among them, the pyrene moiety is an exceptional polymerization core in term of both polymerization capacity and monomer solubility [35–37]. The fluorescent properties of pyrene molecule have been calling attention of researches [39–41]. However, if the optoelectronic properties of some pyrene derivatives are reported in the literature, their bacterial interaction and wetting properties are still missing.

Here, we report for the first time a study of the wettability of substituted hydrocarbon polypyrenes without any fluorocarbon moieties presenting good fluorescence and anti-bacterial properties. An original series of pyrene monomers with various alkyl chains (from C_4H_9 to $C_{12}H_{25}$) and architectures (linear and branched chains) were synthesized (Scheme 1) and electrodeposited. We have studied in particular the influence of the alkyl chain length of the surface morphology, hydrophobicity/oleopho-

bicity and fluorescence. The surfaces were also evaluated towards to the bacterial interaction using two different strains: *Staphylococcus aureus* and *Pseudomonas aeruginosa*. The biggest aim here is to develop a non-wetting surface that avoids biofilm formation and reduce the bacterial adhesion while providing optical functionality and without environmental concern about perfluorocarbon chains.

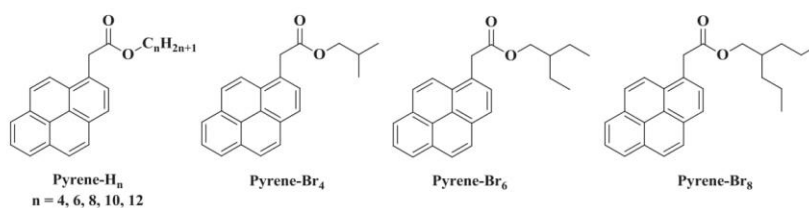
2. Experimental

2.1. Monomer synthesis and characterization

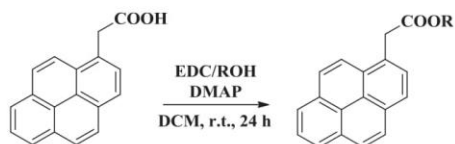
The monomers were synthesized by esterification between 1-pyreneacetic acid and the corresponding alcohol (Scheme 2). For these reactions, 0.5 g of 1-pyreneacetic acid (1.92 mmol), 3.84 mmol of *N*-(3-Dimethylaminopropyl)-*N*-ethylcarbodiimide hydrochloride (EDC), 1.92 mmol of 4-(dimethylamino)pyridine (DMAP) were added to 20 mL of anhydrous dichloromethane. After stirring for 30 min, 3.84 mmol of the corresponding alcohol were added and let stirring for 24 h at room temperature. The solvent was removed under reduced pressure and the product was purified by column chromatography using silica gel (eluent: dichloromethane:cyclohexane 1:1). The monomers were characterized by proton and carbon NMR spectroscopy (1H and ^{13}C NMR) with a W-200 MHz and W-400 MHz (Bruker). Melting points of each monomer were determined via differential scanning calorimetry (Jade DSC-Perkin Elmer) using a thermal scan from 0 °C to 250 °C at a rate of 10 °C min^{-1} . The monomers characterization is presented in the Support Information document.

2.2. Electropolymerization process

The conducting polymer films were performed by monomer oxidation using a potentiostat from Metrohm. An anhydrous acetonitrile solution with 0.1 M of tetrabutylammonium perchlorate (Bu_4NClO_4) and 0.01 M of monomer was realized and inserted inside a glass cell. The connection to the potentiostat was performed with a working electrode, a glassy carbon rod as counter-electrode and a saturated calomel electrode (SCE) as reference electrode. Two different substrates were used as working electrode: 2 cm^2 gold plates for the surface characterization and 8 cm^2 ITO plates for fluorescence and bacterial interaction analysis. The substrates were used without any previous purification. The cyclic voltammetry was used as electrodeposition method in order to obtain highly homogeneous and adherent films [27]. The deposition was performed at a scan rate of 20 mV/s between -0.7 V and a potential slightly lower to the monomer oxidation potential also called as working potential (E^w). Different number of deposition scans (1, 3 and 5) was done in order to study the influence of the polymer growth. The oxidation potential (E^{ox}) and working potential (E^w) are presented in Table S1. After the electrodeposition, the surfaces were washed in acetonitrile and slowly dried.



Scheme 1. Original monomers investigated in this work.



Scheme 2. Synthetic way to the monomers.

Analogous smooth surfaces of each monomer were also prepared by a two-step electropolymerization method to obtain the Young's contact angle (θ^y). First, a thin layer of film was deposited with an imposed potential method and a low charge (1 mC cm^{-2}) in a very low concentration of each monomer ($\pm 2 \text{ mg}$) in the $0.1 \text{ M Bu}_4\text{NClO}_4/\text{acetonitrile}$ solution. A polymer reduction was following by cyclic voltammetry performed at 1 scan from 1.5 V to 0 V vs SCE at a scan rate of 20 mV/s just in the solution containing the $\text{Bu}_4\text{NClO}_4/\text{acetonitrile}$, without the monomer.

2.3. Surface characterization

The infrared (IR) spectra were obtained using a Spectrum Spotlight 300 FT-IR microscope (Perkin Elmer). The spectra were collected using the ATR mode in reflectance on gold plates with a spectral resolution of 4 cm^{-1} and 32 scans. The UV–vis absorbance of the polymers was performed using an Eon Spectrometer (Bio-tek). The surface morphologies were visualized by scanning electron microscopy (SEM) images taken by a 6700 F microscope (JEOL) and 3 kV electron acceleration. The roughness parameters were determined by optical profilometry using the working mode High Mag Phase Shift Interference (PSI), the objective 50X and the field of view $0.5X$. The mean arithmetic roughness (R_a) was obtained on $182 \times 239 \mu\text{m}^2$ areas. The contact angles (θ) were determined by goniometry using liquid probes of different surface tension: water ($\gamma_{LV} = 72.8 \text{ mN m}^{-1}$), diiodomethane ($\gamma_{LV} = 50.0 \text{ mN m}^{-1}$) and hexadecane ($\gamma_{LV} = 27.6 \text{ mN m}^{-1}$). The sessile drop method was used for determining the apparent contact angles (θ) using drops of $2 \mu\text{L}$. The dynamic contact angles were analyzed using the tilted droplet method using water droplets of $6 \mu\text{L}$. The surface was inclined and the maximum angle achieved before the droplet moves was measured. This angle is also called as sliding angle (α). If the droplet does not move after an inclination of 90° , the surface is called sticky. The measures of contact angle and roughness were done in triplicate and the average value will be presented.

The surface free energy (γ_{SV}) and its dispersive (γ_{SV}^D) and polar (γ_{SV}^P) parts of the smooth surfaces were determined using the Owens–Wendt equation ($\gamma_{LV}(1 + \cos \theta) = 2(\gamma_{LV}^D \gamma_{SV}^D)^{1/2} + 2(\gamma_{LV}^P \gamma_{SV}^P)^{1/2}$). Three different liquids (water, diiodomethane and hexadecane) were used which γ_{LV} , γ_{LV}^D and γ_{LV}^P are known, γ_{SV}^D and γ_{SV}^P can be calculated by drawing the function $y = ax + b$ where $y = \gamma_{LV}(1 + \cos \theta)/2(\gamma_{LV}^D)^{1/2}$ and $x = (\gamma_{LV}^P)^{1/2}/(\gamma_{LV}^D)^{1/2}$. Then, $\gamma_{SV}^D = b^2$ and $\gamma_{SV}^P = a^2$ were directly obtained using the software "Drop Shape Analysis". UV–visible absorption spectra of films on ITO surfaces were measured with a Shimadzu UV-2600 double-beam spectrophotometer by using slit widths of 1 nm and scan rate of 600 nm/min . Excitation and fluorescence spectra were measured on a Horiba FluoroMax+ in a front-face configuration with a cuvet holder for solutions or with a film-holder at 30° to 35° orientation. A standard slit width is 1.5 nm and integration time is 0.1 s . Concentration of monomers was below 1 ml/mL . Excitation wavelength was set at 343 nm for emission spectra and emission wavelength was fixed at 395 nm for excitation spectra of

pyrene monomers in DCM. For polypyrene films emission wavelength was fixed around 470 nm for excitation spectra and excitation was 345 nm for emission spectra.

2.4. Bacteria strains

Two collection strains, *S. aureus* (SA) ATCC 27,217 and *P. aeruginosa* (PA) ATCC 15,442 were kept at -80°C in Tryptic Soy Broth (TSB) (bioMérieux, France) containing 20% (vol/vol) glycerol as stock solutions. Before usage, cells were sub-cultured twice in TSB (one 8 h culture, followed by an overnight culture). Bacterial growth and incubation were carried out at 37°C .

2.5. Confocal laser scanning microscopy

Fluorescence images were acquired using Leica TCS SP5-AOBS confocal laser scanning microscope. The surfaces were rinsed by distilled water and imaged using a $\times 63$ – 1.4 numerical aperture plan apochromat oil immersion objective. The size of the xy image was 512×512 pixels (image size for zoom 1: $246.03 \mu\text{m}^2$, zoom 3: $82.01 \mu\text{m}^2$) recorded on 8 bits. UV laser (364 nm) was used as the excitation source regardless the surface and the corresponding fluorescence was collected in the 450 – 550 nm spectral range. Each fluorescence intensity image corresponds to an average of 4 frames.

For bacterial interaction studies, surfaces were incubated for 2 h and 24 h, using glass surfaces as controls. Prior observation, 2 h incubation samples were washed 3 times with 150 mM NaCl sterile solution. For 24 h incubation, culture medium was removed gently, washed and replaced with 150 mM NaCl sterile solution. Bacteria were labeled prior observation with SYTOTM 61 (Life Technologies, France) dye. The excitation source was 633 nm and the fluorescence were collected between 660 – 750 nm . "Image J" software was used in order to quantify bacterial surface coverage on each channel.

3. Results and discussion

3.1. Electrochemical and chemical characterization

To produce highly homogeneous polymer films, the cyclic voltammetry was used as deposition method and surfaces were produced by 1, 3 and 5 deposition scans. A solution of 0.1 M of Bu_4NClO_4 in anhydrous acetonitrile and 0.01 M of each monomer was used to polymerize at a scan rate of 20 mV s^{-1} . These conditions showed to lead the best properties for produce polypyrenes surfaces [27].

The cyclic voltammograms of 5 deposition scans for some of the electropolymerized pyrenes are displayed in Fig. 1. First of all, the polymerization of pyrenes showed a very intense oxidation peak. A high amount of polymer is deposited in the first scan, but it decreases with the number of scans for all the pyrenes studied here. Pyrenes with long alkyl chain showed a single oxidation peak for the monomer and the polymer, which means that they are juxtaposed because the polymer length is extremely short. For short alkyl chains, both linear and branched, the oxidation peak of the monomer and the polymer are farther apart from each other in the first scans indicating a greater difference in the size of their chains. This is not surprising since the short alkyl chain promote a smaller steric hindrance than the long chains. Nevertheless, it was expected that the films are formed by very short oligomer chains (~ 2 – 5 units). Due to the multiple polymerization sites of pyrene and the presence of a substituent, many different oligomers can be formed during polymerization. These results are in com-

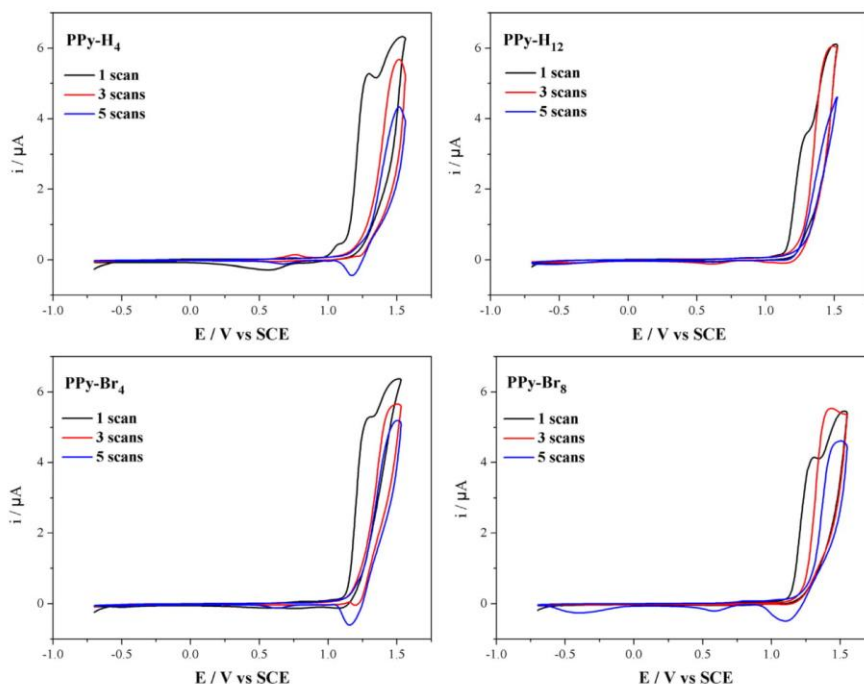


Fig. 1. Cyclic voltammograms of pyrene monomers in 0.1 M $\text{Bu}_4\text{NClO}_4/\text{anhydrous acetonitrile}$ at a scan rate of 20 mV s^{-1} after 5 deposition scans.

plete agreement with the literature [36,42]. Xu and co-workers showed that the electropolymerization of non-substituted pyrene in the same conditions gives oligomers of only 6–11 units [36]. In agreement, Chen and co-workers obtained an average repeat unit of 4 when the monomer (2-(4-(1-pyrenyl)butanoyloxy)ethyl trimethylammonium bromide) was polymerized by a combination of chemical and electrochemical methods [42]. Hence, the pyrene with voluminous substituents (aromatic and fluorinated alkyl chains) reduces the polymer chain length to only some units [37]. It is surprising that oligomers of only few units are sufficiently insoluble to deposit as film, but can be explained by the fact of the pyrene moiety has not a high solubility in acetonitrile. Moreover, pyrene is known to induce extremely strong π -stacking interactions, which also self-assemblies and may highly decrease polymer solubility [43–45].

The UV–Vis spectrum of PPy- H_8 is given in Fig. S1. The UV–vis spectrum of this yellow polymer displayed three peaks at 359 nm, 380 nm and 405 nm, which is in agreement with the literature data [35,36]. Usually, the yellow color in conducting polymers is often due to short polymer chains (short conjugation lengths).

The polymers were characterized by IR spectroscopy using reflectance mode. The IR spectra are displayed in Fig. 2 in which the most intense peaks are highlighted. In all the polymers, a peak around 1730 cm^{-1} is observed which is characteristic of the presence of the ester group and at around $1000\text{--}1200 \text{ cm}^{-1}$ several peaks characteristics from C–O stretching. It is also clear the presence of peaks at around $2800\text{--}3000 \text{ cm}^{-1}$ attributed to the stretching of C–H (stretching vibration of the alkyl chains) and at around

840 cm^{-1} characteristics from C–H bending. The spectra also display a peak at around 1460 cm^{-1} characteristics from C=C bonds (stretching vibration of the pyrene units). Due to the absence of different functional groups, the IR spectra presented similarities for all the polymers.

3.2. Surface characterization

The SEM images of the electrodeposited conducting polymer films (3 scans) are given in Fig. 3. The influence of the alkyl chain length on the surface morphology was found to be considerable important. While less structured surfaces were obtained using long alkyl chains (PPy- H_{12} and PPy- H_{10}), well defined spherical particles were obtained with shorter alkyl chains (PPy- H_8 , PPy- H_6 and PPy- H_4). Upon closer inspection to SEM images, it is observed that the particles size increases as the alkyl chain increases. The diameter of the particles is about $\varnothing \approx 0.8 \mu\text{m}$ for PPy- H_4 , $\varnothing \approx 1.2 \mu\text{m}$ for PPy- H_6 , $\varnothing > 4 \mu\text{m}$ for PPy- H_8 , $\varnothing > 6 \mu\text{m}$ for PPy- H_{10} and $\varnothing > 10 \mu\text{m}$ for PPy- H_{12} . It is clear that for polymers where number of carbons is >8 , the nanospheres become large aggregates of microparticles losing the defined form of the spherical structures generating a surface less structured than for shorter alkyl chains. For the branched-substituted polymers, a similar behavior was observed comparing to the polypyrenes containing linear alkyl chains with equivalent number of carbons.

Usually, the morphology of electrodeposited polymers was found to be highly dependent on the solubility of the oligomers formed in the first instance of the electropolymerization. However,

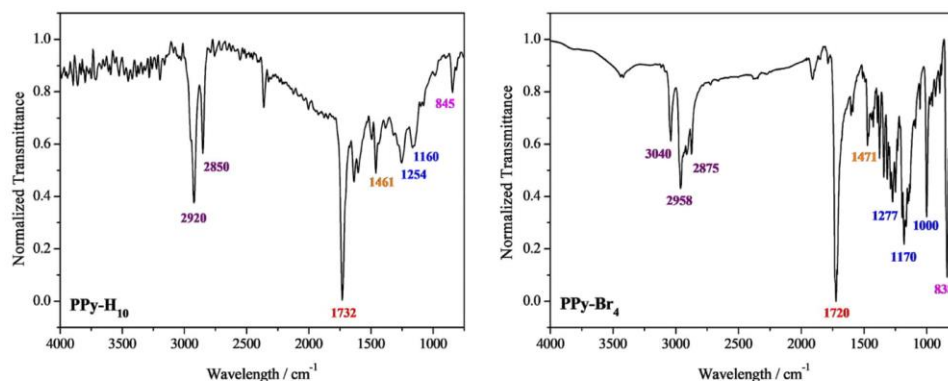


Fig. 2. IR spectra of polypyrenes electropolymerized by cyclic voltammetry in 0.1 M Bu₄NClO₄/anhydrous acetonitrile at a scan rate of 20 mV s⁻¹. Number of scans: 5.

due to the lower polymerization degree, the stability and morphology of the polypyrene films is believed to be governed by the π -stacking interactions between the pyrene units during the polymerization, which decreases their solubility, leading to the polymer precipitation and deposition. Here, the size of the substituents will influence the molecules interactions and, consequently, their solubility and deposition.

These results were confirmed by roughness measurements, as shown in Table 1. Generally, the roughness increased with the number of scan for the polymer surfaces. The Ra measures of PPyrene-H₁₂ and PPyrene-H₁₀ slightly increased between 1 and 3 deposition scans and remained similar for higher number of scans. Here, the increase can be explained by the presence of large wrinkles observed in these films. By contrast, the increase in the roughness of PPyrene-H₈, PPyrene-H₆ and PPyrene-H₄ was extremely important and showed to be 6 times bigger than for the pyrenes containing longer alkyl chains.

The contact angle measured for different probe liquids (water, diiodomethane and hexadecane) are also gathered in Table 1. For PPy-H₁₂ and PPy-H₁₀ the contact angles of the three probe liquids were similar whatever the number of deposition scans. This can be easily explained by the smoothness of the polymer films, which is not significantly affected by the number of deposition scans. These two polymers were slightly hydrophobic ($\theta_w \approx 90^\circ$) and superoleophilic ($\theta_{\text{hexa}} \approx 0^\circ$). By contrast, for PPy-H₈, PPy-H₆ and PPy-H₄, the contact angles of the probe liquids varied with the number of deposition scans. More precisely, the water contact angles often increased while decreased for diiodomethane as the number of deposition scans increased. This is because the electrodeposition of PPy-H₈, PPy-H₆ and PPy-H₄ induced the formation of spherical particles and the surface wettability was highly affected by the roughness. For short alkyl chains, similarities were found once again for the linear and branched-substituents. The first deposition scan showed the lowest θ_w , but the highest θ_{diiodo} for the branched alkyl chains. For 3 and 5 deposition scans, very high θ_w was obtained but with very high water adhesion. A maximum value of $\theta_w = 132^\circ$ was reached for PPy-Br₄ for both 3 and 5 deposition scans differing from PPy-H₄ that shows $\theta_w = 103^\circ$ after 3 deposition scans (Fig. 4). Here, the polymers are extremely rough explaining the high θ_w . Moreover, the dynamic contact angle measurements revealed the sticking behavior of all the surfaces. Water droplets were deposited on each surface and it remained stuck even after surface inclination of 90° .

3.3. Influence of the intrinsic hydrophobicity and the surface structuration on the wetting behavior

To explain the wettability results, smooth surfaces were prepared by changing the polymerization method in order to easily control the polymer growth. These surfaces allowed determining the Young contact angles (θ^Y), which are necessary to use to Wenzel and Cassie-Baxter equations. These θ^Y of the pyrene polymers as well as their respective surface tension are given in Table 2. Roughness measurements confirm the ultra-low roughness of the smooth polymers (Ra = 8.2–10 nm). The influence of the alkyl chain length on the θ^Y was found to be not very important. The polymers were slightly intrinsically hydrophilic ($\theta_{\text{water}}^Y < 90^\circ$, but extremely oleophilic ($\theta_{\text{diiodo}}^Y < 90^\circ$ and $\theta_{\text{hexa}}^Y < 90^\circ$).

Comparing the structured and smooth polymers, the structured surfaces showed a negative impact in the wettability using diiodomethane as a probe liquid for alkyl pyrenes when $n < 8$. Since PPy-H₁₀ and PPy-H₁₂ are quite smooth, no significant changes were observed for all the probe liquids. The most dramatic changes in θ_w from the inherent θ^Y are from PPy-Br₆ and PPy-Br₄. Two models are often used to explain the wetting properties of rough surfaces using θ^Y : Wenzel and Cassie-Baxter [6,7]. The decrease in the surface oleophobicity can be explained by the Wenzel equation, but not the increase in surface hydrophobicity. In the case of the structured surfaces presented here, their high adhesion (sticking behavior) shows that the air fraction inside surface roughness is relatively low. In this case, the surface is in an intermediate state between Wenzel and Cassie-Baxter, also called composite state. This regime can explain the adhesive behavior found on many chemically homogeneous surfaces that have hierarchical topography [46].

The surface tension data presented in Table 2 showed the higher polar components for shorter branched chains which had influence on their wetting behavior (greater hydrophobicity). The lower polar component was found for PPy-H₁₂ as already expect due to the longer alkyl chain. No significant differences were observed for the apolar components of the smooth surfaces.

3.4. Fluorescence properties

3.4.1. Spectroscopic properties of pyrenes derivatives monomers

Normalized absorption, emission and excitation spectra of derivatives pyrenes monomers are given in Fig. S2 and the main

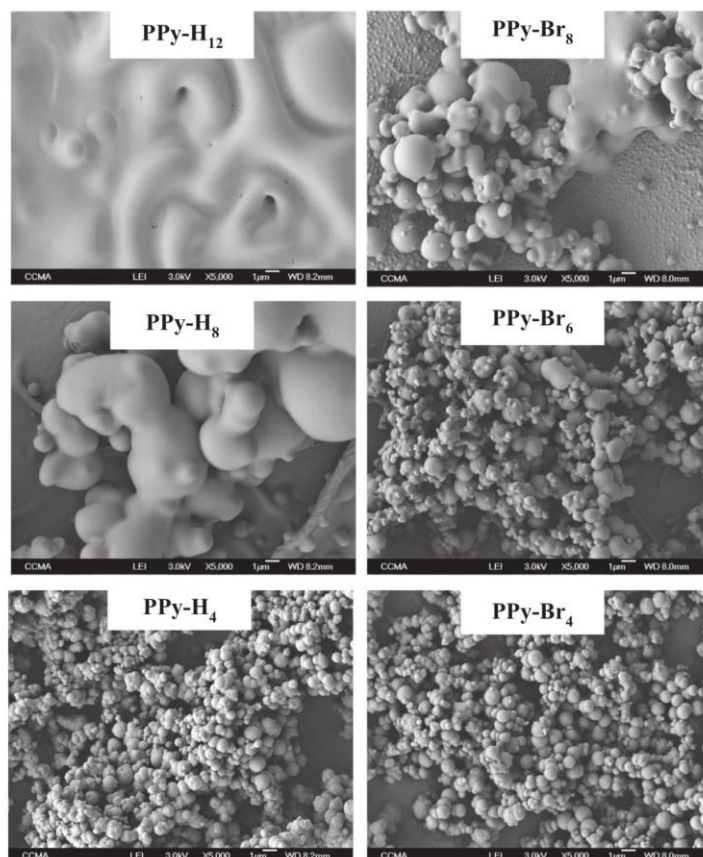


Fig. 3. SEM images of the linear and branched hydrocarbon polymers electrodeposited by cyclic voltammetry (3 scans) in a 0.1 M solution of $\text{Bu}_4\text{NClO}_4/\text{acetonitrile}$.

spectroscopic information are summed up in Table S3. Whatever the substituent (size or architecture), no significant changes are observed between the pyrene derivatives. The absorption spectra of the pyrene derivatives monomers in aerated dichloromethane are similar to the unsubstituted pyrene [37], presenting just a slight bathochromic shift due to the methyl function connected to the aromatic ring which controls the shift of the absorption band [47]. The excitation spectra are superimposable with their respective absorption spectra. It indicates that the structure and the geometry of the molecules did not change in the first electronic excited state S_1 and only one species contributes to the photophysics.

The emission spectra present a relative mirror effect, with two emission bands of same intensity at 378 and 397 nm. For pyrene monomers bearing linear alkyl chains the excimer emission is observed, indicating that due to their smaller steric hindrance, compared to branched analogues, the interaction between monomers increases leading to an excited-state dimer formation. Fluorescence quantum yield of the pyrene derivatives monomers are

between 7 and 10% in aerated dichloromethane. The different substituents do not affect the value, which is very close of the pyrene monomer (7%) [37].

3.4.2. Spectroscopic properties of pyrene derivatives polymers

The polypyrenes films present different absorption and emission spectra compared to the monomers spectra. Fig. 5 depicts the UV–vis absorption and fluorescence emission spectra for PPy-H₁₂ for both monomer and polymer. The polymer spectra show only a single red shifted and broad structureless absorption band. The fine vibrational structure characteristic of the monomer is no longer observed indicating that the oligomerization takes place. The absorption and emission maxima for the polymers are in the range of $\lambda_{\text{abs}} = 358\text{--}382\text{ nm}$ and $\lambda_{\text{em}} = 478\text{--}505\text{ nm}$, respectively (Table S3), differently from their parent monomers (Table S2). The red-shift and broadness shape of the emission spectra is very characteristic from an excimer emission of pyrene and such observations agreed with other works in the literature [37,48].

Table 1
Roughness and apparent contact angles data as a function of the polymer and the number of deposition scans. Polymerization at 0.1 M solution Bu₄NClO₄/acetonitrile.

Polymer	Number of deposition scans	Ra [nm]	θ_{water} [deg]	θ_{diiodo} [deg]	θ_{hexa} [deg]
PPy-H ₁₂	1	125	94.1	48.9	0
	3	450	90.7	52.6	0
	5	390	93.1	45.9	0
PPy-H ₁₀	1	135	88.1	33.5	0
	3	350	91.0	34.1	0
	5	410	99.7	39.2	0
PPy-H ₈	1	650	90.7	20.5	0
	3	1890	106.7	0	0
	5	2750	97.7	0	0
PPy-H ₆	1	630	84.0	13.6	0
	3	1860	110.5	0	0
	5	1720	112.2	0	0
PPy-H ₄	1	25	77.6	0	0
	3	1640	103.7	0	0
	5	480	111.8	0	0
PPy-Br ₈	1	240	94.0	19.0	0
	3	480	103.3	0	0
	5	1240	108.5	0	0
PPy-Br ₆	1	90	89.2	16.0	0
	3	1600	129.8	0	0
	5	1670	128.8	0	0
PPy-Br ₄	1	20	83.0	23.7	0
	3	2075	132.4	0	0
	5	2900	132.4	18.1	0

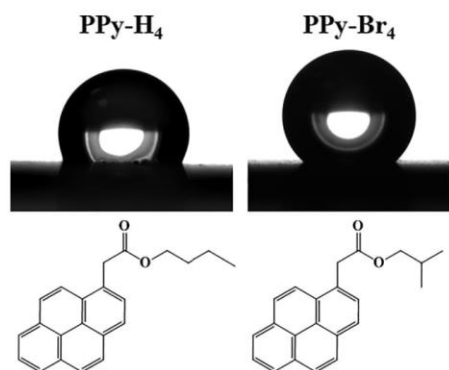


Fig. 4. Images of water droplets deposited on PPy-H₄ and PPy-Br₄ with their respective structures.

The position of the bands in absorption (excitation spectra) does not show any evident correlation with oligomers structure. We should note here that the measurement of absorption spectra or

excitation spectra is quite difficult to achieve (samples are highly absorbing) and it is somehow difficult to determine the band maximum.

Looking at emission spectra in Fig. 6, the polymers containing branched side chains have a blue-shifted emission compared to those bearing linear alkyl groups with the same chain length. Moreover, looking at band shape and full-width at half-maximum (FWHM), for a given chain length, branched oligomers always show thinner emission bands compared to linear ones. Both observations are consistent with differences in aggregation and relative interactions or even due to different proportion concerning oligomers with distinct sizes. Indeed, in branched oligomers one may assume that steric hindrance is higher than in linear ones (for a given chain length), thus aggregation or interaction between oligomers is reduced for branched chains than for linear ones. If the interaction or the aggregation state increases with a linear chain, then a red-shift and broadening of the band is expected as well as for the branched chains. As the size of the chain increases (from $n = 4$ to $n = 8$, as showed in Fig. 6a), higher is the steric hindrance and, consequently, higher is the blue-shift. This behavior changes for long linear chains ($n > 10$) due to the increase in the steric hindrance of the molecules during the polymerization (Fig. 6b).

The fluorescent images showed that all polypyrrole films emitted in the green region. This observation agrees with fluorinated pyrenes reported in the literature [37]. Upon a closer observation,

Table 2
Apparent contact angles of water (θ_w) and roughness data for the smooth corresponding polymers of the non-fluorinated pyrenes. Polymerization at 0.1 M solution Bu₄NClO₄/acetonitrile.

Smooth Polymer	Ra [nm]	Rq [nm]	θ_w [deg]	θ_{diiodo} [deg]	θ_{hexa} [deg]	$\gamma_{\text{SV}}^{\text{D}}$ [mN m ⁻¹]	$\gamma_{\text{SV}}^{\text{O}}$ [mN m ⁻¹]	$\gamma_{\text{SV}}^{\text{E}}$ [mN m ⁻¹]
PPy-H ₁₂	9.3	10.8	88.3	32.6	0	36.8	34.9	1.9
PPy-H ₁₀	10.0	11.9	85.8	32.7	0	37.5	34.9	2.6
PPy-H ₈	8.9	9.9	84.0	32.6	0	39.4	36.6	2.8
PPy-H ₆	9.4	12.1	84.9	33.2	0	37.7	34.8	2.9
PPy-H ₄	9.3	10.5	82.2	38.4	0	37.7	33.7	4.0
PPy-Br ₈	8.8	10.6	81.8	31.8	0	38.9	35.1	3.8
PPy-Br ₆	8.2	9.8	80.8	31.5	0	39.3	35.1	4.2
PPy-Br ₄	9.2	11.4	79.5	36.2	0	39.0	34.2	4.9

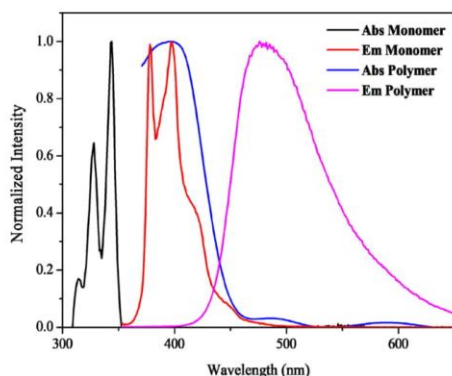


Fig. 5. Absorption and emission spectra (normalization to 1 at the maximum intensity of every spectrum) for the PPY-H₁₂. Absorption spectra of the monomers in DCM (black lines), emission spectra of the monomers in DCM with $\lambda_{exc} = 345$ nm (red lines), absorption spectra of the polymers (blue lines), emission spectra of the polymers with $\lambda_{exc} = 345$ nm (magenta lines). Polymerization in solution 0.1 M Bu₄NClO₄/acetonitrile. Number of scans: 2. Deposition in ITO plates.

the fluorescent intensity of the spherical particles in micro and nanometer size are stronger than the region where it has the least deposited polymer. In fluorescence and transmission confocal microscopy, we were able to observe the aggregates formed using branched and linear alkyl chains as well as the smooth films produced by longer linear chains.

Fig. 7 also shows the fluorescence confocal images and their orthogonal views of the polymeric films PPY-H₄ and PPY-Br₄. In agreement with the SEM images and roughness results, the fluorescence confocal images showed very rough surfaces with many peaks and valleys. Indeed, the thickness of the polymeric films was measured with the orthogonal views. As already explained before, the topography of both architectures with the same size of hydrocarbon chain is quite similar. Here, the average thickness obtained for PPY-H₄ and PPY-Br₄ was $18 \pm 5 \mu\text{m}$ and $20 \pm 8 \mu\text{m}$, respectively. As indicating by the standard deviation, the surfaces

are not homogeneous and the particles are distributed on the surface in many agglomerates. The fluorescence confocal images well corroborate the SEM images and similar topographies are observed whatever the sample is. To sum up, the use of fluorescence imaging is a good alternative to the use of electronic microscopy in order to control the surface morphology.

3.5. Anti-bacterial properties

Due to the versatile properties of the polypyrene films, bacterial interaction tests were also performed under different conditions for PPY-H₄ and PPY-Br₄. It is known that superhydrophobic surfaces provide good bacterial-resistance due to the presence of air inside the surface roughness. However, highly hydrophobic surfaces with microstructures are good candidates to obtain a reduction on the bacterial interaction towards the deposited coatings. For this purpose, the aim here was to evaluate the influence of the surface chemistry, morphology and wettability of these polymer films under two different bacteria strains (Gram-positive and Gram-negative). *Staphylococcus aureus* is Gram-positive bacteria in the form of a coccus with a diameter of 0.5–1 μm while *Pseudomonas aeruginosa* is a bacillus and Gram-negative bacteria from 0.5–1 μm by 1–5 μm [49]. Both *S. aureus* and *P. aeruginosa* have been recognized among the most frequent cause of biofilm-associated infections and recently included by the World Health Organization in the list of the most critical multidrug resistant bacteria considered as particular threat in hospitals [50]. For this reason, they were chosen as representative for this study.

The bacterial interaction on the films was tested by static incubation for 2 h (bacterial adhesion) and 24 h (biofilm formation) with the two bacterial stains (*S. aureus* and *P. aeruginosa*). The quantitative results presented correspond to zoom 1 which represents a larger area of analysis while the confocal images were presented for zoom 3 to provide better observation. A reduction on the bacterial adhesion was obtained for all the polypyrenes compared with the glass control for both strains studied as shown in Fig. 8. The polypyrene films showed a reduction on the bacterial adhesion of 30% as compared to the glass control for *S. aureus* strain. For *P. aeruginosa*, the percentage of bacteria coverage (%cover) on the surface is 7% for PPY-H₄ and 9% for PPY-Br₄, reducing in ~70% the bacterial adhesion towards the control. These results showed a significant reduction of the bacterial adhesion on polypyrene films

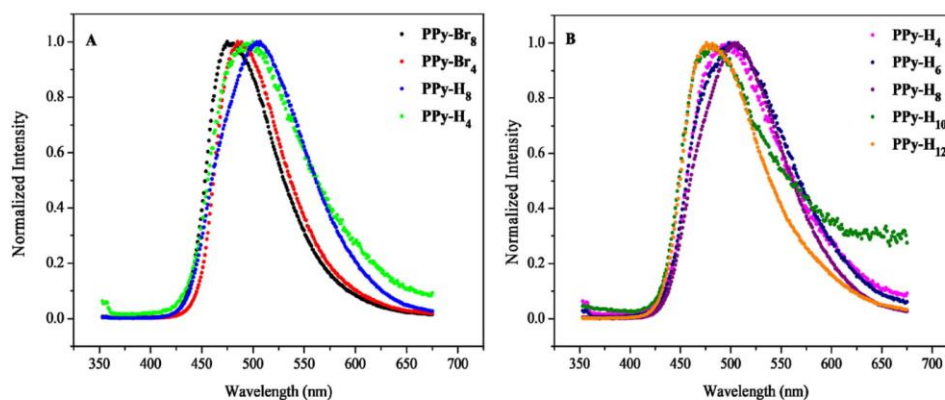


Fig. 6. Emission spectra for the polypyrenes: (a) comparison between the linear and branched chains with different number of carbons ($n = 4$ and $n = 8$); (b) comparison between the linear chains with $4 < n < 12$. Polymerization in solution 0.1 M Bu₄NClO₄/acetonitrile. Number of scans: 2. Deposition in ITO plates.

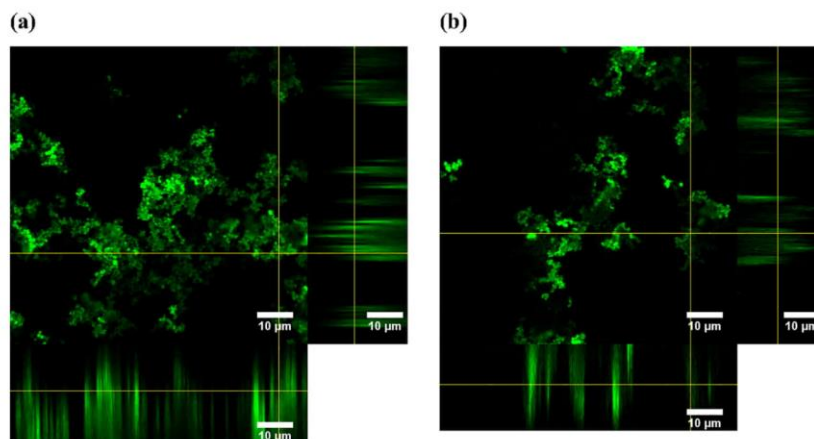


Fig. 7. Confocal fluorescence microscopy and their respective orthogonal views for: (a) PPy-H₄ and (b) PPy-Br₄. Polymerization in solution 0.1 M Bu₄NClO₄/acetonitrile. Number of scans: 2. Deposition in ITO plates. Polymeric films in the green channel, λ_{exc} = 364 nm, λ_{em} = 450–550 nm).

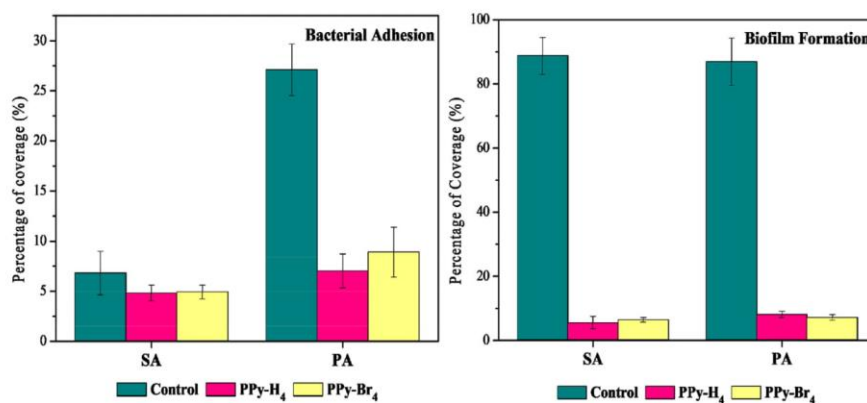


Fig. 8. Average percentage of bacteria coverage (%cover) after incubation of 2 h (bacterial adhesion) and 24 h (biofilm formation) for *S. aureus* (SA) and *P. aeruginosa* (PA) for the polypyrrene surfaces and glass control (zoom 1). Errors bars represent the standard deviation.

independent of the architecture of the chain. Since the hydrophobicity is different between PPy-H₄ and PPy-Br₄, one may assume that such result arises from the roughness and sub microstructures present on the surface.

After longer time of incubation, the biofilm formation could be evaluated. Fig. 8 shows that for *S. aureus* the %cover on the surface is ~90% for the glass control whereas for PPy-H₄ is 5% and for PPy-Br₄ is 6%. Similar results were obtained for *P. aeruginosa*: a %cover is ~90% for the glass control and ~9% for the polypyrrenes. Here we demonstrated that even with a reduction in 30% of the bacterial adherence on polypyrrene surface, it does not necessarily lead to a biofilm attachment on surface. This is a very promising result since the biofilm is considered a major hazard on many potential applications, mainly in the food, pharmaceutical and medical industry.

Several recent efforts were done to design a new generation of surfaces that can repel bacteria and avoid their proliferation and formation of biofilm. The most commonly used ways are to fabricate superhydrophobic surfaces that are known to be efficient to prevent surface contamination by microorganisms or use quaternary ammonium compounds due their known biocide activity. In opposition, the topography of the structure can also affect the interaction between the bacteria and the surface. Many authors had already reported that the surface structure is the key parameter to reduce bacterial adhesion. Bruzaud and co-authors revealed that the bacterial adherence requires the control of surface topography using functionalized PEDOT [10]. A remarkable work about the influence on the ordering of the structures on the bacterial growth was reported by Díaz and co-authors [9]. They showed that the bacteria grown are affected by the nano and microscale of the

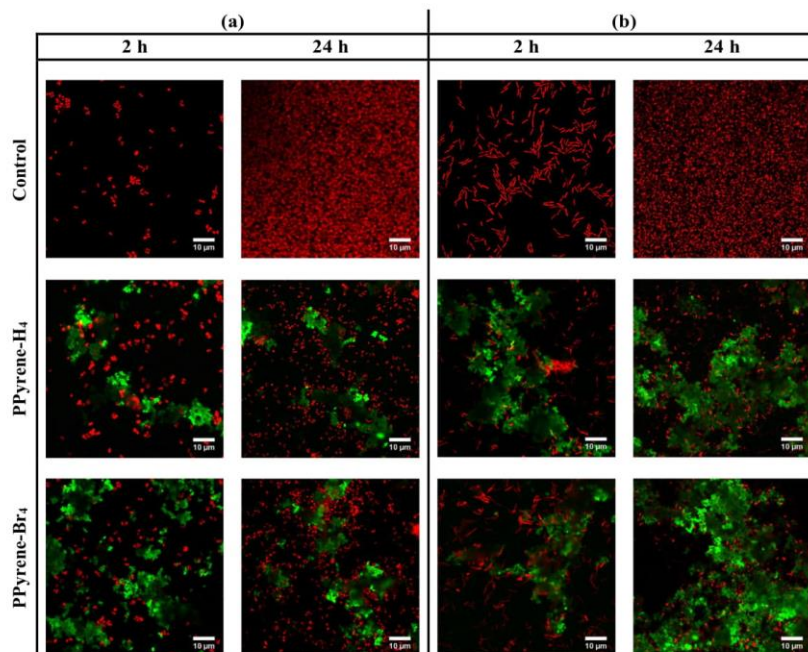


Fig. 9. Fluorescence imaging of the surfaces after 2 h and 24 h incubation of (a) *S. aureus* and (b) *P. aeruginosa*. The surrounding medium is an aqueous saline (150 mM) solution. Images taken at zoom 3. Polymer marked in green channel and SYTO 61 dye (bacteria) in red channel.

topography in the early stages of the biofilm formation. This was the first work reporting the correlation of the bacteria cell shape and attachment with the topography of the surface.

These results presented in Fig. 8 are supported by the confocal images in Fig. 9. Looking forwards to *P. aeruginosa* results, no significant differences were found for the bacterial interaction for PPy-H₄ and PPyBr₄ films in both incubation times. For *S. aureus*, a reduction in ~90% was found for the biofilm formation, but only ~30% on the bacterial adhesion. The difference observed between the two strains can be since *S. aureus* has smaller size than *P. aeruginosa*, being easier attached or mechanically anchored to the microstructures of the polymer film as happened for the short incubation time. However, *P. aeruginosa* showed a higher bacterial%cover for both polymers and incubation times than *S. aureus* because the bacteria size is from 2–5 times bigger and, consequently, presenting a larger coverage area.

Herein, the morphology of the polypyrene surfaces allows a mechanical anchoring between the bacteria and the structure as observed in the confocal images. It is clear that this connection is a physical engagement when no higher%cover of biofilm is observed on the surface for a long incubation time. In the literature are reported many studies where the morphology is the main responsible for the bacterial avoiding [9,51,52], including a natural example of the cicada wings [12,53]. Indeed, the high hydrophobicity of the polypyrene surfaces favors the repellence of the bacteria attachment for both strains.

In resume, the bacterial adhesion was reduced between 30–70% for the polypyrene films for *S. aureus* and *P. aeruginosa*, respectively. Even that the bacteria adhesion was not totally avoided, a

reduction between 91–94% of the biofilm adhesion in comparison with a glass control was observed for both bacterial strains. This work demonstrates the capability of polypyrene films in being highly efficient against biofilm formation even if some bacteria can be adhered.

4. Conclusions

We have shown for the first time the possibility to use pyrene monomers with various alkyl chains (from C₄H₉ to C₁₂H₂₅) and no fluorine atoms to obtain highly structured and hydrophobic properties by electropolymerization that are potentially candidates to be applied such as fluorescent and anti-bacterial coatings. The size of alkyl chain had a huge influence on the surface morphology, but not the architecture of the monomer. Smooth and structured surfaces were obtained with long and short alkyl chains, respectively. With short alkyl chains spherical particles were obtained with a decrease of their mean size as the alkyl chain length decrease until to be less than 1 μm. High hydrophobic properties were obtained for short alkyl chains for both linear and branched structures. The architecture and the size of the monomer seem to influence the fluorescence properties due to the differences in the aggregation. However, all the polypyrenes emit in the green region. Concerning about the bacterial interaction with the surface, the monomer architecture showed to be not so important. Whereas both films have different hydrophobicity, it seems that roughness and nanostructures are more important parameters to avoid bacteria adhesion. Even if the bacterial adhesion is not com-

pletely avoided, the polypyrrene surfaces showed to be highly efficient against the biofilm by reducing in 91–94% the bacteria coverage when compared with the control. These results are extremely encouraging and open the possibility of using new aromatic molecules without fluoride atoms to develop hydrophobic materials with a wide range of applications, such as sensors, membranes and medical devices.

Acknowledgments

This work was supported by a grant from CNPq, Conselho Nacional de Desenvolvimento Científico e Tecnológico - Brazil (Process N° 202280/2014-4) for G. Ramos Chagas's Ph.D. thesis and from the Ministère de l'Éducation Nationale, de l'Enseignement Supérieur et de la Recherche, Université Paris-Sud Paris-Saclay, for G. Moran's Ph.D. thesis (ED 2MIB N°571). This work has also been supported by the Region Ile-de-France in the framework of DIM Nano-K; by LabEx CHARMMMAT and by fédération Lumière Matière (LUMAT FR2764). The authors thank the Centre de Photonique Biomédicale (CPBM) of the Centre Laser de l'Université Paris-Sud (CLUPS/LUMAT FR2764, Orsay, France) for allowing us to use the confocal microscope and L2 microbiology facilities.

Appendix A. Supplementary material

Supplementary data associated with this article can be found, in the online version, at <https://doi.org/10.1016/j.apsusc.2018.04.268>.

References

- [1] S. Guldin, P. Kohn, M. Stefić, J. Song, G. Divitini, F. Ecarla, C. Ducati, U. Wiesner, U. Steiner, Self-cleaning antireflective optical coatings, *Nano Lett.* 13 (2013) 5329–5335.
- [2] Y. Feng, Z. Zhou, X. Ye, J. Xiong, Passive valves based on hydrophobic microfluidics, *Sens. Actuators, A* 108 (2003) 138–143.
- [3] Y. Dou, D. Tian, Z. Sun, Q. Liu, N. Zhang, J.H. Kim, L. Jiang, S.X. Dou, Fish gill inspired crossflow for efficient and continuous collection of spilled oil, *ACS Nano* 11 (2017) 2477–2485.
- [4] P. Lucas, M.A. Solís, D. Le Coq, C. Juncker, M.R. Riley, J. Collier, D.E. Boesevetter, C. Bousard-Pfedel, B. Bureau, Infrared biosensors using hydrophobic chalcogenide fibers sensitized with live cells, *Sens. Actuators, B* 119 (2006) 355–362.
- [5] S. Bhatt, J. Pulyptel, G. Ceccone, P. Lisboa, F. Rossi, V. Kumar, F. Arefi-Khonsari, Nanostructure protein repellent amphiphilic copolymer coatings with optimized surface energy by inductively excited low pressure plasma, *Langmuir* 27 (2011) 14570–14580.
- [6] R.N. Wenzel, Resistance of solid surfaces to wetting by water, *Ind. Eng. Chem.* 28 (1936) 988–994.
- [7] A.B.D. Cassie, S. Baxter, Wettability of porous surfaces, *Trans. Faraday Soc.* 40 (1944) 546–551.
- [8] A. Marmur, Superhydrophobic and superhydrophobic surfaces: from understanding non-wettability to design considerations, *Soft Matter* 9 (2013) 7900–7904.
- [9] C. Díaz, P.L. Schilardi, R.C. Salvarezza, M.F. Lorenzo de Mele, Nano/microscale order affects the early stages of biofilm formation on metal surfaces, *Langmuir* 23 (2007) 11206–11210.
- [10] J. Bruzaud, J. Tarrade, E. Celia, T. Darmanin, E. Givenchy, F. Guittard, J.-M. Herry, M. Guilbaud, M.-N. Bellon-Fontaine, The design of superhydrophobic stainless steel surfaces by controlling nanostructures: a key parameter to reduce the implantation of pathogenic bacteria, *Mater. Sci. Eng. C* 73 (2017) 40–47.
- [11] J. Ma, Y. Sun, K. Gleichauf, J. Lou, Q. Li, Nanostructure on taro leaves resists fouling by colloids and bacteria under submerged conditions, *Langmuir* 27 (2011) 10035–10040.
- [12] E.P. Ivanova, J. Hasan, H.K. Webb, V.K. Truong, G.S. Watson, J.A. Watson, V.A. Baulin, S. Pogodin, J.Y. Wang, M.J. Tobin, C. Löbke, R.J. Crawford, Natural bactericidal surfaces: mechanical rupture of *Pseudomonas aeruginosa* cells by cicada wings, *Small* 8 (2012) 2489–2494.
- [13] P. Thebault, E. Taffin de Givenchy, R. Levy, Y. Vandenberghe, F. Guittard, S. Gëribaldi, Contact-active microbicidal gold surfaces using immobilization of quaternary ammonium thiol derivatives, *Eur. J. Med. Chem.* 44 (2009) 4227–4234.
- [14] L. Caillier, E. Taffin de Givenchy, R. Levy, Y. Vandenberghe, S. Gëribaldi, F. Guittard, Synthesis and antimicrobial properties of polymerizable quaternary ammoniums, *Eur. J. Med. Chem.* 44 (2009) 3201–3208.
- [15] P. Thebault, E. Taffin de Givenchy, S. Gëribaldi, R. Levy, Y. Vandenberghe, F. Guittard, F. Surface and antimicrobial properties of semi-fluorinated quaternary ammonium thiol surfactants potentially usable for self-assembled monolayers, *J. Fluorine Chem.* 131 (2010) 592–596.
- [16] K.R. Shin, Y.S. Kim, G.W. Kim, H.W. Yang, Y. Gun Ko, D.H. Shin, Effects of concentration of Ag nanoparticles on surface structure and in vitro biological responses of oxide layer on pure titanium via plasma electrolytic oxidation, *Appl. Surf. Sci.* 347 (2015) 574–582.
- [17] L. Huang, S. Zhao, Z. Wang, J. Wu, J. Wang, S. Wang, In situ immobilization of silver nanoparticles for improving permeability, antifouling and anti-bacterial properties of ultra filtration membrane, *J. Memb. Sci.* 499 (2016) 269–281.
- [18] T. Xu, L. Wu, Y. Yu, W. Li, J. Zhi, Synthesis and characterization of diamond–silver composite with anti-bacterial property, *Mater. Lett.* 114 (2014) 92–95.
- [19] X.-Q. Dou, D. Zhang, C. Feng, L. Jiang, Bioinspired hierarchical surface structures with tunable wettability for regulating bacteria adhesion, *ACS Nano* 9 (2015) 10664–10672.
- [20] S.H. Yoon, N. Rungraeng, W. Song, S. Jun, Superhydrophobic and superhydrophilic nanocomposite coatings for preventing *Escherichia coli* K-12 adhesion on food contact surface, *J. Food Eng.* 131 (2014) 135–141.
- [21] R. Balint, N.J. Cassidy, S.H. Cartmell, Conductive polymers: towards a smart biomaterial for tissue engineering, *Acta Biomater.* 10 (2014) 2341–2353.
- [22] P.M. Beaujuge, J.R. Reynolds, Color control in π -conjugated organic polymers for use in electrochromic devices, *Chem. Rev.* 110 (2010) 268–320.
- [23] T. Darmanin, F. Guittard, Wettability of conducting polymers: from superhydrophilicity to superoleophobicity, *Prog. Polym. Sci.* 39 (2014) 656–682.
- [24] W. Zhong, Y. Wang, Y. Yan, Y. Sun, J. Deng, W. Yang, Fabrication of shape-controllable polyaniline micro/nanostructures on organic polymer surfaces: obtaining spherical particles, wires, and ribbons, *J. Phys. Chem. B* 111 (2007) 3918–3926.
- [25] G. Ramos Chagas, T. Darmanin, F. Guittard, One-step and templateless electropolymerization process using thienothiophene derivatives to develop arrays of nanotubes and tree-like structures with high water adhesion, *ACS Appl. Mater. Interfaces* 8 (2016) 22732–22743.
- [26] H.-A. Lin, S.-C. Luo, B. Zhu, C. Chen, Y. Yamashita, H.-H. Yu, Molecular or nanoscale structures? the deciding factor of surface properties on functionalized poly(3,4-ethylenedioxythiophene) nanorod arrays, *Adv. Funct. Mater.* 23 (2013) 959–965.
- [27] G. Ramos Chagas, T. Darmanin, G. Godeau, S. Amigoni, F. Guittard, F. Superhydrophobic properties of electrodeposited fluorinated polypyrrenes, *J. Fluorine Chem.* 193 (2017) 73–81.
- [28] S.-C. Luo, J. Sekine, B. Zhu, H. Zhao, A. Nakao, H.-H. Yu, Polydiethoxythiophene nanodots, nanowires, nano-networks, and tubular structures: the effect of functional groups and temperature in template-free electropolymerization, *ACS Nano* 6 (2012) 3018–3026.
- [29] E. Poverenov, M. Li, A. Bitler, M. Bendikov, Major effect of electropolymerization solvent on morphology and electrochromic properties of PEDOT films, *Chem. Mater.* 22 (2010) 4019–4025.
- [30] T. Darmanin, F. Guittard, Enhancement of the superoleophobic properties of fluorinated PEDOP using polar glycol spacers, *J. Phys. Chem. C* 118 (2014) 26912–26920.
- [31] S. Taleb, T. Darmanin, F. Guittard, Elaboration of voltage and ion exchange stimuli-responsive conducting polymers with selective switchable liquid-repellency, *ACS Appl. Mater. Interfaces* 6 (2014) 7953–7960.
- [32] G. Zhu, J. Xu, R. Yue, B. Lu, J. Hou, Novel poly-bridged-naphthalene with blue-light-emitting property via electropolymerization, *J. Appl. Polym. Sci.* 123 (2011) 2706–2714.
- [33] G. Ramos Chagas, T. Darmanin, F. Guittard, Nanostructured superhydrophobic films synthesized by electrodeposition of fluorinated polyindoles, *Beilstein J. Nanotechnol.* 6 (2015) 2078–2087.
- [34] W.-Q. Zhou, H.-P. Peng, J.-K. Xu, H.-Y. Xia, S.-Z. Pu, Electrochemical polymerization of phenanthrene in mixed electrolytes of boron trifluoride diethyl etherate and concentrated sulfuric acid, *Polym. Int.* 57 (2008) 92–98.
- [35] B. Lu, S. Zhen, L. Zhao, G. Zhang, D. Mo, J. Xu, A novel solution-processable amino-group-substituted oligopyrene: synthesis, electropolymerization, properties, and application in fluorescent chemosensor, *Synth. Met.* 198 (2014) 155–160.
- [36] L. Xu, F. Tong, X. Lu, K. Lu, Q. Lu, Multifunctional polypyrrene/silica hybrid coatings with stable excimer fluorescence and robust superhydrophobicity derived from electrodeposited polypyrrene films, *J. Mater. Chem. C* 3 (2015) 2086–2092.
- [37] G. Ramos Chagas, X. Xie, T. Darmanin, K. Steenkeste, A. Gaucher, D. Prim, R. Méallet-Renault, G. Godeau, S. Amigoni, F. Guittard, Electrodeposition of polypyrrenes with tunable hydrophobicity, water adhesion, and fluorescence properties, *J. Phys. Chem. C* 120 (2016) 7077–7087.
- [38] W. Acree, S. Tucker, A. Zvaizne, K. Street, J. Fetzer, H.-F. Grützmacher, Polycyclic aromatic hydrocarbon solute probes. part VII: evaluation of additional coronene derivatives as possible solvent polarity probe molecules, *Appl. Spectrosc.* 44 (1990) 477–482.
- [39] B.W. Rawe, C.M. Brown, M.R. MacKinnon, B.O. Patrick, G.J. Bodwell, D.P. Gates, A *c*-pyrenyl poly(methylene phosphine): oxidation “turns on” blue photoluminescence in solution and the solid state, *Organometallics* 36 (2017) 2520–2526.
- [40] M. Chhatwal, A. Kumar, S.K. Awasthi, M. Zharnikov, R.D. Gupta, An electroactive metallo–polypyrrene film as a molecular scaffold for multi-state volatile memory devices, *J. Phys. Chem. C* 120 (2016) 2335–2342.
- [41] M. Chhatwal, A. Kumar, R.D. Gupta, S.K. Awasthi, A pyrene-based electropolymerized film as a solid-state platform for multi-bit memory

- storage and fluorescence sensing of nitroaromatics in aqueous solutions, *J. Mater. Chem. C* 4 (2016) 4129–4133.
- [42] Y. Chen, H. Bai, Q. Chen, C. Li, G. Shi, A water-soluble cationic oligopyrene derivatives: spectroscopic studies and sensing applications, *Sens. Actuators, B* 138 (2009) 563–571.
- [43] S. Picarra, P.T. Gomes, J.M.G. Martinho, Fluorescence study of the coil - globule transition of a poly(ϵ -caprolactone) chain labeled with pyrenes at both ends, *Macromolecules* 33 (2000) 3947–3950.
- [44] T. Costa, J. Seixas De Melo, H.D. Burrows, Fluorescence behavior of a pyrene-end-capped poly(ethylene oxide) in organic solvents and in dioxane–water mixtures, *J. Phys. Chem. B* 113 (2009) 618–626.
- [45] S. Chen, J. Duhamel, M.A. Winnik, Probing end-to-end cyclization beyond Willemski and Fixman, *J. Phys. Chem. B* 115 (2011) 3289–3302.
- [46] A. Marmor, Hydro- hygro- oleo- omni-phobic? terminology of wettability classification, *Soft Matter* 8 (2012) 6867–6870.
- [47] Y. Niko, S. Kawauchi, S. Otsu, K. Tokumaru, G. Konishi, Fluorescence enhancement of pyrene chromophores induced by alkyl groups through $\sigma - \pi$ conjugation: systematic synthesis of primary, secondary, and tertiary alkylated pyrenes at the 1, 3, 6, and 8 positions and their photophysical properties, *J. Org. Chem.* 78 (2013) 3196–3207.
- [48] J.B. Birks, L.G. Christophorou, Excimer fluorescence spectra of pyrene derivatives, *Spectrochim. Acta* 19 (1963) 401–410.
- [49] J.G. Holt, N.R. Krieg, P.H.A. Sneath, J.T. Staley, *Bergey's manual of determinate bacteriology*, 9th ed.; Wilkins, W. & Ed.; Baltimore, MD, 1994.
- [50] Organization, W. H. Global priority list of antibiotic-resistant bacteria to guide research, discovery, and development of new antibiotics.
- [51] D. Perera-Costa, J.M. Bruque, Studying the influence of surface topography on bacterial adhesion using spatially organized microtopographic surface patterns, *Langmuir* 30 (2014) 4633–4641.
- [52] L. Liu, B. Ercan, L. Sun, K.S. Ziemer, T.J. Webster, Understanding the role of polymer surface nanoscale topography on inhibiting bacteria adhesion and growth, *ACS Biomater. Sci. Eng.* 2 (2016) 122–130.
- [53] S.M. Kelleher, O. Habimana, J. Lawler, B.O. Reilly, S. Daniels, E. Casey, A. Cowley, Cicada wing surface topography: an investigation into the bactericidal properties of nanostructural features, *ACS Appl. Mater. Interfaces* 8 (2016) 14966–14974.

[View publication stats](#)

4.4 Article 4: “Superhydrophobic and fluorescent properties of fluorinated polypyrene surfaces using various polar linkers prepared via electropolymerization”

G. Ramos-Chagas, **G. Morán**, R. Méallet-Renault, A. Gaucher, D. Prim, D.E. Weibled, S. Amigoni, F. Guittard and T. Darmanin



Contents lists available at ScienceDirect

Reactive and Functional Polymers

journal homepage: www.elsevier.com/locate/react

Superhydrophobic and fluorescent properties of fluorinated polypyrene surfaces using various polar linkers prepared via electropolymerization



Gabriela Ramos Chagas^a, Gabriela Morán Cruz^b, Rachel Méallet-Renault^b, Anne Gaucher^c, Damien Prim^c, Daniel Eduardo Weibel^d, Sonia Amigoni^a, Frédéric Guittard^a, Thierry Darmanin^{a,*}

^a Université Côte d'Azur, NICE Lab, IMREDD, 06200 Nice, France

^b Université Paris-Sud, Université Paris-Saclay, Institut des Sciences Moléculaires d'Orsay (ISMO), CNRS, F-91405 Orsay, France

^c UMR CNRS 8180, Institut Lavoisier de Versailles, Université de Versailles St-Quentin, 78035 Versailles, France

^d Department of Chemical Physics, Chemical Institute, Universidade Federal do Rio Grande do Sul, Porto Alegre 91501-970, RS, Brazil

ARTICLE INFO

Keywords:
Superhydrophobic
Fluorescence
Electropolymerization
Wettability
Pyrene

ABSTRACT

Superhydrophobic and fluorescent polypyrene surfaces were synthesized by an electropolymerization process. Six different linkers (ester, thioester, amide, carbamate, thiocarbamate and urea) are used to introduce fluorinated chains (lengths of 4, 6 and 8 carbons) onto pyrene moiety. The electropolymerized surfaces were analyzed by their morphology, surface chemistry, wettability and fluorescence. The linkers and the length of the fluorinated chain influence on both surface chemistry and morphology confirmed by XPS and SEM analysis, respectively. Superhydrophobic surfaces were obtained for ester, thioester, carbamate and thiocarbamate series while high hydrophobic surfaces for amide and urea series. Here, we show the possibility to control the surface hydrophobicity, oleophobicity and liquid adhesion with both the linker and the fluorinated chain length. For example, N–H groups seem to induce a decrease in the static contact angle (θ_w) and in the surface structuration due to their polarity generating smoother surfaces (as for amide and urea series) and yielding to a red-shift in the emission spectra (showed for amide, carbamate, thiocarbamate and urea). The emission of all the polypyrene films is red-shifted compared to the pyrene monomers (excimer emission) and in the green region independently of the side chain. Here, we show that the nature of the heteroatom that connects the pyrene moiety to the fluorinated chain also does great impact on the surface morphology, wetting and fluorescence properties.

1. Introduction

The observation and understanding of wetting phenomena in Nature has opened new strategies for innovative material design [1,2]. The most famous example is the lotus leaves with their self-cleaning properties (Cassie-Baxter state) but other natural species are able, for example, to resist to water wetting during rainfall, to leave in soil, to see in fogging environments or to capture water droplets in arid environments [3–6]. Towards this last aim, the researches have been fascinating trying to mimic natural surfaces to obtain similar properties. Studies on nano and microstructured surfaces with super-wetting behaviour based on biomimicry have been increasing exponentially since 2000s due to their potential applications as coatings for anti-corrosion [7], anti-bacterial [8], anti-icing materials [9], etc. The superhydrophobicity found in the lotus leaves is defined by an apparent contact angle with water $\theta_w > 150^\circ$ and low hysteresis H . It can be reached for example combining surface structures often at a micro/

nanoscale with low surface energy materials. In opposition, the so called parahydrophobicity, which are characterized by both high θ_w and H , can also be found in the nature in the rose petals, gecko foot and cicada wings, for example [10]. They can capture water droplets even in arid and hot environments. High water adhesion can be obtained by using materials of high surface energy and/or with surface structures allowing a higher solid-liquid interface.

Many methods have been used to fabricate artificially the structures and properties found in the nature, such as electrospinning [11], plasma polymerization [12], dip-coating [13], layer-by-layer [14], electropolymerization [15], etc. Electrochemical methods, such as electropolymerization or electrodeposition, consist in a fast and low-cost method that guarantees the electrosynthesis, deposition and structuration of the film in only one-step. Moreover, it is a versatile technique because many parameters influence the morphology and the surface chemistry of the film, such as the electrolyte, the solvent, the method, etc. [16,17] Metals and conducting polymers can be deposited

* Corresponding author.

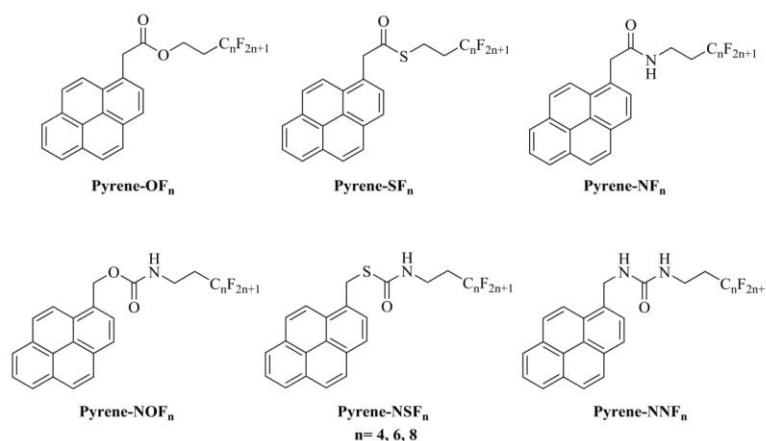
E-mail address: thierry.darmanin@unice.fr (T. Darmanin).

<https://doi.org/10.1016/j.reactfunctpolym.2018.12.001>

Received 31 August 2018; Received in revised form 27 November 2018; Accepted 2 December 2018

Available online 14 December 2018

1381-5148/ © 2018 Elsevier B.V. All rights reserved.



Scheme 1. Original monomers synthesized and studied in this work.

playing an extremely important role in both the electrosynthesis capacity but also in the surface morphology and wettability [18–22].

Conducting polymers are extremely promising materials due to their unique optoelectronic properties with the possibility to introduce various dopants (smart materials) and especially for their high capacity to form various self-assembled structures in solution or directly on substrates [23]. By introducing hydrophobic substituents such as fluorinated chains, superhydrophobic and even sometimes superoleophobic properties with high stability/robustness can be obtained. It was also shown that the linker and the spacer between the hydrophobic chain and the polymerization core have also an important role [24,25]. For example, superoleophobic properties were obtained by a judicious choice of short fluorinated-chain (C_4F_9)-based linkers [24].

Pyrene moiety has been called the attention for their combined fluorescent and superhydrophobic properties [26,27]. Even though the pyrene derivatives present good potential for application in surface science, their use in this field remain scarce. The study of fluorescent superhydrophobic coating is usually limited to only self-assembly method and few fluorescent materials, such as quantum dots or dyes [28–31]. The restriction ways for its manufacture prevents the academic and technological advance for the preparation of robust fluorescent and superhydrophobic coatings.

Here, to advance the research about pyrene moiety, three different fluorinated chains (C_4F_9 , C_6F_{13} and C_8F_{17}) were grafted on pyrene moiety using six different linkers: ester (Py-OF_n), thioester (Py-SF_n), amide (Py-NF_n), carbamate (Py-NOF_n), thiocarbamate (Py-NSF_n) and urea (Py-NNF_n), being *n* the number of carbons on the fluorinated chain. The monomers studied in this work are summarized in Scheme 1. Here our purpose is to evaluate the impact of the combination linker/

side chain on the superhydrophobicity, morphology and fluorescence of the pyrene films after the electropolymerization process.

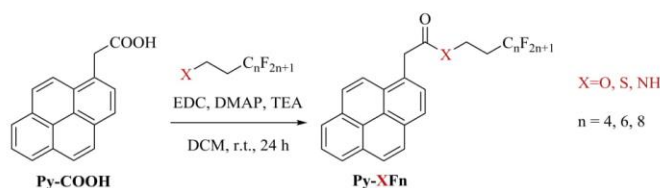
2. Experimental section

2.1. Monomer synthesis and characterization

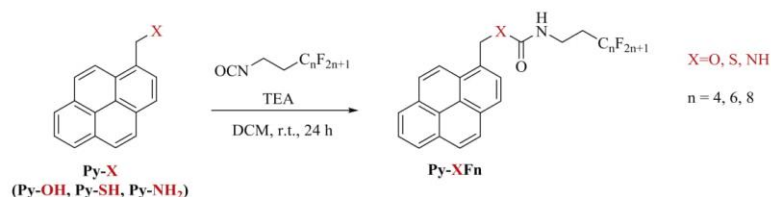
The synthesis of pyrene monomers bearing ester, thioester and amide were performed by the coupling between 1-pyrene acetic acid and the corresponding fluorinated alcohol, thiol and amine, respectively, in anhydrous dichloromethane using EDC as coupling agent in presence of DMAP and TEA (Scheme 2). The series of pyrene monomers containing carbamate, thiocarbamate and urea linkers were synthesized as reported in Scheme 3 based on the nucleophilic addition of modified pyrenes containing alcohol, thiol and amine groups with fluorinated isocyanates in presence of TEA as a base. The monomers were characterized by proton, fluorine and carbon NMR spectroscopy (1H , ^{19}F and ^{13}C NMR) with a W-200 MHz and W-400 MHz (Bruker). Melting points of each monomer were determined via differential scanning calorimetry (Jade DSC-Perkin Elmer) using a thermal scan from 0 °C to 250 °C at a rate of 10 °C min⁻¹. The monomers synthesis and characterization were presented in the Support Information document (see also Scheme S1).

2.2. Electrodeposition of conducting polymers

An Autolab potentiostat (Metrohm) was used for the electropolymerization experiments. A three-system electrode was used with a working electrode, a carbon-rod as the counter electrode and a



Scheme 2. Synthetic route to synthesize the fluorinated pyrenes bearing ester, thioester and amide linkers.



Scheme 3. Synthetic route to synthesize the fluorinated pyrenes bearing carbamate, thiocarbamate and urea linkers.

saturated calomel electrode (SCE) as a reference. Two different substrates were used for the surface characterization: 2 cm² gold-coated silicon plates for the surface characterization and 8 cm² indium tin oxide (ITO)-coated glass plates for fluorescence study. A 0.1 M solution of tetrabutylammonium perchlorate (Bu₄NClO₄) in anhydrous acetonitrile was used as an electrolyte and 0.01 M of each monomer was added inside a glass cell under argon. The monomer oxidation potential

was first determined by cyclic voltammetry ($E^{\text{ox}} = 1.46\text{--}1.55$ V vs SCE at 10 mV/s). The cyclic voltammetry was also used as a deposition method because it allows to obtain films highly homogeneous and with a good adherence in the working electrode [17]. The polymer films were obtained using a scan rate of 20 mV/s and the scans were done between -0.7 V to a potential slightly lower to the monomer oxidation potential, also called as a working potential, E^{w} (Table S1). Surfaces

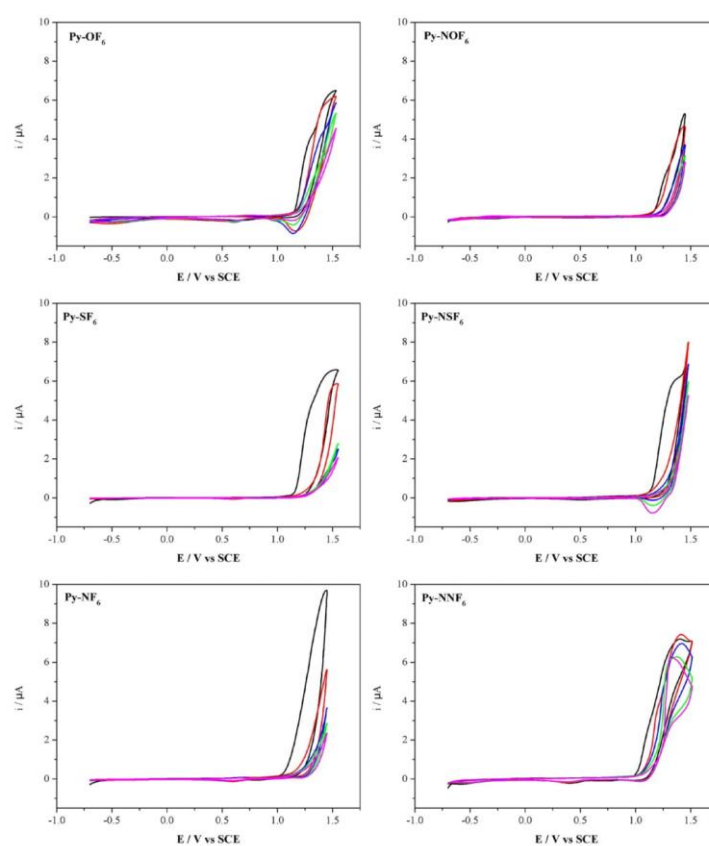
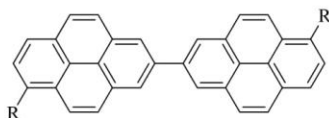


Fig. 1. Cyclic voltammograms of the fluorinated pyrene monomers in 0.1 M Bu₄NClO₄/anhydrous acetonitrile at a scan rate of 20 mV·s⁻¹. Black line: scan 1, red line: scan 2, blue line: scan 3, green line: scan 4, magenta line: scan 5. (For interpretation of the references to colour in this figure legend, the reader is referred to the web version of this article.)



Scheme 4. Example of dimers obtained during the polymerization of substituted pyrenes.

were prepared after deposition of 1, 3 and 5 deposition scans to study the polymer growth.

Analogous smooth surfaces of each monomer were also prepared by a two-step electrodeposition method to obtain the Young's contact angle (θ^V) in 2 cm^2 gold plates. First, a thin layer of film was deposited with an imposed potential method and a low charge (1 mC cm^{-2}) in a very low concentration of each monomer ($\pm 2\text{ mg}$) in the $0.1\text{ M Bu}_4\text{NClO}_4/\text{acetonitrile}$ solution. A polymer reduction was following by cyclic voltammetry performed at 1 scan from 1.5 V to 0 V vs SCE at a scan rate of 20 mV/s just in the solution containing the $\text{Bu}_4\text{NClO}_4/\text{acetonitrile}$, without addition of the monomer.

2.3. Surface characterization

Contact angles measurements were determined by the sessile drop method using a DSA30 goniometer (Krüss) where droplets of $2\ \mu\text{L}$ were gently deposited on the surface at room temperature using a microsyringe. The images were captured using the software "Drop Shape Analysis System". Liquids of different surface tensions (γ_{LV}) were used

to evaluate the wettability: deionized water (72.8 mN/m), diiodomethane (50.0 mN/m) and hexadecane (27.6 mN/m). When the surfaces had high contact angles, the dynamic contact angles were analyzed using the tilted-drop method. In this method, droplets of $6\ \mu\text{L}$ were deposited and the surface was inclined until the drops roll off until the maximum inclination of the surface, also called as sliding angle (α). The advanced (θ_{adv}) and receding (θ_{rec}) contact angles are taken just before the droplet moving giving the hysteresis $H = \theta_{\text{adv}} - \theta_{\text{rec}}$. If the droplet does not move after an inclination of 90° , the substrate is called sticky. The Owens–Wendt equation ($\gamma_{\text{LV}}(1 + \cos \theta) = 2(\gamma_{\text{LV}}^{\text{D}}\gamma_{\text{SV}}^{\text{D}})^{1/2} + 2(\gamma_{\text{LV}}^{\text{P}}\gamma_{\text{SV}}^{\text{P}})^{1/2}$) was used to determine the surface free energy (γ_{SV}) and its dispersive ($\gamma_{\text{SV}}^{\text{D}}$) and polar ($\gamma_{\text{SV}}^{\text{P}}$) parts but only for the smooth surfaces. Three different liquids (water, diiodomethane and hexadecane) were used for which γ_{LV} , $\gamma_{\text{LV}}^{\text{D}}$ and $\gamma_{\text{LV}}^{\text{P}}$ are known γ_{SV} and $\gamma_{\text{SV}}^{\text{P}}$ were calculated by drawing the function $y = ax + b$ where $y = \gamma_{\text{LV}}(1 + \cos \theta)/2(\gamma_{\text{LV}}^{\text{D}})^{1/2}$ and $x = (\gamma_{\text{LV}}^{\text{P}})^{1/2}/(\gamma_{\text{LV}}^{\text{D}})^{1/2}$. Then, $\gamma_{\text{SV}}^{\text{D}} = b^2$ and $\gamma_{\text{SV}}^{\text{P}} = a^2$ were determined. In our case, $\gamma_{\text{SV}}^{\text{D}}$ and $\gamma_{\text{SV}}^{\text{P}}$ were directly obtained using the software "Drop Shape Analysis".

The mean arithmetic roughness (Ra) of the surfaces was determined by an optical profilometry (Wyko NT 1100 of Bruker). The measurements were done with the High Mag Phase Shift Interference (PSI), the $50\times$ objective and the $0.5\times$ field of view and the data were taken using the software "Vision". The scanning electron microscopy (SEM) images were given by a 6700F microscope (JEOL) and 3 kV electron acceleration. The IR spectra were obtained using a Spectrum Spotlight 300 FT-IR microscope (Perkin Elmer). The spectra were collected using the reflectance mode on gold plates with a spectral resolution of 4 cm^{-1} and 32 scans.

XPS spectra were obtained in a conventional electron spectrometer

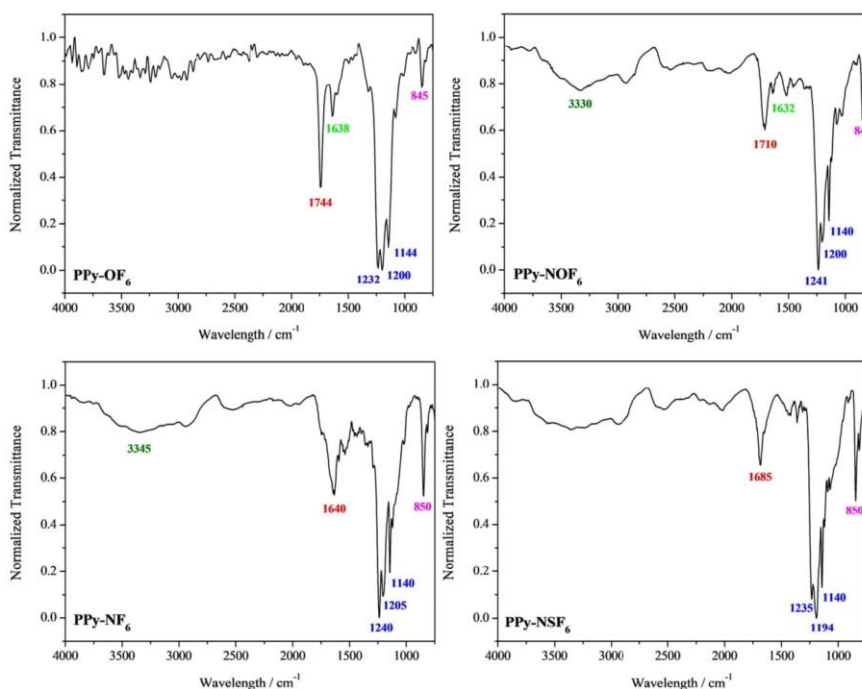


Fig. 2. IR spectra of the fluorinated polypyrenes in $0.1\text{ M Bu}_4\text{NClO}_4/\text{acetonitrile}$ at a scan rate of 20 mV/s . Number of scans: 5.

(Omicron N.T. GmbH, Germany) equipped with a high performance hemispherical energy analyzer and with a seven-channeltron detector. Mg K α radiation was used as excitation source. Survey spectra were recorded, with pass energy of 50 eV, whereas selected atomic signals were acquired with 10 eV of pass energy. In the spectra, the position of the C–C/C–H was specified and other peaks of different carbon environments were fixed, relative to this peak, set at 285.0 eV. XPS spectra were analyzed and peak-fitted after subtraction of the Shirley background using Gaussian–Lorentzian peak shapes obtained from the CasaXPS software package.

2.4. Confocal laser scanning microscopy and emission spectra

Fluorescence images were acquired using Leica TCS SP5-AOBS confocal laser scanning microscope. The surfaces were rinsed by distilled water and imaged using a $\times 63$ –1.4 numerical aperture plan apochromat oil immersion objective. The size of the xy image was 512×512 pixels (image size for zoom 1: $246.03 \times 246.03 \mu\text{m}^2$, zoom 3: $82.01 \times 82.01 \mu\text{m}^2$) recorded on 8 bits. UV laser (364 nm) was used as the excitation source regardless the surface and the corresponding fluorescence was collected in the 450–550 nm spectral range. Each fluorescence intensity image corresponds to an average of 4 frames.

Emission spectra were recorded using zoom 1 with an excitation wavelength of 364 nm, 10 nm bandwidth and an average of 2 frames and the fluorescence spectra using zoom 3.

3. Results and discussion

3.1. Chemical and electrochemical characterization

The electrochemical polymerization was carried out by cyclic voltammetry using a solution of 0.1 M of Bu_4NClO_4 in anhydrous acetonitrile and 0.01 M of each monomer. These conditions proved efficacy to obtain best properties to produce highly hydrophobic polypyrrenes [17]. The polymers were electrodeposited by 1, 3 and 5 deposition scans from -0.7 V to E^{ox} (1.40–1.59 V) at a scan rate of 20 mV/s.

The cyclic voltammograms displayed in Fig. 1 show a decrease in the polymer growth with the increase of the fluorinated chain and the number of scans. The ester, carbamate and thiocarbamate series of polypyrrenes showed similar characteristics for the electropolymerization. A constant deposition of the polymer film with a gradual reduction of the oxidation peaks was noticed. For the thioester and amide series, a drastic reduction after the first scans was observed suggesting a reduction on the thickness of the deposited polymer layer. Differing from

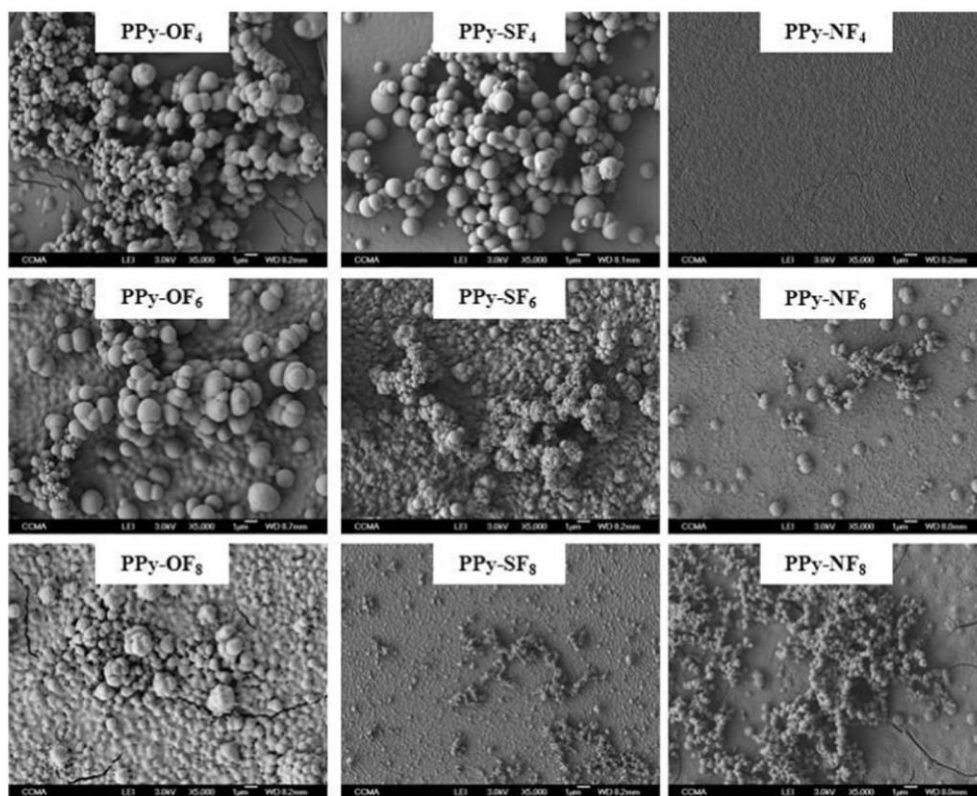


Fig. 3. SEM images of the fluorinated polymers (ester, thioester and amide) electrodeposited by cyclic voltammetry (3 scans) in a 0.1 M solution of Bu_4NClO_4 /acetonitrile. Magnifications: $5000\times$.

Table 1

Apparent and dynamic contact angles and roughness data as a function of the polymer and the number of deposition scans of the fluorinated polypyrenes bearing ester, thioester and amide linkers. Polymerization at 0.1 M solution Bu₄NClO₄/acetonitrile.

Polymer	Number of deposition scans	Ra [nm]	θ_{water} [deg]	H_{water}	α_{water}	θ_{diiodo} [deg]	θ_{hexa} [deg]
PPy-OF ₈	1	60	125.0	Sticky		130.6	91.2
	3	180	157.8	1.5	2.0	130.0	97.5
	5	250	156.3	16.0	15.2	131.0	85.6
PPy-OF ₆	1	45	136.5	Sticky		103.0	74.6
	3	580	159.4	1.1	1.1	137.8	93.3
	5	1150	160.0	0.9	1.0	135.8	95.0
PPy-OF ₄	1	65	116.4	Sticky		85.2	49.3
	3	460	157.6	4.1	3.8	105.7	43.2
	5	630	155.9	29.7	21.6	108.8	36.8
PPy-SF ₈	1	16.7	128.9			103.5	72.3
	3	34.6	127.1	Sticky		100.9	74.9
	5	26.2	122.0			99.3	73.4
PPy-SF ₆	1	149.5	155.6	36.5	19.7	118.8	82.1
	3	583.6	157.8	0.5	1.0	144.2	123.6
	5	849.1	156.0	0.6	1.0	147.6	113.3
PPy-SF ₄	1	23.2	109.7	Sticky		82.6	55.7
	3	136.7	154.5	1.6	9.7	100.8	58.0
	5	525.5	127.3	Sticky		97.0	57.6
PPy-NF ₈	1	22.3	118.1			97.7	66.1
	3	81.2	151.4	Sticky		112.1	61.4
	5	111.4	140.8			105.9	76.0
PPy-NF ₆	1	15.9	124.6			109.0	79.0
	3	85.6	130.7	Sticky		103.1	72.8
	5	79.4	118.0			92.7	75.8
PPy-NF ₄	1	7.6	99.7			77.0	45.9
	3	10.2	116.4	Sticky		102.6	59.1
	5	53.8	109.0			95.1	60.9

the other pyrenes, for urea series the oxidation and reduction peaks of the monomers and the corresponding polymers are further away from each other. Indeed, the urea linker induced higher intermolecular interactions which may decrease the substituent flexibility, mobility and may also decrease the steric hindrance. It is known that long fluorinated chains can induce two different effects in the polymerization: first, it can increase the steric hindrance due to the increase in the substituent chain; and second, it can decrease the steric hindrance due to the decrease in the substituent mobility [32,33].

Moreover, the oxidation and reduction potentials of the corresponding polymers are very close to that of the monomers which indicates that the polymer chain lengths are also very short. As reported in the literature, non-substituted pyrene electropolymerized in similar conditions gives oligomers of only 6–11 units [26]. This is expected due to the numerous polymerization sites in the pyrene molecule. Furthermore, by a combination of electrochemical and chemical methods, Chen and co-workers obtained an average repeat unit of 4 when the monomer (2-(4-(1-pyrenyl)butanoyloxy)ethyltrimethylammonium bromide) was polymerized [34]. The high steric hindrance of pyrene with voluminous substituents reduces the polymer chain length to only some units. However, due to the multiple polymerization sites of pyrene moiety, numerous different oligomers can be formed during the polymerization. An example of a dimer of pyrene derivative is given in Scheme 4. It is surprising that oligomers of only few units are sufficiently insoluble to deposit as film, but it can be explained by the fact that pyrene is known to induce extremely strong π -stacking interactions allowing self-assemblies and fast deposition on the substrate [35–37].

The polymeric films were characterized by FTIR spectroscopy as showed in Fig. 2. The IR spectra show the characteristics peaks from C=O and C–H in around 1700 and 845 cm⁻¹, respectively. The position of the peaks of the carbonyl groups is slightly shifted due to the use of different linkers. The nature of the linker and the presence of different intermolecular interactions on the polymer films influence the energy of carbonyl stretching due to their inductive and mesomeric forces. As expected, no influence in the frequency of C=O stretching was observed regardless of the size of the fluorinated chains. The peaks

around 1100–1300 cm⁻¹ are attributed to the stretching of C–F present in these pyrenes. For the amide, carbamate, thiocarbamate and urea series, a peak at nearly 3300 cm⁻¹ is attributed to the N–H stretching.

3.2. Surface characterization

The SEM images and the roughness data are given in Fig. 3 and Table 1 for the ester, thioester and amide series and in Fig. 4 and Table 2 for the carbamate, thiocarbamate and urea series. As shown for the non-fluorinated molecules, the polymerization of substituted pyrenes induces a deposition of spherical particles of different sizes. A clear trend of decreasing roughness with the increase of the fluorinated chain is observed within the ester, thioester, carbamate and thiocarbamate series. Regarding the nano-particle size for PPy-NSF_n series, for example, the diameter decreases with the number of carbons: $\varnothing \approx 800$ nm for $n = 4$, $\varnothing \approx 500$ nm for $n = 6$ and $\varnothing \approx 350$ nm for $n = 8$.

On surfaces with short fluorinated chains, the nanospheres are more defined and in a bigger amount compared with the longer fluorinated chains. In opposition, the deposition of PPy-NF_n and PPy-NNF_n form relatively smooth surfaces with nano-scale topography. This result is not surprising since the monomers containing amide and urea moieties are more polar and, consequently, form more soluble polymers, thus generating surfaces smoother and/or less structured. Generally, in the case of the fluorinated pyrenes, the surface of the spherical particles is not smooth, but nanostructured as showed Fig. 5. Indeed, it is known that a dual-scale surface roughness can have a high impact on the superhydrophobic properties and can highly reduce the contact angle hysteresis [35]. The summary of the mean apparent contact angles (θ) of liquids differing by their surface tension (water, diiodomethane and hexadecane), the hysteresis (H) and sliding angles (α) is given in Tables 1 and 2.

Superhydrophobic properties with very low H and α were obtained for PPy-OF_n and PPy-NOF_n series and for PPy-SF_n and PPy-NSF_n when $n < 8$. Concerning the morphological aspect, the increase on the fluorinated chain from $n = 6$ to $n = 8$ decreases θ_w in good agreement

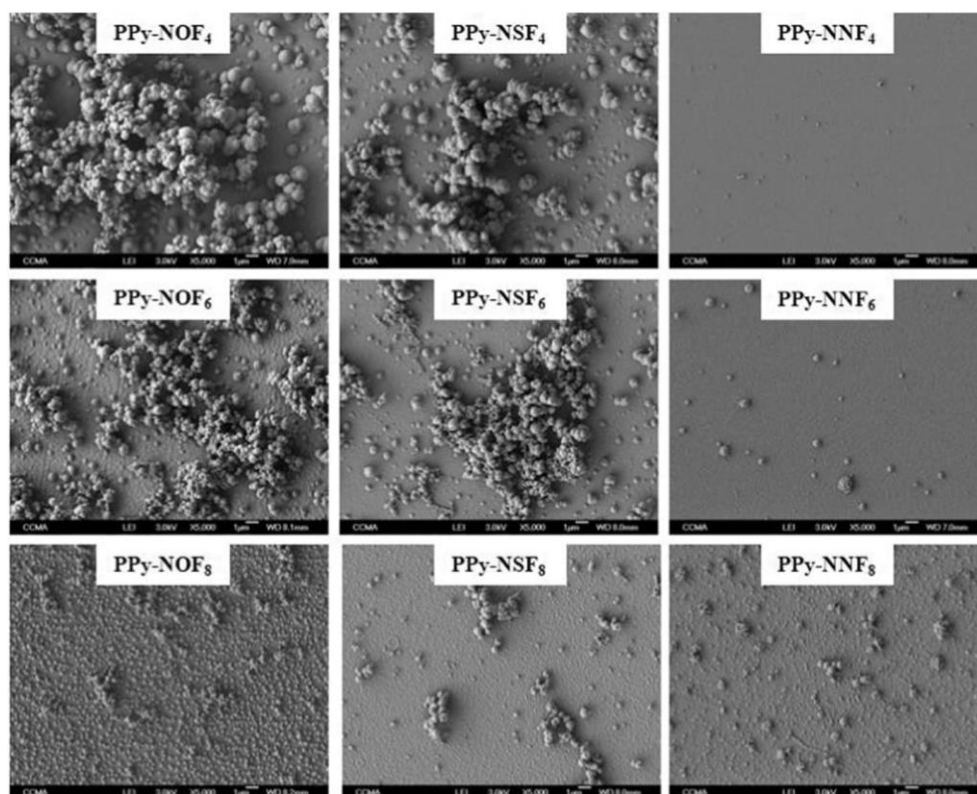


Fig. 4. SEM images of the fluorinated polymers (carbamate, thiocarbamate and urea) electrodeposited by cyclic voltammetry (3 scans) in a 0.1 M solution of $\text{Bu}_4\text{NClO}_4/\text{acetonitrile}$. Magnifications: $5000\times$.

with the formation of less structured surfaces as showed by the SEM images. The superhydrophobicity can be explained by the presence of micro and nanostructures observed on these polymer films. The surfaces composed by polymers with amide and urea linker present high θ_w , but also higher H and α . Regarding PPy-NF_n and PPy-NNF_n series, the most hydrophobic surface was obtained for 3 and 5 deposition scans, respectively, independently of the chain length. It is already expected that the amide and urea series showed the less hydrophobic surfaces because of their linker polarity and, consequently, the formation of less structured surfaces.

Indeed, XPS spectroscopy was used to analyze the chemical aspect of the as-prepared superhydrophobic surfaces with very low H and α : PPy-OF₆, PPy-SF₆ and PPy-NOF₆. XPS wide scan spectra of electrodeposited films by cyclic voltammetry (1 scan) are shown in Fig. 6. Three main signals corresponding to Fluorine (F 1s, 689.2 eV), Oxygen (O 1s, 532.7 eV) and Carbon (C 1s, 285–294.2 eV) contributions appeared in the survey spectra. PPy-SF₆ and PPy-NOF₆ films showed additional signals of Sulfur and Nitrogen in lower amounts (2.5% and 0.8% respectively). As observed in the survey spectra, the elemental F 1s composition calculated is over 25% with only one cyclic voltammetry scan for PPy-OF₆, PPy-SF₆ and PPy-NOF₆ films. This high amount of fluorine in the surface region led to the high hydrophobicity

observed previously. When the number of scans increased to three, for example, the amount of fluorine in the surface slightly increased (results not shown), but due to the increase in roughness (see Tables 1 and 2) the surfaces were converted in superhydrophobic with very low H and α . Fig. 6 also shows the deconvolution of the C 1s peaks that can be decomposed into five, six and seven main components for PPy-OF₆, PPy-SF₆ and PPy-NOF₆, respectively. The signals can be assigned to the following functional groups: C–C/C–H including C=C (285.2 eV), C–S (285.7 eV), C–N (286 eV), C–O (287 eV), C=O (289 eV), COO (290 eV), CF₃-CF₂- (292 eV) and CF₃ (294 eV) [38]. The C 1s deconvolution shows clearly the presence of fluorinated functionalities in high relative concentration in the surface region.

It is not surprising that the surfaces having the best hydrophobicity are also the most oleophobic. The carbamate series presented the best oleophobicity for both liquids, achieving the superoleophobicity for diiodomethane ($\theta_{\text{diiodo}} = 150.3^\circ$) and highly oleophobic properties for hexadecane ($\theta_{\text{hexa}} = 106^\circ$) due to their surface structure and the use of low surface energy compounds. Fig. 7 shows the images of the water droplets of water, diiodomethane and hexadecane for the PPy-NOF₆. As expected, PPy-OF_n series is also highly oleophobic for diiodomethane and in the limit between oleophilicity and oleophobicity using hexadecane. Therefore, PPy-SF_n, PPy-NF_n, PPy-NSF_n and PPy-NNF_n are

Table 2

Apparent and dynamic contact angles and roughness data as a function of the polymer and the number of deposition scans of the fluorinated polypyrrenes bearing carbamate, thiocarbamate and urea linkers. Polymerization at 0.1 M solution $\text{Bu}_4\text{NClO}_4/\text{acetonitrile}$.

Polymer	Number of deposition scans	Ra [nm]	θ_{water} [deg]	H_{water}	α_{water}	θ_{diiodo} [deg]	θ_{hexa} [deg]
PPy-NOF ₈	1	36.3	132.6	Sticky		108.5	79.1
	3	63.8	157.7	4.3	5.2	140.4	104.3
	5	75.3	157.4	2.1	3.2	148.4	103.4
PPy-NOF ₆	1	35.5	124.9	Sticky		109.4	75.9
	3	316.4	156.7	1.7	2.4	150.3	106.0
	5	447.1	157.6	1.4	3.2	147.9	86.9
PPy-NOF ₄	1	74.0	123.2	Sticky		97.5	58.7
	3	1400.0	156.0	3.2	2.3	146.9	72.7
	5	2500.0	156.8	4.5	2.6	147.8	66.1
PPy-NSF ₈	1	17.0	122.2			94.2	67.2
	3	26.5	119.5	Sticky		98.4	65.8
	5	30.6	123.6			103.2	68.5
PPy-NSF ₆	1	14.0	121.2	Sticky		97.3	59.1
	3	96.4	126.9	Sticky		101.7	67.0
	5	69.7	153.0	2.0	7.0	115.1	64.3
PPy-NSF ₄	1	16.4	108.8	Sticky		87.5	40.5
	3	197.2	155.7	1.0	2.0	110.9	55.1
	5	311.9	155.1	Sticky		123.6	68.7
PPy-NNF ₈	1	12.5	116.5	Sticky		97.6	75.8
	3	17.9	126.8	Sticky		113.4	91.0
	5	46.0	155.6	3.0	6.0	132.6	95.7
PPy-NNF ₆	1	7.1	109.7			94.0	66.0
	3	9.2	111.1	Sticky		95.4	72.3
	5	25.4	122.6			100.3	75.7
PPy-NNF ₄	1	7.5	107.0			87.4	61.6
	3	10.4	108.1	Sticky		91.2	59.8
	5	7.0	105.1			87.5	58.4

oleophobic and oleophilic for diiodomethane and hexadecane, respectively.

However, to give a better explanation of the structural-chemical effect on the wettability, smooth surfaces ($Ra = 6.8\text{--}10.0\text{ nm}$) were prepared (Table 3). PPy-OF_n and PPy-SF_n (for $n = 6$ or 8) are

intrinsically hydrophobic ($\theta_w^V > 90^\circ$) which may explain the higher wetting properties for the structured polymers. In contrast for $n = 4$ a slight hydrophilicity is observed. However, for the monomers with amide, carbamate, thiocarbamate and urea, an intrinsically hydrophilic behavior is observed ($\theta_w^V < 90^\circ$), which may be explained by the

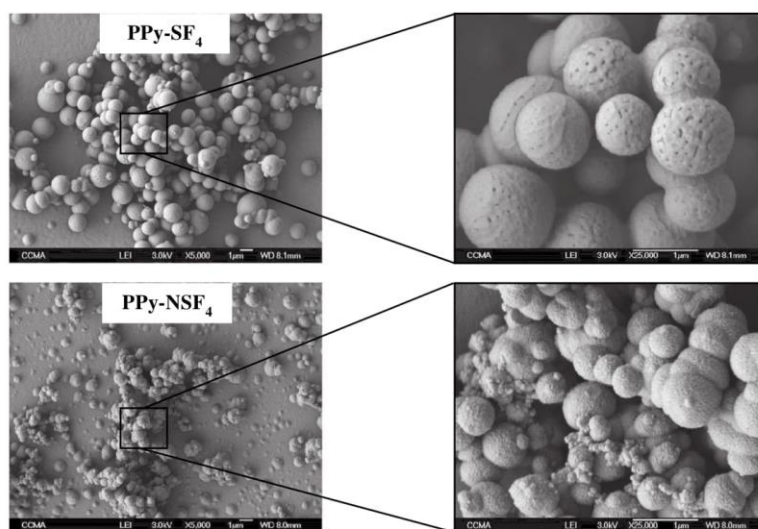


Fig. 5. SEM images of the fluorinated polymers using thiol and thiocarbamate linkers at high magnification (25,000 ×). Electropolymerization by cyclic voltammetry (3 scans) in a 0.1 M solution of $\text{Bu}_4\text{NClO}_4/\text{acetonitrile}$.

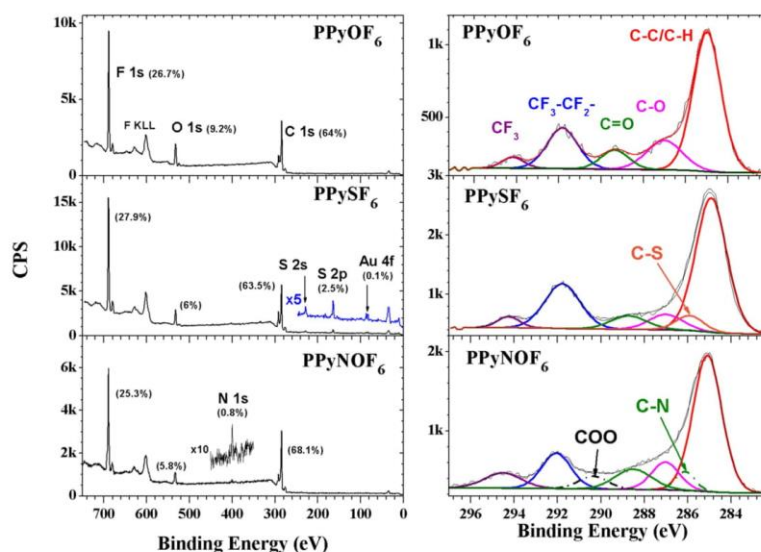


Fig. 6. Survey (left) and high-resolution (right) XPS spectra for the C 1s region of the fluorinated polymers (ester, thioester and carbamate) electrodeposited by cyclic voltammetry (1 scan) in a 0.1 M solution of $\text{Bu}_4\text{NClO}_4/\text{acetonitrile}$.



Fig. 7. Picture of the droplets deposited on PPy-NOF₆ surfaces with all probe liquids. Electropolymerization by cyclic voltammetry (3 scans) in a 0.1 M solution of $\text{Bu}_4\text{NClO}_4/\text{acetonitrile}$.

presence of N–H bonds favoring the affinity with water. Here, even with long fluorinated chains that present very low surface energy, the presence of polar N–H bonds shows a strong influence on the wettability due to their high polarity. This result is supported by the literature where monomers derived from thiophenes containing a carbamate linker showed $\theta_w^v < 90^\circ$ which were attributed by the high polarity of the linker group [39]. The series with less polar linkers, such as ester, thioester, carbamate and thiocarbamate, presented a higher improvement in their hydrophobicity compared with the amide and urea linker due to their lower polarity. Analyzing the interaction between the smooth surfaces and liquids with lower surface tension, we observed no significant changes for θ_{diiodo}^v and very low θ_{hexa}^v . PPy-SF₈

Table 3

Apparent contact angles and roughness data for the smooth corresponding polymers of the non-fluorinated pyrenes. Polymerization at 0.1 M solution $\text{Bu}_4\text{NClO}_4/\text{acetonitrile}$.

Smooth polymer	Ra [nm]	θ_w [deg]	θ_{diiodo} [deg]	θ_{hexa} [deg]	γ_{sv} [mN m ⁻¹]	γ_{sv}^0 [mN m ⁻¹]	γ_{sv}^v [mN m ⁻¹]
PPy-OF ₈	9.7	92.8	59.2	18.9	29.6	27.6	2.0
PPy-OF ₆	9.8	90.2	43.4	15.8	33.9	32.0	1.9
PPy-OF ₄	10.0	85.7	36.7	9.9	36.7	33.9	2.8
PPy-SF ₈	9.9	97.1	62.3	26.3	27.3	26.0	1.3
PPy-SF ₆	9.3	95.6	56.6	19.8	29.5	28.2	1.3
PPy-SF ₄	7.0	87.8	44.7	11.7	34.7	32.2	2.5
PPy-NF ₈	8.7	89.3	55.3	13.0	31.7	29.0	2.7
PPy-NF ₆	7.3	82.5	46.9	11.0	35.8	31.4	4.4
PPy-NF ₄	6.8	86.6	33.0	9.8	37.2	34.8	2.4
PPy-NOF ₈	8.1	84.4	45.9	0	34.9	31.1	3.8
PPy-NOF ₆	8.6	85.0	47.9	0	34.9	31.4	3.5
PPy-NOF ₄	8.3	83.6	44.4	0	36.1	32.3	3.8
PPy-NSF ₈	8.6	78.4	43.2	0	38.3	32.6	5.7
PPy-NSF ₆	8.6	84.2	39.0	0	36.9	33.6	3.3
PPy-NSF ₄	8.1	81.9	36.4	0	38.1	34.1	4.0
PPy-NNF ₈	8.6	83.2	37.3	0	37.5	33.9	3.6
PPy-NNF ₆	8.5	83.7	41.1	0	36.7	33.1	3.6
PPy-NNF ₄	8.3	82.1	43.6	0	36.8	32.5	4.3

shows the highest intrinsically wetting: $\theta_{\text{diiodo}}^{\text{V}} = 62.3^\circ$ and $\theta_{\text{hexa}}^{\text{V}} = 26.3^\circ$.

Hence, most of the results obtained with water cannot be explained with the Wenzel equation. In the case of liquids with lower surface tension such as diiodomethane and hexadecane, for example, a slight increase of θ^{V} is observed for the fluorinated polypyrenes even if they are highly oleophilic. As proposed by Marmur [40], a parahydrophobic surface is able to trap a high amount of air inducing a high increase in θ even if $\theta^{\text{V}} < 90^\circ$. This can explain the surfaces with a sticky behavior (PPy-NF_n and PPy-NNF_n series). In the case of the superhydrophobic surfaces (high θ and low H and a), the presence of a dual-scale surface roughness allows to trap a high amount of air between the different liquids and the surface as described by the Cassie-Baxter equation [41]. The surface energy data presented in Table 3 showed a lower polar component for PPy-OF_n and PPy-SF_n, which can explain their highest $\theta_{\text{w}}^{\text{V}}$. For the other polymers no significant changes were observed.

From these results, the nature of the heteroatom (O, S and N) which connect the linker with the pyrene unit does greatly impact in the wetting behaviour. While for polymers using thioester, thiocarbamate, amide or urea linkers, a wide range of wettability was obtained for water- and oleo-phobicity of the structured surfaces, for the ester and carbamate series a suitable superhydrophobicity and highly oleophobicity was obtained from 3 deposition scans.

3.3. Fluorescent properties

The pyrene monomer has calling attention of the researches for their unique fluorescent properties. It is known that their absorption and emission may be affected by the polymerization method and the functionalization on the monomer unit [8,26]. Here we will present a brief study concerning the fluorescence properties for the fluorinated polypyrenes ($n = 6$) using different linkers.

Fig. 8 depicts fluorescence emission spectrum for the various films. The polypyrenes films emission spectrum present a single and broad structureless band. While the pyrene monomers displayed a structured emission spectra shape [42], a red-shift and broadness shape of the emission spectra is observed for the fluorinated polypyrenes deposited on the surfaces. This behaviour is very characteristic from an excimer emission of pyrene and such observations are in agreement with the literature [43]. As shown by Konishi and co-workers, it is likely that the methylene group which is connected to the aromatic ring controls the red shift in the absorption band [44]. Indeed, since the characteristic

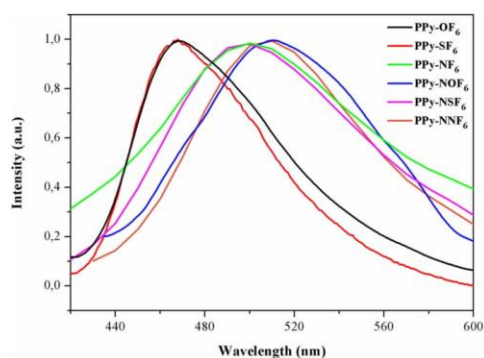


Fig. 8. Emission spectra (normalized to 1 at the maximum intensity of each spectrum) for the fluorinated polypyrenes ($n = 6$) with different linkers. Emission (λ_{em} : 364 nm) of films. Polymerization in solution 0.1 M Bu₄NClO₄/acetonitrile. Number of scans: 2. Deposition on ITO substrates.

Table 4
Spectroscopic parameters of fluorinated polypyrene. Polymerization in solution 0.1 M Bu₄NClO₄/acetonitrile. Number of scans: 2. Deposition in ITO plates.

Surfaces	$\lambda_{\text{em,max}}$ (nm)	FWHM _{em} (cm ⁻¹)
PPy-OF ₆	468	3204
PPy-SF ₆	468	2979
PPy-NF ₆	500	5081
PPy-NOF ₆	510	3854
PPy-NSF ₆	500	4279
PPy-NNF ₆	510	3419

spectral shape of the pyrene monomer is no longer seen, it confirms the oligomerization of the fluorinated pyrenes.

Concerning the maximum position, two films show a quite different behaviour from the others: PPy-OF₆ and PPy-SF₆ with a 468 nm emission maximum, whereas all other films the emission stands around 500–510 nm (Table 4). Looking at the full width at half maximum (FWHM) in emission, a similar trend exists: PPy-OF₆ and PPy-SF₆ have smaller FWHM (respectively 3204 and 2979 cm⁻¹) than for the other linkers (between 3419 and 5081 cm⁻¹). In emission, the presence of the nitrogen atom seems important due to the increase in the polarity of the film. For the ester and thiol series, the effect of aggregation due to the hydrogen bonds is smaller than for the other linkers (amide, carbamate, thiocarbamate and urea). One may assume that if the interaction or the aggregation state increases, then a red-shift and broadening of the band is expected.

Moreover, fluorescence confocal images for the polypyrenes using different linkers and the same chain length ($n = 6$) in Fig. S1 show all the polymer films emitted in the green region. This observation agrees with the literature: the pyrene emission can be in the blue region [45–48], but also in the green region [26,48,49]. In another case, as reported by Rajagopal and co-authors, the formation of green-yellow-orange luminescent crystals could be achieved due to the decrease in the π - π interactions (π -stacking) causing a systematic blue-shift in the emitted light in the crystalline state [50]. Thereby, the emission of pyrene (monomer, oligomer, polymer) will normally depend of the excimer emission. The fluorescence intensity of the spherical particles formed on the surface are much stronger compared with places that have less polymer deposited and the micro and nanometer size of the particles are completely consistent with SEM images. Indeed, in agreement with the roughness and SEM data, the confocal images (Fig. S1) and the confocal orthogonal views (Fig. 9) showed a rougher and more structured surface for ester, thioester, carbamate and thiocarbamate series than for amide and urea series. The thickness of the polymeric films could be also estimated by the orthogonal views: PPy-OF₆ around 10–20 μm , PPy-SF₆ around 8–10 μm , PPy-NOF₆ around 10 μm and PPy-NNF₆ around 5–8 μm (not possible to measure the z-stack for PPy-NF₆ and PPy-NSF₆). These values are not the precise thickness and they will depend of the zone, but they could provide an estimate of the real thickness of these surfaces. Indeed, here we confirm that the fluorescence confocal images well corroborate the SEM images and similar topographies are observed whatever the sample is.

4. Conclusion

In this work we showed the electropolymerization of tunable superhydrophobic surfaces using pyrene derivatives differing by their fluorinated chain length (from 4 to 8 carbons) and by the linker that connects it to the pyrene moiety (ester, thioester, amide, carbamate, thiocarbamate and urea) with fluorescent properties. Both factors showed to influence the morphology, wetting properties and fluorescence. The N–H group showed a huge impact in the electropolymerization process due to its higher polarity yielding smoother surfaces and, consequently, lower θ_{w} . Indeed, for the chemical aspect, intrinsically hydrophobic polymers were obtained for the ester and

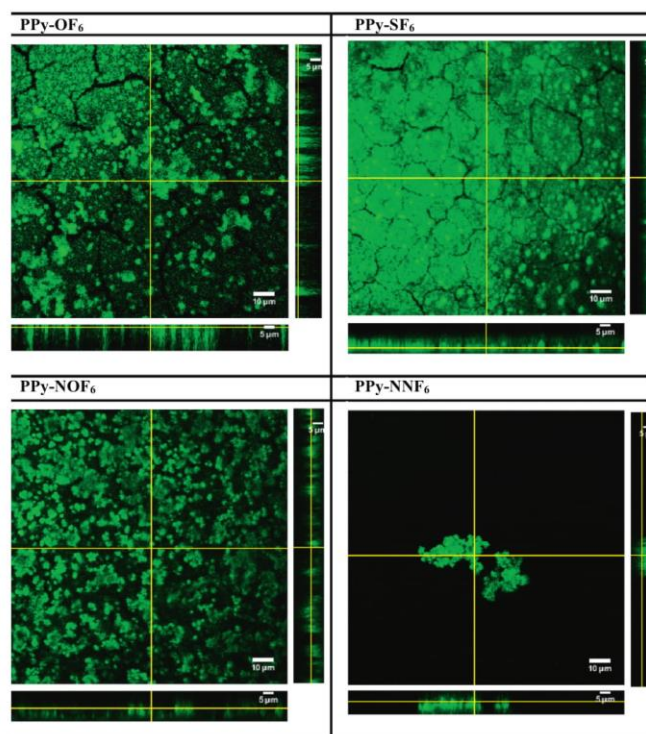


Fig. 9. Confocal fluorescence microscopy and their respective orthogonal views. Polymerization in solution 0.1 M $\text{Bu}_4\text{NClO}_4/\text{acetonitrile}$. Number of scans: 2. Deposition in ITO plates. Polymeric films in the green channel, $\lambda_{\text{exc}} = 364 \text{ nm}$, $\lambda_{\text{em}} = 450\text{--}550 \text{ nm}$. The surrounding medium is water. (For interpretation of the references to colour in this figure legend, the reader is referred to the web version of this article.)

thioester series (no presence of the N–H group) in comparison with the amide, carbamate, thiocarbamate and urea series (intrinsically hydrophilic). Then, superhydrophobic surfaces were obtained for ester, thioester, carbamate and thiocarbamate series and parahydrophobic surfaces for amide and urea series. Indeed, the presence of N–H seems to also influence the fluorescence properties: a red-shift emission is observed for amide, carbamate, thiocarbamate and urea series due to the increase in the aggregation. On the other hand, a softer aggregation effect is observed for ester and thioester groups due to hydrogen bonds and the absence of N–H groups. A green emission is observed for all the surfaces independently of the linker and the length of the chain. This work showed a facile process to fabricate superhydrophobic and fluorescent polymer films and described the impact of the heteroatom from the linker in their properties (morphology, wettability, surface chemistry and fluorescence). Indeed, it opens new doors to explore the pyrene derivatives and their functionalities on the domain of surface science.

Acknowledgments

This work was supported by a grant from CNPq, Conselho Nacional de Desenvolvimento Científico e Tecnológico - Brazil (Process N° 202280/2014-4) for the PhD thesis of Gabriela Ramos Chagas.

Appendix A. Supplementary data

The monomer synthesis and electrochemical potential as well as supplementary fluorescence pictures can be found online at <https://doi.org/10.1016/j.reactfunctpolym.2018.12.001>.

References

- [1] W. Barthlott, M. Mail, B. Bhushan, K. Koch, Plant surfaces: structures and functions for biomimetic innovations, *Nano-Micro Lett.* 9 (23) (2017) 1–40.
- [2] T. Darmanin, F. Guitard, Superhydrophobic and Superoleophobic Properties in Nature, *Mater. Today* 18 (2015) 273–285.
- [3] G.S. Watson, D.W. Green, B.W. Cribb, C.L. Brown, C.R. Meritt, M.J. Tobin, J. Vongsivut, M. Sun, A.-P. Liang, J.A. Watson, Insect analogue to the lotus leaf: a planthopper wing membrane incorporating a low-adhesion, nonwetting, superhydrophobic, bactericidal, and biocompatible surface, *Appl. Mater. Interfaces* 9 (2017) 24381–24392.
- [4] L. Feng, Y. Zhang, J. Xi, Y. Zhu, N. Wang, F. Xia, L. Jiang, Petal effect: a superhydrophobic state with high adhesive force, *Langmuir* 24 (8) (2008) 4114–4119.
- [5] B. Bhushan, M. Nosonovsky, The rose petal effect and the modes of superhydrophobicity, *Philos. Trans. R. Soc.* 368 (2010) 4713–4728.
- [6] M. Gürsoy, M.T. Harris, A. Carletto, A.E. Yaprak, M. Karaman, J.P.S. Badyal, Bioinspired asymmetric-anisotropic (Directional) fog harvesting based on the arid climate plant *eremopyrum orientale*, *Colloids Surfaces A* 529 (2017) 959–965.
- [7] J. Li, R. Wu, Z. Jing, L. Yan, F. Zha, Z. Lei, One-step spray-coating process for the fabrication of colorful superhydrophobic coatings with excellent corrosion resistance, *Langmuir* 31 (2015) 10702–10707.
- [8] G. Ramos Chagas, G. Morán Cruz, G. Giraudon-Colas, F. Savina, R. Méallet-Renault,

- S. Amigoni, F. Guittard, T. Darmanin, Anti-bacterial and fluorescent properties of hydrophobic electrodeposited non-fluorinated polypyrenes, *Appl. Surf. Sci.* 452 (2018) 352–363.
- [9] S. Farhadi, M. Farzaneh, S.A. Kulnich, Anti-icing performance of superhydrophobic surfaces, *Appl. Surf. Sci.* 257 (14) (2011) 6264–6269.
- [10] C.R. Szczepanski, F. Guittard, T. Darmanin, Recent advances in the study and design of parahydrophobic surfaces: from natural examples to synthetic approaches, *Adv. Colloid Interf. Sci.* 241 (2017) 37–61.
- [11] Z. Liu, H. Wang, X. Zhang, C. Wang, C. Lv, Y. Zhu, Durable and self-healing superhydrophobic surface with bistratal gas layers prepared by electrospinning and hydrothermal processes, *Chem. Eng. J.* 326 (2017) 578–586.
- [12] D. Kontziampasis, G. Bouloousis, A. Smyrnakis, K. Ellinas, A. Tseripi, E. Gogolides, Biomimetic, antireflective, superhydrophobic and oleophobic PMMA and PMMA-coated glass surfaces fabricated by plasma processing, *Microelectron. Eng.* 121 (2014) 33–38.
- [13] C.B. Contreras, G. Chagas, M.C. Strumia, D.E. Weibel, Permanent superhydrophobic polypropylene nanocomposite coatings by a simple one-step dipping process, *Appl. Surf. Sci.* 307 (2014) 234–240.
- [14] J. Yang, H. Li, T. Lan, L. Peng, R. Cui, H. Yang, Preparation, characterization, and properties of fluorine-free superhydrophobic paper based on layer-by-layer assembly, *Carbohydr. Polym.* 178 (2017) 228–237.
- [15] M. Nicolas, Acids and alkali resistant sticky superhydrophobic surfaces by one-pot electropolymerization of Perfluoroalkyl Alkyl Pyrrole, *J. Colloid Interface Sci.* 343 (2010) 608–614.
- [16] G. Ramos Chagas, T. Darmanin, F. Guittard, One-step and templateless electropolymerization process using thienothiophene derivatives to develop arrays of nanotubes and tree-like structures with high water adhesion, *ACS Appl. Mater. Interfaces* 8 (34) (2016).
- [17] G. Ramos Chagas, T. Darmanin, G. Godeau, S. Amigoni, F. Guittard, Superhydrophobic properties of electrodeposited fluorinated polypyrenes, *J. Fluor. Chem.* 193 (2017) 73–81.
- [18] L. Wu, J.E. Graves, A.J. Copley, Mechanism for the development of Sn-Cu alloy coatings produced by pulsed current electrodeposition, *Mater. Lett.* 217 (2018) 120–123.
- [19] P.N.S. Casciano, R.L. Benevides, R.A.C. Santana, A.N. Correia, P. Lima-Neto, Factorial design in the electrodeposition of Co-Mo coatings and their evaluations for hydrogen evolution reaction, *J. Alloys Compd.* 723 (2017) 164–171.
- [20] R. Akbari, G. Ramos Chagas, G. Godeau, M. Mohammadzadeh, F. Guittard, T. Darmanin, Intrinsically water-repellent copper oxide surfaces; an electro-crystallization approach, *Appl. Surf. Sci.* 443 (2018) 191–197.
- [21] S. Lupu, F. Javier Del Campo, F. Xavier Muñoz, Sinusoidal voltage electrodeposition and characterization of conducting polymers on gold microelectrode arrays, *J. Electroanal. Chem.* 687 (2012) 71–78.
- [22] H.J. Nogueira Pedrosa Dias Mello, M. Mulato, Influence of galvanostatic electrodeposition parameters on the structure-property relationships of polyaniline thin films and their use as potentiometric and optical pH sensors, *Thin Solid Films* 656 (2018) 14–21.
- [23] C. Li, H. Bai, G. Shi, Conducting polymer nanomaterials: electrosynthesis and applications, *Chem. Soc. Rev.* 38 (8) (2009) 2397–2409.
- [24] T. Darmanin, F. Guittard, Superoleophobic surfaces with short fluorinated chains? *Soft Matter* 9 (25) (2013) 5982–5990.
- [25] T. Darmanin, F. Guittard, Highly polar linkers (Urea, Carbamate, Thiocarbamate) for superoleophobic/superhydrophobic or oleophobic/hydrophilic properties, *Adv. Mater. Interfaces* 2 (2015) (1500081/1–7).
- [26] L. Xu, F. Tong, X. Lu, K. Lu, Q. Lu, Multifunctional polypyrrole/silica hybrid coatings with stable excimer fluorescence and robust superhydrophobicity derived from electrodeposited polypyrrole films, *J. Mater. Chem. C Mater. Opt. Electron. Dev.* 3 (2015) 2086–2092.
- [27] G. Ramos Chagas, X. Xie, T. Darmanin, K. Steenkeste, A. Gaucher, D. Prim, R. Méaller-Renault, G. Godeau, S. Amigoni, F. Guittard, Electrodeposition of polypyrenes with tunable hydrophobicity, water adhesion, and fluorescence properties, *J. Phys. Chem. C* 120 (13) (2016) 7077–7087.
- [28] L. Hou, C. Wang, L. Chen, S. Chen, Multiple-structured nanocrystals towards bifunctional photoluminescent-superhydrophobic surfaces, *J. Mater. Chem.* 20 (2010) 3863–3868.
- [29] J. Hong, W.K. Bae, H. Lee, S. Oh, K. Char, F. Caruso, J. Cho, Tunable superhydrophobic and optical properties of colloidal films coated with block copolymer micelles/micelle multilayers, *Adv. Mater.* 19 (2007) 4364–4369.
- [30] S. Yang, L. Wang, C.-F. Wang, L. Chen, S. Chen, Superhydrophobic thermoplastic polyurethane films with transparent/fluorescent performance, *Langmuir* 26 (23) (2010) 18454–18458.
- [31] S. Yang, C. Zhou, J. Liu, M. Yu, J. Zheng, One-step interfacial synthesis and assembly of ultrathin luminescent AuNPs/silica membranes, *Adv. Mater.* 24 (2012) 3218–3222.
- [32] K. Honda, M. Morita, H. Otsuka, A. Takahara, Molecular aggregation Structure and surface properties of poly (Fluoroalkyl Acrylate) thin films, *Macromolecules* 38 (2005) 5699–5705.
- [33] K. Honda, M. Morita, O. Sakata, S. Sasaki, A. Takahara, Effect of surface molecular aggregation state and surface molecular motion on wetting behavior of water on poly(fluoroalkyl Methacrylate) thin films, *Macromolecules* 43 (2010) 454–460.
- [34] Y. Chen, H. Bai, Q. Chen, C. Li, G. Shi, A water-soluble cationic oligopyrene derivative: spectroscopic studies and sensing applications, *Sensors Actuators B Chem.* 138 (2009) 563–571.
- [35] S. Piçarra, P. Gomes, J.M.G. Martinho, Fluorescence study of the coil-globule transition of a Poly(ϵ -Caprolactone) chain labeled with pyrenes at both ends, *Macromolecules* 33 (2000) 3947–3950.
- [36] T. Costa, J. Seixas De Melo, H. Burrows, Fluorescence behavior of a Pyrene-End-capped Poly(ethylene Oxide) in organic solvents and in dioxane-water mixtures, *J. Phys. Chem. B* 113 (2009) 618–626.
- [37] S. Chen, J. Duhamel, M. Winnik, Probing end-to-end cyclization beyond willemski and fixman, *J. Phys. Chem. B* 115 (2011) 3289–3302.
- [38] D. Briggs, *Surface Analysis of Polymers by XPS and Static SIMS*, Cambridge University, Cambridge, 2005.
- [39] C. Szczepanski, T. Darmanin, F. Guittard, Using poly(3,4-Ethylenedioxythiophene) containing a carbamate linker as a platform to develop electrodeposited surfaces with tunable wettability and adhesion, *RSC Adv.* 5 (2015) 89407–89414.
- [40] A. Marmur, Hydro- hydro- oleo- omni-phobic? Terminology of wettability classification, *Soft Matter* 8 (2012) 6867–6870.
- [41] A.B.D. Cassie, S. Baxter, Wettability of porous surfaces, *Trans. Faraday Soc.* 40 (5) (1944) 546–551.
- [42] J.V. Morris, M.A. Mahaney, J.R. Huber, Fluorescence quantum yield determinations. 9, 10-diphenylanthracene as a reference standard in different solvents, *Fluoresc. Quantum Yield Determ.* 80 (9) (1976) 969–974.
- [43] J.B. Birks, L.G. Christophorou, Excimer fluorescence spectra of pyrene derivatives, *Spectrochim. Acta* 19 (1963) 401–410.
- [44] Y. Niko, S. Kawauchi, S. Otsu, K. Tokumaru, G. Konishi, Fluorescence enhancement of pyrene chromophores induced by alkyl groups through $\sigma - \pi$ conjugation: systematic synthesis of primary, secondary, and tertiary alkylated pyrenes at the 1, 3, 6, and 8 positions and their photophysical properties, *J. Organomet. Chem.* 78 (2013) 3196–3207.
- [45] L. Qin, B. Lu, J. Xu, G. Zhang, S. Zhang, Novel functionalized conjugated polypyrrole with polyacrylate: synthesis, electrochemistry, luminescence, and chemical sensing properties, *RSC Adv.* 4 (2014) 28368–28376.
- [46] B.W. Rawe, C.M. Brown, M.R. MacKinnon, B.O. Patrick, G.J. Bodwell, D.P. Gates, A C-Pyrenyl poly(methylene phosphine): oxidation “turns on” blue photoluminescence in solution and the solid state, *Organometallics* 36 (2017) 2520–2526 (acs.organomet.6b00880).
- [47] B. Lu, S. Zhen, L. Zhao, G. Zhang, D. Mo, J. Xu, A novel solution-processable amino-group-substituted oligopyrene: synthesis, electropolymerization, properties, and application in fluorescent chemosensor, *Synth. Met.* 198 (2014) 155–160.
- [48] B. Lu, J. Xu, C. Fan, F. Jiang, H. Miao, Facile electrosynthesis of nitro-group-substituted oligopyrene with bicolored emission, *Electrochim. Acta* 54 (2008) 334–340.
- [49] L. Xu, J. Zhao, R. Liu, H. Liu, J. Liu, H. Wang, Electrosyntheses and characterizations of novel electrochromic and fluorescent copolymers based on 2,2-bithiophene and pyrene, *Electrochim. Acta* 55 (28) (2010) 8855–8862.
- [50] S.K. Rajagopal, V.S. Reddy, M. Hantharan, Crystallization induced green-yellow-orange emitters based on benzopyrenes, *CrystEngComm* 18 (27) (2016) 5089–5094.

Conclusions & Perspectives

The use of electropolymerization for the elaboration of micro- and nanostructured surfaces with tunable wettability is an emerging field of investigation. The global aim of this work was to characterize new polymer films: their surface wettability, morphology, photophysical properties and for some of them the anti-bioadhesion properties were as well investigated.

Herein, we demonstrated the potential application of polypyrene films to serve as coatings to prevent bacterial adhesion. Studying fluorinated and nonfluorinated surfaces with different hydrophobicity, it was shown that it is not completely necessary to obtain highly superhydrophobic surfaces to prevent bacterial adhesion. More importantly, the combination between wettability and the topography (micro- and nanostructuring) of the film seemed to play a crucial role.

A reduction between 30-70% in the early bacterial adhesion for non-fluorinated polypyrene and between 60-90% for fluorinated polypyrene was obtained for *S. aureus* and *P. aeruginosa* strains. For longer incubation times, polypyrene surfaces demonstrated a high efficiency against biofilm attachment and reduced by 90-99% the bacteria coverage. These results demonstrate the capability of these surfaces to be used as coatings to prevent bacterial adhesion.

Yet, after participating and presenting this work to the scientific community some important questions to be investigated have arisen: what is the average life and durability of these films? Are they reusable? Are they mechanically resistant? Is there any toxic effect due to their composition and could they be used for eukaryotic cells? Some of these questions shall be further investigated.

For new applications, through another collaboration with Universidad de Valle de Guatemala, it was possible to catch the attention of Dr. Luis Zea, who supervises the study of new materials to prevent biofilm adhesion to be used on the space through a NASA-funded project "Biofilm in Space", from the University of Colorado, Boulder. Finally, in context of this collaboration, new films are being studied by changing pyrene core to another moiety. From this films, new application such as gas-storage are being envisioned. Having a fluorescent material gives the advantage to control if the material is

deteriorated, or not stable over time (either by imaging the topography or measuring the spectra).

In the following chapter another kind of surfaces will be presented, surfaces to kill bacteria.

Chapter 5: Killing Bacteria Surfaces

Introduction

As described in the previous chapters, two general approaches are traditionally followed to obtain antibacterial properties: an antifouling route to prevent bacterial adhesion and antibacterial properties promoting bacteria death (1-6). In the previous chapter, the study and characterization of new antibacterial materials such as *repelling-bacteria* coatings to prevent bacterial adhesion were shown (7-10). Among *killing-bacteria* methods, antimicrobial photodynamic therapy (aPDT), has emerged as a promising approach since it relies on the use of coatings producing reactive oxygen species upon irradiation. This is done in the presence of a photosensitizer, avoiding the use of antibiotics and inorganic antimicrobial agents, which might require a delivery system or might be a threat to the environment (11-16). Another advantage is that most biological entities (bacteria, viruses, parasites and yeast) are highly sensitive to reactive oxygen species, thus these surfaces can also be used against these organisms (15, 17).

This last part of the manuscript will focus on the efficiency of photopolymerized *surfaces to kill* bacteria. They release singlet oxygen upon irradiation. Our input relies on the studies to characterize the antimicrobial effect of the coatings made by an innovative photochemical process to be used on material surfaces for medical applications. The photopolymerization process has many advantages such as a low energy consumption process (visible irradiation), room temperature operation, a very fast polymerization rate with high conversion rate and precise spatial control on where the polymerization takes place (13, 18). The innovation of this project relies on the use of a natural dye: curcumin, which is used both as photosensitizer for the initiation of the polymerization and as a reactive oxygen species promoter for the synthesis of permanent antibacterial coatings (13, 19, 20).

This project was done with the contribution of two main collaborators, whose input and expertise will be described next:

Jean-Pierre Malval from the Institut de Science des Matériaux de Mulhouse (IS2M), his specialty is the fabrication of micro and nanostructured surfaces either by self-assembly, grafting or photopolymerization and their applications. J.P. Malval designed, prepared and characterized the new photopolymerized surfaces including curcumin dye (*Curcumin-grids*, $15 \times 15 \mu\text{m}^2$ and $30 \times 30 \mu\text{m}^2$, Figure 5.2), prepared by Two-Photon Stereolithography (TPS). Details of their manufacturing process will not be described in this manuscript (remaining confidential until publication).

Davy-Louis Versace from the Institut De Chimie Et Des Matériaux Paris-Est- UMR 7182 (Enseignant-Chercheur Univ.Paris-Est Créteil), his specialty relies on the synthesis and characterization of biosourced and biofunctional polymers by photochemistry. D.L. Versace supervised surface incubation with the bacteria and controlled the irradiation process.

Similar to the previous chapter, for this collaboration our main task was to analyze what happens after the irradiation process. For this, fluorescence microscopy was used as our main tool to determine the efficiency of the film to kill bacteria. In the next part, the results obtained from live / dead tests upon irradiation will be discussed.

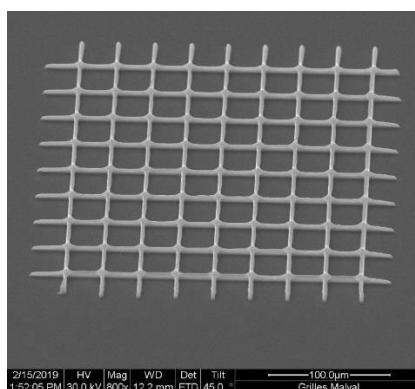


Figure 5.2 SEM image of the Curcumin grids ($30 \times 30 \mu\text{m}$) prepared by Jean-Pierre Malval and Davy-Louis Versace, studied in this project.

- (1) S. Krishnan *et al.*, Advances in polymers for anti-biofouling surfaces, *J. Mater. Chem.*, 2008, 18, 3405.
- (2) I. Banerjee *et al.*, Antifouling coatings: recent developments in the design of surfaces that prevent fouling by proteins, bacteria, and marine organisms, *Adv. Mater.*, 2011, 23, 690.
- (3) R. Poupart *et al.*, Photoactivable Surface of Natural Poly(3-hydroxybutyrate-co-3-hydroxyvalerate) for Antiadhesion Applications, *ACS Biomater. Sci. Eng.*, 2015, 1, 525.
- (4) G. M. Manecka *et al.*, Green Photoinduced Modification of Natural Poly(3-hydroxybutyrate-co-3-hydroxyvalerate) Surface for Antibacterial Applications, *ACS Sustainable Chem. Eng.*, 2014, 2, 996.
- (5) S. El Habnoui *et al.*, Mild Methodology for the Versatile Chemical Modification of Polylactide Surfaces: Original Combination of Anionic and Click Chemistry for Biomedical Applications, *Adv. Funct. Mater.*, 2011, 21, 3321.
- (6) M. L. W. Knetsch and L. H. Koole, New Strategies in the Development of Antimicrobial Coatings: The Example of Increasing Usage of Silver and Silver Nanoparticles, *Polymers*, 2011, 3, 340.
- (7) G. Moran & R. Méallet-Renault, Superhydrophobic Surfaces Toward Prevention of Biofilm-Associated Infections, *Bacterial Pathogenesis and Antibacterial Control*, IntechOpen, DOI: 10.5772/intechopen.72038. Available from: <https://www.intechopen.com/books/bacterial-pathogenesis-and-antibacterial-control/superhydrophobic-surfaces-toward-prevention-of-biofilm-associated-infections>
- (8) G. Moran *et al.*, Superhydrophobic polypyrene films to prevent *Staphylococcus aureus* and *Pseudomonas aeruginosa* biofilm adhesion on surfaces: high efficiency deciphered by fluorescence microscopy, *Photochem. Photobiol. Sci.*, 2018, 17, 1023.
- (9) G. Ramos-Chagas *et al.*, Anti-bacterial and fluorescent properties of hydrophobic electrodeposited non-fluorinated polypyrenes, *Applied Surface Science*, 2018, 452, 352.
- (10) G. Ramos-Chagas *et al.*, Superhydrophobic and fluorescent properties of fluorinated polypyrene surfaces using various polar linkers prepared via electropolymerization, *Reactive and Functional Polymers*, 2019, 135, 65.

- (11) Z. Markovic *et al.*, The mechanism of cell-damaging reactive oxygen generation by colloidal fullerenes, *Biomaterials*, 2007, 28, 5437.
- (12) M. Condat *et al.*, Development of photoactivable glycerol-based coatings containing quercetin for antibacterial applications, *RSC Advances*, 2016, 6, 18235.
- (13) M. Condat *et al.*, Photoinduced curcumin derivative-coatings with antibacterial properties, *RSC Advances*, 2015, 5, 85214.
- (14) A. Valkov *et al.*, Polymer-Immobilized Photosensitizers for Continuous Eradication of Bacteria, *Int. J. Mol. Sci.*, 2014, 15, 14984.
- (15) M. Tim *et al.*, Strategies to optimize photosensitizers for photodynamic inactivation of bacteria, *J. Photochem. Photobiol. B*, 2015, 150, 2.
- (16) R. Cahan *et al.*, Light-activated antibacterial surfaces comprise photosensitizers, *Photochem. Photobiol.*, 2011, 87, 1379.
- (17) G. Jori *et al.*, Photodynamic therapy in the treatment of microbial infections: basic principles and perspective applications, *Lasers Surg Med.*, 2006, 38, 5, 468.
- (18) M. Kaur & A.K. Srivastava, Photopolymerization: A Review, *Journal of Macromolecular Science - Part C - Polymer Reviews*, 2002, 42, 4, 481.
- (19) K.I. Priyadarsini *et al.*, Photophysics, photochemistry and photobiology of curcumin: Studies from organic solutions, bio-mimetics and living cells. *Journal of Photochemistry and Photobiology C: Photochemistry Reviews*, 2009, 10, 2, 81.
- (20) J. Zhao *et al.*, A new role of curcumin: as a multicolor photoinitiator for polymer fabrication under household UV to red LED bulbs, *Polym. Chem.*, 2015, 6, 5053.

5.1 Article 5: “Highly Virulent Bactericidal Effects of Curcumin-based μ -Cages Fabricated by Two-Photon Polymerization.”

D.L. Versace, G. Moran, M. Belqat, A. Spangenberg, R. Méallet-Renault,
S. Abbad-Andalousi, V. Brezová and J.P. Malval

Submitted

Highly Virulent Bactericidal Effects of Curcumin-based μ -Cages Fabricated by Two-Photon Polymerization.

Davy-Louis Versace^[a], Gabriela Moran^[b], Mehdi Belqat^[c], Arnaud Spangenberg^[c], Rachel Méallet-Renault^[b], Samir Abbad-Andaloussi^[d], Vlasta Brezová^[e] and Jean-Pierre Malval*^[c]

Abstract: A new antibacterial strategy is reported based on the two-photon fabrication of three-dimensional curcumin-embedded μ -cages. Such devices were designed to entrap and kill *S. aureus* bacteria upon visible light irradiation. The proposed concept mainly relies on the pivotal role of curcumin which is sequentially used as two-photon active free radical initiator and as photogenerator of reactive oxygen species within the cages μ -volumes. We show that these μ -cages exhibit extremely high antimicrobial properties leading to 95 % bacteria mortality after only 10 min irradiation whereas the same photoactive materials polymerized in thin-film configuration hardly impacts the bacteria viability. A pre-concentration mechanism of photogenerated oxygen species is proposed to account for this bactericidal effect whose virulence can be strikingly switched-on by increasing the light exposure time from 5 to 10 min.

Hospital-acquired nosocomial infections constitute a major public health issue which is responsible for thousands deaths worldwide every year. These infections have been classified as one of the greatest concerns by the World Health Organization. The indiscriminate use of antibiotics in various activity sectors has also accelerated the emergence of multi-drug resistant strains. As a consequence, the projected mortality rate in 2050 may reach 10 million annually due to bacteria infections, which is far higher than the mortality rate for cancer. In this context, considerable research efforts have been invested to cope with this growing societal threat. A very large panel of antimicrobial strategies have been proposed such as the development a small molecule inhibitors which directly interfere with bacterial homeostasis^[1], the design of stimuli-responsive materials incorporating drug delivery functionalities^[2-4], the use of bactericidal organic^[5] or inorganic^[6] nanoparticles. Of particular interest,

the antimicrobial coatings which constitute a versatile therapeutic platform for biomedical applications^[6-8] offer two distinctive operating modes : repelling or bactericidal actions. In this latter case, the photodynamic inactivation of bacteria based on light-sensitive nature-inspired surfaces appears as one of the most promising strategies^[3, 7, 9]. In line with this approach, we present herein an innovative 'one-pot' surface two-photon patterning method which takes advantage of the multi-faceted properties of curcumin (**Figure 1A**). This natural dye which exhibits very interesting photocytotoxicity^[4, 10, 11] and two-photon activable reactivity has been associated with a triacrylate resin allowing the microscale patterning of periodic 3D μ -cages upon two-photon polymerization. Such a nonlinear excitation mode offers a mean to spatially control the photoinitiating reactions and thereby fabricate intricate 3D-structures^[12, 13]. The curcumin-embedded μ -cages are judiciously employed as pre-concentrators for photogenerated antimicrobial agent leading to an original trap and an efficient way of killing bacteria whose mechanism and efficiency are presented hereafter.

Figure 1B shows the one-photon absorption (1PA) spectrum of curcumin (**CUR**) in acetonitrile (ACN) along with its corresponding excitation anisotropy spectrum recorded in triacetin. The low-energy region of the 1PA spectrum is dominated by a single intensive band ($\epsilon \sim 65000 \text{ M}^{-1} \text{ cm}^{-1}$) located in the 310-500 nm range. This band mainly corresponds to a strongly allowed $S_0 - S_1$ transition whose electronic configuration implies π -delocalization all along the main axis of the chromophore and exhibits a charge transfer character from the two external phenol subunits (donors) to the central β -diketone core (acceptor). Such a significant conjugation length which is extended to the entire backbone of **CUR** should be connected to the hydrogen lability of the central CH_2 group which promotes the formation of the planar conjugated enol form^[14, 15]. The presence of a single electronic transition (S_0-S_1) within the longest wavelength absorption band agrees very well with the invariance of the excitation anisotropy in this spectral region. In addition, this anisotropy strongly decreases below 390 nm from a value of ca. 0.33 to 0.18 and remains stable in the 315-340 nm range. These latter effects obviously indicate the presence of higher energy transitions, presumably S_0-S_2 one, with a distinctive electronic symmetry as that observed for the S_0-S_1 transition. The two-photon absorption (2PA) spectrum of **CUR** in ACN is also depicted in **Figure 1B**. The 2PA spectrum is plotted against half the excitation wavelength to have a direct comparison with the 1PA spectrum. The main 2PA band of **CUR** ($\lambda_{\text{max}} = 740 \text{ nm}$) presents a moderate intensity with a δ_{max} of about 110 GM. As shown in **Figure 1B**, such a band is largely blue shifted with respect to lowest energy 1PA band and should presumably correspond to the two-photon active S_0-S_2 electronic transition. According to the dipole selection rules associated to centrosymmetric quadrupole-like

- [a] Dr. D.-L. Versace
ICMPE, CNRS-UPEC UMR 7182
Université Paris-Est Créteil (UPEC)
94320 Thiais (France)
E-mail: versace@icmpe.cnrs.fr
- [b] Dr. G. Moran, Prof. R. Méallet-Renault
ISMO, CNRS – Building 520
Université Paris-Saclay, Univ. Paris-Sud
91405 Orsay (France)
- [c] Dr. M. Belqat, Dr. A. Spangenberg, Dr. J.-P. Malval
IS2M, CNRS
Université Haute Alsace
68057 Mulhouse (France)
E-mail: jean-pierre.malval@uha.fr
- [d] Dr. S. Abbad-Andaloussi
Laboratoire Eau, Environnement et Systèmes Urbains (LEESU),
UMR MA 102, Université Paris-Est Créteil (UPEC)
61, avenue du général de Gaulle
94320 Thiais (France)
- [e] Prof. Vlasta Brezová, Institute of Physical Chemistry and Chemical
Physics, Faculty of Chemical and Food Technology, Slovak
University of Technology in Bratislava, SK-812 37 Bratislava
(Slovak Republic)

Supporting information for this article is given via a link at the end of the

structures, the S_0-S_1 transition of **CUR** is theoretically two-photon forbidden. However, one clearly observes that the dye 2PA spectrum displays a weakly intensive shoulder in the 400–450 nm range suggesting that the S_0-S_1 transition remains partially allowed with a $\delta_{800\text{ nm}}$ of about $\sim 25\text{ GM}$ for instance. This effect should be ascribed to a geometrical relaxation forming a conformation with lower symmetry. Therefore, it is clear that **CUR** can be excited upon NIR two-photon excitation. The singlet excited state of curcumin mainly deactivates through non radiative deactivation pathways implying internal conversion upon H-transfer within the enol structure^[16, 17].

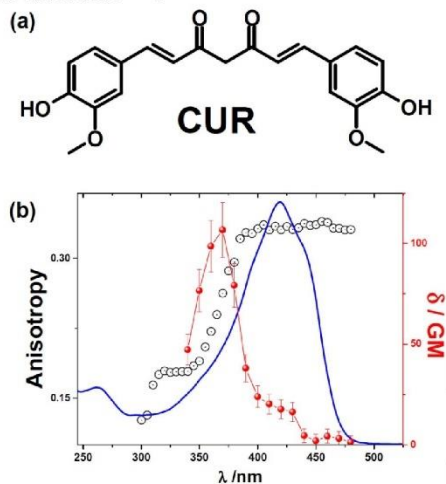


Figure 1. (a) Molecular structure of curcumin (**CUR**). (b) 1PA (full line) and 2PA (full circles) absorption spectra of **CUR** in acetonitrile. Excitation anisotropy spectrum in triacetin (open circles). The 2PA spectrum is plotted against half of the excitation wavelength.

Because of the keto-enol equilibrium of the heptadienone moiety of **CUR**, it has been previously demonstrated that curcumin acts as a very efficient H-donor^[15] reactant due to the two labile hydrogens of central CH_2 . In parallel, the curcumin triplet excited species is an efficient H-abstractor and its self-quenching rate measured by Gorman *et al.*^[16, 17] ($k_{\text{sq}} = 5 \times 10^8\text{ M}^{-1}\text{ s}^{-1}$) exhibits one of the highest value observed for aromatic ketones. As a consequence, curcumin exhibits an amphoteric-like feature with regards to its H-donor and H-abstractor propensity. Therefore, we used this very interesting property to promote two-photon induced free radical polymerization on the basis of a simple one-component formulation associating the pentaerythritol triacrylate monomer (PETIA) and **CUR** (4 %w). A drop of the latter resin is placed on the top of a glass microscope slide which surface was previously treated with (3-acyloxypropyl)trimethoxysilane to promote adhesion of the two-photon patterned structure. The 3D microstructures were generated by exciting the acrylate resin at 800 nm using a 40X, 0.65-NA objective. The micro-sized pattern was impressed into the resin by 3D translation of the laser focus point. The final structure is obtained by dissolving away the nonpolymerized resin using ethanol. **Figures 2A–B** show the

scanning electron micrographs (SEMs) for different views of a typical $290 \times 290\ \mu\text{m}$ grid composed by periodic $30 \times 30\ \mu\text{m}$ square cages which will be used to entrap *S. aureus* bacteria. The dimension of the cages has been modulated going from 15 to $45\ \mu\text{m}$ lateral size. The height was maintained constant and has an average value of about $4.1 \pm 0.4\ \mu\text{m}$ which is \sim four times higher than *S. aureus* feature size and consequently sufficient to trap the bacteria. Interestingly, and according to fluorescence studies, not all **CUR** react during the two-photon polymerization and are embedded into the polymer microstructure as shown in **Figures 2C–D** which present a fluorescence image of the μ -grid and its corresponding fluorescence spectrum which matches that of **CUR** in PETIA monomer (**Figure S1**). Interestingly, any fluorescence of **CUR** was not observed inside the grid after rinsing, demonstrating thus that the diffusion of **CUR** did not occur.

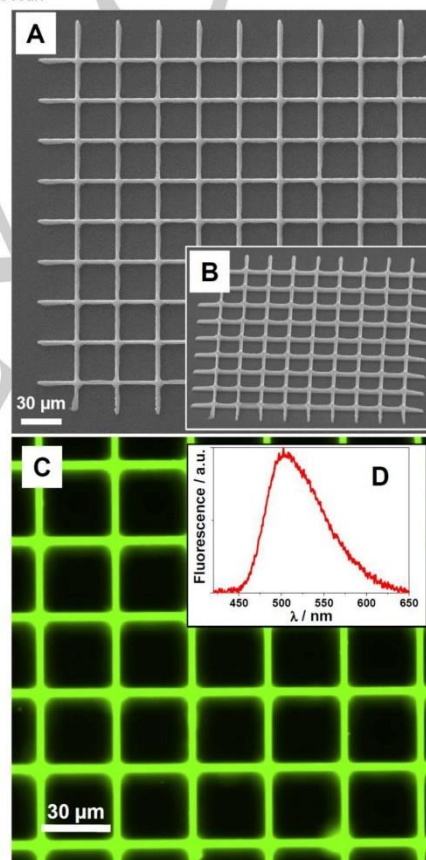


Figure 2. **A.** SEM of a $290 \times 290\ \mu\text{m}$ grid composed by periodic $30 \times 30\ \mu\text{m}$ square cages fabricated by 2P induced polymerization (λ_{ex} : 800 nm, E_{ex} = 20 μJ). **B.** 45° tilted view. **C.** Fluorescence image of the two-photon patterned microgrid. **D.** Recorded fluorescence spectrum of embedded **CUR** within the grid.

It is clear that such a curcumin-embedded material constitutes an abundant source of photosensitizers that can be used for the generation of reactive oxygen species (ROS) within the confined environment of the μ -cages. To evaluate the antibacterial effects of these μ -cages, *S. aureus* ATCC6538 strains have been cultivated within the cages. The bacteria were incubated aerobically in Luria-Bertani (LB) broth overnight at 37 °C, under stirring. The resulting cultures were diluted to an optical density (OD 600 nm) of 0.05 in sterile LB broth. The μ -cages were entirely immersed in 3 mL of the bacterial solution during 20h incubation. Half of the samples were kept in the dark and used as references, the others ones were irradiated for distinctive durations going from 5 to 60 min. The *S. aureus* samples were then co-stained with FM@5-95 dye and propidium iodide (PI). FM@5-95 is a green fluorescent dye which stains both live and dead bacteria membranes whereas PI is a red fluorescent dye which tags only the dead bacteria cells^[18]. The fluorescent images of cages entrapping bacteria were collected using confocal microscopy. **Figure 3A** typically shows reference (non-irradiated) and 10 min-irradiated 15 x 15 μ m cages with entrapped *S. aureus* bacteria. **Table S1** gathers all the bacteria mortality rates in various operating conditions. **Tables S2-S12** show data with and without irradiation on curcumin microgrids as well as controls on glass slide substrates, TPO-based micro-cages and curcumin-based films.

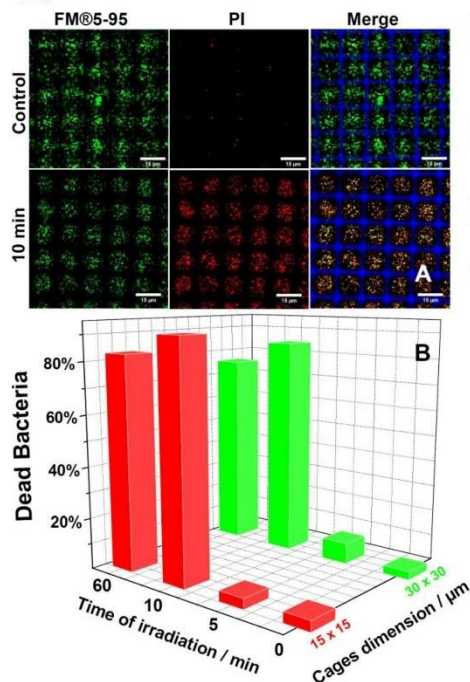


Figure 3. A. Fluorescence images of *S. aureus* entrapped in 15 x 15 μ m cages without (top) and after (bottom) irradiation (10 min). **B.**

Antibacterial efficiency of μ -cages as function of the irradiation time and the cages dimension.

First, the majority of the incubated bacteria remain alive when the samples are kept in the dark during 24 h. This control experiment confirms the absence of any cytotoxicity of the curcumin-embedded materials. By contrast, when the cages are irradiated during only 10 min, a very strong increase of bacteria mortality is observed with a rate higher than 90 %. It should be emphasized that 10 min irradiation appears as an optimum value since 60 min irradiation leads to equivalent antibacterial effect (**Figures S2-S3, Tables S2-S5**). The influence of cages lateral dimension on the antibacterial activity has been also investigated as shown in **Table S4 and Figure S3**. One clearly observes that a 2- or 3-fold increase of the cages size does not affect significantly the amount of dead bacteria whose mortality rate remains higher than 80 % after 10 min irradiation. As comparative experiments, similar polyacrylate-based cages with 15 μ m feature size have been fabricated using Lucirin TPO-L (4 %w in PETIA) as alternative two-photon initiator. Such an acyl phosphine oxide photoinitiator is routinely used for 3D-stereolithography^[12] and leads to a final patterned material which is perfectly transparent to the visible-light irradiation source used (see **Figure S4**). Therefore, on the basis of the same methodology used for CUR, we observed that the mortality rate of bacteria hardly reaches ~ 10 % even after 60 min of irradiation (**Figure S5; Tables S6-S7**). Results are compared with glass slide surfaces (**Figure S5, Tables S8-S10**). Such reference experiments clearly confirm that bacteria mainly survive when entrapped within transparent polyacrylate cages and visible-light irradiation has a weak influence on bacterial death. It should also be emphasized that the overall time-scale for the bacteria inactivation process should comprise three distinctive sequences: *i*) the photogeneration of ROS *ii*) their subsequent diffusion *iii*) the occurrence of a transient diffusion regime leading to a pre-concentration effect of antibacterial agents. Since the bacteria mortality remains very high even with a 3-fold increase of the μ -cages lateral size, it should be inferred that this overall time-scale is presumably short in such manner that majority of bacteria are rapidly exposed to the lethal dose of ROS. To demonstrate the role of the μ -cages as pre-concentrators, the antibacterial performances of the cages have been compared to that of a photopolymerized thin-film using the same curcumin-based formulation (**Figure S6, Tables S11 and S12**). A drop of the triacrylate resin was spread on a glass slide then cured at 365 nm yielding a 20 μ m thick film. Note that the fluorescence spectrum recorded from the film remains perfectly comparable to that of the curcumin embedded in μ -cages. As shown in **Tables S1 and S12**, after 10 min irradiation, more than 95 % of bacteria still remain alive at the film surface which drastically contrasts to the 95 % of dead bacteria within the μ -cages. Therefore, it is clear that the μ -metric dimension of the two-photon patterned cages plays a decisive role for the bactericidal properties. The pre-concentration of ROS within the μ -cages presumably stems from a light-triggered transient regime in which the amount of photogenerated ROS is high enough to promote a strong increase of the local concentration. In order to modulate such a pre-concentration effect, the time of irradiation has been reduced to 5 min. As a striking result, we observed a quasi-suppression of the μ -cages antimicrobial properties (**Figure 3B, Tables S1 and**

S3). Such a threshold effect between 10 and 5 min irradiation indicates the occurrence of an induction time necessary to reach the lethal concentration of reactive species. This induction time also suggests that the reactive species which is mainly responsible for bacteria mortality results from a multi-step reaction whose kinetics leads to a drastic acceleration of its production after this induction period.

The photocytotoxicity^[10, 11] of curcumin is well established and previous investigations^[9, 10, 19, 20] have shown that the irradiation of the dye in aqueous medium potentially generates various reactive oxygen species such as the singlet oxygen (¹O₂), the superoxide (O₂^{•-}) and its conjugate acid (HO₂[•]), the hydroxyl radical ([•]OH) and the hydrogen peroxide (H₂O₂). In our present 'non-contact' μ -cage approach, a relatively long lifetime species is necessary due to its long range diffusion and its further accumulation within the μ -volumes. In this context, the singlet oxygen can be clearly excluded since its lifetime in aqueous medium is very short ($\sim 2 \mu\text{s}$ ^[21]) with a related mean free path in the 100 nm range^[22]. Despite its short lifetime in water, the superoxide O₂^{•-} constitutes a very interesting candidate since this transient radical can subsequently generate other active species with longer lifetime such as H₂O₂^[19, 23]. In order to demonstrate the effective photogeneration of the superoxide, EPR spin-trapping experiments were performed during *in situ* light-exposure of **CUR** in water/ACN medium. **Figure 4** displays the EPR spectrum measured in a continuously irradiated solution of **CUR** in presence of 5-(*tert*-butoxycarbonyl)-5-methyl-1-pyrroline *N*-oxide (BMPO).

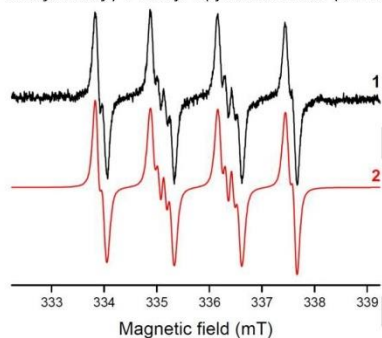


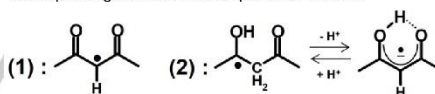
Figure 4. Experimental (1) and simulated (2) EPR spectra of spin-adducts obtained during *in-situ* LED@VIS exposure ($\lambda > 420 \text{ nm}$) of an aerated solution of **CUR** in mixed solvent water/acetonitrile (1:1, vol.) in presence of spin trapping agents BMPO.

BMPO is a suitable spin trap for the simultaneous detection of superoxide radical anions and hydroxyl radicals due to the improved stability of superoxide spin-adduct in the aqueous media ($t_{0.5} = 23 \text{ min}$) and limited transformation of [•]BMPO-O₂H to [•]BMPO-OH. The EPR spectrum clearly corresponds to the generation of [•]BMPO-O₂[•]/O₂H spin-adducts only, *i.e.* conformer I (O₂^{•-}, $a_N = 1.290 \text{ mT}$, $a_H^\beta = 1.165 \text{ mT}$; $g = 2.0059$; $c_{\text{rel}} = 52.1 \%$) and conformer II (HO₂[•], $a_N = 1.287 \text{ mT}$, $a_H^\beta = 0.929 \text{ mT}$; $g = 2.0059$; $c_{\text{rel}} = 47.9 \%$) due to the presence of two diastereoisomers^[24]. The EPR spin-trapping measurements clearly identify O₂^{•-} and its conjugate acid HO₂[•] as photogenerated radical species. Since the pK_a of HO₂[•] / O₂^{•-} is about 4.8 ^[19, 23], the acid-base equilibrium in

neutral pH should be largely displaced in favour of O₂^{•-}. Therefore, the detected perhydroxyl radical (HO₂[•]) presumably stems from an acid base reaction between superoxide and **CUR** ($pK_a^1 \sim 7.8$) as previously observed for similar *o*-methoxyphenol derivatives^[25]. Moreover, O₂^{•-} is known to be unstable in aqueous medium and undergoes a fast disproportionation in H₂O forming O₂ and hydroperoxide anion (HO₂⁻) as follows^[19, 23]:



The hydroperoxide anion (HO₂⁻) which is a strong Brønsted base leads quantitatively to its conjugate acid (H₂O₂) in aqueous medium. Therefore, the hydrogen peroxide can be produced upon a multiple-step sequence which first implies a light-triggered electron transfer reaction to O₂ yielding O₂^{•-}. The role of the S₁ state of **CUR** as potential electron donor can be excluded since its emission lifetime is insensitive to the presence of dissolved oxygen. By contrast, the T₁ state of **CUR** is very sensitive to oxygen with a high bimolecular rate constant^[16] of $\sim 3 \times 10^9 \text{ M}^{-1} \text{ s}^{-1}$. However this deactivation pathway mainly corresponds to a triplet-triplet energy transfer ($S_A \sim 1$) yielding ¹O₂ species which are known to be hardly reactive to **CUR**^[16]. As previously indicated, the triplet self-quenching reaction of **CUR** constitutes an additional deactivation process which has been used to promote free radical two-photon polymerization. Due to the large amount of embedded curcumin into the photopatterned polymer (4 % w), such a self-quenching reaction should remain active upon the irradiation of the μ -cages. According to the H-transfer mechanism which mainly implies the β -diketone group, two short-lived carbon-centered radicals are generated^[14, 15]. Their corresponding structures are depicted as follows:



The radical (1) produced upon an H-abstraction reaction can be scavenged by O₂ to generate a peroxy radical^[26] whereas the ketyl radical (2) is less sensitive to oxygen and can undergo a fast deprotonation in protic medium^[27] to form the radical anion of curcumin (**CUR**^{•-}). This latter reducible species constitutes a very good candidate for the subsequent production of superoxide. In order to highlight the reactivity of **CUR**^{•-} in presence of oxygen, we have performed spectroelectrochemical measurements of **CUR** in ACN. The radical anion of **CUR** was electrogenerated at the surface of a transparent platinum gauze electrode by applying a constant potential allowing the one-electron reduction of **CUR**. This potential was adjusted to minimize the simultaneous reduction of oxygen when working in aerated conditions (see **Figure S7**). **Figure 5A** depicts the time dependent changes of the absorption spectrum of **CUR** in N₂-saturated acetonitrile during the first 30 s of the reduction reaction. The longest wavelength absorption of **CUR** rapidly collapses in concomitance with the growth of a new broad band in the 530-650 nm range which corresponds to the absorption band **CUR**^{•-}. Interestingly, when performing the same experiment in presence of oxygen (**Figure 5B**), the amount of radical anion is divided by more than a factor 2 and a new absorption band gradually increases in the 430-530 nm range. The presence of an isosbestic point at 444 nm denotes the

occurrence of a fast equilibrium reaction. All these spectral changes in presence of oxygen clearly confirm the significant reactivity of $\text{CUR}^{\cdot-}$ in presence of dissolved oxygen. Once electrogenerated, $\text{CUR}^{\cdot-}$ is rapidly oxidized by oxygen generating $\text{O}_2^{\cdot-}$ and CUR . Both by-products consequently react to each other through an acid base reaction^[25] yielding HO_2^{\cdot} and the enolate base form of CUR . In order to demonstrate that the presence of $\text{CUR}^{\cdot-}$ can effectively generate the hydrogen peroxide (H_2O_2) as an ultimate product, a large amount of radical anion was electrogenerated upon 1 min reduction of a similar N_2 -degassed ACN solution of CUR . After 30 min re-oxygenation of the solution allowing the total consumption of $\text{CUR}^{\cdot-}$, an aliquot of 300 μL is rapidly transferred into an aqueous basic solution of luminol whose chemiluminescence is monitored at 420 nm.

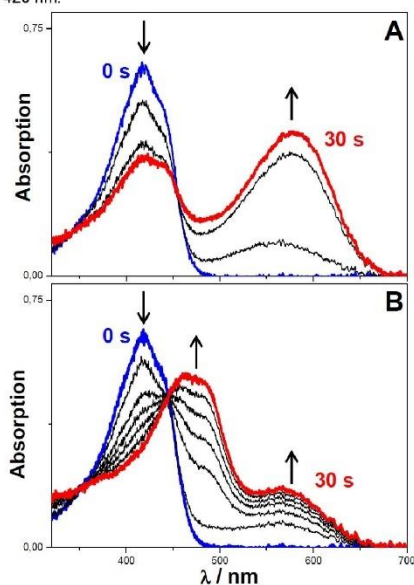


Figure 5. Time-dependent changes of the absorption spectrum of CUR in N_2 -degassed (A) and aerated (B) ACN solutions upon reduction reaction at constant potential of -1.04 V / SCE . ($[\text{CUR}] = 0.5 \text{ mM}$, $\text{TBAPF}_6 = 0.1 \text{ M}$)

As shown in **Figure S8**, the introduction of the aliquot leads to a very strong increase of the chemiluminescence signal which demonstrates that the luminol is oxidized presumably due to the presence of a long-time living oxidizing agent such as H_2O_2 . Note that a control experiment implying an ACN solution of CUR without the electrolysis step does not lead to any chemiluminescent reaction with luminol.

In summary, we have developed an original bactericidal strategy based on the two-photon fabrication of polyacrylate μ -cages with embedded curcumin. One of the angular stones of this approach relies on the three-faceted properties of this natural dye which was sequentially used as two-photon active chromophore, H-donor/H-abstractor initiator and ROS photogenerator. Such μ -cages exhibit a very impressive

photocytotoxicity with a bacteria mortality rate of 95 % after only 10 min irradiation. A pre-concentration mechanism of H_2O_2 within the cages μ -volumes is responsible for this strong oxidative stress whose virulence can be strikingly switched-off by a simple modulation of the irradiation time.

Acknowledgments.

Dr. Davy-Louis VERSACE would like to thank French Research National Agency (ANR), UPEC and ICMPE for financial support. Vlasta BREZOVÁ thanks Ministry of Education, Science, Research and Sport of the Slovak Republic for funding within the scheme "Excellent research teams" and Scientific Grant Agency of the Slovak Republic (VEGA Project 1/0026/18) for financial support. This work was supported by a grant from the Ministère de l'Éducation Nationale, de l'Enseignement Supérieur et de la Recherche, Université Paris-Sud Paris-Saclay, for Gabriela Moran's Ph.D. thesis (ED 2MIB N°571).

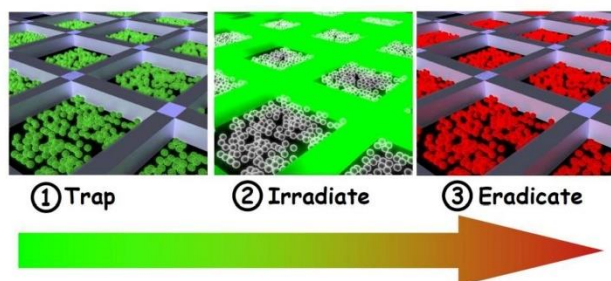
We thank the Centre de Photonique Biomédicale (CPBM) of the Centre Laser de l'Université Paris-Sud (CLUPS/LUMAT FR2764, Orsay, France) for allowing us to use the confocal microscope and L2 microbiology facilities.

Keywords: Antimicrobial Materials • Two-Photon Polymerization • Curcumin

- [1] A. N. D. Puncti Hewage, H. Yao, B. Nammalwar, K. K. Gnanasekaran, S. Lovell, R. A. Bunce, K. Eshelman, S. M. Phaniraj, M. M. Lee, B. R. Peterson, K. P. Battaille, A. B. Reitz and M. Rivera, *J. Am. Chem. Soc.* **2019**, *141*, 8171-8184.
- [2] V. Dubovoy, A. Ganti, T. Zhang, H. Al-Tameemi, J. D. Cerezo, J. M. Boyd and T. Asafa, *J. Am. Chem. Soc.* **2018**, *140*, 13534-13537.
- [3] M. Karimi, P. Sahandi Zangabad, S. Baghace-Ravari, M. Ghazadeh, H. Mirshekari and M. R. Hamblin, *J. Am. Chem. Soc.* **2018**, *139*, 4584-4610.
- [4] M. W. Tibbitt, J. E. Dahlman and R. Langer, *J. Am. Chem. Soc.* **2016**, *138*, 704-717.
- [5] A. Gupta, R. F. Landis, C.-H. Li, M. Schurr, R. Das, Y.-W. Lee, M. Yazdani, Y. Liu, A. Kozlova and V. M. Rotello, *J. Am. Chem. Soc.* **2018**, *140*, 12137-12143.
- [6] Q. Wu, G. Wei, Z. Xu, J. Han, J. Xi, L. Fan and L. Gao, *ACS Appl. Mater. Interfaces* **2018**, *10*, 25026-25036.
- [7] D. Campoccia, L. Montanaro and C. R. Arciola, *Biomaterials* **2013**, *34*, 8533-8554.
- [8] S. Noimark, C. W. Dunnill, M. Wilson and I. P. Parkin, *Chem. Soc. Rev.* **2009**, *38*, 3435-3448.
- [9] L. N. Silva, K. R. Zimmer, A. J. Macedo and D. S. Trentin, *Chem. Rev.* **2016**, *116*, 9162-9236.
- [10] M. Condat, P. E. Mazeran, J. P. Malval, J. Lalcvéc, F. Morlet-Savary, E. Renard, V. Langlois, S. Abbad Andaloussi and D. L. Versace, *RSC Adv.* **2015**, *5*, 85214-85224; T. A. Dahill, P. Bilski, K. J. Reszka and C. F. Chignell, *Photochem. Photobiol.* **1994**, *59*, 290-294.
- [11] E. M. Bruzell, E. Morisbak and H. H. Tonnesen, *Photochem. Photobiol. Sci.* **2005**, *4*, 523-530.
- [12] C. N. LaFratta, J. T. Fourkas, T. Baldacchini and R. A. Farrer, *Angew. Chem. Int. ed.* **2007**, *46*, 6238-6258.
- [13] S.-Y. Yu, G. Schrodj, K. Mougjin, J. Dentzer, J.-P. Malval, H.-W. Zan, O. Soppera and A. Spangenberg, *Advanced Materials* **2018**, *30*, 1805093.
- [14] S. V. Jovanovic, C. W. Boone, S. Steenken, M. Trinoga and R. B. Kaskay, *J. Am. Chem. Soc.* **2001**, *123*, 3064-3068.
- [15] S. V. Jovanovic, S. Steenken, C. W. Boone and M. G. Simic, *J. Am. Chem. Soc.* **1999**, *121*, 9677-9681.

- [16] C. F. Chignell, P. Bilskj, K. J. Reszka, A. G. Motten, R. H. Sik and T. A. Dahl, *Photochem. Photobiol.* **1994**, *59*, 295-302.
- [17] A. A. Gorman, I. Hamblett, V. S. Srinivasan and P. D. Wood, *Photochem. Photobiol.* **1994**, *59*, 389-398.
- [18] Z. Wang, K. Dong, Z. Liu, Y. Zhang, Z. Chen, H. Sun, J. Ren and X. Qu, *Biomaterials* **2017**, *113*, 145-157.
- [19] M. Hayyan, M. A. Hashim and I. M. AlNashif, *Chem. Rev.* **2016**, *116*, 3029-3085.
- [20] D. Zhang, S. Yan and W. Song, *Environ. Sci. Technol.* **2014**, *48*, 12645-12653.
- [21] P. B. Merkel and D. R. Kearns, *J. Am. Chem. Soc.* **1972**, *94*, 1029-1030.
- [22] M. K. Kuimova, G. Yahioglu and P. R. Ogilby, *J. Am. Chem. Soc.* **2009**, *131*, 332-340; S. Hatz, L. Poulsen and P. R. Ogilby, *Photochem. Photobiol.* **2008**, *84*, 1284-1290.
- [23] D. T. Sawyer and J. S. Valentine, *Acc. Chem. Res.* **1981**, *14*, 393-400.
- [24] H. Zhao, J. Joseph, H. Zhang, H. Karoui, and B. Kalyanaraman, *Free Radic. Biol. Med.* **2001**, *31* 599-606
- [25] C. P. Andrieux, P. Hapiot and J. M. Saveant, *J. Am. Chem. Soc.* **1987**, *109*, 3768-3775; B. Mishra, K. Indira Priyadarsini, M. K. Bhide, R. M. Kadam and H. Mohan, *Free Radical Res.* **2004**, *38*, 355-362.
- [26] R. S. Davidson in *Radiation Curing in Polymer Science and Technology, Vol. III*, Fouassier, J. P., Rabek, J. F.; Elsevier Science Publishers Ltd., London, **1993**.
- [27] S. F. Yates and G. B. Schuster, *J. Org. Chem.* **1984**, *49*, 3349-3356; J.-P. Malval, M. Jin, L. Balan, R. I. Schneider, D.-L. Versace, H. Chaumeil, A. Defoin and O. Soppera, *J. Phys. Chem. C* **2010**, *114*, 10396-10402; F. Orrica and M. A. J. Rodgers, *Photochem. Photobiol.* **2001**, *74*, 745-751.

Graphical abstract.



An original 'trap and kill' bacteria strategy based on the two-photon fabrication of 3D curcumin-embedded μ -cages has been developed. The designed μ -cages used as H_2O_2 pre-concentrators exhibit a highly virulent photocytotoxicity leading to a bacteria mortality rate of about 95 % after only 10 min of visible irradiation.

General Conclusion & Perspectives

In the present work, the study of different surfaces was done with the main objective to contribute in the long term to the fight of AMR. For this, three main projects were presented: a) Bacterial detection, b) Repelling bacteria surfaces and c) Killing bacteria surfaces. All these projects had a common methodology, which was the implementation of nanotechnology on their design and the use of fluorescence microscopy to determine their efficiencies on bacterial interaction studies. Fluorescence microscopy is a very powerful technique, very well-known by scientists over the world. Such technic is now more and more available, and gives to the user many advantages over techniques like electron microscopies: it is easy to use, it has lower cost and allows the visualization of live microorganisms (like bacteria). Besides, the application of nanotechnology confers 'new' properties to materials, like the electropolymerized nanostructured films which prevent bacterial attachment or the micro grids killing bacteria presumably due to the diffusion of a singlet oxygen and finally the transfer of pH-sensitive nanoparticles to glass to detect cells growth. To conclude, a summary of the main results of each chapter will be done.

First, the synthesis and characterizations of different types of FNPs were carried out successfully. New types of particles were obtained for the first time (FNP_{Red} -with high 'red' BODIPY per particle-, FNP_{G-DIBO} and FNP_{R-DIBO}). FNP_{Red} were the main players in the manuscript, meanwhile FNP_{DIBO} will lead to future studies. The surface charge of the different particles was estimated by ζ -potential. The hydrodynamic radius of the FNPs was characterized by DLS (Dynamic Light Scattering) and NTA (Nanoparticle Tracking Analysis). Concentration was estimated by NTA. TEM (Transmission Electron Microscopy) image analysis allowed for dried diameter estimation. In summary, all FNPs are polydispersed but a mean diameter could be estimated (FNP_{Green}: 80 nm, FNP_{Red}: 110 nm, FNP_{G-DIBO}: 100 nm and FNP_{R-DIBO}: 130 nm). The absorption and emission of FNPs corresponded well to the dyes in the core (green or red- BODIPY). After grafting fluorescein amine (FA) on red FNPs, the spectroscopic characteristics were studied at various pH. The pKa of the grafted fluorescein was determined to be close to the tabulated one(pKa: 6.11). Following, fluorescence quantum yield and lifetime were measured and it was extremely difficult to quantify and probe energy transfer from them. Nevertheless the FNP_{Red-FA} plot of intensity ratio ('green' vs 'red' contributions) shows a very nice pH sensitivity in between

5.5 and 7, which is the perfect window for biological applications such as bacterial growth. Thus, we proceed to our main objective.

Glass-substrates were functionalized by gas-phase silanization and further peptide-coupling was used to graft the different elements for the ratiometric sensor (FNP_{Red} + FA). Then new pH sensitive surfaces were characterized by different techniques. XPS was mainly used to determine the elementary composition of the surfaces after piranha activation, silanization and grafting of the nanoparticles. Different states of Nitrogen allowed to obtain an evolution of the chemical composition at each step allowing to conclude about the presence of the chemical moieties grafted on the surface.

AFM (Atomic Force Microscopy) and SEM (Scanning Electronic Microscopy) allowed to determine the coverage of the FNP on the surface and to qualitatively evaluate the homogeneity of the coverage. The photophysical properties were found to be in good agreement with the spectroscopic properties from the grafted elements in suspension (FNP_{Red} and FA). Similarly to FNPs in suspension, a good pH-sensitivity between 5 and 8 was obtained. From bacterial growth study, the pH could be predicted by knowing the ratio $\alpha_{520/600}$. Nevertheless, more data have to be acquired to correlate the ratio and the bacterial growth efficiently, moreover the methodology to measure pH should be improved. This will be carried out in the coming weeks. To the best of our knowledge, for the first time a pH-sensitive surface was used to detect bacterial growth with a ratiometric measurement.

Then, new micro and nanostructured fluorescent surfaces prepared by electropolymerization were introduced. By changing their polymerization parameters and monomers nature it was possible to tune their topography and thus their wettability. Firstly, a review explaining the main concepts about superhydrophobicity was presented, including their application to medical environments. Different fluorinated and nonfluorinated surfaces with different hydrophobicity were characterized and their efficacy to prevent bacterial adhesion was studied. Besides and most importantly, for the first time, multifunctional (luminescent and superhydrophobic) films allowing to co-localize bacteria and substrate were published. A reduction between 30-70% in the early bacterial adhesion for non-fluorinated polypyrene and between 60-90% for fluorinated polypyrene was obtained for *S. aureus* and *P. aeruginosa*. Polypyrene surfaces demonstrated a high efficiency against biofilm attachment, reduced by 90-99%.

Finally, curcumin-grids prepared by photopolymerization were investigated and their efficiency to kill bacteria was studied. These curcumin-grids surfaces have proven to effectively kill up to $90 \pm 9\%$ *S. aureus* upon irradiation (with a short time of 10 min) due to the assumption of the release of a singlet oxygen. Such coatings proved to be more efficient in term of irradiation time when compared to other studies.

To conclude, this manuscript presents the main results of different projects with the main objective to tune surface properties to either avoid / kill bacteria or detect their growth. In the long term, such surfaces shall be helpful to fight AMR. The complexity and richness of this project arises from the different interfaces studied: liquid-solid-gas, organic and physical-chemistry and microbiology. Besides this project represents the collaboration of many contributors who permitted to achieve our objectives and enriched the project with their scientific discussions and contributions. To conclude, this is an ongoing work, new improvements are being envisioned and further studies will be done.

For pH-sensitive surfaces, as mentioned before, the work will be continued by a PhD student thanks to a CSC grant. Besides, a postdoctoral fellow will work on heavy metals detection using similar surfaces. Further work will be done to improve the sensitivity of the surfaces and to develop a microfluidic system. For DIBO FNPs, other applications such as specific cell targeting should be which are highly attractive for cancer research.

For the electropolymerized films, as mentioned before, new films are being studied (and another publication has been submitted) by changing pyrene core to another chemical moiety. These new films present nanostructures (like tubes) that could be used for gas-storage or another applications such as in drug delivery and catalysis. Besides, for polypyrene films, many questions remained unanswered (such as mechanical stability) and should be investigated due to the antibacterial properties already proven of the materials.

And lastly, as stated before, the curcumin-grids are part of an ongoing project, and many of the remained questions will be further investigated. To ensure the singlet oxygen is diffused more experiments shall be conducted, such as labeling with a reactive oxygen species (ROS) reagents (Molecular Probes).

